UNIVERSITY OF OKLAHOMA

GRADUATE COLLEGE

MOLECULAR DYNAMICS STUDIES OF BENZENE-d_6 ASSOCIATED WITH BLACK CARBON MATERIALS BY LINE SHAPE ANALYSIS OF STATIC SOLID-STATE ^{2}H NUCLEAR MAGNETIC RESONANCE SPECTRA

A DISSERTATION

SUBMITTED TO THE GRADUATE FACULTY

in partial fulfillment of the requirements for the

Degree of

DOCTOR OF PHILOSOPHY

By

LUCINDA A. BROTHERS
Norman, Oklahoma
2009

Downloaded from SHAREOK. Persistent Handle URL: https://hdl.handle.net/11244/319502

MOLECULAR DYNAMICS STUDIES OF BENZENE-d_6
ASSOCIATED WITH BLACK CARBON MATERIALS
BY LINE SHAPE ANALYSIS OF STATIC SOLID-STATE
^{2}H NUCLEAR MAGNETIC RESONANCE SPECTRA

A DISSERTATION APPROVED FOR THE
DEPARTMENT OF CHEMISTRY AND BIOCHEMISTRY

BY

Dr. Richard W. Taylor, Chair

Dr. Mark A. Nanny

Dr. Ralph A. Wheeler

Dr. Robert L. White

Dr. Charles V. Rice

© Copyright by LUCINDA A. BROTHERS 2009
All Rights Reserved.

ACKNOWLEDGMENTS

Thank you, Lord Jesus.

I wish particularly to thank my research advisor, Dr. Mark Nanny, for his careful patience in guiding me to look at as many possible aspects of my data as possible, in carefully evaluating it, and for presenting such interesting and challenging problems to me and all of his students. I am very grateful for my committee members, Dr. Taylor, Dr. Wheeler, Dr. White, and Dr. Rice. Even during the early part of my research, their insightful questions and suggestions gave me refreshed perspectives on my work. I thank all of the students in Dr. Nanny's lab, past and present, including Dr. Nopawan Ratasuk, Dr. Lixia Chen, Dr. Hongxia Lei, Dr. Praveen Gadeed, Dr. Carolina Salazar, Tu Pham, and Christopher Pape, and also my classmates, fellow students, and staff members from the Chemistry Department and the Department of Civil Engineering and Environmental Science, from whom I learned much. I extend my thanks to Dr. Margaret A. Eastman, our research associate and NMR expert *extraordinaire* at Oklahoma State University, for the tremendous amount that I learned from her, still much less than she had to teach. I also thank the O.U. Graduate Fellowship Program and G.A.A.N.N. Fellowship Program and the National Science Foundation for financial support.

The support (moral and financial) of my family has been essential to me throughout my long work as a student. My late father's love of science has always inspired me, and the encouragement from both him and my mother has been empowering. My son stood by me through my academic pursuits, and I have always drawn courage from him to carry on when things are difficult. I also thank my brothers and sisters and extended family for their love and prayers. My longtime love, Dr. William E. Full, has always done his best to help me, whether with little things or solving research problems.

Lastly, I acknowledge all my teachers and professors, particularly those at the Geology and Chemistry Departments from both Wichita State University and the University of Oklahoma, notably my Masters' advisor, Dr. Michael H. Engel.

TABLE OF CONTENTS

Page

LIST OF TABLES xi

LIST OF FIGURES xiv

ABSTRACT xxi

1. INTRODUCTION 1

1.1. Background – General 2

1.1.1. Occurrence and significance of black carbons (BCs) 2

1.1.2. Chemical and porosity structures of BCs 4
1.1.2.1. Graphite 5
1.1.2.2. Soot 7
1.1.2.3. Chars 9
1.1.2.4. BC model substances – Activated carbon 12
1.1.2.5. BC model Substances – Engineered carbon nanoparticles 14
1.1.2.5.1. BC model substances – carbon nanoparticles 15
1.1.2.5.2. BC model substances – carbon nanotubes 16

1.1.3. Sorption interactions of benzene with black carbons 19
1.1.3.1. Isotherm models of HOCs with BCs during the sorption processes 19
1.1.3.2. Models of molecular interactions between HOC/BCs during sorption 23
1.1.3.2.1. LFERs for vapor/solid sorption in environmental systems 24
1.1.3.2.2. Thermodynamics of benzene adsorption on BCs from vapor/solid isotherms 27

1.1.3.3. Surface diffusion 34
1.1.3.3.1. Surface diffusion overview. 34
1.1.3.3.2. LFERs and enthalpy/entropy compensation (EEC) effects in surface diffusion 37
1.1.3.3.3. Fractal dimension, FHH equation, and their relation to surface diffusion 40
1.1.3.3.4. Spectroscopic observations of the motion of benzene on graphite 46

1.2 Observation of molecular motion using ^{2}H static solid-state nuclear magnetic resonance (NMR) 47
1.2.1. Theory 47
1.2.2. Previous ^{2}H NMR studies of the motion of benzene-d_6 associated with solids 54

1.3. Research question 60

References 62

2. EXPERIMENTAL. 76

2.1. Samples and preparation for ^{2}H static solid-state NMR analysis 76
2.1.1. BC solid phases 76
2.1.2. Sample preparation 77

2.2 Static solid-state ^{2}H NMR experiments 78
2.2.1. Instrumental parameters 78
2.2.2. Lineshape analysis of ^{2}H static solid-state NMR spectra 79

2.3 X-ray diffraction and N_2 adsorption experimental parameters 80

References 81

3. BLACK CARBON MATERIALS CHARACTERIZATION USING X-RAY DIFFRACTION (XRD) AND N_2 ADSORPTION 83

3.1. Introductory Summary 83

3.2. Experimental 87

3.3. Results 88
3.3.1. X-ray diffraction 88
3.3.2. N_2 adsorption isotherms 91

3.4. Summary 102

References 103

4. THE MOTION OF BENZENE-d_6 MOLECULES DIFFUSING ON THE SURFACE OF DIESEL SOOT AT VARIABLE TEMPERATURES AND LOADINGS 106

4.1. Introduction 106

4.2. Experimental 108
4.2.1. Materials and sample preparation 108
4.2.2. NMR Analysis and quantitative calibration for soot samples 109

4.3. ^{2}H NMR spectra and simulated fit results 114
4.3.1. ^{2}H NMR spectra for 1% w/w loading 114
4.3.1.1. Type of motion 114
4.3.1.2. Aging 118
4.3.2. Arrhenius data for the pseudoisotropic reorientational motion of 1% w/w loading 120
4.3.3. ^{2}H NMR spectra for variable-loaded samples 127

4.4. Conclusions 132

References 133

5. THE MOTION OF BENZENE-d_6 MOLECULES ON AMORPHOUS CARBON NANOPARTICLES OBSERVED WITH STATIC SOLID-STATE ^{2}H NMR SPECTRA 138

5.1. Introduction 138

5.2. Experimental 141
5.2.1. Materials characterization 141
5.2.2. Sample preparation 141

5.3. Results: ^{2}H static solid-state NMR spectra 143

5.4. Conclusions 153

References 154

6. THE MOTION OF BENZENE-d_6 MOLECULES ON LOW-SURFACE-AREA GRAPHITE (LSAG) OBSERVED WITH STATIC SOLID-STATE ^{2}H NMR SPECTRA 156

6.1. Introduction 156

6.2. Experimental: materials and sample preparation 157

6.3. ^{2}H NMR spectra and results for low-surface-area graphite 160
6.3.1. ^{2}H static solid-state NMR spectra, 25°C 160
6.3.2. ^{2}H static solid-state NMR spectra at variable temperatures 163

6.4. Conclusions 168

References 168

7. THE MOTION OF BENZENE-d_6 MOLECULES ON CARBON NANOTUBES OBSERVED WITH STATIC SOLID-STATE ^{2}H NMR SPECTRA 170

7.1. Introduction 170

7.2. Experimental 177
7.2.1. Materials characterization 177
7.2.2. Sample preparation 179
7.2.3. Quantitation 180

7.3. Results 181
7.3.1. ^{2}H solid-state NMR spectra of benzene-d_6 on CNTs 181
7.3.2. Aging 184
7.3.3. Arrhenius data for the pseudoisotropic reorientational motion 187

7.4. Conclusions 197

References 198

8. THE MOLECULAR MOTION OF BENZENE-d_6 ON MICROPOROUS, HETEROGENEOUS BLACK CARBONS (BCs) 204

8.1. Introduction 204

8.2. Experimental 208

8.3. Results: ^{2}H static solid-state NMR spectra of benzene-d_6 at variable temperatures and ages 210
8.3.1. Distinctively broad spectra. 210
8.3.2. Indicators of motional models from the character of the spectra. 214
8.3.3. Arrhenius behavior of benzene-d_6 on maple wood char 219
8.3.4. Arrhenius behavior of benzene-d_6 on activated carbon 224

8.4. Conclusions 227

References 228

9. COMPARISON OF THE MOLECULAR MOTION OF BENZENE-d_6 ON DIFFERENT BLACK CARBONS (BCs) 231

9.1. Introduction 231

9.2. Experimental 234

9.3. Results: static solid-state ^{2}H NMR spectra 236
9.3.1. Differences in ^{2}H NMR spectra for benzene-d_6 on different BCs 236
9.3.2. Comparison of Arrhenius behavior among benzene-d_6 on different BCs 237
9.3.3. Compensation effects, enthalpy/entropy correlations and fractal dimensions 242
9.3.4. General remarks 251

9.4. Conclusions 253

References 254

10. SUGGESTIONS FOR FUTURE RESEARCH 260

10.1. Molecular motion of benzene-d_6 on a natural wood char combusted at different temperatures 260

10.2. Visualization of fractal pore networks using static solid-state ^{2}H NMR of benzene-d_6 and N_2 adsorption analysis. 261

References 263

APPENDICES 266

A1. Sample preparation and benzene-d_6 calibration details 266
A1.1. Vapor deposition system 266
A1.1.1. Manifold design and construction 266
A1.1.2. Calibration of the mass of benzene vapor within the manifold 267
A1.1.3. Sealing accurate quantities of benzene-d_6 within NMR sample tubes 269
A1.2. Calibration of the quantity of benzene-d_6 with sample tubes using NMR peak area 271
A1.2.1. Preparation of the NMR calibration curve 271
A1.2.2. Plotting the sample areas on the NMR calibration curve. 274
A1.3. Note about least-squares fitting procedure 278
References 279

A2. Deuterium Fitting Program (DFP) 280
A2.1. Library Creation Program 280

A2.2. Visualization of modeled motion: Euler angles and stereonet projection 282
A2.3. Fitting of experimental spectra 284
References 294

A3. Static solid-state ^{2}H nuclear magnetic resonance (NMR) quantitation for benzene-d_6 on carbon nanotube (CNT) at different ages: spectra with NMR areas 295
A3.1. CNS samples 295
A3.2. CNW samples 398
A3.3. Sample SWCNT2 302

A4. Fits of sample ACTC2 with an attempted motional model showing preferential orientation of benzene molecules in micropores 303

LIST OF TABLES

Page

Table 1.1 Enthalpies of adsorption for benzene and related compounds on graphite 29

Table 1.2 Surface fractal dimensions for different solid phases. 44

Table 1.3 Motional modes and energies of activated for benzene-d_6, measured with static solid-state ^{2}H NMR on different solid phases 60

Table 2.1 Properties of black carbon samples 76

Table 3.1 Summary of X-ray diffraction results for black carbons 89

Table 3.2 Pore size distributions for black carbon materials 96

Table 3.3 Fractal dimensions for black carbons from the Frenkel-Hill-Halsey equation 101

Table 4.1 Characteristics of diesel soot (NIST #2975) 110

Table 4.2 Samples of benzene-d_6 on NIST #2975 soot 110

Table 4.3 NMR quantitation for soot samples at different temperatures . . 112

Table 4.4 Peak widths at half-height ($\delta\nu$) of the ^{2}H static solid-state spectra of benzene-d_6 on Soot1 at different ages 119

Table 4.5 Arrhenius plots of benzene-d_6 on Soot1 at different ages using DFP and peak width 124

Table 4.6 Jump rates and peak widths for Arrhenius of variable loaded samples 129

Table 4.7 Arrhenius data for benzene-d_6 on soot at different loadings using both DFP and peak width 131

Table 5.1 Characteristic of carbon nanoparticles 138

Table 5.2 Samples of benzene-d_6 on carbon nanoparticles 142

Table 5.3 Peak widths at half-height ($\delta\nu$) of the ^{2}H static solid-state

spectra of benzene-d_6 on CNP samples at different ages and temperatures 146

Table 5.4 Arrhenius data for benzene-d_6 on CNP at different ages using both DFP and the peak width method 151

Table 6.1 Characteristics of low-surface-area graphite 157

Table 6.2 Samples of benzene-d_6 on low-surface-area graphite 158

Table 6.3 Spectral data from the ^{2}H static solid-state spectra of benzene-d_6 on low-surface-area graphite at different temperatures 165

Table 6.4 $\delta\nu$ (Hz) of the static solid-state ^{2}H NMR spectra of benzene-d_6 on low-surface-area graphite samples at different temperatures 166

Table 7.1 Characteristics of CNTs 178

Table 7.2 Samples of benzene-d_6 on CNTs 180

Table 7.3 Peak widths at half-height, $\delta\nu$, for pseudoisotropic peaks at early ages for benzene-d_6 on CNT samples 184

Table 7.4 Peak widths at half-height, $\delta\nu$, for pseudoisotropic peaks from different ages for benzene-d_6 on CNW2 185

Table 7.5 NMR peak areas, normalized to the value at 15°C, for benzene-d_6 on CNT samples 188

Table 7.6 Arrhenius data of benzene-d_6 on SWCNT from peak widths . . 192

Table 7.7 D_0 values for CNTs diffusion on inner and outer tube surface and in interstices 194

Table 8.1 Elemental composition and polar functionalities of MWC and AC 204

Table 8.2 Pore and surface area properties of AC and MWC 204

Table 8.3 Samples of benzene-d_6 on MWC and AC 209

Table 8.4 Peak widths at half-height ($\delta\nu$) of the ^{2}H static solid-state spectra of benzene-d_6 on AC at different temperatures and ages 211

Table 8.5 Peak width at half-height ($\delta\nu$) of the ^{2}H static solid-state spectra

of benzene-d_6 on MWC at different temperatures and ages . . . 213

Table 9.1 Correlation times and energies of activation for benzene-d_6 on various solid phases measured with static solid-state ^{2}H NMR 238

Table 9.2 Ratios of E_a/Q_0^{st} for benzene-d_6 on different solids 243

Table 9.3 Diffusivity, fractal dimensions, and pore sizes for BCs and others 246

Table A1.2 Calibration NMR area values for neat benzene-d_6 272

Table A3.1 Peak widths at half-height, δν (kHz), for CNS samples at different ages 297

Table A3.2 Spectral areas for CNS samples at different ages 298

Table A3.3 Peak widths at half-height, δν (kHz), for CNW samples at different ages 301

Table A3.4 Spectral areas for CNW samples at different ages 301

LIST OF FIGURES

Page

Figure 1.1 Scanning electron microscopic (SEM) images of different types of black carbons (BCs) 2

Figure 1.2 Chemical structure of graphite 6

Figure 1.3 SEM image of Carbopack C capillary column 7

Figure 1.4 SEM image of NIST SRM#2975 soot. 7

Figure 1.5 Transmission electron microscopic (TEM) images of diesel soot and lampblack soot 8

Figure 1.6 SEM of wood char 9

Figure 1.7 SEM of oak bark 10

Figure 1.8 SEM of beech wood char 11

Figure 1.9 Diagrammatic representation of the structure of activated carbon . 12

Figure 1.10 High-resolution TEM images of activated carbon 13

Figure 1.11 Diagrams of major types of carbon nanomaterials and their hybridization states 14

Figure 1.12 TEM images of the product of laser ablation of graphite rod. 15

Figure 1.13 Single-walled carbon nanotube (SWCNT) diagram, showing tube diameter and chiral angle 16

Figure 1.14 TEM images of multi-walled carbon nanotubes (MWCNTs) and double-walled carbon nanotubes (DWCNT). 17

Figure 1.15 TEM images of MWCNT, turbostratic graphitic structure, and Fe impurities 18

Figure 1.16 Diagram of benzene molecules on graphite plane at different orientations 32

Figure 1.17 Idealized static solid-state NMR spectra. 50

Figure 1.18 Diagram of transformation of an electric field gradient tensor from

the principal axis system to the laboratory frame 52

Figure 1.19 Motional models included with the Deuterium Fitting Program (DFP): isotropic (ISO), large-angle wobble (LAW), and small-angle-wobble (SAW) 53

Figure 1.20 Structure and variable-temperature (VT) spectra of neat solid Benzene 54

Figure 1.21 VT static solid-state ^{2}H NMR spectra of benzene-d_6 on mesoporous silica 55

Figure 1.22 Static solid-state ^{2}H NMR spectra and possible interactions of benzene-d_6 with Ca-montmorillonite 56

Figure 1.23 Static solid-state ^{2}H NMR VT spectra of benzene-d_6 on a zeolite 57

Figure 1.24 Static solid-state ^{2}H NMR VT spectra of benzene-d_6 as a guest in $Cd(py)_2\{Ag(CN)_2\}_2$ 57

Figure 1.25 Static solid-state ^{2}H NMR VT spectra of benzene-d_6 on graphitized carbon black (Carbopack B) 58

Figure 3.1 Schematic depiction of adsorption in slit-shaped graphitic pores . 84

Figure 3.2 Idealized I.U.P.A.C. isotherms 86

Figure 3.3 Powder X-ray diffractograms for black carbon materials 88

Figure 3.4 N_2 adsorption isotherms on low-surface-area graphite, carbon nanoparticles, and soot 91

Figure 3.5 N_2 adsorption isotherms on MWCTN 93

Figure 3.6 N_2 adsorption isotherms on activated carbon and maple wood char 95

Figure 3.7 Pore size distributions for low-surface-area graphite and carbon nanoparticles 97

Figure 3.8 Pore size distribution for activated carbon 98

Figure 3.9 Pore size distributions for multi-walled carbon nanotubes 99

Figure 3.10 Plots of the Frankel-Hill-Halsey equation for the N_2 adsorption data 100

Figure 4.1 NMR quantitation plot for benzene-d_6 on soot samples from 3600-scan spectra (variable loaded samples 113

Figure 4.2 Soot1 VT experimental and simulated ^{2}H static solid-static NMR spectra of benzene-d_6 115

Figure 4.3 VT experimental and simulated ^{2}H static solid-state static NMR spectra of benzene-d_6 for duplicate 1% soot samples 116

Figure 4.4 Soot1 peaks widths at half-height ($\delta\nu$) vs. temperature for different Ages 119

Figure 4.5 Soot1 averaged peaks widths at half-height ($\delta\nu$) vs. temperature from different ages 120

Figure 4.6 Soot1 NMR areas for 3600-scan spectra from different ages and temperatures 121

Figure 4.7 Soot1 experimental and simulated spectra with 20μs and 40μs techo values at variable temperature and the same age 122

Figure 4.8 Arrhenius plots for the reorientational jump rates of benzene-d_6 on Soot1 at different ages 123

Figure 4.9 Arrhenius plots for the reorientational jump rates of benzene-d_6 on Soot1 at all ages 124

Figure 4.10 Variable temperature ^{2}H static solid-state NMR spectra of benzene-d_6 (experimental and simulated) at three different submonolayer loadings on soot 128

Figure 4.11 Arrhenius plots for the reorientational jump rates of benzene-d_6 on soot at three different monolayer loadings (experimental and simulated) 130

Figure 4.12 Plot of the variation of D_0 and E_a with surface coverage 131

Figure 4.13 Plot of the pre-exponential factor vs. E_a (compensation effect) . . 132

Figure 5.1 ^{2}H static solid-state NMR spectra of benzene-d_6 on carbon nanoparticles CNP1 at different ages and temperatures 144

Figure 5.2 ^{2}H static solid-state NMR spectra of benzene-d_6 on CNP2 at different ages and temperatures 145

Figure 5.3 Peak width at half-height ($\delta\nu$) vs. temperature for ^{2}H static solid-state NMR spectra of benzene-d_6 on CNP1 and CNP2 147

Figure 5.4 NMR spectral areas for data collected with 3600 scans, CNP1 and CNP2 for different ages and temperatures 149

Figure 5.5 Arrhenius for CNP1 using jump rates obtained from both DFP fitting and peak width 150

Figure 5.6 Arrhenius for CNP2 using jump rates obtained from both DFP fitting and peak width 150

Figure 5.7 Energies of activation for the pseudoisotropic jump motion of benzene-d_6 on duplicate CNP samples at different ages 150

Figure 6.1 (also Figure 2.1) Crystallographic structure of graphite 156

Figure 6.2 ^{2}H NMR spectra of benzene-d_6 on graphite at 25°C with loadings and relaxation times as specified in the figure. 160

Figure 6.3 VT static solid-state ^{2}H NMR spectra of benzene-d_6 on low-surface-area graphite (1% w/w loading) 164

Figure 6.4 Arrhenius plot of the jump rate calculated using the peak width method from the spectra in Figure 2 of sample GRAPH1 166

Figure 7.1 Diagrammatic illustration of armchair (top and bottom edges) and zigzag (side edges) of graphene 171

Figure 7.2 Diagrammatic illustration of a Stone-Wales defect 171

Figure 7.3 Diagrammatic illustration of edge-associated defects in CNTs . . 172

Figure 7.4 TEM of bamboo-MWCNT and a trace of the carbon walls showing the terminal edges of the graphene plane 172

Figure 7.5 Teardrop structure in CNTs from oxygen attachment of CNT exterior 173

Figure 7.6 Modeled adsorption sites for benzene on CNTs 175

Figure 7.7 Computational model of the optimized position of benzene adsorbed to a 9,9 SWCNT (in the center of the tube) 175

Figure 7.8 ^{2}H NMR solid-state experimental spectra of benzene-d_6 on carbon nanotubes 182

Figure 7.9 Peak widths at half-height ($\delta\nu$) for spectra of benzene-d6 on CNT samples less than 5 days old spectrum 183

Figure 7.10 Arrhenius plot for benzene-*d*6 on SWCNT2 using jump rates calculated from the peak width 188

Figure 7.11 Arrhenius plots for benzene-d_6 on CNW at different ages using jump rates calculated from the peak width equation 190

Figure 7.12 Arrhenius plots for benzene-d_6 on CNS at different ages using jump rates calculated from the peak width equation. 191

Figure 7.13 Compensation effect plot for CNT samples 196

Figure 8.1 ^{2}H NMR static solid-state spectra of benzene-d_6 on AC at different temperatures and ages 211

Figure 8.2 ^{2}H NMR static solid-state spectra of benzene-d_6 (experimental overlain by simulated) on 1% w/w loading of MWC at variable temperatures and ages. 212

Figure 8.3 Diagram of a motional model for benzene in clathrate and experimental spectra 216

Figure 8.4 Diagram of a motional model for benzene inside a channel and simulated spectra 216

Figure 8.5 NMR area vs. temperature for days 135-7 on maple wood char (MWC) 220

Figure 8.6 Arrhenius plots for jump rate of modeled motions on MWC . . . 221

Figure 8.7 Longitudinal relaxation times for MWC at variable temperatures and ages after sealing 222

Figure 8.8 Arrhenius plot for the C_6 rotation of MWC samples aged 135-7 days calculated from T_1 values 222

Figure 8.9 ^{2}H NMR static solid-state spectra of benzene-d_6 (experimental overlain by simulated) on 10% w/w loading of MWC at 25°C and 0°C 224

Figure 8.10 Experimental VT static solid-state ^{2}H NMR spectra of benzene-d_6 on ActC2 (77 days) overlain by ISO/LAW/SAW simulations. . . 225

Figure 8.11 Arrhenius plot for Sample ActC2 for pseudoisotropic motion . . 226

Figure 9.1 ^{2}H static solid-state NMR spectra of benzene-d_6 on different BCs at 25°C and -25°C 236

Figure 9.2 Arrhenius plots for all BCs 238

Figure 9.3 Compensation effect plot for surface diffusivity of benzene-d_6 on all BCs and other solids 245

Figure 9.4 Plots of correlation time and diffusivity of benzene-d_6 vs. fractal dimension for benzene-d_6 on BCs and other solids 248

Figure 9.5 Plot of correlation time vs. diffusivity of benzene-d_6 on BCs and other solids 250

Figure 9.6 Diagram of possible packing arrangement of CNTs 252

Figure A1.1 Vapor deposition manifold schematic 266

Figure A1.2 Calibration line for benzene-d_6 injected vs. benzene detected in manifold 268

Figure A1.3 Calibration line for benzene-d_6 loaded vs. normalized NMR area 273

Figure A1.4 Normalized areas of benzene-d_6 loaded on samples plotted on the NMR calibration line 275

Figure A2.1 Diagrammatic illustration of a large-angle wobble 280

Figure A2.2 Step-by-step illustration of the transformation of the Euler angles from the initial to the final PAS by the use of stereonets 285

Figure A2.3 Stereonet map of some of the final PAS Euler angles (motional sites) 286

Figure A2.4 Sample DFP fit of an experimental spectra 288

Figure A2.5 Simulated spectra selected by DFP as components of the fit shown in Figure A1.4 288

Figure A3.1 VT ^{2}H static solid-state NMR spectra, experimental overlain by ISO simulation for Sample CNS1, age 1-2 days 295

Figure A3.2 VT ^{2}H static solid-state NMR spectra, experimental overlain by ISO simulation for Sample CNS1, age 77-119 days 296

Figure A3.3 VT ^{2}H static solid-state NMR spectra, experimental overlain by ISO simulation for Sample CNS1, age 164-254 days 296

Figure A3.4 VT ^{2}H static solid-state NMR spectra, experimental overlain by ISO simulation for Sample CNS3, age 1-2 days 297

Figure A3.5 VT ^{2}H static solid-state NMR spectra, experimental overlain by ISO simulation for Sample CNW2, age 1-4 days 298

Figure A3.6 VT ^{2}H static solid-state NMR spectra, experimental overlain by ISO simulation for Sample CNW2, age 80-81 days 299

Figure A3.7 VT ^{2}H static solid-state NMR spectra, experimental overlain by ISO simulation for Sample CNW2, age 56 and 194 days 299

Figure A3.8 VT ^{2}H static solid-state NMR spectra, experimental overlain by ISO simulation for Sample CNW4, age 1-2 days 300

Figure A3.9 VT ^{2}H static solid-state NMR spectra, experimental overlain by ISO simulation for Sample CNW4, age 21 days 300

Figure A3.10 VT ^{2}H static solid-state NMR spectra, experimental overlain by ISO simulation for Sample SWCNT2, age 1 day 302

Figure A4.1 Fits of experimental motional models to the static solid-state ^{2}H NMR spectra of benzene-d_6 in the micropores of activated carbon 303

Figure A4.2 Plot of the % of wag motion vs. temperature in the fits shown in Figure A4.1 304

Figure A4.3 Plot of the angle of the wobble-like motion vs. temperatu43 in the fits shown in Figure A4.1 304

Figure A4.4 Arrhenius plots for the fitted motion in Figure A3.1. 305

ABSTRACT

Black carbons in the atmosphere, in soils, and in sediments strongly sorb hydrophobic organic contaminants and function as agents of transport, sequestration, and catalysis. There is a need to examine the specific sorption mechanisms involved after attempts to predict field concentrations of these toxic compounds have been in error, and batch isotherm studies did not provide sufficient information. The specific sorption mechanisms, including the influence of the pore characteristics of the solid phase, remain poorly understand. In this study, by using line shape analysis of static solid-state ^{2}H NMR spectra at variable temperatures, ages, and loadings, the molecular motion of benzene-d_6 sorbed onto different black carbon materials have been examined for the effects of sorbate-sorbent surface chemical interactions and pore structures. The implications of the sorbent's motional influences on the sorbate are discussed for applications in environmental science, catalysis, and materials chemistry.

The microporosity of the solid phases have been tied to the effects of aging on sorbent behavior implying that microporosity is important for hydrophobic organic contaminant sequestration. The energy of activation of benzene on graphite has been measured at 10.1 ($\pm$1.1) kJ/mol, a significantly higher value than previous researchers. Relative to diesel soot, the path of benzene as it diffuses on the surface is controlled by the spherical shape of the grains and pores. The energy of activation on carbon nanoparticles and carbon nanotubes are lower than for planar graphite and is attributed to amorphous chemistry of the carbon nanoparticles and deviation from

graphitic planarity in the case of the carbon nanotubes. The materials dominated by microporosity reduce the rate of benzene diffusion and constrain its rotational motion. Finally, the surface diffusivity values, assuming that the benzene molecule moved around the surface of the smallest available pores, were found to correlate with the surface fractal dimension.

1. INTRODUCTION

Understanding the sorption interaction of hydrophobic organic contaminants (HOC) with graphenic black carbon (BC) materials that occur in environmental settings is fundamental to predicting the fate and transport of these contaminants [1, 2]. A great deal of study on sorption mechanisms is based on linear free-energy relationship (LFER) interpretations of batch isotherm experimental data, and these LFERs form the basis for important predictive models which have been developed by several groups, notably Schwarzenbach and coworkers [2] for environmentally occurring BCs, primarily for aqueous applications. In addition, for gas and vapor sorbates on graphitic BC sorbents in industrial and laboratory settings, several research groups [3-5] have recently developed theoretical models of isotherm equations based on density functional theory, grand canonical Monte Carlo methods, molecular dynamics and other theoretical approaches. However, very little experimental confirmation is available of the assumptions implicit in the empirical parameters used to construct the theoretical isotherms by these workers, e.g., the use of graphite as model black carbon surface [1, 6], the predominance of a π-π type van der Waals' interaction in the sorption mechanism of benzene [1, 7], and the effect of pore structure on chemical interaction [8]. In particular, little is known about the molecular motion of sorbate molecules as this motion is influenced by the surface forces which derive from these sorbate-sorbent interactions. This is especially true for physisorbed molecules, such as benzene on black carbon, which may not display detectable changes in vibrational spectra commonly used to measure chemisorption [9].

1.1 BACKGROUND – GENERAL

1.1.1 Occurrence and significance of BCs

Soots, chars, and anthropogenic residues of combustion comprise a heterogeneous group of environmentally occurring substances, samples of which are depicted in scanning electron micrographs (SEMs) in Figure 1.1 [2]. BCs are

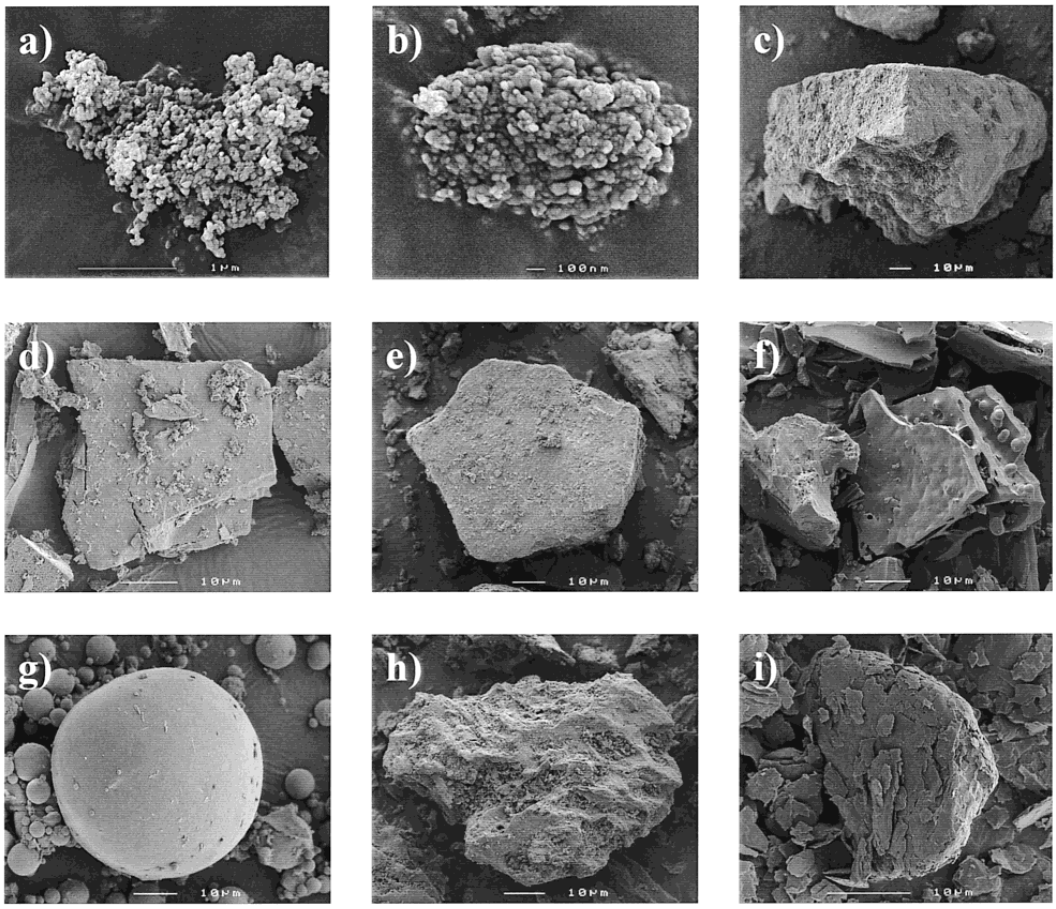

Figure 1.1. SEM images of different types of soot and soot-like materials from [10]: a) traffic soot, (b) oil soot, (c) wood soot, (d) coal soot, (e) coal, (f) charcoal, (g) fly ash, (h) activated carbons, and (i) graphite. The structure of diesel soot #2975 is comparable to plates a) and b), which display a morphology of clustered nanospheroids with internal onion-like layering. The image of a maple wood char sample corresponds to that shown in c) and f), which contain residual wood structures. The platey layers of graphite can be seen in i).

resistant to chemical and biological degradation and are particularly important as sorbents of low-polarity organic compounds [11-13]. Early papers identified

geosorbents [1, 14]) or hard carbon [15] as special components of the organic matter fraction of soils and sediments responsible for apparent sequestration of hydrophobic organic contaminants. Later the term black carbon came into usage [16, 17], and Chiou's group has designated the term high surface-area carbonaceous material (HSACM) [18], [13, 19]. Golding, Smirnik and Bucheli [20] have stated that "black carbon, in its various forms, is a hydrophobic sorbent composed of parallel aromatic sheets which are separated at distances of 30-40 nm and crosslinked by short aliphatic linkages . . . ." Bucheli and Gustafsson [17] described a "condensed carbon facies," and recently Cornelissen and others [11], in a 2005 review, have used the term "carbonaceous geosorbents" and included coal, kerogen in this category.

BC materials are important environmental sinks and transport agents for polyaromatic hydrocarbons (PAHs), volatile organic compounds (VOCs), and similar toxic contaminants [16]. Significant man-made sources of environmental BC include soot from diesel exhaust, coal dust, and industrial carbon black particulates [14]. Activated carbons and carbon blacks are important for preparatory and analytical laboratory applications [21-23], and industrial applications include removal of unwanted chemical, purification of water, filters, pigments, electrodes, fillers, binders and other applications [24-28]. Natural sources of black carbon input into the environment consist of chars from forest fires and eroded detritus from outcrops of coals and kerogen-rich rocks [14, 29].

In soils and sediments, where BCs function as sinks and transport agents for hydrophobic contaminants, these particles account for less than 15% of the total organic carbon (OC) in most soils while exhibiting a ten-fold greater sorptive

activity for hydrophobic contaminants over the remaining OC [11, 16]. In the air, soot or coal dust particles can act as irritants in themselves [30, 31] as well as serving as transport agents for toxic hydrophobic substances, such as PAHs, to human lungs, eyes and membranes [32, 33] In natural aqueous systems, BCs involve additional distribution equilibria with the aqueous phase and the soil/sediment components [2, 14, 16, 34-36]. In each of the above natural settings, the surface interaction of BCs with HOCs is fundamental to the distribution and bioavailability of those compounds.

1.1.2 Chemical and porosity structures of BCs

Black carbons are composed predominantly (over 80%) of the element carbon and include some rigid component of six-carbon aromatic rings which extend into a highly porous framework of graphenic plates or sheets [8, 37]). A primary model compound for a condensed carbon structure is the mineral graphite [36], in which flat graphene layers are held together by van der Waals forces [38], but with added structural peculiarities (e.g., curved sheets) [39], defects (e.g., surface pits) [23, 40]), and noncarbon impurities (N,S,O) [8, 37, 41]). Oxygen-containing functionalities (-COOH and –OH) commonly occur on the edges [1, 4, 7, 17, 21]. Chars, in particular, contain a significant ionic component (6110 mg/kg total Ca, Mg, Na, K has been reported by Bronemann et al. [18]). Whereas the mineral graphite serves as a model for the π-electron aromatic surface of black carbons, which is generally considered to account for most of the chemical sorption characteristics of black carbons towards hydrophobic organic contaminant sorbates [4, 5, 42], the most common physical model with respect to black carbons' pore

structure and chemical heterogeneity is activated carbon [12, 43]. This is reasonable for BCs which serve as source materials for activated carbons (coconut shells, olive pits, or coal), but less so for hydrocarbon soot [22, 44, 45].

A dominant characteristic of black carbons important for sorbent behavior is the high surface area and abundant micro- and mesoporosity, particularly for activated carbons and char [2]. Again to refer to Golding, Smirnik and Bucheli [20] "the high microporosity of black carbon allows for . . . high surface areas . . . and [planar] compounds penetrate between the aromatic sheets [and] association with the matrix is enhanced through strong adsorptive π-π molecular attraction." Additionally, particle morphology can vary greatly among the different types of black carbons, resulting in characteristic pore shapes and sizes [17, 38]. In addition, curvature of the black carbon sorbent surface can affect the energy of the aromatic bonds in the surface graphene layers [46], and both surface curvature and pore dimension can restrict the ability of planar molecules, such as benzene, to align themselves into a configuration that maximizes the energy of adsorption [39, 47]. Each class of black carbon material used as a sample in this study will be discussed in more detail in the paragraphs that follow.

1.1.2.1 *Graphite*

Graphite consists of sheets of aromatic carbon rings held in layers by van der Waals forces and is a naturally occurring mineral constituent of metamorphic rocks [42]. In addition to its affinity for hydrocarbon sorption, the extended π-bonds of the surface aromatic ring system give the mineral its electrical conductivity [28, 48]. High sorption capacities are, however, dependent on small particle sizes because

crystalline graphite has no intraparticle porosity and commonly very low specific surface area (SSA) [49]. Its platey crystal habit (Figure 1) derives from its layered chemical structure (Figure 1.2). Commercially available porous synthetic graphites vary widely in grain size and structural heterogeneity, including exfoliated graphite, which is produced by chemical oxidation with subsequent heat-shock [49] as well as pillared or intercalated graphite products [50], which we will not consider here.

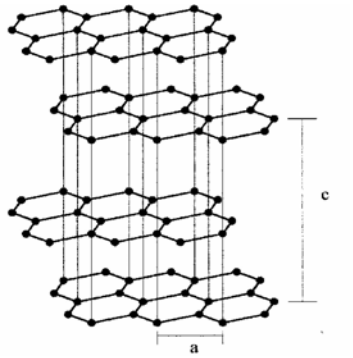

Figure 1.2. Chemical structure of graphite, a (2.46Å) and c (6.67Å) indicate the dimensions of the hexagonal unit cell [51, 52].

Numerous studies in the literature [4], including some benzene motional studies using static solid-state ^{2}H NMR [53-55], utilize Graphon or Carbopack B as the graphitic solid phase. These are graphitized carbon blacks formed from carbon blacks subjected to additional anaerobic heating at very high temperatures (e.g., 3100°C for Sterling MT [56]), creating an "aggregate of small polyhedral particles each face of which is a 001 plane of the graphite lattice" [57]. A primary reason for utilizing a Carbopack graphitic phase (100 m^2/g SSA) over a powder crystalline graphite sample (4 m^2/g SSA) is that the greater surface area enhances the amount of benzene in the sample and, thus, improves the signal-to-noise ratio of spectroscopic measurement made on the benzene. However, Carbopack B has a

particle diameter of 40 nm [53] and a cubic-to-spherical particle morphology Figure 1.3), so that a more planar, if lower surface area, graphite may be a better model substance for a planar homogeneous graphenic surface.

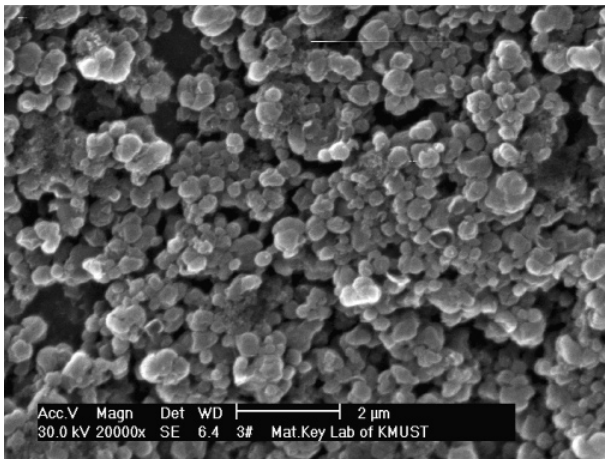

Figure 1.3. SEM image of the inner surface of the bonded Carbopack C (assumed to be similar to Carbopack B) capillary column from [58].

1.1.2.2 *Soot*

Soot is the fine-grained particulate matter which results from the incomplete combustion of hydrocarbons. Diesel soots (Figure 1.4) range in size from a few to over 50 µm [10] and are characteristically nanometer-sized particles of cubic or nanometers spheroid-shaped onion-like carbon deposits which cluster into grape-like aggregates [10, 59]. The onion-like spheroids, shown in the transmission electron micrograph (TEM) and high-resolution transmission electron micrograph (HRTEM) in Figures 1.5, typically contain some micropores (< 2nm), although it is the mesopores (between 2 and 50 nm) around the aggregated spheroids which dominate the pore-size distribution [59]. Muller et al. [60] show that, although lampblack is often used as a surrogate for diesel soot because of its predominant

carbon composition and its occurrence as aggregates of spheroids, its internal structure shows some important differences [60]. The authors explain that diesel soots contain an inner core, visible using TEM (Figure 5), which consists of

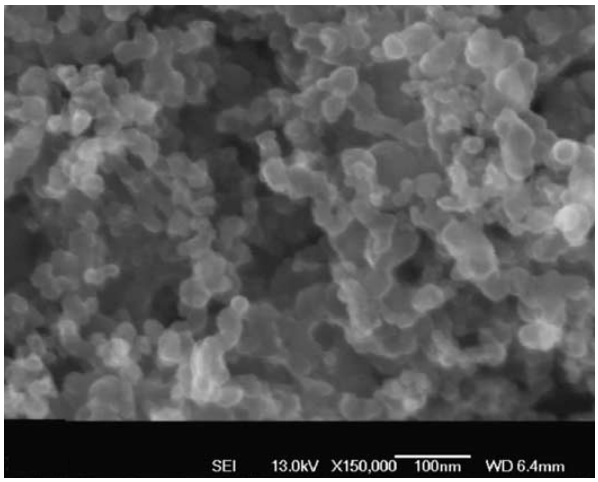

Figure 1.4. SEM of NIST SRM #2975 Soot showing an abundance of spherically shaped mesopores at 5-50 nm dia. [61].

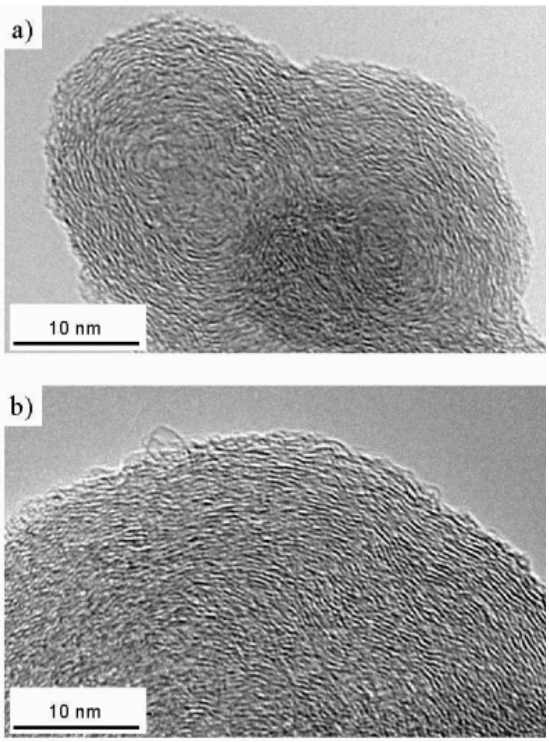

Figure 1.5. TEM (left) and HRTEM (right) micrographs of diesel soot (a) and lampblack soot (b) from [60].

disordered, large PAH molecules, and a 10 nm thick shell of turbostratically stacked "graphene basic structure units" of 2-3 nm in width. Lampblack has a thicker shell (10-100 nm) of turbostratic graphene, is more graphitic (greater planarity of the graphene basic structural units), has a smaller surface area and fewer PAHs and C-O functionalities [60].

1.1.2.3 *Chars*

Chars are the residues of the incomplete combustion of plant materials which often contain remnant structures derived from their original plant material (Figure 1.1 - c and f, Figures 1.6, 1.7 and 1.8) and can contain heteroatoms and even

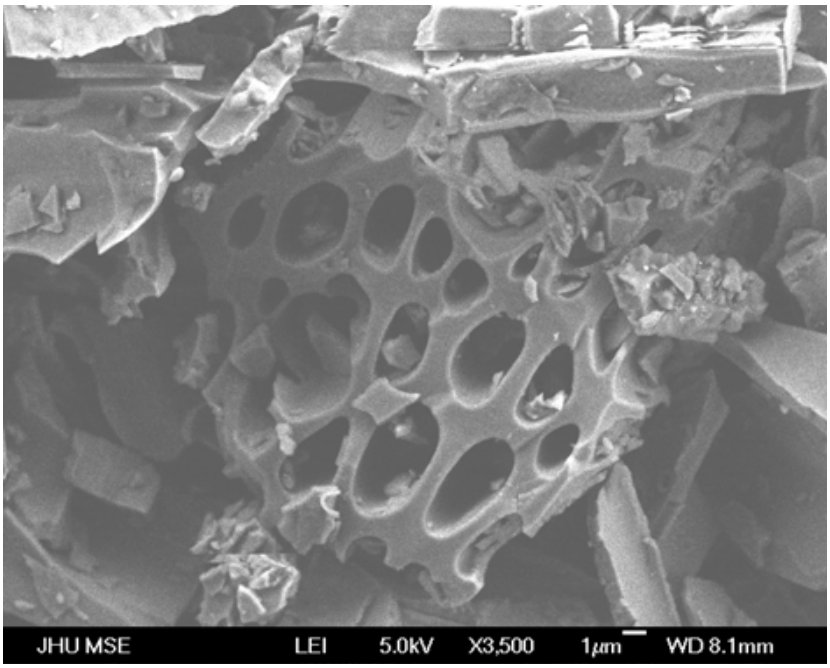

Figure 1.6. SEM of wood char, showing residual cellulose structure [62].

ions [10, 18, 61]. Chars are the most chemically heterogeneous of the black carbons because, unlike, for example, soots, which originate as nonpolar hydrocarbons

before oxidation, chars are the direct oxidation product of biomaterials. Their characteristics are dependent not only on the original chemical composition and structure (such as type of wood), but also on the particle sizes and conditions of combustion [63]. The median reported SSA is 201 m^2/g [11], and the carbon content varies from 20-90%, increasing as charring proceeds and the development of graphenic carbon is enhanced [8]. Other elements (S, P, Cl, K, Mg, Ca, Si) have been measured at less than 1% in char from straw and beech wood [64], but there is considerable variability in composition among chars [18]. In their living state, obviously, they contained amino acids, carbohydrates and other polar biomolecules, and complex ionic reaction products, such as hydroquinone, pimaric acid and many others, have been reported associated with the formation of chars [65]. The

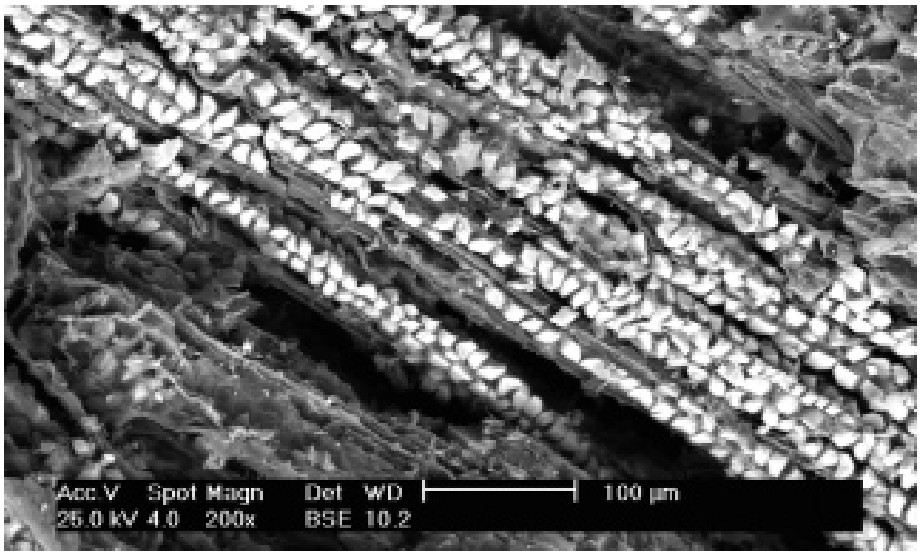

Figure 1.7. SEM of oak bark showing a large amount of calcium crystals [66].

inorganic divalent and monovalent ions can result in the formation of salt deposits within the char pores (Figure 1.7). The conditions of char formation strongly affect the product composition, and higher pyrolysis temperatures result in a greater

fraction of carbon and consequent lesser amounts of oxygen as well as higher surface areas [41]. Partly because activated carbons are also the product of the pyrolysis of plant residues, albeit under very controlled conditions, chars are often assumed to be similar to activated carbons in their pore structure with slit-shaped micropores and mesopores (Figure 1.8) and carbon surface functionality (graphenic). This assumption has been upheld by characterization studies (e.g.,

a)

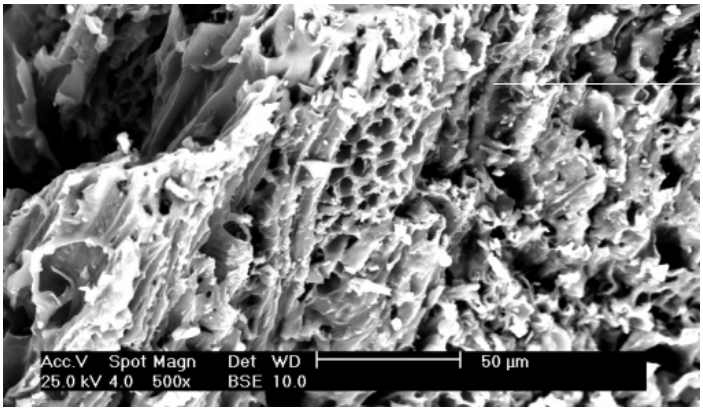

b)

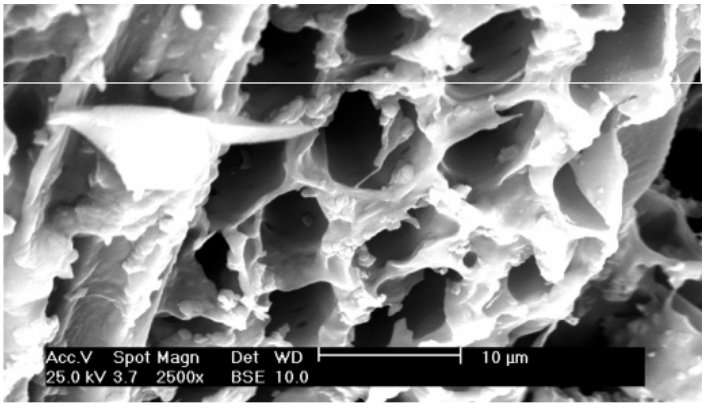

Figure 1.8. SEM of beech wood char a) and b), showing cracks and pores [66].

specific surface areas, elemental composition, Boehm titration, batch isotherm studies) performed by several researchers [8, 43, 67]. These studies showed that chars contain abundant micropores, high surface areas, high carbon content, and

affinity for nonpolar or neutral sorbates. Chars in nature have obviously formed under a variety of conditions, and those which formed at higher temperatures (above 500°C) are generally carbonized to a much greater extent [45]. In a recent study by [37], the authors charred pine needles at successively higher temperatures (100°C to 900°C), performed aqueous isotherm analysis of HOCs on the product along with surface characterization, and observed a decrease in partitioning to an amorphous organic matter phase and an increase in adsorption to a rigid porous black carbon phase as they charring temperature increased.

1.1.2.4 *BC Model Substances – Activated Carbon*

Activated carbons are synthesized by the combustion of coconut shells or similar materials under controlled anaerobic conditions and consist of a disordered

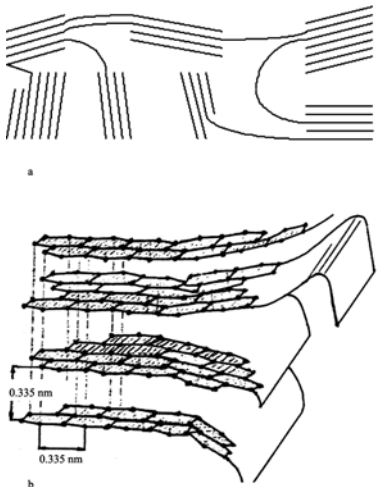

Figure 1.9. Diagrammatic representations of the structure of activated carbon [68]

enhancing the existing porosity as combustion proceeds by using water molecules in arrangement of slit-shaped micropores (Figure 1.9) between graphenic pore walls

[22]. Activated carbons are synthesized with the purpose of retaining and steam to "prop" open the pores, and, thus, while the actual number of pores is conserved during activation, the surface area of the product is greatly increased [22]. Numerous adsorption studies have revealed the adsorption of hydrophobic organic compounds within activated carbon to occur on a graphenic aromatic carbon surface, modeled to exist as abundant slit-shaped pores [40, 69]. However, recent aberration-corrected soft X-ray imaging (Figure 1.10) have detected pentagonal rings, which would cause curvature in the slit-shaped pores, and further, the

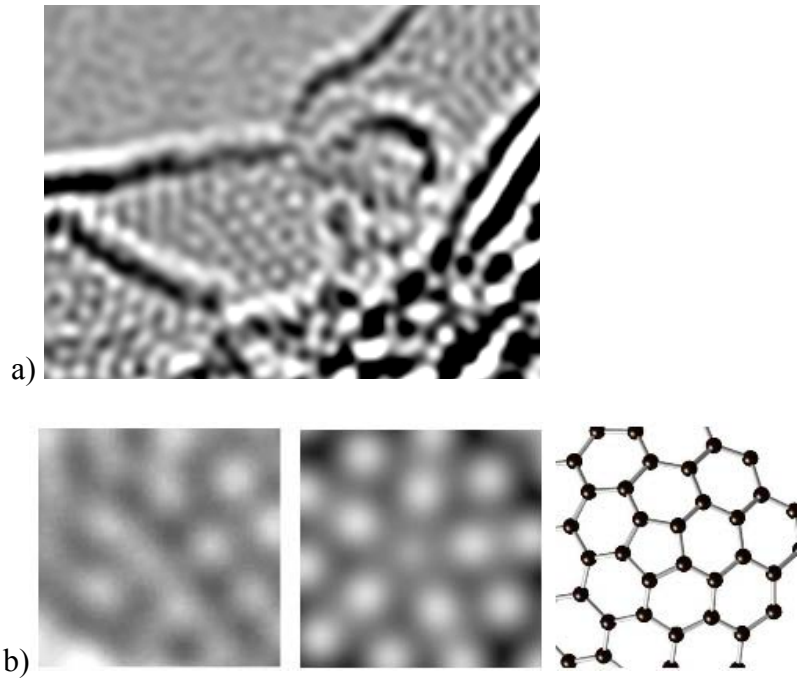

Figure 1.10. a) and b) are HRTEM of activated carbon, heat treated to 2000°C with aberration-corrections and a modeled structure including a pentagonal ring [39].

associated near-edge X-ray absorption fine structure (NEXAFS) analysis was interpreted to indicate that, although a predominance of phenolic and oxygenated

functionalities occur on the surface an anthracite activated carbon, it is the aromatic carbon groups with which a sorbate PCB interacts [12]. The polar surface sites, although abundant, are considered to be of greater importance for polar sorbates [14, 43, 70, 71]. However, hydration of these sites has been has been interpreted to result in blocked access of nonpolar molecules to some of the micropores [70-72].

1.1.2.5 *BC Model Substances – Engineered Carbon Nanoparticles*

The following materials, diagrammatically displayed in Figure 1.11, are all taken from a class of compounds referred to recently by several authors as engineered carbon nanoparticles (ECNP) [73]. Although they are being identified

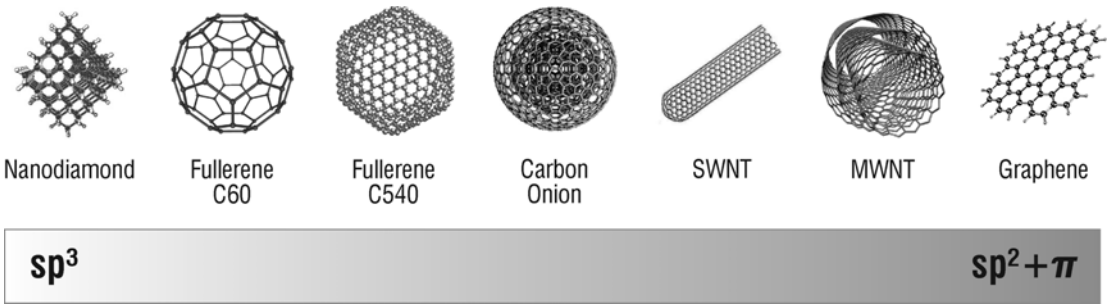

Figure 1.11. Major types of recent engineered carbon nanomaterials and their dominant hybridization states [38].

as elements of soots, chars, carbon blacks, and other combustion residues already known, their newly discovered, unique structures, electronic and optical properties make them subjects of intense study for materials scientists for a wide range of applications, e.g., environmental remediation, sensing devices for pollutants, and energy storage [51, 74-78]. However, the potential ECNPs have as environmental hazards in themselves is poorly understood [73, 78]. In this work, we are focusing on the sorption properties of BCs with respect to benzene (a representative

hydrophobic organic compound) in an effort to understand the sorption mechanisms and interactions as they are affected by a range of pore geometries and carbon surface chemistries.

1.1.2.5.1 *BC Model Substances – Carbon Nanoparticles*

The carbon nanoparticles (sometimes called carbon soot) employed in this study are synthesized via laser ablation and have an amorphous structure, according to the Sigma-Aldrich catalog. There are other types of carbon nanoparticles which are similar to buckyballs or the soot described above [74]. Amorphous carbon consists of carbon atoms bonded in 6-membered aromatic graphenic rings of disordered orientations (not stacked), rings containing other than 6 carbon atoms, and both sp^2 and sp^3 hybridized carbon atoms and is referred to by some workers as"diamond-like" because of the presence of sp^3 sites [79]. There exists various degrees of sp^2 clustering in an amorphous matrix [79, 80]. In a TEM study by

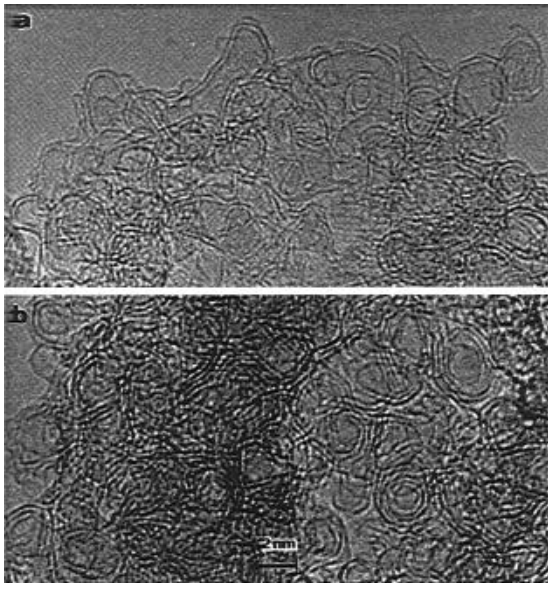

Figure 1.12. TEM images of the product of laser ablation of a graphite rod at room temperature, showing spheroids of highly developed graphitic curled sheets [81].

Iijima et al. [81], carbon nanoparticles (Figure 1.12) formed by the laser ablation of graphite in an Ar carrier gas at room temperature and at 900°C show spheroids of 2-3 nm diameters with curled graphitic sheet structures imbedded in amorphous carbon. However, at 1200°C, the graphitic spheroids begin to anneal into bonded agglomerates with fullerene structures, and the particles size increases from 10-20 nm in diameter.

1.1.2.5.2 BC Model Substances – Carbon Nanotubes

Carbon nanotubes (CNTs) (Figures 11,12,13,14), both single and multi-walled, are a new category of black carbon materials, having unique chemical,

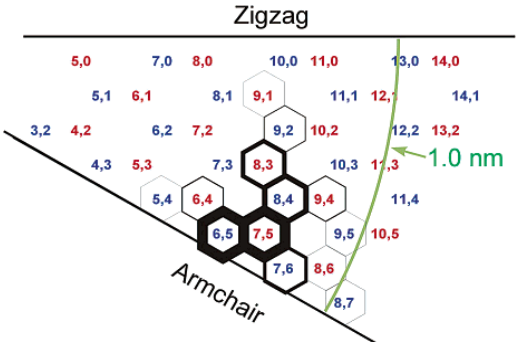

Figure 1.13 Diagram showing the chiral angle, nanotube inner diameter and configuration for single-walled carbon nanotubes [75].

optical, and electrical properties [22]. Their uniform porosity is also a feature of interest for applications such as gas storage [82]. CNTs are often synthesized by sparc discharge and condensed around a metal filament (chemical vapor deposition), but methods of preparation are currently under active investigation [75]. Single-walled carbon nanotubes can be thought of as a rolled graphene sheet, resulting in obvious distortion of the normally planar graphitic functionality [83]. Each graphene tube contains a certain configuration (Figure 1.13), zigzag or armchair,

and an angle away from planarity (chirality) which determines its diameter [47, 75], and these structural differences affect the electronic structure of the π electrons [83].

Multi-walled carbon nanotubes (MWCNTs) (Figure 1.14) are similar to single-walled tubes, but the multilayered walls provide three-dimensional graphite domains, and the interior surface may include a greater number of abrupt discontinuities than in the single-walled varieties [84]. Thus, the walls of MWCNT can resemble turbostratic graphite because of the abundance of defects and isolated graphitic domains [84], or they can exist as tube-in-tube structures [47]. Stone-Wales defects, in which the hexagonal aromatic rings are replaced by a 5-7-7-5-membered ring configuration can occur, opening up the defect carbons to

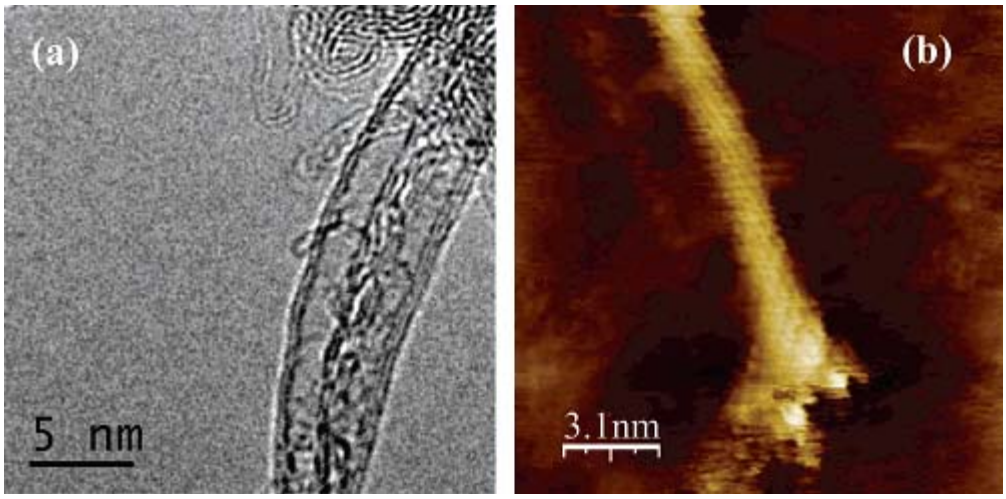

Figure 1.14. a) TEM of double and triple-walled nanotubes; b) STM of DWCNT with open end covered by amorphous carbon [85].

Nucleophilic attack [38]. Remnants of metal catalyst and amorphous carbon nanoparticles can exist, within the tubes or attached to the outer surfaces. Tubes

have been produced with multiple inner tubules irregularly wrapped in outer tube graphene layers. Whenever a tube-in-tube structure exists, each tube has its own configuration and chirality and the interaction energies between these configurations is unknown [85, 86].However, just as high temperature anaerobic treatment can

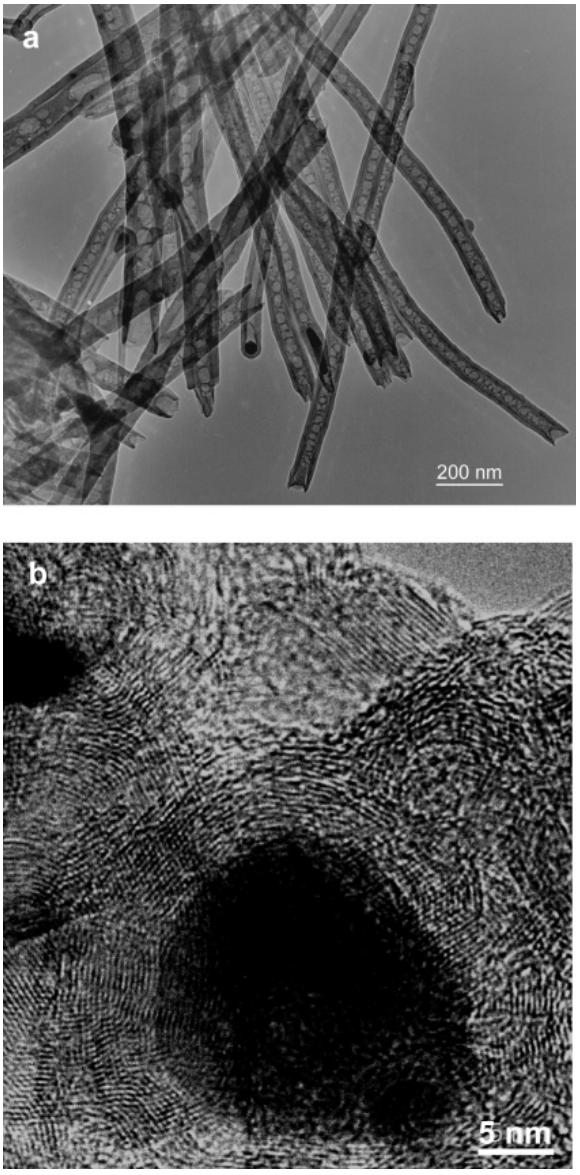

Figure 1.15. TEM image of MWCNT from [84] a) showing several tubes; b) showing the turbostratic graphitic structure and Fe impurities (dark particles).

produce a more graphitically ordered structure in carbon blacks, similar treatment of low-temperature MWCNTs synthesized with chemical vapor deposition (CVD) can produce a highly graphitic tube that is more stable to oxidative attack [87]. Figure 1.15 shows cleaned, separate tubes and uncleaned tubes with catalyst remaining in the center.

1.1.3 Sorption Interactions of Benzene with Black Carbons

1.1.3.1 Isotherm Models of HOC/BC Sorption Processes

In recent years, a number of batch isotherm studies have been performed which measure the distribution of benzene, PAHs and other hydrophobic contaminants across environmental phases, such as between particle/air or soil/water, and then analyzing these results by fitting the data to predictive isotherms, based on assumptions about the nature of the substrate and the sorbate/substrate chemical interactions [1, 6, 15, 19, 45]. Researchers have fitted the data primarily to one or more isotherm model equations, e.g., Freundlich, Henry's law, Langmuir, or Polanyi-Dubinin-Manes, and sometimes information about the sorption mechanism can be obtained [1]. For instance, a good fit to a Langmuir plot implies that the sorption mechanism adheres to the major assumption inherent in the Langmuir model: monolayer only adsorption onto a limited number of active sorption sites on the surface. In addition to analysis based upon isotherm shape, several predictive LFER have been developed that correlate the Henry's law equilibrium constants obtained in the experimental plots to specific properties or interaction mechanisms [2, 88], and these will be discussed below. A majority of the environmental studies have focused on aqueous systems of soils and sediments,

,which measure K_d, the solid/water distribution coefficient, defined as:

$$K_d = C_{solid} / C_{water}, \quad \textbf{Eqn}. 1.1$$

where concentrations are reported in units of g/L. However, because HOCs preferentially sorb into organic phases within the soil, the organic-carbon normalized distribution constant, K_{OC}, has been adopted for interpreting data on such systems, where

$$K_d = f_{OC} * K_{OC}, \quad \textbf{Eqn}. 1.2$$

where f_{OC} is the fraction of organic carbon in the solid phase [17].

Such isotherms of vapor or aqueous HOCs in equilibrium with natural organic matter (NOM) are commonly linear, indicative of a liquid/liquid partitioning-type sorption process, which, would fit well to a Henry's law plot. The Henry's law constant, K^H is defined as the equilibrium between a substance in its vapor phase in equilibrium with an aqueous solution ([57, 89]),

$$K^H = p / C_W, \quad \textbf{Eqn}. 1.3$$

where p is the partial pressure of the compound, and C_W is its concentration in the aqueous phase. Similarly, a fit to a vapor/solid type of Henry's law distribution can be considered as fitted to a Freundlich equation with a Freundlich exponent, n, equal to 1:

$$K_F = C_{solid} / p^{(1/n)}, \quad \textbf{Eqn}. 1.4$$

where K_F is the Freundlich coefficient, and C_{solid} is the concentration of sorbate in the solid phase. Similarly, for a similar aqueous/solid distribution,

$$K_F = C_{solid} / C_W^{(1/n)}, \quad \textbf{Eqn}. 1.5$$

where C_W is the concentration of the sorbate in an aqueous phase in equilibrium

with that solid phase. The aqueous K_F is more commonly used in environmental studies. However, as detailed by Luthy [1] for studies on aqueous systems, in actual field settings, applications of fate and transport models based on the fraction of organic carbon in the sample are often incorrect and indicate that a significant part of the HOCs appear to undergo sequestration by a black carbon component of the soil or sediment, when present ([1, 29, 45, 90, 91]. In response, Bucheli and Gustafsson [17] have modified the distribution equation in aqueous systems to include a component due to black carbon referred as K_{BC} or K_{SC} [2], where

$$K_d = f_{OC} * K_{OC} + f_{SC} * K_{SC} \text{ [17]}. \qquad \textbf{Eqn}. 1.6$$

The above paragraphs include a number of references to aqueous studies because, although the present work involves only vapor/solid equilibria between benzene and BC materials, the same types of isotherm approaches and equations are utilized, and, also, most of the molecular interactions between sorbate and substrate surface are the same (except for the hydrophobic and sorbate/water interactions) [2, 91]. The mechanism of sorption of HOCs to BC, which is the focus of this study, differs, however, fundamentally from the partitioning process of HOCs into natural organic matter (NOM). This difference is exemplified in the nonlinear concave-down isotherms for solid phases that contain BC [6, 16, 91]. Such a shape, as mentioned above, can indicate Langmuir adsorption (filling of a limited number of active surface sites), and can be fitted to a Langmuir equation:

$$b = k_b / k_f = \theta / [P * (1 - \theta)], \qquad \textbf{Eqn}. 1.7$$

where b is the Langmuir constant, θ is the fractional monolayer coverage, k_f is the forward rate constant, k_b the backward rate constant, and P the gas pressure of the

vapor phase [9]. Further, the Henry's law constant is related to the Langmuir adsorption constant, b, according to

$$K_P = b*S_{1\text{-}ML}, \qquad \textbf{Eqn}.\ 1.8$$

where $S_{1\text{-}ML}$ is the surface concentration at full monolayer coverage, and, at low pressures, where the isotherm is linear, $K_P \sim b$ [89].

Another isotherm model which can be fitted to a concave-down isotherm is the PDM equation, which also assumes a specific sorption capacity, limited not by surface area but by the total pore volume, which may be quite large [92]. Polanyi [44] considered vapor/solid isotherms to depict a process of pore filling, and the Polanyi equation is similar to the Kelvin equation, which relates the size of condensed droplets to vapor pressure [9], can be written as

$$\ln (p/p_s) = 2\gamma V_m/rRT, \qquad \textbf{Eqn}.\ 1.9$$

where p is equilibrium vapor pressure, p_s saturation vapor pressure, γ surface tension, R the universal gas constant, T temperature, V_m the molar volume of the sorbate, and r the droplet (pore) radius [59, 93]. Examination of the Kelvin equation makes clear that condensation of a liquid occurs at lower pressures (p) with smaller pore/droplet radii (r). (Note that the meniscus of the liquid within the capillary has a negative radius of curvature, and, therefore, r is negative and p is lowered.) The Polanyi adsorption equation defines the adsorption potential, ε,

$$\varepsilon = RT\ ln(p_S/p), \qquad \textbf{Eqn}.1.10$$

assumes that a surface potential extends from the pore walls into the center of the pore, affecting 3-4 monolayers of sorbate molecules, and that the properties of the adsorbate are identical to properties o f the liquid [3, 9]. In addition, the well depth

of the surface potential is magnified by overlapping force fields as the pore walls are closer together in smaller pores [2]. Dubinin and coworkers [5, 9, 69] extended the Polanyi model for adsorption on activated carbons [9, 94] to calculate an adsorption potential, *A*,

$$\theta = \exp [- (A/\beta E_0)^2], \qquad \textbf{Eqn}.1.11$$

where θ is the fraction adsorbed, β is an affinity coefficient used to categorize the sorbate (β = 1 for benzene) and E_0 is the characteristic energy of the activated carbon and varies with the structure of the activated carbon [69], particularly the pore width, *w*,

$$w = w_0 \exp [- (A/\beta E_0)^2]. \qquad \textbf{Eqn}.1.12$$

1.1.3.2 Models of Molecular Interactions between HOC/BC during Sorption

For quantifying the molecular interactions of benzene and other HOCs on BC, there are at least two approaches. First, several workers have examined LFERs for PAHs and HOCs on BC, based on types of chemical interactions (π-π, dispersive, H-bonding, electron donor/acceptor) and on steric constraints [32]. Second, thermodynamic values and isotherm fits are used to examine both adsorption and pore filling. The use of computer simulations of molecular interactions to generate model isotherms as well as thermodynamic and kinetic values provides additional detail and insight into the molecular interactions of sorption onto BCs and can be used to validate assumptions. In addition, because of the similarity of black carbons to activated carbons and carbon blacks, as elaborated in the previous section, the extensive literature for sorption of benzene on activated carbons and carbon blacks can be utilized to understand the sorption of benzene to

BCs in environmental systems. In the following paragraphs, the LFER equations developed for environmental systems will first be explained, and, second, a brief introduction to the extensive work modeling the interaction of benzene with activated carbon and graphite and the associated isotherm equations and thermodynamic values will be provided.

1.1.3.2.1 LFERs for vapor/solid sorption in environmental systems

A Henry's law constant for sorption onto particulate matter, sometimes termed K_P [89, 95-97], is used to define a linear isotherm for a sorbate (usually vapors or gases) onto a solid surface at low concentrations. Linear sorption of a vapor to a solid may occur via a liquid-like partitioning process, *ab*sorption, or via *ad*sorption onto limited sites [95, 98], although Kp is applicable only for sorption at low concentrations [99]. For higher concentration, multilayers develop, and an equation which accounts for this, such as Brunauer-Emmett-Teller (BET), must be applied [32, 99, 100]. In the most thorough and detailed of the LFER models for HOC sorption, Schwarzenbach's group [97, 98, 100-102] have defined a set of parameters for vapor/solid sorption which extend the solubility parameters they have developed for environmental systems based on the work of Abraham, which are similar to the Hildebrand parameters used in chromatographic settings [103]. In their model, for any compound adsorbing onto any surface, the following equation predicts the distribution coefficient, $K_{i\ surf/air}$ (m^3/m^2), if the values of the parameters in the equation below are known [98]. These parameters are broken into three categories: (1) a van der Waals interaction parameter ($K_{i\ hexadecane/air}$ for the sorbate, and $(\gamma^{vdW}_{suef})^{0.5}$ for the surface), (2) an electron acceptor (EA) interaction parameter

($\Sigma\beta^{H}_{12}$ for the sorbate and EA_{surf} for the surface), and (3) an electron donor interaction parameter (α^{H}_{12} for the sorbate and ED_{surf} for the surface) [2]. For BC (EC, for elemental carbon, as the authors designate it), the $(\gamma^{vdW}_{suef})^{0.5}$ is 8.08, the EA_{surf} is 0.48, and the ED_{surf} is 0.75 [99, 100]. The parameters are determined using inverse gas chromatography with the surface of water as a reference.

$$\log K_{i\ surf/air}\ (m^3/m^2) = C_{surf} / C_{air} = (moles \bullet m^{-2}) / moles \bullet m^{-3}) = m^3 / m^2$$

$$= 0.135 \log K_{i\ hexadecane/air} (\gamma^{vdW}_{suef})^{0.5} + 5.11\ \Sigma\beta^{H}_{12} EA_{surf} + 3.60\ \Sigma\alpha^{H}_{12}\ ED_{surf} - 8.47 \qquad \textbf{Eqn}.1.13$$

The authors specify that the value of the last term in the equation, -8.47, is theoretically calculated for *ad*sorption onto a surface. Therefore, if experimental data shows an offset from this value, an *ab*sorptive component would be indicated. However, for NIST SRM #2975 (the sample used in this study), only adsorption was indicated [99]. The log $K_{surf/air}$ for benzene on the soot was calculated to be -5.23, and experimentally verified with the inverse gas chromatographic experiments [99]. The authors' treatment is thermodynamically rigorous, and, in order to compare the value with K_P values reported by some other workers, it is necessary to convert the units using the surface area of the black carbon and its density [97, 100, 101].

Other workers have developed predictive LFER models for K_P based solely on the vapor pressure, P^{o}_{L}, the subcooled vapor pressure, $^{*}P_{L}$, or the octanol/water or octanol/air coefficients, K_{OW} and K_{OA}, respectively. Mader and Pankow [96] have reported the following LFER between K_P and vapor pressure for HOCs, especially useful for volatile and semivolatile compounds [96]:

$$\log K_P = m \log P^o_L + b, \qquad \textbf{Eqn}.1.14$$

and have specified that m should be equal to -1 for absorption. Goss and Schwarzenbach [97] have disputed the -1 value, however . Mackay [95] described a similar empirical equation for absorption, derived theoretically, but which can be abbreviated using approximation to unknown values in the equation to various forms, e.g.,

$$K_P = RT\, f_{OM} / 10^6\, M_{OM}\, \gamma_{OM}\, P_L, \qquad \textbf{Eqn}.1.15$$

where R is the gas constant, T the temperature in Kelvin, M_{OM} and γ_{OM} are the molar mass and activity coefficient of the sorbent organic matter, and P_L is the vapor pressure of the sorbate. The authors [95] also describe an associated LFER for adsorption,

$$K_P = [RT\, N_s\, A_{TSP} \exp(Q_d - Q_v) / RT] / P_L, \qquad \textbf{Eqn}.1.16$$

where N_s is the number of adsorptive sites per unit area (m^2) on the surface, A_{TSP} is the surface area of the filtered atmospheric particles, and Q_d and Q_v are the heats of desorption and vaporization of the compound, respectively. It is clear that the latter equation is conceptually related to the BET equation for multilayer adsorption by nature of the ($Q_d - Q_v$) term. Mackay has suggested that a similar correlation between P_L and K_{OA} gives a LFER they feel is more practically applied for absorption [95]:

$$K_P = 1.23 \times 10^{-12}\, f_{OM}\, K_{OA}, \qquad \textbf{Eqn}.1.17$$

where K_{OA} is the octanol/air partition coefficient for the sorbate of interest. More recently, Lohmann and Lammel [6] have suggested a dual-mode OM/BC model for sorption to BC-rich atmospheric particulates,

$$K_P = 10^{-12} (f_{OM}\ 1/\delta_{oct}\ K_{OA} + f_{BC}\ 1/\delta_{BC}\ K_{soot/air}\ A_{atmBC} / A_{soot}), \qquad \textbf{Eqn}.1.18$$

where δ_{oct} is the density of octanol, δ_{BC} is the density of the BC, $K_{soot/air}$ is the soot/air partition coefficient for a reference soot (e.g., NIST SRM #2975), and A_{atmBC} / A_{soot} is the ratio of the surface area of the BC in the atmospheric particles to that of the reference soot [6]. Despite the apparent applicability of the Polanyi-Dubinin-Manes pore-filling treatment of vapor sorption onto activated carbon to vapor sorption onto BCs in activated carbon, this treatment has not been found in the environmental literature with respect to vapor/solid sorption on environmental sorbents.

To summarize, the LFER models are extremely useful, and as a catalog of parameters are developed, should be extremely useful for predicting fate and transport and planning remediation strategies, and the associated batch isotherm studies which have been performed to define these they LFERs have provided a wealth of useful information. However, the various conditions for which a given set of data are applicable is somewhat daunting, and choosing the appropriate model is still unclear at this time. Because of the complexity of these systems, further insight into adsorption mechanisms needs to be done in order to clarify the selection of the most applicable model to a given a problem

1.1.3.2.2 Thermodynamics of benzene adsorption on BCs from vapor/solid isotherms

In addition to fitting batch isotherm data to model isotherms and applications of LFERs, values for the isosteric heat of adsorption Q_0^{st}, which can be obtained

from several methods, are fundamental to understanding sorption mechanisms. The values are in the ranges of physisorption for a nonporous surface [104]. The measurements of the isosteric heat of adsorption for benzene on Sterling graphites, which are highly crystalline graphitized carbon black [40], fall between 40-43 kJ/mol for monolayer and submonolayer loading at 20°C, and, at higher temperatures, the value is 40 kJ/mol. Isirkyan and Kiselev [40] report that, over the monolayer range of benzene on graphite, the net heat of adsorption, which is the difference between the heat of adsorption and the heat of vaporization (33.7 kJ/mol for benzene at 20°C) is 9.0 kJ/mol. For graphites lacking in microporosity (the first group in Table 1.1), the heat of adsorption increases at lower temperatures and is larger for the oxidized sample, presumably due to H^{+}-π chemisorbed interactions with acidic oxygenated surface functionalities. For parallel experiments with both benzene and *n*-pentane, the heat of adsorption of benzene is always greater, except on the MWCNT at 250°C. For the porous carbons (the second group of Table 1.1), most of the heats of adsorption are much higher, attributable to the Polanyi enhanced adsorption potential which occurs in very narrow pores [104]. Two samples of MWCNTs and the soot are the only samples with heats smaller than on the Sterling graphite. This may results from curvature of the aromatic surface (which distorts the π electrons of graphite from a planar aromatic arrangement) [46], or to disorder in the graphite crystalline development which weakens the adsorption potential of the surface [23, 105].

The classic early work for adsorption enthalpy and isotherms of benzene on Sterling graphite by Kiselev and Isirikyan [40] and Pierce and Ewing [56] from the

Table 1.1. Experimental enthalpies of adsorption for benzene at submonolayer coverage

Solid Phase	Temperature	Heat of Adsorption of Benzene (kJ/mol)	Related Compound	Heat of Adsorption of Related Compound (kJ/mol)	Method	Reference
Sterling graphite	-15°C	46.4			VT PI[a]	[b]
Sterling graphite	20°C	42.7-43.4	*n*-hexane	47.3-55.2	C PI[c]	[d]
Sterling graphite	20°C	42.7-44.4			GC[e]	[f]
Sterling graphite	25°C	41.8-43.5			VT PI[a]	[g]
Sterling graphite	100°C	41.0	*n*-pentane	36.8	GC[h]	[i]
Sterling graphite	125°C	39.3	*n*-pentane	37.2	GC[h]	[j]
Sterling graphite, oxidized	125°C	49.0-51.9	*n*-pentane	36.4-38.9	GC[h]	[j]
HOPG	250°C	41.1-52.5	*n*-pentane	31.5-32.4	GC[h]	[k]
CNF	250°C	33.7	*n*-pentane	27.5	GC[h]	[k]
NIST SRM #2975	-15°C	37.5			VT PI[a]	[l]
Activated carbons	25°C	75-45			C PI[c]	[m]
Microporous carbon film	25°C	85-60			C PI[c]	[n]
PICA HP mesopores	25°C	66-50			C PI[c]	[n]
ar-MWCNT	25°C	45-60			C PI[c]	[n]
o-MWCNT	25°C	37-59			C PI[c]	[n]
MWCNT	35°C	22.8-38.1	*n*-hexane	-23.9 to 35.3	GC[g]	[o]
SWCNT	60°C	54.4			C MI[p]	[q]
SWCNT	60°C		thiophene	54.4-57.8	C MI[p]	[q]
SWCNT	60°C		cyclohexane	48.5	C MI[p]	[q]
MWCNT	250°C	34.7	*n*-pentane	36.9	GC[h]	[k]
NaY zeolite	50°C	70			C MI[p]	[r]
Si	40°C	55			GC[h]	[s]

[a]isotherms measured using vapor pressure gauge collected at variable temperature; [b][106]; [c]isotherms measured using vapor pressure gauge and calorimetric detection of heat; [d][40]; [e]gas chromatography; [f][57]; [g][107]; [h]gas chromatography; [i][57]; [j][108]; [k][76]; [l][32]; [m][109]; [n][3]; [o][110]; [p]isotherms collected using a microbalance and calorimetric detection of heat; [q][111]; [r][112]; s[113].

early 1960's included plots of the ΔH_{ads} at several loading levels below a calculated monolayer, and these data showed that the heat of adsorption for benzene remains nearly constant at monolayer and submonolayer loadings. This is in contrast to the behavior of most sorbates (e.g., *n*-hexane [40]), which show strong increases in the value of ΔH_{ads} from very low loadings to a maximum at one monolayer . The influence of lateral interactions (also referred to as fluid/fluid potential) with neighboring adsorbed molecules accounts for the ΔH_{ads} increase in most molecules,

and in this classic paper [40, 56], the authors concluded that benzene molecules do not experience significant lateral interaction, but are limited by strong interaction with graphite at specific sites. However, later studies have shown that benzene molecules do interact significantly [114], and it has been suggested [114, 115] further that the reason for the lack of an increase in ΔH_{ads} as the loading approaches one monolayer is that the benzene molecules change their angles of orientation relative to the graphitic surface. Instead of lying flat, some of the molecules orient themselves at an angle [116], estimated by Do and Do to be 45° [4, 116] . The existence of a slanted orientation of benzene on graphite was demonstrated by Tabony et al [115], in which the authors observed that the ^{1}H chemical shift induced by the ring current effect of magnetic field anisotropy of the graphite surface changed with loading. An upfield shift of 35 ppm was calculated for a benzene molecule laying flat on the graphite surface with the proton 3Å from the surface, and the shift is 18 ppm for the furthest protons of a benzene molecule perpendicular to the surface [115]. Other experimental evidence for the angled orientation of some of the benzene molecules adsorbed on surfaces is the fact that, in several studies, the molecular area of benzene measured by "inverse" BET calculation from adsorption isotherms of benzene is $36Å^2$ [104] instead of the $43Å^2$ [117], as calculated from molecular mechanics. In addition, the orientation of benzene molecules in the crystalline state occurs in a T-shaped orientation and gives a herringbone appearance over several layers [118].

However, there is also spectroscopic evidence for the flat configuration at low temperatures. Bardi et al. [119] have observed in-register images of benzene

molecules on graphite at 140K using low-energy electron diffraction, and Meehan et al. [120] have observed neutron diffraction images of the benzene molecule on graphite at temperatures as warm as 200K, although they report the area of the benzene molecule at 37Å^2. At 130-140K, benzene undergoes a two-dimensional (2D) phase transition between 2D solid and liquid phases. This transition has also been observed with ^{2}H NMR [53] and neutron diffraction [120]. The relative amounts of benzene molecules of flat to slanted benzene orientations over a range of temperatures and the associated diffusion rates, have been modeled by Do and Do [4], using density functional theory, grand canonical Monte Carlo methods and other approaches, and, as stated above, Do and Do calculate an average orientation of 45° for the molecules which are not flat.

At temperatures below 200K and at very low loading, the benzene molecules lay flat, but at temperatures above 200K, especially near 298K (the temperatures at which our experiments were conducted), there remains a question as to the orientation of the benzene molecule on the surface of graphite (Figure 1.16). Do and Do in 2006 [4], building on the work of Vernov and Steele [114, 121], explain that benzene cannot be modeled as a single point, but must be considered as six sites. Each site has a Lennard-Jones type potential function due to dispersion interactions, and an electrostatic term is added to account for the benzene's large quadrupole moment [4]. Adjusting for the surface mediation due to the quadrupole of the aromatic π-electrons of graphite electrons [122] and maximizing the fluid/fluid interactions between the aromatic π-electrons of benzene have produced the following diagrammatic representation of the orientations of a submonolayer

ensemble of benzene molecules on a graphite surface. In addition, the modeled variation of benzene density with distance from the graphite surface shows a peak

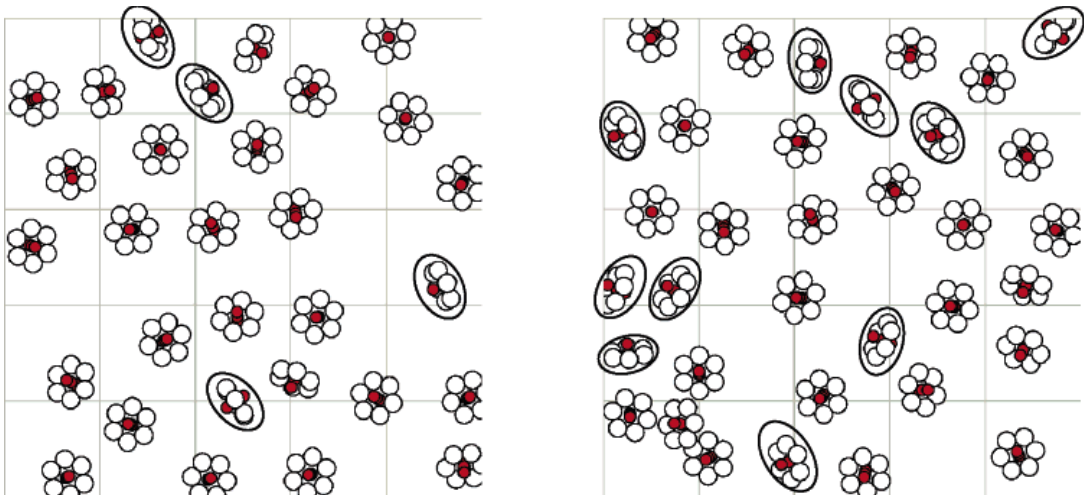

Figure 1.16. Diagrammatic representation of the orientation of benzene molecules on the surface of benzene at 273K (right 300 Pa, left 2000 Pa): from Do and Do [105] after Vernov and Steele [114].

3.35 nm from the surface, attributable to benzene laying flat on the surface, but, especially as a monolayer loading is approached, the model also predicts a smaller peak 4.5 nm from the surface. This second peak Do and Do [4] attribute to benzene molecules oriented at angle to the surface. This is in accord with the work of Hentscke, who modeled the average orientation of benzene at 298K as 35° to the surface of graphite [123].

The above discussion pertained to ideal graphite surfaces or to meso- or macroporous graphite, and how the benzene molecule interacts with that surface. As discussed above, activated carbons are dominated by microporosity and BCs in general have unique pore structures as well as surface chemistry with greater heterogeneity and complexity than an ideal graphite. Several research groups (e.g.,

groups with Do, Jaroniec, or Gauden) have published papers in recent years modeling adsorption isotherms on activated carbon or carbon blacks, utilizing the interaction models discussed above and various approaches to pore structure [5, 23, 94, 124, 125]. Gauden's group, in particular, states that theoretically calculated values for the enthalpy and entropy of adsorption are often not in accord with experiment, and this error may be due to assuming that the adsorbed vapor behaves like a liquid, rather than a solid [3, 124]. Thermodynamic values, $\Delta H_{adsorption}$ and $\Delta S_{adsorption}$, for benzene on different activated carbons at different loadings, measured using calorimetry, fall between $\Delta H_{vaporization}$ and $\Delta S_{crystallization}$ [3]. The modeling of N_2 isotherms in carbon nanotubes is also a subject of active investigation [5, 93, 126]. Assumptions about the shapes of the pores affect the calculated value of the pore width, as indicated by the pore shape terms in the above equations. In the Kelvin equation for drop size, the term V/r is a spherical distribution. Commonly used isotherm models have been devised for spherical, cylindrical and slit-shape pores, and a pore shape must commonly be assumed in order to use the isotherm data to determine a pore size distribution, e.g., Barrett-Joyner-Halenda (BJH) or Dollimore-Heal (DH) algorithms for spherical, density functional theory (DFT) or Dubinin-Radushkevich (DR) for slit-shaped pores [9]. The difficulty in modeling the adsorption isotherms of benzene due to pore sizes and shapes are exaggerated for micropores because the assumptions behind the Polanyi-Dubinin-Manes (PDM) isotherm equation breaks down [3], and, as noted by Chiou and Manes, the PDM models show large deviations for systems which involve steric exclusion from micropores [92]. These are questions which may be

effectively answered by observing the molecular motion of benzene. For example, if the state of benzene adsorbed in micropores is intermediate between solid and liquid, studies of the motion of such constrained benzene might confirm such a constraint and, in addition, reveal the type of restricted rotation which is occurring.

1.1.3.3 Surface Diffusion

1.1.3.3.1 Surface Diffusion Overview

Miyabe and Guiochon state that "surface diffusion should be considered as molecular diffusion restricted by the adsorbate interactions in the potential field of the adsorbent" [127]. It has long been recognized that surface diffusion (SD) is an activated process [128-132], which can be described by the following equation:

$$D_s = D_{s0} \exp(E_a/RT) \qquad \textbf{(Eqn.} 1.19)$$

where D_s is the rate of surface diffusion as unit area/time. D_{s0} is D_s at zero concentration and represents the geometrical configuration of adsorption sites. It is related to surface area, and, in porous media, to tortuosity and the fractal dimension [131, 133]. Similarly, given a constant (or average) jump distance, the equation can be restated in terms of jump rate, k, or residence time τ at an adsorption site:

$$1/\tau = k = k_0 \exp(E_a/RT). \qquad \textbf{(Eqn}. 1.20)$$

The pre-exponential factor, k_0, represents the jump rate for a lattice gas in the absence of adsorption (zero coverage), affected only by interactions with nearest neighbors and temperature [134]. Absolute rate theory, statistical mechanical treatments, and related modeling approaches have been applied by a few workers, as outlined in the review article by Choi et al. [131], notably Anton [134], Gomer [135], Chen and Yang [136], and Kapoor and Yang [137], but the authors

predominantly deal with catalytic chemisorption systems. Miyabe and Guiochon analyze the process of surface diffusion in chromatographic systems as a combination of (1) a hole-making process in the mobile phase and (2) a bond-breaking process between the adsorbate molecule and the solid phase [138], and they compare surface diffusion in liquid/solid systems to gas/solid system with identical solid phases. In a series of papers [127, 139-141], the authors demonstrate that the bond-breaking process, which exhibits a correlation between E_a of SD and Q^{st}, is the same with both liquid and gas mobile phases, and the difference in the surface diffusion between the two systems lies in the hole-making step, which correlates to E_a of molecular diffusion in gas systems and the E_a of viscosity in liquid systems [138]. Additionally, Choi et al. [131] have provided an excellent review of surface diffusion (SD), which predominantly focuses on gas phase sorbates, and describes surface adsorption as either mobile or stationary, with three basic models for surface diffusion, all of which are activated processes: the hopping model, the random walk model, and the hydrodynamic model. In general, activated jumps involve a potential energy well at the active adsorption sites surrounded by a significant energy barrier which must be overcome in order for the molecule to jump. Although this condition is most descriptive of chemisorption ($\Delta H_{adsorption}$ excess of ca. 80 kJ/mol)[104], it is also valid for physisorption processes as long as the energy of activation (E_a) is greater than kT, where k is the Boltzman constant [142], and is applied successfully for neat solvents [140]. Therefore, the rotational jump model inherent in the motional models employed by the Deuterium Fitting Program (DFP), a program which simulates the static solid-state ^2H NMR spectra of

deuterated molecules for specified motions and is similar to MXQET by Vold's group, lends itself well to an interpretation of the data in this study, despite the fact that the technique should be most sensitive for benzene molecules which are localized sufficiently to produce a Pake pattern.

For a hopping model of surface diffusion on a homogeneous surface, generally, a plot of diffusivity versus loading shows that diffusivity increases up to the region of monolayer coverage and then begins to decrease as multilayers are formed [131]. The E_a for surface diffusion frequently correlates to the isosteric heat of adsorption [129, 138, 140], and also exhibits characteristic patterns depending on the sorbate and sorbent with respect to loading in the submonolayer to early monolayer coverage region [116]. A multilayer diffusivity decrease is attributed to a reduction in entropy due to crowding at higher surface loadings [131]. Haul and Boddenberg [143] recorded a maximum diffusivity for benzene on Aerosil at near 50% monolayer coverage. It is possible that, inasmuch as most of the studies involve small molecules that are gaseous at room temperature, the effect of "crowding" may occur at a lower loading for benzene than for smaller molecules. The pore structure of sorbent may also play a role here. Multilayer formation is difficult to distinguish from capillary condensation in micropores [131]. As discussed above, for benzene, a fraction of the molecules on graphite changes from a flat to a slanted configuration as submonolayer loading increases to reduce surface crowding. Rigby (2003) suggests that the measured values for surface diffusion are dominated by a fraction of sorbate molecules, attached at low energy sites, "flying" over the surface, and that as much as 40% of the sorbed molecules have very short

jump distances. As discussed above, the isosteric heat of benzene on graphite, the model interaction, does not change with loading because of the entropic adjustment of configuration. Therefore, if benzene-graphite sorption is a reasonable model for benzene on BCs in general, then a trend of E_a of surface diffusion with submonolayer loading for benzene on BC may indicate surface heterogeneity.

Compensation effects (correlations of entropy with enthalpy for a given reaction) are observed with both the adsorption thermodynamics [76] and the kinetics of surface diffusion for benzene [131, 138, 144], as are correlations between the energy of activation of surface diffusion and the enthalpy of adsorption, mentioned in the paragraph above [129, 140]. At lower loadings, the sites with higher energies of adsorption are occupied, and the benzene molecules have more space to move between these few sites. As the loading increases, entropy increases due to lateral interactions between neighboring adsorbed benzene molecules. This is the traditional explanation, elaborated by Arena et al. [145]. Rigby takes exception [144], saying the increase in entropy had to do with higher occupancy of similar sites grouped together.

1.1.3.3.2 LFERs and enthalpy/entropy compensation (EEC) effects in surface diffusion

The correlation between E_a and Q_0^{st} is a Hammett-type (kinetic vs. thermodynamic) LFER, and, like other LFERs [2], its value has been associated in general with the mechanism of adsorption, for which values of ~0.5 and ~0.25 occur with physisorption and chemisorption, respectively [129, 130]. The original data used to develop this hypothesis was compiled by Sladek et al. [130] from published data and was categorized based on types of sorbates (polar or nonpolar), sorbents

(conducting or insulating), and adsorption bonds (van der Waals, covalent, or ionic). The conceptual model for adsorption which leads to the ratio E_a/Q_0^{st} being less than one is similar to that for the Brunauer-Emmet-Teller (BET) equation: namely, that the 1st layer of molecules adsorbed onto a solid surface is held more strongly than the 2nd layer, which is held more strongly than the 3rd layer, . . etc. By the time the 4th or 5th layer is reached, the attraction to the adsorbed layer does not exceed the attraction to surrounding sorbate molecules, i.e., the bulk liquid-state conditions exist [9, 104]. The major criticism of the BET model is its neglect of lateral interactions, and this led to the development of the Frenkel-Halsey-Hill (FHH) equation, which treats multilayer adsorption as a slab [104]. Thus, the FHH equation provides one method for calculating thickness of the adsorbed layer [146, 147], and the exponent of the equation was subsequently used to measure the surface fractal dimension [148, 149].

As addressed in a number of publications by Miyabe and Guiochon [127, 138-141] with associated researchers studying the mechanism of adsorption of various sorbates on octadecyl-silica columns in reversed-phase liquid chromatography, the ratio of E_a/Q_0^{st} is one of a number of LFERs and enthalpy/entropy compensation (EECs) effects which occur for this and other surface systems. Q^{st} has been related to boiling point and to K, the equilibrium constant at for adsorption, and D_{s0} to E_a, the pre-exponential factor for surface diffusivity and its energy of activation, respectively. The authors mention two possible objections to their approach [140, 150]. First, many researchers believe that the mechanism of adsorption onto a C_{18} column is partitioning (not a gas/solid

interaction). However, C_{18} is a solid at room temperature [151], and, even at higher temperatures, the specific mechanisms of retention in reversed-phase chromatographic systems remain poorly understood, especially with respect to shape selectivity. Poole and Schuette [21] state that the partitioning occurs within a multilayer-like zone of the mobile phase closest to the C_{18}, and this is supported by the strong influence that variations on the mobile phase exert upon chromatographic separation and performance. In addition, Miyabe and Guiochon have compared gas/solid adsorption data on C_{18} columns to reversed-phase liquid chromatography (RPLC) systems for the same sorbate molecules (including benzene), and have shown, based on LFERs, that the mechanism of surface diffusion is the same [127]. The second objection is a more general skepticism about EECs in general. However, the particular meaning of EECs varies considerably from system to system, and some workers have concluded that all EECs are simply the result of sampling or statistical error, or simply a result of the form of the Arrhenius equation [150, 152, 153]. Further, some researchers state that an EEC must have an isokinetic point to be valid [153]. Liu et al. [152] have reviewed these objections and concluded that a correlation between enthalpy and entropy is a sufficient identifier. In any case, EECs are widely cited in studies of surface processes, such as adsorption and catalysis [76, 129, 131, 145, 153-156].

For the surface diffusivity of sorbates, in particular benzene, which exhibit an EEC on a set of solid phases, Rigby states that the EEC indicates that the mechanism of adsorption and surface diffusion is the same on each solid phase [157]. This is in accord with the early work of Sladek, Gilliland, et al. [129, 130],

mentioned above. Further, however, Rigby suggests that τ_0, which, measured by ^2H static solid-state NMR, is "the limiting value of the correlation time as temperature tends to infinity" [157], and, therefore, "is inversely proportional to the area within [a] limiting jump range" [157]. Based on these relationships, Rigby [158] derived an equation with related τ_0 to the surface fractal dimension.

$$\tau_0 / \tau_0 r = \sigma^{(d - dr)/2}, \qquad \textbf{Eqn}.1.21$$

where σ indicates the area of the sorbate molecule (benzene) and $\tau_0 r$ and dr are the correlation time and surface fractal dimension, respectively, for a reference solid. Based on this equation, he predicts the fractal dimension from static solid-state ^2H NMR data for several others solids that he analyzed, and also for Carbopack B, using Grundke and Boddenberg's [53] results. Thus, because of the similarity of Rigby's approach to this study, at least in analytical techniques, his equations can be tested in this work.

1.1.3.3.3 Fractal dimension, FHH equation, and their relation to surface diffusion

As explained by Pfeifer and Avnir [148], a surface has a fractal dimension with a value which can range between two and three. The lower limit of two represents a completely smooth surface on which sorbate molecules will exist as a 2D liquid or solid. As the surface becomes more convoluted, some of the sorbate molecules will lie at an acute angle with respect to other sorbate molecules, and, as the surface reaches the limits of convolution, the adsorbate can be though of as "dissolved" in the solid matrix with bulk 3D properties. In order to explain the measurement of surface fractal dimension by adsorption techniques, the authors present the conceptual model in which a number of balls are placed atop the edges

of a square and the number of balls, N(r), as a function of the radius of the balls, r, approaches $(\pi r^2)^{-1}$ as the radius approaches zero. If a cube is covered in balls instead of a square, the function N(r) approaches $(\pi r^3)^{-1}$ as r approaches zero. In these two examples, the exponent of the radius indicates the dimensionality of the system (2 or 3), and, in general, the function N(r) defines the dimensionality of the substrate, according to the following equation:

$$D_s = - \lim (r \rightarrow 0) [\log N(r) / \log r], \qquad \textbf{Eqn}.1.22$$

where D_s is the fractal dimension of the substrate for all values of r. Extending this conceptual model to a physical system, if the square is replaced by a solid substrate, and the balls by adsorbate molecules, then N(r) becomes n, the number of molecules in a monolayer, and r becomes σ, the diameter of the adsorbate molecule, and, consequently, n is proportional to $(\sigma^{Ds})^{-1}$. Values of D_s between 2 and 3 are due either to (1) surface heterogeneity, which is described by Jaroniec [149] to consist of "various irregularities from cracks, steps, flaws, impurities and differing atomic species," or (2) to heterogeneous pore size distributions in microporous materials [148].

The FHH equation (below) was originally developed in the 1940's and 1950's for interpretations of the growth of mono- and multilayers using gas/solid isotherm data [146, 149, 159, 160]

$$p/p_0 = \exp (-a/\theta^r), \qquad \textbf{Eqn}.1.23$$

where θ is surface coverage, a is a constant, and r describes the nature of the adsorbing forces [159]. When r is small, van der Waals forces predominate, and when r is larger, condensation forces are more important [159]. The role of

"cooperative adsorption" between molecules in multilayers is the basis for the FHH isotherm equation, as distinct from both (1) site-limited Langmuir adsorption and (2) a constant adsorption energy for each adsorbed layer assumed in the BET model [159]. Especially for multilayers greater than 2, [146] has described the adsorbed molecules as a "slab" of liquid, possessing bulk liquid density, under the influence of a surface potential field, resembling the Polanyi model. Thus, the FHH model been labeled a "slab" or "thick-film" model of adsorption [160, 161]. Following the initial work of Pfeiffer and Avnir [148], Avnir and Jaroniec [162] modified the FHH equation to the Dubinin-Radushkevich isotherm equation, a form of the thermodynamically based Polanyi equation, for use in determining pore size distributions. After further thermodynamic derivation based on the Kiselev modifications (using surface tension of the liquid and the Kelvin equation) to the Polanyi equation [163], the FHH equation, below, has been used commonly as a tool for measuring the surface fractal dimension of solids,

$$\ln (V / V_m) = C + S \ln (P_0 / P), \qquad \textbf{Eqn}.1.24$$

where V is the volume of N_2 adsorbed, V_m is the volume of N_2 in a monolayer, P_0 is the saturation pressure of N_2, P is the vapor pressure of N_2 for the given V, C is a constant, S is a constant related to the fractal dimension, described below [144, 164].

Although the initial theoretical development of the FHH equation focused on capillary condensation, there are commonly two regions of linear slope in plots of the FHH equation, (1) the capillary condensation and (2) monolayer adsorption, and either of thes e regions can be used to calculate the surface fractal dimension [165-

169] In the literature [149, 157, 166, 169], there is some lack of clarity as to the correct choice of regions for a given sample and, similarly, which of the two possible equations (below) to use for calculating the fractal dimension from the selected slope, S,

$$S = (D_s - 3) / 3 \qquad \textbf{Eqn}.1.25(a)$$

$$S = D_s - 3 \qquad \textbf{Eqn}.1.25(b)$$

The first equation is applicable for monolayer coverage where van der Waals' forces are most important in adsorption, and the second equation is applicable for multilayer regions where capillary condensation is most important. However, the second equation is often applicable in the monolayer region because surface roughness enhances capillary condensation and may obscure the van der Waals' adsorption regime. Usually, only one of the equations will result in a D_s value that is between 2 and 3, and thus the choice is made. Tang et al. [169] suggest restricting application of the FHH equation for fractal determination to use of the monolayer region and have followed Ismail and Pfeiffer [165] in specifying that equation (b) be used for slopes more negative than -0.333 and equation (a) otherwise.

There are several methods for measurement of the surface fractal dimension other than gas adsorption, including dynamic light scattering, image analysis, small-angle X-ray scattering. However, in the comparative study of different methods (NMR not being one of them) for evaluating the surface fractal dimension of activated carbon fibers, Tang et al.[169] favored using the FHH plot of the N_2 isotherm for accuracy and simplicity. Nitrogen gas is a particularly good probe for

surface geometry because of its small molecular size (16.2 $Å^2$), its very low interaction with most solid surfaces, and its regular molecular orientation in the 2D phase due to lateral interactions between the quadrupoles of adjacent sorbed N_2

Table 1.2. Surface fractal dimensions for different solid phases

Solid Phase	Fractal Dimensio	σ	Method
Carbon black N990	1.97	±0.09	a,d
Graphon	2.04	±0.16	b,e
Vulcan 3G	2.07	±0.01	b,e
Bovine serum albumin particles smooth	2.12	±0.04	a,f
Graphon	2.25	±0.16	a,e
Carbon fiber	2.38	±0.03	a,d
Bovine serum albumin particles rough	2.39	±0.03	a,f
MWCNT	2.532		a,g
Carbon fabric	2.56	±0.03	a,d
SWCNT	2.625		a,h
Activated carbons	2.3-2.8		a,i
Carbopack B	2.226	±0.004	c,j,n
Pt/alumina cat	2.31	±0.01	c,k,n
Alumina	2.35	±0.01	c,k,n
Sol-gel silica G1	2.525	±0.007	a,l,n
Fumed silica C1	2.611	±0.004	a,l,n
Sol-gel silica G2	2.639	±0.011	a,l,n
Pt/G1 cat	2.71	±0.01	c,m,n
Pd/G2 cat	2.73	±0.01	c,m,n

[a]FHH; [b]particle size; [c2]H NMR; [d][165]; [e][172]; [f][169]; [g][173]; [h][174]; [i][175]; [j][53]; [k][176]; [l][158]; [m][157]; [n]plottted in Figure 3 of Rigby [157].

molecules [170]. Rigby et al., in a series of papers [133, 144, 157, 158, 171], has used solid-state ^2H NMR of C_6D_6 loaded at one monolayer coverage on different solid phases to measure fractal dimensions. First, the correlation time, τ_0, of the C_6D_6 is determined from an Arrhenius plot, and then the fractal dimension is

calculated with the correlation time of a reference sample, τ_{0r}, and its surface fractal dimension, d_r, using Eqn. 1.19, which is related to the compensation effect observed in the surface diffusion rates over for specific ranges of temperatures.

Table 1.2 lists surface fractal dimensions for several solid phases. Although the surface fractal dimension is a measure of self-similar surface roughness, the precise definition of surface roughness, as it can be measured, is lacking. Jaroniec's definition above implies that chemical heterogeneity as well as pore size distribution contribute to surface roughness which is described by a fractal dimension [149]. A value very near 2.0, which has been measured by some methods for Graphon [172]and Aerosil [148], indicates a very smooth, homogeneous surface, and larger values (up to 3.0) indicate more surface roughness. But Drake et al. [166] stated that D_s measured by FHH does not contain information regarding sorbate morphology, and, similarly, Neimark and Unger [170] concluded that the fractals indicated the roughness of the pore walls and not the geometry of the channel. However, the authors also presented one example, a crystalline apatite, where the surface in general have values that commonly range from 2.3 to 2.8, Erhberger-Dolle [167] reported that heat treating activated carbons creates pores that are larger, more chemically homogeneous, and decrease the fractal dimension from 2.8 to 2.1 in one sample. However, in a similar study on CNTs, Sun et al. [174] did not observe any change in fractal dimension after heat treating, and Rigby performed a similar study on silica sol gels and found no difference in the fractal dimension after heat treatment [144]. Nevertheless, despite ambiguity about the nature of surface roughness, for this study , the link between the surface diffusion of benzene and the

surface fractal dimension of solid phases observed by Rigby can provide information about the nature of the benzene/black carbon interaction, especially because the fractal behavior of environmental sorbents in general, particularly as it may impact slow sorption process, is currently an active area of study [177, 178].

1.1.3.3.4. Spectroscopic observations of the motion of benzene on graphite

Various spectroscopic techniques can be used to characterize benzene adsorbed to a surface, including infrared, XRD, Raman [179], fluorescence spectroscopy, and most of these techniques are somewhat sensitive to motion in that thermal motion introduces uncertainty into the measurements. An example mentioned above, Bardi et al. [119] published an low-energy electron diffraction image of benzene on graphite that shows an "in register" √7 x √7 2D unit cell of benzene molecules, which would mean that at least 7 benzene molecules must remain flat at this temperature on the graphite surface for the brief duration of the scan. Similarly, STM studies of benzene have been accomplished on graphite and revealed the HOMO/LUMO changes in the graphite substrate when interacting with an adsorbed benzene and well as imaging the adsorbed benzene itself [180]. A chemisorbed benzene molecule, for instance, on platinum (18), will show different vibrational spectra (infrared and Raman) than the free species, but the interactions of BC with benzene involve physisorption rather than chemisorption. However, for molecules not strongly adsorbed to the surface, the vibrational spectra may remain unchanged, although the physisorption interactions will still affect the motional trajectories of the adsorbed molecules, although increasingly techniques that have traditionally been restricted to chemisorbed species are being applied to physisorbed molecules [9].

However, spectroscopic techniques which are sensitive to motional frequencies have be used to characterize the physisorption of benzene to various solid phases with great utility [142]. It is well known that an average value of diffusion generally is 10^{-5} cm/s, which corresponds well to the rotational frequencies for many molecules. Therefore, the most commonly used spectroscopic techniques for measuring diffusion are those which observe the rotational motion of molecules, particularly NMR [181], neutron scattering , Raman, and fluorescence. The last two present problems due to excitation signal absorption and/or interference when examining black carbon materials. Because deuterons relax from their excited spin states via a quadrupolar mechanism (which responds to fluctuating electric field gradients that occur as the molecule moves *by itself* rather than by the dipolar mechanism that occurs in spin ½-nuclei, such as ^{1}H and ^{13}C, which is dependent on nuclei from atoms *nearby*), the ^{2}H NMR signal is a good tool with which to observe molecular rotational motion [142, 181, 182] Further, the molecular motion of benzene on a graphitized carbon black has been observed spectroscopically by Boddenberg's group using ^{2}H NMR, ^{1}H NMR, and pulsed-field gradient NMR [53, 55, 143, 176, 183, 184].

1.2 OBSERVATION OF MOLECULAR MOTION USING ^{2}H STATIC SOLID-STATE NMR

1.2.1 Theory

Following is a brief introduction of NMR taken from standard texts [181, 185, 186]. All NMR spectroscopy involves the excitation of the nuclear magnetic spin state of some of the nuclei from a lower to a higher level by means of a radio frequency pulse. When the sample is within the probe and the magnetic field of the

NMR instrument, the nuclei precess at the characteristic Larmor frequency, producing a net magnetization aligned toward the instrument's static field, B_0, the *z* direction. When some of the nuclei absorb energy from the excitation pulse, their spin orientations will flip opposite to B_0, resulting in a bulk magnetization component perpendicular to B_0, the *x* or *y* direction, and, after cessation of excitation, will flip back (relax) to their lower energy states. Because the electronic signal results from this relaxation, the mechanism of relaxation is important to signal interpretation. For spin ½-nuclei, such as ^{1}H and ^{13}C, relaxation is predominantly via dipole-dipole interactions, in which the nuclei transfers its magnetization to neighboring nuclei which is rotating at the appropriate frequency.

However, ^{2}H is spin 1, has an electric quadrupole moment, and relaxes predominantly through a quadrupole mechanism, which is a more effective and rapid relaxation mechanism than through dipole-dipole interactions [186, 187]. As in other types of NMR coupling, the quadrupole coupling splits the ^{2}H peak to produce a doublet which is centered around the Larmor frequency. The value of the observed quadrupole splitting, ν_Q, is given by

$$\nu_Q = \pm (3/8)(e^2qQ/h\ (3cos^2\theta - 1\text{-}\eta\ sin^2\theta\ cos^2\phi), \qquad \textbf{Eqn}.1.26$$

where e^2qQ/h is the quadrupole coupling constant, experimentally determined to be 189.33 kHz for benzene [188]. The electric quadrupole moment of the nucleus, *eQ*, where *e* is the charge of a proton, and *Q* is an intrinsic property of each nucleus. The largest component of the electric field gradient (EFG) tensor is *eq*, where *e* is the charge on the electron, and *q* is intrinsic property of a particular nucleus in a particular molecule [188]. The largest component of the EFG, which has the value

eq, is defined to be the *Z*-direction of the EFG and of the principal axis system (PAS) [189]. In benzene, the EFG *Z*-direction is oriented along the electron cloud of the C-D bonds [190]. The angles θ and ϕ are the polar angles relating the *Z*-axis of the principal axis system to the *z*-axis of B_0 [187]. The asymmetry parameter, η, has a value of 0.04 for benzene and depends on the shape of the EFG tensor, **V**,

$$\eta = (V_{xx} - V_{yy}) / V_{zz} = (V_{xx} - V_{yy}) / eq \text{ [187]}. \qquad \textbf{Eqn}.1.27$$

For benzene, the principal axis system is defined by V_{zz} (largest) going through the C-D bond in the plane of the ring, V_{yy} (intermediate) is the C_6 axis; and V_{xx} is coincident with the C_2 axis that lies in the ring plane and bisects the C-C bonds [189, 190].

Commonly, in liquid samples at room temperature, the doublet is obscured by the increased line width of the deuteron NMR signal [181]. The line width of the deuteron peaks is wider than for proton peaks because of the rapid quadrupolar relaxation rate [181, 182]. However, in solid-state NMR of powder samples (in the absence of sample spinning), the peak shape is very different, consisting of a sharp intensity maximum followed by an inverse exponential tailing of intensity across the frequency scale [187]. The effective static magnetic field which is experienced by a particular deuteron, $B_{0\text{-eff}}$, is diminished if the molecule is oriented less than 90° to the direction of B_0, and this effect is termed chemical shift anisotropy. A quadrupolar nucleus does not have a spherical magnetic field, but an oblate shape [181, 191]. The resulting internal electric field gradient changes in response to variations in external electric fields caused by motion of the bonding electrons close to the deuteron (in benzene-d_6, the C-D bond especially) as the overall molecule

rotates. As a consequence, the NMR lineshape of the nucleus under observation is strongly affected by the molecular motion, and, thus, analysis of this lineshape reveals information about the motion [187, 191]. If the molecule is not moving, this spread of chemical shift values around the Larmor frequency in Fig. 1.17(a) is due solely to the random orientation of the powder particles within the sample: the intensity maximum occurs for orientations of 90° to the instrument's field [191]. For ^{2}H, the I=1 produces a mirror image of ^{1}H signal (Fig 1.17b), and this is called the Pake pattern, after the scientist who first discovered it in the early 1950's [181]. If a ^{2}H nucleus is undergoing rapid isotropic motion, however, the resulting spectrum will be a single Lorentzian peak, similar to a liquid NMR spectrum or to a

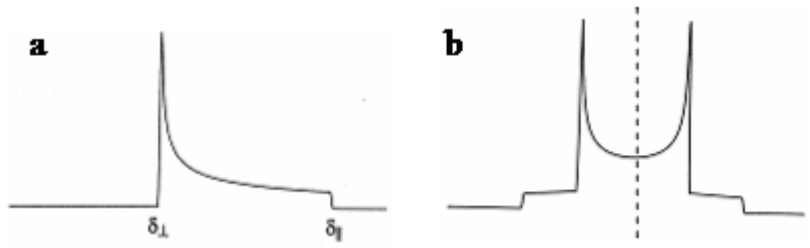

Figure 1.17. a) An idealized spin-1/2 static solid spectrum, showing the maximum and minimum amplitudes for a static sample at chemical shifts corresponding to orientations perpendicular and parallel, respectively, to B_0, b) an idealized Pake pattern for a spin-1 nucleus [181]; the dotted line indicates the Larmor frequency.

solid NMR spectrum with a sample spinning at the magic angle [182, 192, 193]. Further, just as in the liquid NMR spectrum of an exchanging proton, lowering the temperature can allow resolution of a single peak into two (one for each position), because at the lowered temperature, the deuterated molecule will "stay in place" long enough for the spectrum to display a Pake peak [194]. Thus, by analyzing the

line shape of the static solid-state ^{2}H spectrum, one can observe the motion of the molecule of interest for solid samples or for samples which include a significant solid component, and, additionally, by molecular dynamics simulation of the spectrum, one can describe this motion [190].

Quadrupole echo pulse sequences are employed to observe static ^{2}H NMR spectra: $90^o_x - \tau_1 - 90^o_y - \tau_2 -$ acquire, where τ_1 and τ_2 are the echo delays [187]. Echo sequences in general serve to refocus signals which deviate over time due to magnetic field inhomogeneity or coupling [185]. It is important that the Fourier transform of the free induction decay (FID) begin at the top of the echo signal (the maximum focus) [187]. Otherwise, some of the signal will missed due to dephasing, and the intensities of some of the frequencies will be lowered from their actual intensities, distorting the peak shape [187]. The FID is simulated according to the following equation, as explained in detail by Greenfield [190],

$$E(\tau_1,\tau_2) = \mathbf{1} \bullet \boldsymbol{\sigma}(\tau_1,\tau_2) = \mathbf{1} \bullet \exp[\mathbf{A}\tau_2]\exp[\mathbf{A}^*\tau_1]\boldsymbol{\sigma}(0) \qquad \textbf{Eqn}.1.28$$

where E is the signal intensity, $\boldsymbol{\sigma}$ is a matrix of complex transverse magnetization vectors at each orientation site, and

$$\mathbf{A} = i\boldsymbol{\Omega} + \mathbf{K}, \qquad \textbf{Eqn}.1.29$$

where $\boldsymbol{\Omega}$ is the site frequency matrix and $\mathbf{K}$ is the kinetic rate matrix [190, 195]. The site frequency, Ω_{ii}, or ω_i, is related to the second-rank quadrupole coupling tensor, $T^{(2)}$, in the laboratory (LAB) frame,

$$\omega_i = (3/2)^{1/2} T_0^{(2)\mathrm{LAB}}, \qquad \textbf{Eqn}.1.30$$

and the motions of molecule are related to this tensor by two transformations, where the subscripts p and q indicate the transformation components [190, 195]. One

transformation, $D_{pq}^{(2)}*(\phi,\theta,\psi)$, rotates the principal axis system (PAS) , which is conventionally a crystal with the quadrupole coupling tensor oriented to the z-axis, through the Euler angles (ϕ,θ,ψ) to the location of the site of motion, and a second transformation, $D_{0p}^{(2)}*(\alpha,\beta,\gamma)$, rotates this orientation through another set of Euler angles (α,β,γ) to the laboratory frame (LAB) [190, 195],

$$T_0^{(2)\mathrm{LAB}} = \sum_{pq} D_{0p}^{(2)}*(\alpha,\beta,\gamma) D_{pq}^{(2)}*(\phi,\theta,\psi) T_q^{(2)\mathrm{PAS}} \qquad \textbf{Eqn}.1.31$$

Figure 1.18 illustrates diagrammatically a single rotation of this type, in this case, from the PAS to the LAB directly. Combinations of molecular motions (more than one motional frame) can be simulated as detailed in the landmark work of Greenfield [190]. For our study, we used the Deuterium Fitting Program developed

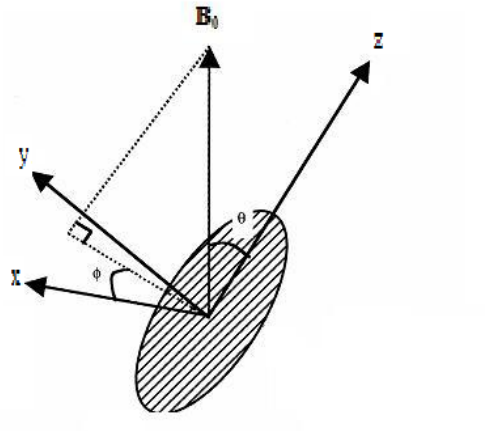

Figure 1.18. Diagram of a single transformation directly from the PAS (the oval indicating the crystallite) to the LAB frame, showing the polar angles θ and ϕ, which are also the Euler angles β and α, respectively [187].

by Eastman and Nanny [195], which is similar to the MXQET program of Vold's group [190, 192]. In both of these programs, the user generates a library of spectra after inputting parameters, such as the kinetic (jump rate) values, the motional mode (e.g., nearest neighbor exchange only or all sites exchange, and a description of the

motion (a list of each site to which the molecule jumps during that motion as specified by their Euler angles). DFP, which is considerably more "user friendly" than MXQET, also contains an automatic fitting component. Three common types of benzene-d_6 jump motions (Figure 1.19) are incorporated into the Deuterium Fitting Program: (1) small-angle wobble (SAW) which is a motion defined by rotation of the benzene around its C_6 axis with a wobble of the molecular plane around its normal to the BC surface at angles of $< 25^o$; (2) large-angle wobble (LAW) which is a motion similar to SAW, but with a larger molecular plane wobble

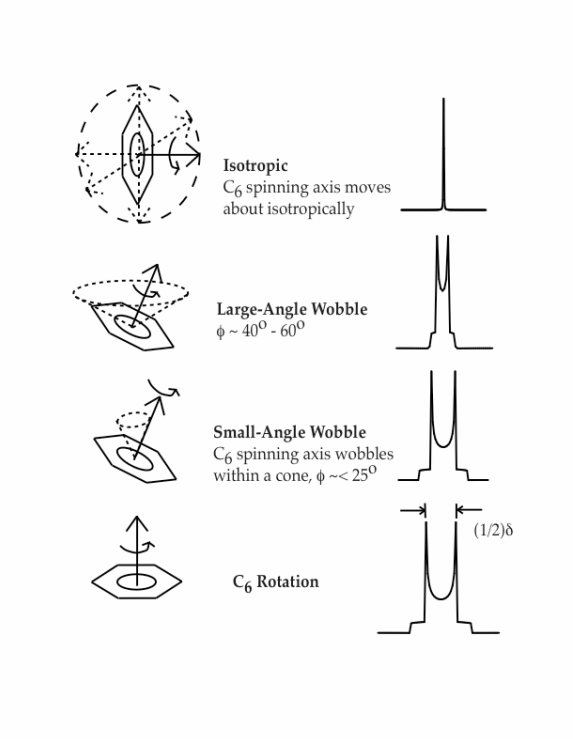

Figure 1.19. Motional models incorporated into DFP: (ISO) isotropic motion, modeled to jump to the 32 sites of dodecahedron; the (LAW), large-angle wobble and (SAW) small-angle wobble, modeled to perform jumps of the C_6 axis to 10 sites on a cone (6 on the cone edge, 3 along a middle cone, and one in the direct center of the cone; jump rates and wobble angles can be specified by the user [195].

angle of 40° to 60°; and (3) isotropic "tumbling" (ISO) of the benzene-d_6 molecule.

1.2.2 Previous ^{2}H NMR studies of the motion of benzene on solids

The ISO, SAW and LAW motions have been observed in several ^{2}H NMR studies of benzene associated with solid phases. In an early application of MXQET, Ok et al. [192] looked at solid (140K-87K), neat, fully deuterated benzene, and fitted the spectra to a SAW model (Figure 1.20). Some important motional studies of benzene-d_6 associated with solid phases using ^{2}H NMR involve zeolites [142, 194, 196], clays [188], alumina [176, 183], clathrates [189, 192, 197, 198], and graphites [53-55, 143]. Gedat et al. [142] observed freezing point depression (below 5.5^{o}C) and combinations of ISO and SAW motions in samples of benzene-d_6

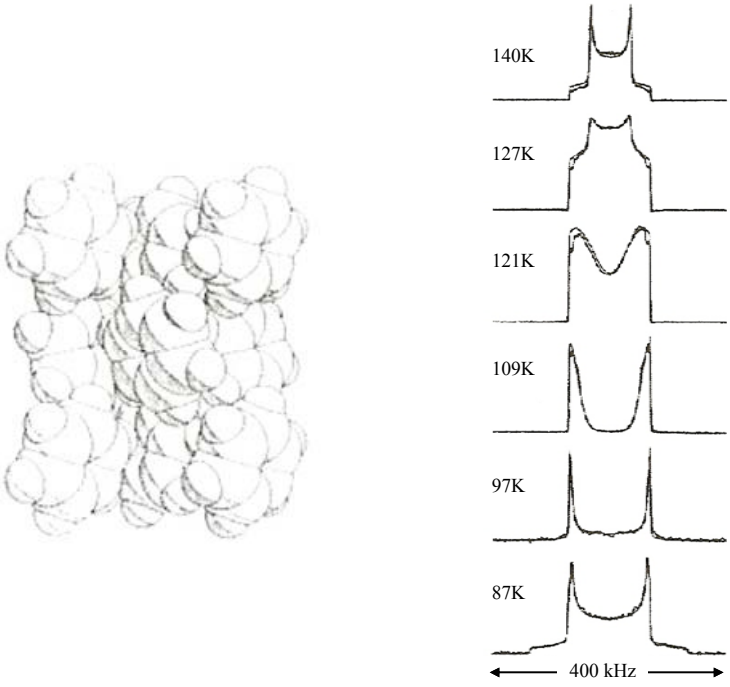

Figure 1.20. a) space-filling model of crystalline benzene [192]; b) solid-state static ^{2}H NMR spectra of benzene-d_6 with SAW simulated spectra (dotted lines).

loaded onto zeolite SBA-15, which has cylindrical pores of 8 nm diameter with "rough" walls (Figure 1.21). The authors concluded that the SAW represented the motion of benzene-d_6 crystallites in the center of the pore and the ISO signal results from benzene-d_6 close to the pore walls, which exert a surface force on the adjacent benzene-d_6 and disrupt the process of benzene crystal formation. Another pertinent study was that of Xiong and Maciel [188] with benzene-d_6 on Ca-montmorillonite. These workers also found a mixture of ISO and SAW at temperatures below the freezing point of benzene, especially in the 3.9% w/w loaded samples. However, in

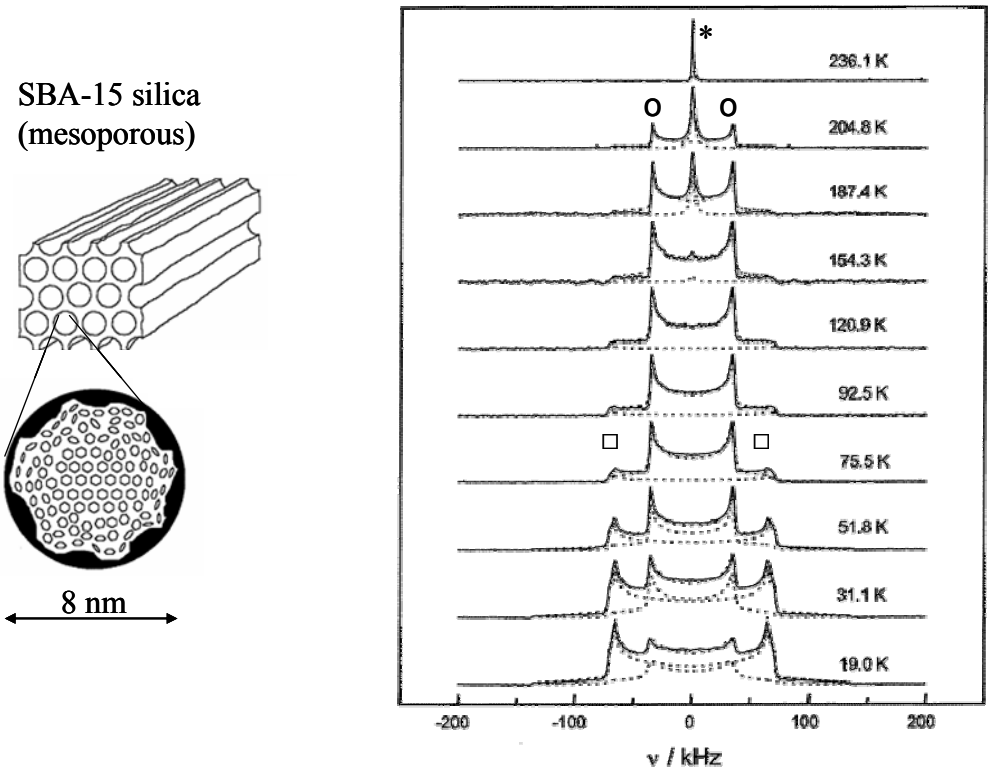

Figure 1.21. Variable-temperature ^{2}H NMR static solid-state spectra of benzene-d_6 in pores of SBA-15 mesoporous silica at 85% saturation; isotropic peak * is due to disordered molecules near the pore edges; inner Pake patterns ^{o}, $^{□}$, due to SAW, C6 motions, respectively. Modified from [142].

addition, in the 1.2% w/w loaded samples, they observed SAW and LAW at room temperature and attributed this restricted motion to π-Ca^{2+} interactions (Figure 1.22). Auerbach et al. [194] compared the motion of benzene on two zeolites whichdiffer in the Si-Al ratios and thus in the number of Na^{+} binding sites. These authors considered the benzene motion to consist primarily of hopping between cation sites,but proposed a cartwheel motion of the benzene molecule as it moves through the zeolite cavity from one site to another or between adjacent cavities (Figure 1.23). Another study, performed on benzene-d_6 in a carceplex, produced spectra similar to those observed for our maple wood char sample, and the authors [198] concluded the spectra was due to very complicated motion, possibly the result of the influence of the symmetry of the clathrate voids on the molecular motion. The effect of the symmetry of the surrounding cavity on the motion of benzene-d_6

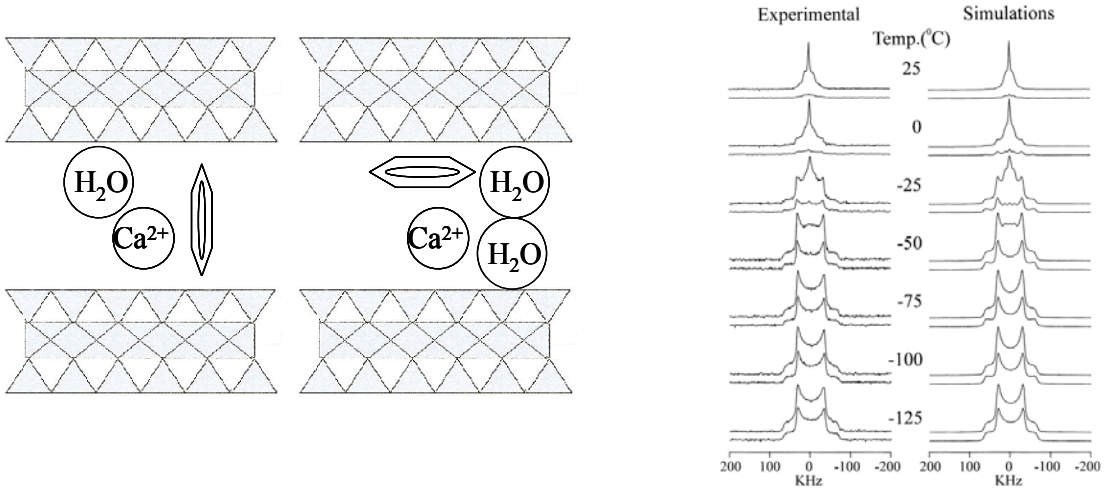

Figure 1.22. (right) Diagrammatic representations of possible configurations for the binding of benzene within the expandable interlayers, 1.0-1.5 nm [199, 200] of 2:1 Ca-montmorillonite clay (interlayer ions and molecules not to scale). The upper and lower phyllosilicate sheets are composed of an inner layer of octahedrally coordinated alumina sandwiched by two layers of tetrahedrally coordinated silica groups. The Ca^{2+} ions in the interlayer serve to charge balance the layers. Benzene is hypothesized to undergo π-cation bonding with the Ca^{2+} ion. (left) Variable-temperature static solid-state ^{2}H NMR experimental and simulated spectra of 1.2% benzene on Ca-montmorillonite from [188].

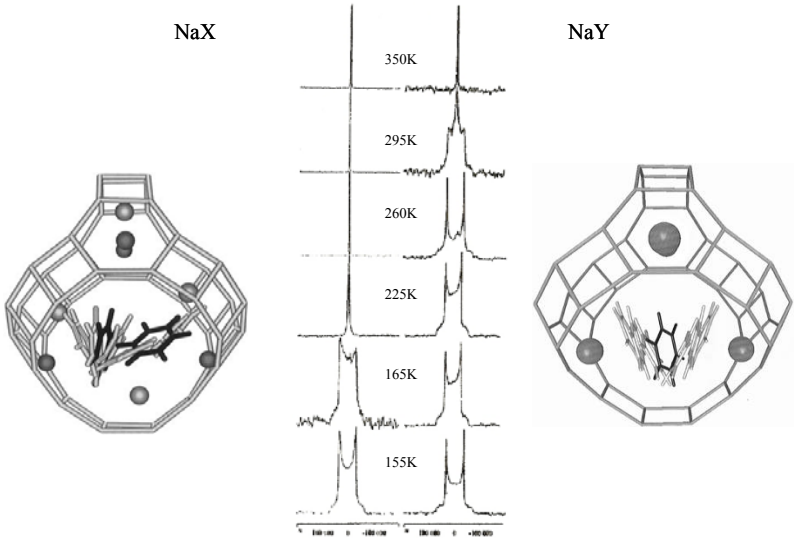

Figure 1.23. Static solid-state ^{2}H NMR variable temperature spectra of benzene on zeolite and a diagram of the modeled motion for (left) Na-X with 1.2 Si-Al and (right) Na-Y with 1.7 Si-Al after [194]. The authors suggest that both models display a "cartwheel" motion and Na-X also has "gliding" motion through the cavity.

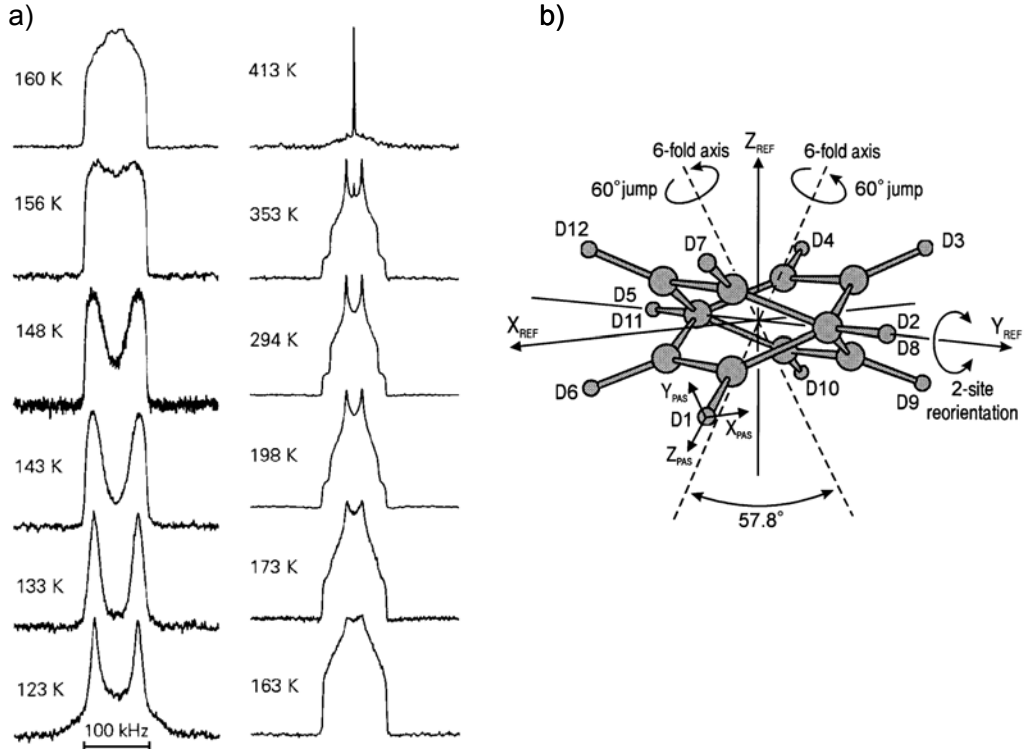

Figure 1.24. Experimental static solid-state ^{2}H NMR variable temperature spectra for guest benzene in $Cd(py)_2\{Ag(CN)_2\}_2$ and a diagrammatic representation of its motion from [189].

guest molecules in $Cd(py)_2\{Ag(CN)_2\}_2$ was also detected by Nishikiori et al. [189], who modeled the motion as a combination of C6 rotation and an "out-of-plane" wagging motion (Figure 1.24) modulated by forces due to the cavity symmetry, which changed with temperature.

Boddenberg and others [54, 55] has examined the motion of benzene on graphite and other surfaces using ^2H NMR in several papers (Fig 1.25). Boddenberg and Beerwerth [176, 183] have examined changes in the values of the longitudinal relaxation time (T1) and the transverse relaxation time (T2) with temperature and field strength of both deuterated and protonated benzene molecules

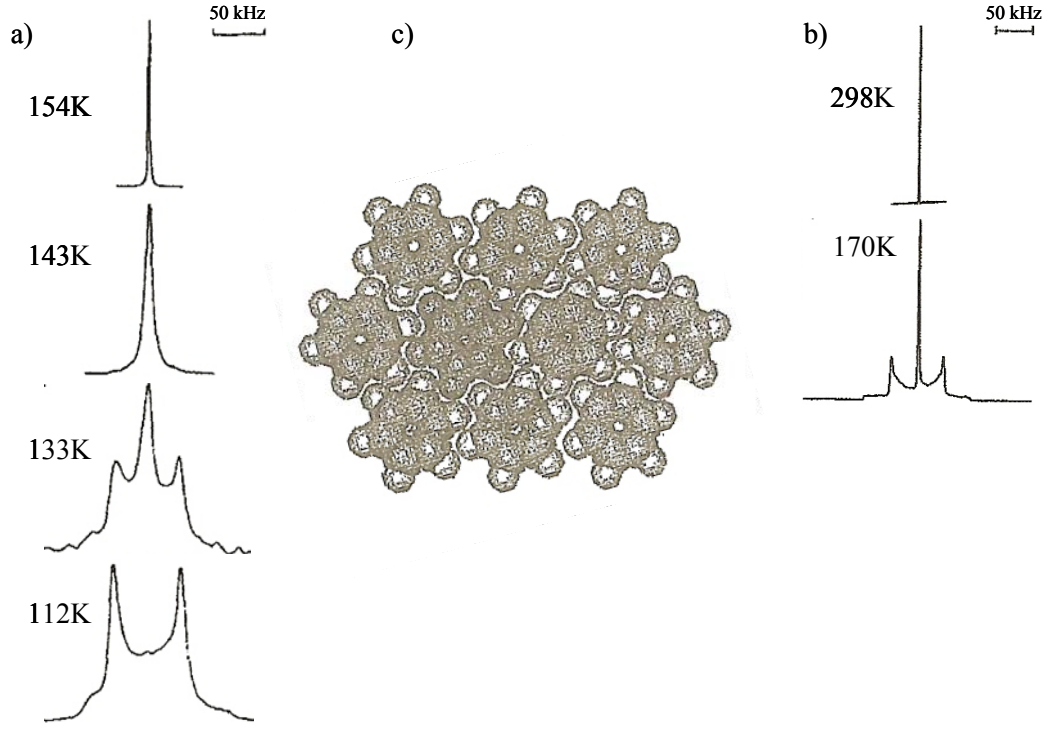

Figure 1.25. Static solid-state ^2H NMR variable temperature spectra of C_6D_6; a) 1 monolayer on Carbopack B graphitized carbon black (15); c) 10 monolayers of C_6D_6 on Graphon [55]; b) diagram of the packing of benzene molecules on a nonpolar surface, such as graphite [54].

on alumina and analyzed the rotational anisotropy and surface diffusion by application of the correlation functions outside of the region of extreme narrow for which T_1 data is usually applied. The authors devised an anisotropic rotation/libration/surface diffusion (ALS) motional model, which is similar to a combination of ISO, SAW and LAW, and involved C_6 rotation, wobbling of the C6 axis and translational motion (interpreted as either sliding across the grain surface or jumping from grain to grain). In a study most closely related to this work, Grundke and Boddenberg [53] have looked at benzene-d_6 on a graphitized carbon black (Carbopack B), using isotropic peak width ($\delta\upsilon$) to calculate rotational correlation times, τ_C. The authors interpreted a sharp break in linearity of the $\delta\upsilon$ versus 1/T plot as indicative of the initial crystallization of the benzene-d_6, probably as a 2D solid. Voss and Boddenberg [54] concluded that when benzene is packed as a 2D solid on a nonpolar surface, the molecule must jump and tilt in order to perform a C_6 rotation (Figure 1.24), and this motion accounts for the E_a for surface diffusion [54].

In addition to the motions interpreted from the lineshape of the static 2H solid-state NMR spectra, the energy of activation, E_a, and pre-exponential factor, τ_0, of the Arrhenius equation provides information about the interaction of the benzene with the solid phase. It is helpful to compare some different motional modes for benzene with the measured E_as for those motions. For example, benzene within cyclophosphazene channels executes some motions with very low E_a (2.1 and 4.2 kJ/mol), lower even than neat liquid benzene (4.5 and 8.1 kJ/mol). The E_a values fall between ca. 5 and 8 kJ/mol for benzene on nonpolar to moderately polar surfaces. For surfaces with cation-π bonding, the E_a values are even higher than

crystalline benzene (16.5 kJ/mol), and for systems such as clathrates, which allow minimal space for the benzene to move because of cavity size and symmetry, the E_a values are the largest, between ca. 18-30 kJ/mol (Table 1.3).

Table 1.3. Motional modes and their energies of activation for benzene-d_6 on various solid phases measured with static solid-state ^{2}H NMR

Substrate	Reference	Motion	$E_{a\ (kJ/mol)}$	temp range
cyclophosphazene channels	a	C_6	2.1	190K-300K
cyclophosphazene channels	a	tumbling along axis channel	4.2	190K-300K
neat liquid	b	tumbling	4.5	260K-360K
alumina (h-Al_2O_3)	c	C_6	4.9	77K-250K
SBA-15 mesoporous silica	d	C_6	6	20K-60K
zeolite Na-Y	c	C_6	7.4	77K-250K
Carbopack B	c	C_6	7.9	77K-250K
neat liquid	b	C_6	8.1	260K-360K
Ca-Mont 1.2% load	e	SAW	8.3	148K-198K
Ca-Mont 3.8% load	e	ISO	8.8	173K-223K
Zeolite, Na-Y	f	cartwheel	14	155K-350K
neat benzene	g	SAW	16.5	87K-252K
solid neat	d	C_6	16.8	88K-206K
cyclophosphazene	h	C_6	18.2	123K-403K
cyclophosphazene	h	out-of-plane		123K-403K
K-zeolite, ZSM-5	i	cation hopping	20	100K-350K
Zeolite, Na-X	f	cartwheel	23.5	155K-350K
inclusion	j	SAW	24.9	124K-290K
carceplex	k	C_6	25.8	310K-400K
carceplex	k	C_4 (wobble symmetry ?)		
K-zeolite, ZSM-5	l	cation hopping and bulk	28.3[m]	220K-373K
SBA-15 mesoporous silica	d	C_6 to ISO	30.6[n]	189K-219K

[a][201]; [b][202]; [c][54]; [d][142]; [e][188]; [f][194]; [g][192]; [h][197]; [i][203]; [j][192]; [k][198]; [l][196]; [m]associated with phase changes; [n]estimated average.

1.3 RESEARCH QUESTION

The research question of this dissertation is: What is the molecular motion of benzene-d_6 as it interacts with different black carbon solid phases, and what information does this provide about the sorption mechanism? And what implications does this have for the nanochemistry of benzene or other PAHs on both environmentally important and industrial BCs? Motional studies can be expected to

show different activation energies for the observed motions and possibly different types of motion or orientations for molecules at different distances from the surface (i.e., different loadings). In addition, if dual modes of sorption are occurring on the BC material itself (e.g., soot covered with layers of *in situ* PAHs), the static solid-state ^{2}H NMR spectrum could be expected to display a dual-mode spectra (to show two motional modes in proportion to the number of molecules executing each motion). However, studies of the molecular motion of adsorbed gases and vapors on graphites and activated carbons may reveal evidence for preferred adsorption to defect sites or indicate the occurrence of restricted motion in very small pores.

The motional models and activation energies obtained in this work specifically (1) address the assumptions used by theoretical researchers reviewed above about the interaction energies and orientations of benzene as it undergoes sorption interactions on BC, (2) validates catalysis mechanistic data and theory by previous workers, (3) provides knowledge of the mechanism of sorption on BCs surfaces which may be used to design improved sorbents, improved catalytic reaction processes, predict the influence of naturally occurring BCs on the fate and transport of VOCs and PAHs in the environment, and (4) assist in the design of improved BC sorbents for environmental contaminants. By combining the molecular dynamics results from these spectroscopic studies with interaction models currently in use, future workers may be able to carry this process further with greater quantitative specificity.

In this work, in order to accomplish this characterization of the molecular-level interaction mechanisms between BC and benzene, the molecular motion of its fully deuterated analog, benzene-d_6, was observed as it associated with a variety of

BC materials in a vapor-solid phase system using static solid-state ^{2}H nuclear magnetic resonance (NMR) spectroscopy. The BCs selected are considered to represent end-member materials: (1) pure graphite is comprised of flat, planar aromatic carbon rings in a crystalline structure; (2) carbon nanoparticles are graphenic carbon with considerable structural disorder, often referred to as amorphous; (3) multi-walled carbon nanotubes can be treated as physical models of a graphenic pore throat. We have also chosen two more heterogeneous, but standard BC materials: (4) an activated carbon; (5) an NIST #2975 diesel soot, a well-characterized BC with some oxygenated functionalities which commonly occurs in natural systems. Lastly (6), a well-characterized maple wood char was chosen as a substrate: a natural environmentally occurring sample of a BC which may incorporate features from any or all of the above standards. Since BCs exhibit strong adsorption of aromatic compounds in batch sorption experiments, we hypothesized that motion of benzene-d_6 molecules on BC sorbents would be similar to its motion on other solid sorbents, e.g., zeolites, namely, SAW and LAW motions with some amount of ISO. However, as explained in the following chapters, the spectra of benzene-d_6 on BCs were surprisingly different from our expectation and different from each other.

References

1. Luthy, R. G.; Aiken, G. R.; Brusseau, M. L.; Cunningham, S. D.; Gschwend, P. M.; Pignatello, J. J.; Reinhard, M.; Traina, S. J.; Weber, W. J.; Westall, J. C., Sequestration of hydrophobic organic contaminants by geosorbents. *Environmental Science & Technology* **1997,** *31*, (12), 3341-3347.
2. Schwarzenbach, R. P.; Gschwend, P. M.; Imboden, D. M., *Environmental Organic Chemistry, 2nd ed.* John Wiley and Sons Inc.: New York, NY, 2003.
3. Gauden, P.; Terzyk, A. P.; Rychlicki, G.; Kowalczyk, P.; Lota, K.; Raymundo-Pinero, E.; Frackowiak, E.; Beguin, F., Thermodynamic properties of

benzene adsorbed in activated carbons and multi-walled carbon nanotubes. *Chemical Physics Letters* **2006,** *421*, 409-414.
4. Do, D. D.; Do, H. D., Adsorption of benzene on graphitized thermal carbon black: reduction of the quadrupole moment in the adsorbed phase. *Langmuir* **2006,** *22*, 1121-1128.
5. Jaroniec, M.; Madey, R., A comprehensive theoretical description of physical adsorption of vapors on heterogeneous microporous solids. *Journal of Physical Chemistry* **1989,** *93*, 5225-5230.
6. Lohmann, R.; Lammell, G., Adsorptive and absorptive contributions to the gas-particle partitioning of polycyclic aromatic hydrocarbons: state of knowledge and recommended parametrization for modeling. *Environmental Science & Technology* **2004,** *38*, (14), 3793-3803.
7. Endo, S.; Grathwohl, P.; Schmidt, T. C., Absorption or adsorption? Insights from molecular probles *n*-alkanes and cycloalkanes into modes of sorption by environmental solids. *Environmental Science & Technology* **2008,** *42*, 3989-3995.
8. Braida, W. J.; Pignatello, J. J.; Lu, Y.; Ravikovitch, P. I.; Neimark, A. V.; Xing, B., Sorption hysteresis of benzene in charcoal particles. *Environmental Science & Technology* **2003,** *37*, 409-417.
9. Adamson, A.; Gast, A. P., *Physical Chemistry of Surfaces*. John Wiley & Sons: New York, 1997; p 784.
10. Jonker, M. T. O.; Koelman, A. A., Sorption of polycyclic aromatic hydrocarbons and polychlorinated biphenyls to soot and soot-like materials in the aqueous environment: mechanistic considerations. *Environmental Science & Technology* **2002,** *36*, (3725-3734).
11. Cornelissen, G.; Gustafsson, O.; Bucheli, T. D.; Jonker, M. T. O.; Koelmans, A. A.; van Noort, P. C. M., Extensive sorption of organic compounds to black carbon, coal, and kerogen in sediments and soils: mechanisms and consequences for distribution, bioaccumulation, and biodegradation. *Environmental Science & Technology* **2005,** *39*, (18), 6881-6895.
12. Yoon, T. H.; Benzerara, K.; Ahn, S.; Luthy, R. G.; Tyliszczak, T.; Brown, G. E., Jr., Nanometer-scale chemical heterogeneities of black carbon materials and their impacts on PCB sorption properties: soft X-ray spectromicroscopy study. *Environmental Science & Technology* **2006,** *40*, 5923-5929.
13. Chiou, C. T.; Kile, D. E., Deviations from sorption linearity on soils of polar and nonpolar organic compounds at low relative concentrations. *Environmental Science & Technology* **1998,** *32*, (3), 338-343.
14. Allen-King, R. M.; Grathwohl, P.; Ball, W. P., New modeling paradigms for the sorption of hydrophobic organic chemicals to heterogeneous carbonaceous matter in soils, sediments and rocks. *Advances in Water Resources* **2002,** *25*, 985-1016.
15. Young, T. M.; Weber, W. J., Jr., A distributed reactivity model for sorption by soils and sediments. 3. Effects of diagenetic processes on sorption energetics. *Environmental Science & Technology* **1995,** *29*, 92-97.
16. Accardi-Dey, A.; Gschwend, P. M., Assessing the combined roles of natural organic matter and black carbon as sorbents in sediments. *Environmental Science & Technology* **2002,** *36*, 21-29.

17. Bucheli, T. D.; Gustafsson, O., Quantification of the soot-water distribution coefficient of PAH's provides mechanistic basis for enhanced sorption observations. *Environmental Science & Technology* **2000,** *34*, 5144-5151.
18. Bornemann, L. C.; Kookana, R. S.; Welp, G., Differential sorption behaviour of aromatic hydrocarbons on charcoals prepared at different temperatures from grass and wood. *Chemosphere* **2007,** *67*, 1033-1042.
19. Chiou, C. C.; Kile, D. E.; Rutherford, D. W.; Sheng, G.; Boyd, S. A., Sorption of selected organic compounds from water to a peat soil and its humic-acid and humin fractions: potential sources of the sorption nonlinearity. *Environmental Science & Technology* **2000,** *34*, (7), 1254-1258.
20. Golding, C. J.; Smernik, R. J.; Birch, G. F., Investigation of the role of structural domains identified in sedimentary organic matter in the sorption of hydrophobic organic compounds. *Environmental Science & Technology* **2005,** *39*, 3925-3932.
21. Poole, C. F.; Schuette, S. A., *Contemporary Practice of Chromatography*. Elsevier: New York, 1984.
22. Bonsal, R. C.; Goyal, M., *Activated Carbon Adsorption*. Taylor and Francis: Boca Raton, FL, 2005; p 497.
23. Do, D. D.; Do, H. D., Characterization of micro-mesoporous carbonacenous materials. Calculations of adsorption isotherm of hydrocarbons. *Langmuir* **2002,** *18*, 93-99.
24. Dewey, C. S.; Lefforge, P. K., Moisture sorption by carbon black. *Industrial and Engineering Chemistry* **1932,** *24*, 1045-1050.
25. Schoenfeld, F. K., Surface chemistry of carbon black: effect on vulcanization of rubber. *Industrial and Engineering Chemistry* **1935,** *27*, 571-577.
26. Krishnankutty, N.; Vannice, M. A., Effect of pretreatment on surace area, porosity and adsorptionj properties of a carbon black. *Chemistry of Materials* **1995,** *7*, 754-763.
27. Gusev, A. A., Micromechanical mechanism of reinforcement and losses in filled rubbers. *Macromolecules* **2006,** *39*, 5960-5962.
28. Skoog, D. A.; West, D. M., *Fundamentals in Analytical Chemistry, 4th Edition*. CBS College Publishing: New York, New York, 1982; p 859 p.
29. Karapanagioti, H.; Childs, J.; Sabatini, D. A., Impacts of heterogeneous organic matter on phenanthrene sorption: different soil and sediment samples. *Environmental Science & Technology* **2001,** *35*, 4684-4690.
30. Jia, G.; Wang, H.; Yan, L.; Wang, X.; Pei, R.; Yan, T.; Zhao, Y.; Guo, X., Cytotoxicity of carbon nanomaterials: single-wall nanotube, multi-wall nanotube, and fullerene. *Environmental Science & Technology* **2005,** *39*, 1378-1383.
31. Braun, A.; Mun, B. S.; Huggins, F. E.; Huffman, G. P., Carbon speciation of diesel exhaust and urban particulate matter NIST standard reference materials with C(1s) NEXAFS spectroscopy. *Environmental Science & Technology* **2007,** *41*, 173-178.
32. Aubin , D. G.; Abbatt, J. P., Laboratory measurements of thermodynamics of adsorption of small aromatic gases to *n*-hexane soot surface. *Environmental Science & Technology* **2006,** *40*, 179-187.

33. Aubin , D. G.; Abbatt, J. P., Adsorption of gas-phase nitric acid to n-hexane soot: thermodynamics and mechanism. *Journal of Physical Chemistry A* **2003,** *107*, 11030-11037.
34. Li, J.; Werth, C. J., Modeling sorption isotherms of volatile organic chemical mixtures in model and natural solids. *Environmental Ttoxicology and Chemistry* **2002,** *21*, 1377-1383.
35. Nguyen, T. H.; Sabbah, I.; Ball, W. P., Sorption nonlinearity for organic contaminants with diesel soot: method development and isotherm interpretation. *Environmental Science & Technology* **2004,** *38*, 3595-3603.
36. Zhu, D.; Pignatello, J. J., Characterization of aromatic compounds sorptive interactions with black carbon (charcoal) assisted by graphite as a model. *Environmental Science & Technology* **2005**, (37).
37. Chen, B.; Zhou, D.; Zhu, L., Transitional adsorption and partition of nonpolar and polar aromatic contaminants by biochars of pine needles with different pyrolytic temperatures. *Environmental Science & Technology* **2008,** *42*, (14), 5137-5143.
38. Mauter, M. S.; Elimelech, M., Environmental applications of carbon-based nanomaterials. *Environmental Science & Technology* **2008,** *42*, (16), 5843-5859.
39. Harris, P. J. F.; Liu, Z.; Suenaga, K., Imaging the atomic structure of activated carbon. *Journal of Physics: Condensed Matter* **2008,** *20*.
40. Isirikyan, A. A.; Kiselev, A. V., The absolute adsorption isotherms of vapors of nitrogen, benzene and *n*-hexane, and the heats of adsorption of benzene and *n*-hexane on graphitized carbon blacks. I. graphitized thermal blacks. *Journal of Physical Chemistry* **1961,** *65*, (4), 601-607.
41. Chun, Y.; Sheng, G.; Chiou, C. T.; Xing, B., Compositions and sorptive properties of crop residue-derived chars. *Environmental Science & Technology* **2004,** *38*, 4649-4655.
42. Keiluweit, M.; Kleber, M., Molecular-level interactions in soils and sediments: the role of aromatic #-systems. *Environmental Science & Technology* **2009**.
43. Chun, Y.; Sheng, G.; Chiou, C. T., Evaluation of current techniques for isolation of chars as natural adsorbents. *Environmental Science & Technology* **2004,** *38*, 4227-4232.
44. Manes, M., Activated carbon adsorption fundamentals. In *Encyclopedia of environmental analysis and remediation*, John Wiley & Sons: New York, 1998; pp 15-25.
45. Sander, M.; Pignatello, J. J., Characterization of charcoal adsorption sites for aromatic compounds: Insights drawn from single-solute and bi-solute competitive experiments. *Environmental Science & Technology* **2005,** *39*, 1606-1615.
46. Gotovac, S.; Honda, H.; Hattori, Y.; Takahashi, K.; Kanoh, H.; Kaneko, K., Effect of nanoscale curvature of single-walled carbon nanotubes on adsorption of polycyclic aromatic hydrocarbons. *Nanoletters* **2007,** *7*, (3), 583-587.
47. Pan, B.; Xing, B., Adsorption mechanisms of organic chemicals on carbon nanotubes. *Environmental Science & Technology* **2008,** *42*, (24), 9005-9013.
48. Pimenta, M. A.; Dresselhaus, G.; Dresselhaus, M. S.; Cancado, L. G.; Jorio, A.; Saito, R., Studying disorder in graphite-based systems by Raman spectroscopy. *Physical Chemistry Chemical Physics* **2007,** *9*, 1276-1291.

49. Hristea, G.; Budrugeac, P., Characterization of exfoliated graphite for heavy oil sorption. *Journal of Thermal Analysis and Calorimetry* **2008,** *91*, (3), 817-823.
50. Connan, H. G.; Reedy, B. J.; Marshall, C. P.; Wilson, M. A., New nanocarbons: rod milling and annealing of graphite in the presence of yttrium. *Energy and Fuels* **2004,** *18*, 1607-1614.
51. Sun, G.; Kurti, J.; Kertesz, M.; Baughman, R. H., Variations of the geometries and band gaps of single-walled carbon nanotubes and the effect of charge injection. *Journal of Physical Chemistry B* **2003**, (107).
52. Zeng, Z.; Nateson, K., Relationship of carbon crystallization to the metal-dusting mechanism of nickel. *Chemistry of Materials* **2003,** *15*, 872-878.
53. Grundke, V.; Boddenberg, B., One and two component adsorption layers of *n*-hexane and benzene on graphite studied by ^{2}H NMR spectroscopy. *Molecular Physics* **1993,** *79*, (6), 1215-1226.
54. Voss, V.; Boddenberg, B., Anisotropic reorientation dynamics of benzene molecules adsorbed on graphite, alumina, and zeolite Y. *Surface Science* **1993,** *298*, (241-250).
55. Boddenberg, B.; Grosse, R., A deuteron NMR study on a benzene multilayer on graphite. *Z. Naturforsch* **1987,** *421*, 272-274.
56. Pierce, C.; Ewing, B., Areas of uniform graphite surfaces. *Journal of Physical Chemistry* **1964,** *68*, 2562-2568.
57. Vidal-Madjar, C.; Gonnord, M.-F.; Goedert, M.; Guiochon, G., Gas solid chromatographic measurements of the change in the heat capacity during adsorption on graphitized thermal carbon blacks. *Journal of Physical Chemistry* **1975,** *79*, (7), 732-741.
58. Yuan, L.-M.; Ren, C.-X.; Li Li, P. A.; Yan, Z.-H.; Zi, M.; Li, Z.-Y., Single-walled carbon nanotubes used as stationary phase in GC. *Anal. Chem.* **2006,** *78*, 6384-6390.
59. Nguyen, T. H.; Ball, W. P., Absorption and adsorption of hydrophobic organic contaminants to diesel and hexane soot. *Environmental Science & Technology* **2006,** *40*, 2958-2864.
60. Muller, J.-O.; Su, D. S.; Jentoft, R. E.; Wild, U.; Schlogl, R., Diesel engine exhaust emission: oxidative behavior and microstructure of black smoke soot particulate. *Environmental Science & Technology* **2006,** *40*, 1231-1236.
61. Nguyen, T. H.; Brown, R. A.; Ball, W. P., An evaluation of thermal resistance as a measure of black carbon content in diesel soot, wood char, and sediment. *Organic Geochemistry* **2004,** *35*, 217-234.
62. Nguyen, T. H.; Cho, H.-H.; Poster, D. L.; Ball, W. P., Evidence for a pore-filling mechanism in the adsorption of aromatic hydrocarbons to a natural wood char. *Environmental Science & Technology* **2007,** *41*, (4), 1212-1217.
63. Dall'Ora, M.; Jensen, P. A.; Jensen, A. D., Suspension combustion of wood: influence of pyrolysis conditions on char yield, morphology, and reactivity. *Energy and Fuels* **2008,** *22*, (5), 2955-2962.
64. Knudsen, J. N.; Jensen, P. A.; Lin, W.; Dam-Johnsen, K., Secondary capture of chlorine and sulfur during thermal conversion of biomass. *Energy and Fuels* **2005,** *19*, (2), 606-617.

65. Medeiros, P. M.; Simoneit, B. R. T., Source profiles of organic compounds emitted upon combustion of green vegetation from temperate climate forests. *Environmental Science & Technology* **2008,** *42*, (22), 8310-8316.
66. Branca, C.; Di Blasi, C.; Elefante, R., Devolatilization and heterogeneous combustion of wood fast pyrolysis oils. *Ind. Eng. Chem Res* **2005,** *44*, 799-810.
67. Zhu, D.; Kwon, S.; Pignatello, J., Adsorption of single-ring organic compounds to wood charcoals prepared under different thermochemical conditions. *Environmental Science & Technology* **2005,** *39*, 3990-3998.
68. Robens, E.; Staszczuk, P.; Dabrowski, A.; Barczak, M., The origin of nanopores. *Journal of Thermal Analysis and Calorimetry* **2005,** *79*, 499-507.
69. Dubinin, M. M.; Polyakov, N. S.; Kadlez, O.; Kataeva, L. I.; Petukhova, G. A., Heterogeneous microporous structures and adsorption properties of carbon adsorbents. 12.* Porous structure and adsorption properties of active carbons. *Russian Chemical Bulletin* **1993,** *42*, (8), 1304-1308.
70. Turov, V. V.; Gun'ko, V. M.; Leboda, R.; Bandosz, T. J.; Skubiszewska-Zieba, J.; Palijczuk, D.; Tomaszewski, W.; Zietek, S., Influence of organics on the structure of water adsorbed on activated carbons. *Journal of Colloid and Interface Science* **2002,** *253*, 23-34.
71. Chiang, Y.-C.; Chiang, P.-C.; Chang, E. E., Effects of surface characteristics of activated carbons on VOC adsorption. *Journal of Environmental Engineering* **2001**, (January, 2001).
72. Fletcher, A. J.; Uygur, Y.; Thomas, K. M., Role of surface functional groups in the adsorption kinetics of water vapor on microporous activated carbons. *Journal of Physical Chemistry C* **2007,** *111*, 8394-8399.
73. Navarro, E.; Baun, A.; Behra, R.; Hartman, N. B.; Filser, J.; Miao, A.-J.; Quigg, A.; Santschi, P. H.; Sigg, L., Environmental behavior and ecotoxicity of engineered nanoparticles to algae, plants, and fungi. *Ecotoxicology* **2008,** *17*, 372-386.
74. Murr, L. E.; Bang, J. J.; Esquivel, E. V.; Guerrero, P. A.; Lopez, D. A., Carbon nanotubes, nanocrystal forms, and complex nanoparticle aggregates in common fuel-gas combustion sources and ambient air. *Journal of Nanoparticle Research* **2004,** *6*, 241-251.
75. Bachilo, S. M.; Balzano, L.; Herrera, J. E.; Pompeo, F.; Resasco, D. E.; Weisman, R. B., Narrow (*n,m*)-Distribution of single-walled carbon nanotubes grown using a solid supported catalyst. *Journal of the American Chemical Society Communications* **2003,** *125*, 11186-11187.
76. Diaz, E.; Ordonex, S.; Vega, A., Adsorption of volatile organic compounds onto carbon nanotubes, carbon nanofibers, and high-surface-area graphites. *J. Colloid and Interface Science* **2007,** *305*, 7-16.
77. Chen, W.; Duan, L.; Zhu, D., Adsorption of polar and nonpolar organic chemicals to carbon nanotubes. *Environmental Science & Technology* **2007,** *41*, 8295-8300.
78. Buseck, P. R.; Adachi, K., Nanoparticles in the Atmosphere. *Elements* **2008,** *4*, 389-394.
79. Ferrari, A. C.; Robertson, J., Interpretation of Raman spectra of disordered and amorphous carbon. *Physical Review B* **2000,** *61*, (20), 14,095-14,107.

80. Scilletta, C.; Servidori, M.; Orlando, S.; Cappelli, E.; Barba, L.; Ascarelli, K. P., Influence of substrate temperature and atmosphere on nano-graphene formation and texturing of pulsed Nd YAG laser-deposited carbon films. *Applied Surface Science* **2005,** *252*, 4877-4881.
81. Iijima, S.; Wakabayashi, T.; Achiba, Y., Structures of carbon soot prepared by laser ablation. *Journal of Physical Chemistry* **1996,** *100*, 5839-5843.
82. Hilding, J.; Grulke, E. A.; Sinnott, S. B.; Qian, D.; Andrews, R.; Jagtoyen, M., Sorption of butane on carbon multiwall nanotubes at room temperature. *Langmuir* **2001,** *17*, (24), 7540-7544.
83. Tournus, F.; Latil, S.; Heggie, M. I.; Charlier, J.-C., π-stacking interaction between carbon nanotubes and organic molecules. *Physical Review B* **2005,** *72*.
84. Zhu, Z.; Su, D.; Weinberg, G.; Schlogl, R., Supermolecular self-assembly of graphene sheets; formation of tube-in-tube nanostructures. *Nanoletters* **2004,** *4*, 2255-2259.
85. Giusca, C. E.; Tison, Y.; Stolojan, V.; Borowiak-Palen, E.; Silva, S. R. P., Inner-tube chirality determination for double-walled carbon nanotubes by scanning tunneling microscopy. *Nanoletters* **2007,** *7*, (5), 1232-1239.
86. Li, F.; Chou, S. G.; Ren, W.; Gardecki, J. A.; Swan, A. K.; unlu, M. S.; Goldberg, B. B.; Cheng, H.-M.; Dresselhaus, M. S., Identification of the constituents of double-walled carbon nanotubes using Raman spectra taken with different laser-excitation energies. *Journal of Materials Research* **2003,** *18*, (5), 1251-1258.
87. Wang, J.; Yin, G.; Shao, Y.; Wang, Z.; Gao, Y., Investigation of further improvement of platinum catalyst durability with highly graphitized carbon nanotubes support. *Journal of Physical Chemistry C* **2008,** *112*, (15), 5784-5789.
88. Cousins, I. T.; Mackay, D., Gas-particle partitioning of organic compounds and its interpretation using relative solubilities. *Environmental toxicology and chemistry* **2001,** *35*, (4), 643-647.
89. Nguyen, C.; Do, D. D., Onset of the Henry constant for supercritical adsorption into carbonaceous porous materials. *Journal of Physical Chemistry B* **2001,** *105*, 1823-1828.
90. Xia, G.; Ball, W. P., Polanyi-based models for the competitive sorption of low-polarity organic contaminants on a natural sorbent. *Environmental Science & Technology* **2000,** *34*, (7), 1246-1253.
91. Kleineidam, S.; Schth, C.; Grathwohl, P., Solubility-normalized combined adsorption-partitioning sorption isotherms for organic pollutants. *Environmental Science & Technology* **2002,** *36*, (21), 4689-4697.
92. Chiou, C. T.; Manes, M., Application of the Polanyi adsorption potential theory to adsorption fro solution on activated carbon. IV. Steric factors, as illustrated by the adsorption of planar and octahedral metal acetylacetonates. *Journal of Physical Chemistry* **1973,** *77*, 809-813.
93. Inoue, S.; Ickikuni, N.; Suzuki, T.; Uematsu, T.; Kaneko, K., Capillary condensation of N_2 on multiwall carbon nanotubes. *Journal of Physical Chemistry B* **1998,** *102*, 4689-4692.
94. Ismadji, S.; Bhatia, S. K., A modified pore-filling isotherm for liquid-phase adsorption in activated carbon. *Langmuir* **2001,** *17*, 1488-1498.

95. Mackay, D.; Cousins, I. T., Gas-particle partitioning of organic compounds and its interpretation using relative solubilities. *Environmental Science & Technology* **2001,** *35*, (4), 643-647.
96. Mader, B. T.; Pankow, J. T., Study of the effects of particle-phase carbon on the gas/particle partitioning of semivolatile organic compounds in the atmosphere using controlled field experiments. *Environmental Science & Technology* **2002,** *36*, (23), 5218-5228.
97. Goss, K.-U.; Schwarzenbach, R. P., Gas/solid and gas/liquid partitioning of organic compounds: critical evaluation of the interpretation of equilibrium constants. *Environmental Science & Technology* **1998,** *32*, (14), 2025-2032.
98. Goss, K.-U., Adsorption of organic vapors on polar mineral surfaces and on a bulk water surface: development of an empirical predictive model. *Environmental Science & Technology* **1994,** *28*, (4), 640-645.
99. Roth, C. M.; Goss, K.-U. a. S., Rene P., Sorption of a diverse set of organic vapors to diesel soot and road tunnel aerosols. *Environmental Science & Technology* **2005,** *39*, 6632-6637.
100. Roth, C. M.; Goss, K.-U.; Schwarzenbach, R. P., Adsorption of a diverse set of organic vapors on the bulk water surface. *Journal of Colloid and Interface Science* **2002,** *252*, 21-30.
101. Goss, K.-U.; Schwarzenbach, R., Empirical prediction of heats of vaporization and heats of adsorption of organic compounds. *Environmental Science & Technology* **1999,** *33*, (19), 3390-3393.
102. Goss, K.-U., Conceptual model for the adsorption of organic compounds from the gas phase to liquid and solid surfaces. *Environmental Science & Technology* **1997,** *31*, 3600-3605.
103. Kamlet, M.; Carr, P. W.; Taft, R. W.; Abraham, M. H., Linear solvation energy relationship. 13.[1] Relationship between the Hildebrand solubility parameter, δ_H, and the solvatochromic parameter, π^*. *Journal of the American Chemical Society Communications* **1981,** *103*, 6062-6066.
104. Gregg, S. J.; Sing, K. S. W., *Adsorption, Surface Area, and Porosity*. Academic Press: New York, NY, 1982.
105. Do, D. D.; Do, H. D., Modeling of adsorption on nongraphitized carbon surface: GCMC simulation studies and comparison with experimental data. *Journal of Physical Chemistry B* **2006,** *110*, 17531-17538.
106. Pierce, C.; Ewing, B., Localized adsorption on graphite surfaces. *Journal of Physical Chemistry* **1967,** *71*, (11), 3408-3413.
107. Pierotti, R. A.; Smallwood, R. E., The adsorption of benzene on homogeneous substrates. *Journal of Colloid and Interface Science* **1966,** *22*, 469-481.
108. Elkington, P. A.; Curthoys, G., Heats of adsorption on carbon black surfaces. *Journal of Physical Chemistry* **1969,** *73*, (7), 2321-2326.
109. Gauden, P. A.; Terzyk, A. P.; Cwiertnia, M. S.; Rychlicki, G.; Newcombe, G.; Kowalczyk, P., Benzene adsorption on carbonaceous materials: The influence of pore structure on the state of the adsorbate. *Applied Surface Science* **2006,** *253*, 2525-2539.

110. Shih, Y.-h.; Li, M.-s., Adsorption of selected volatile organic vapors on multiwall carbon nanotubes. *Journal of Hazardous Materials* **2008,** *154*, 21-28.
111. Crespo, D.; Yang, R. T., Adsorption of organic vapors on single-walled carbon nanotubes. *Ind. Eng. Chem Res* **2006,** *45*, (16), 5524-5530.
112. Coker, E. N.; Jia, C.; Karge, H. G., Adsorption of benzene and benzene derivatives onto zeolite H-Y studied by microcalorimetry. *Langmuir* **2000,** *16*, 1205-1210.
113. Bakaev, V. A.; Bakaeva, T. I.; Pantano, C. G., On inverse adsorption chromatography. 2. Determination of isotherms and heats of adsorption as well as energy distributions of adsorption sites. *Journal of Physical Chemistry* **2007,** *111*, 7473-7486.
114. Vernov, A.; Steele, W. A., Computer simulations of benzene adsorbed on graphite. 2. 298K. *Langmuir* **1991,** *7*, 2817-2820.
115. Tabony, J.; White, J. W.; Delachaume, J. C.; Coulon, M., Nuclear magnetic resonance studies of the melting and orientation of benzene adsorbed upon graphite. *Surface Science* **1980,** *95*, L282-L288.
116. Do, D. D.; Nicholson, D.; Do, H. D., On the anatomy of the adsorption heat versus loading as a function of temperature and adsorbate for a graphitic surface. *Journal of Colloid and Interface Science* **2008,** *325*, 7-22.
117. Webster, C., Edwin; Drago, R. S.; Zerner, M. C., Molecular dimensions for adsorptives. *Journal of the American Chemical Society Communications* **1998,** *120*, 5509-5516.
118. Cox, E. G., Crystal structure of benzene. *Reviews of Modern Physics* **1958,** *30*, (1), 159-162.
119. Bardi, U.; Magnanelli, S.; Rovida, G., LEED study of benzene and naphthalene monolayers adsorbed on the basal plane of graphite. *Langmuir* **1987,** *3*, 159-163.
120. Meehan, P.; Rayment, T.; Thomas, R. K.; Guillermo, B.; White, J. W., Neutron diffraction from benzene adsorbed on graphite. *J.C.S. Faraday 1* **1980,** *76*, 2011-2016.
121. Vernov, A.; Steele, W. A., Computer simulations of benzene adsorbed on graphite. 1. 85K. *Langmuir* **1991,** *7*, 3110-3117.
122. Do, D. D.; Do, H. D., Effects of quadrupole moments of graphite surface on adsorption of simple gases on graphitized thermal carbon black. *Colloids and Surfaces A: Physicochem. Eng. Aspects* **2007,** *300*, 50-59.
123. Fodi, B.; Hentschke, R., Molecular dynamics simulation of a binary hydrocarbon mixture near an adsorbing wall: benzene/I-heptane on graphite. *Langmuir* **1998,** *14*, 429-437.
124. Gauden, P. A.; Terzyk, A. P.; Rychlicki, G.; Kowalczyk, P.; Cwiertnia, M. S.; Garbacz, J. K., Estimating the pore size distribution of activated carbons from adsorption data of different adsorbates by various methods. *Journal of Colloid and Interface Science* **2004,** *273*, 39-63.
125. Furmaniak, S.; Terzyk, A. P.; Gauden, P. A.; Rychlicki, G., Simple models of adsorption in nanotubes. *Journal of Colloid and Interface Science* **2006,** *295*, 310-317.
126. Inoue, S.; Hanzawa, Y.; Kaneko, K., Prediction of hysteresis disappearance

in the adsorption isotherm of N_2 on regular mesoporous silica. *Langmuir* **1998,** *14*, 3079-3081.
127. Miyabe, K.; Guiochon, G., Comparison of the characteristics of adsorption equilibrium and surface diffusion in liquid-solid and gas-solid adsorption on C_{18}-silica gels. *Journal of Physical Chemistry B* **2004,** *108*, 2987-2997.
128. Ross, J. W.; Good, R. J., Adsorption and surface diffusion of *n*-butane on spheron 6 (2700°) carbon black. *Journal of Physical Chemistry* **1956,** *60*, 1167-1171.
129. Gilliland, E. R.; Baddour, R. F.; Perkinson, G. P.; Sladek, K. J., Diffusion on surfaces. I. Effect of concentration on the diffusivity of physically adsorbed gases. *Ind. Eng. Chem.; Fundam.* **1974,** *13*, 95-99.
130. Sladek, K. J.; Gilliland, E. R.; Baddour, R. F., Diffusion on surfaces. II. Correlation of diffusivities of physically and chemically adsorbed species. *Ind. Eng. Chem Res* **1974,** *13*, (2), 100-105.
131. Choi, J.-G.; Do, D. D.; Do, H. D., Surface diffusion of adsorbed molecules in porous media: monolayer, multilayer, and capillary condensation regimes. *Ind. Eng. Chem. Res.* **2001,** *40*, 4005-4031.
132. Carman, P. C.; Raal, F. A., Diffusion and flow of gases and vapours through micropores. III. Surface diffusion coefficients and activation energies. *Proceedings of the Royal Society of London. Series A. Mathematical and Physical Sciences* **1951,** *209*, (1096), 38-58.
133. Rigby, S. P., Predicting surface diffusivities of molecules from equilibrium adsorption isotherms. *Colloids and Surfaces A: Physicochem. Eng. Aspects* **2005,** *262*, 139-149.
134. Anton, A. B., Mechanism, configurational degeneracy, and mass action in transition-state rate functions for adsorption-desorption reactions. *J. Phys. Chem.* **1993,** *97*, (1942-1951), 1942-1951.
135. Gomer, R., Diffusion of adsorbates on metal surfaces. *Rep. Prog. Phys.* **1990,** *53*, 917-1002.
136. Chen, N.; Yang, R. T., Ab initio molecular orbital study of the unified mechanism and pathways for gas-carbon reactions. *Journal of Physical Chemistry A* **1998,** *102*, 6348-6356.
137. Kapoor, A.; Yang, R. T., Surface diffusion on energetically heterogeneous surfaces. *AIChE Journal* **1989,** *35*, (10), 1735-1738.
138. Miyabe, K.; Guiochon, G., Thermodynamic characteristics of surface diffusion in reversed-phase liquid chromatography
Journal of Physical Chemistry B **1999**, (103), 11086-11097.
139. Miyabe, K.; Suzuki, M., Adsorption characteristics of octadecysilyl-silica gel in gaseous systems. *AIChE Journal* **1994,** *39*, (11), 1791-1798.
140. Miyabe, K.; Shigeya, T., Analysis of surface diffusion phenomena in liquid phase adsorption. *Journal of Physical Chemistry B* **1997,** *101*, 7773-7779.
141. Miyabe, K.; Guiochon, G., Correlation between surface diffusion and molecular diffusion in reversed-phase liquid chromatography. *Journal of Physical Chemistry B* **2001,** *105*, 9202-0209.
142. Gedat, E.; Schreiber, A.; Albrecht, J.; Emmler, T.; Shenderovich, I.; Findenegg, G. H.; Limbach, H.-H.; Buntknowsky, G., ^{2}H solid-state NMR study of

benzene-d_6 confined in mesoporous silica SBA-15. *Journal of Physical Chemistry B* **2002,** *106*, 1977-1984.
143. Boddenberg, G.; R., H.; Opperman, G., NMR spin echo studies on mobility and diffusion of benzene adsorbed on silica. *Journal of Colloid and Interface Science* **1972,** *38*, 210-216.
144. Rigby, S. P., A model for the surface diffusion of molecules on a heterogeneous surface. *Langmuir* **2003,** *19*, 364-376.
145. Arena, M. V.; Deckert, A. A.; J.L., B.; George, S. M., Surface diffusion and desorption of pentane isomers on Ru(001)
Journal of Physical Chemistry **1990,** *94*, 6792-6797.
146. Hill, T. L., Theory of physical adsorption. *Advances in Catalysis* **1952,** *4*, 211-258.
147. Rudzinski, W.; Lee, S.-L.; Panczyk, T.; Yan, C.-C. S., A fractal approach to adsorption on heterogeneous solids surface. 2. Thermodynamic analysis of experimental adsorption data. *Journal of Physical Chemistry B* **2001,** *105*, 10857-10866.
148. Pfeifer, P.; Avnir, D., Chemistry in noninteger dimensions between two and three. I. Fractal theory of heterogeneous surfaces. *Journal of Chemical Physics* **1983,** *79*, (7), 3558-3565.
149. Jaroniec, M., Evaluation of the fractal dimension from a single adsorption isotherm. *Langmuir* **1995,** *11*, 2316-2317.
150. Gritti, F.; Guiochon, G., Effect of surface coverage of C18-bonded silica particles on the obstructive factor and intraparticle diffusion mechanism. *Chemical Engineering Science* **2006,** *61*, 7636-7650.
151. Aldrich Catalog. In Sigma-Aldrich Chemical Company.
152. Liu, L.; Guo, Q. X., Isokinetic relationship,isoequilibrium relationship, and enthalpy-entropy compensation. *Chemical Reviews* **2001,** *101*, 673-695.
153. Bond, G. C.; Keane, M. A.; Kral, H.; Lercher, J., Compensation phenomena in heterogeneous catalysis: general principles and a possible explanation. *Catalysis Reviews* **2000,** *42*, (3), 323-383.
154. DeAngelis, M. A.; Glines, A. M.; Anton, A. B., Precursor and overlayer structural effects in the interaction of CO with Ni(110). *J. Chem. Phys.* **1992,** *96*, (11), 8585-8594.
155. Fletcher, A. J.; Thomas, K. M., Compensation effect for the kinetics of adsorption/desorption of gases/vapors on microporous carbon materials. *Langmuir* **2000,** *16*, 6253-6266.
156. Kobayashi, T.; Babu, P. K.; Chung, J. H.; Oldfield, E.; Wieckowski, A., Coverage dependence of CO surface diffusion on Pt nanoparticles: an EC-NMR study. *Journal of Physical Chemistry C* **2007,** *111*, 7078-7083.
157. Rigby, S. P., Fractal theory for the compensation effect observed in a surface diffusion process studied using deuteron NMR. *Langmuir* **2002,** *18*, 1613-1618.
158. Rigby, S. P., NMR and modelling studies of structural heterogeneity over several lengthscales in amorphous catalyst supports. *Catalysis Today* **1999,** *53*, 207-223.
159. Halsey, G., Physical adsorption on non-uniform surfaces. *Journal of Chemical Physics* **1948,** *16*, (10), 931-937.

160. Yin, Y., Adsorption isotherm on fractally porous materials. *Langmuir* **1991,** *7*, 216-217.
161. Pfeifer, P.; Wu, Y. J.; Cole, M. W.; Krim, J., Multilayer adsorption on a fractally rough surface. *Physical Review Letters* **1989,** *62*, (17), 1997-2000.
162. Avnir, D.; Jaroniec, M., An isotherm equation for adsorption on fractal surfaces of heterogeneous porous materials. *Langmuir* **1989,** *5*, 1431-1433.
163. Neimark, A. V.; Hanson, M.; Unger, K. K., Fractal analysis of the distribution of high-viscosity fluids in porous supports. *Journal of Physical Chemistry* **1993,** *97*, 6011-6015.
164. Qi, H.; Ma, J.; Wong, P.-z., Adsorption isotherms of fractal surfaces. *Colloids and Surfaces A: Physicochem. Eng. Aspects* **2002,** *206*, 401-407.
165. Ismail, M. K. I.; Pfeifer, P., Fractal analysis and surface roughness of nonporous carbon fibers and carbon blacks. *Langmuir* **1994,** *10*, 1532-1538.
166. Drake, J. M.; Yacullo, L. N.; Levitz, P.; Klafter, J., Nitrogen adsorption on porous silica: model dependent analysis. *Journal of Physical Chemistry* **1994,** *98*, 380-381.
167. Ehrburger-Dolle, F., Some new correlations between Dubinin-Radushkevich and Freundlich equations and fractal dimension of microporous solids. *Langmuir* **1994,** *10*, 2052-2055.
168. Ehrburger-Dolle, F., Analysis of the derived curves of adsorption isotherms. *Langmuir* **1997,** *13*, 1189-1198.
169. Tang, P.; Chew, N. Y. K.; Chan, H.-K.; Raper, J. A., Limitation of determination of surface fractal dimension using N_2 adsorption isotherms and modified Frenkel-Halsey-Hill theory. *Langmuir* **2003,** *19*, 2632-2638.
170. Neimark, A. V.; Unger, K. K., Method of discrimination of surface fractality. *Journal of Colloid and Interface Science* **1993,** *158*, 412-419.
171. Rigby, S. P.; Gladden, L. F., The prediction of transport properties of porous media using fractal models and NMR experimental techniques. *Chemical Engineering Science* **1999,** *54*, 3503-35512.
172. Avnir, D.; Farin, D.; Pfeifer, P., Chemistry in noninteger dimensions between two and three. II. Fractal surfaces of adsorbents. *Journal of Chemical Physics* **1983,** *79*, (7), 3566-3571.
173. Kanyo, T.; Konya, Z.; Kukovecz, A.; Berger, F.; Dekany, I.; Kirkcsi, I., Quantitative characterization of hydrophilic-hydrophobic properties of MWNTs surfaces. *Langmuir* **2004,** *20*, 1656-1661.
174. Sun, C.-H.; Li, F.; Cheng, H.-M.; Lu, G.-Q., Fractal effects on the measurement of the specific surface areas of single-walled carbon nanotubes. *Carbon* **2005,** *43*, 1785-1787.
175. Diduszko, R.; Swiatkowski, A.; Trznadel, B. J., On surface of micropores and fractal dimension of activated carbon determined on the basis of adsorption and SAXS investigations. *Carbon* **2000,** *38*, 1153-1162.
176. Boddenberg, B.; Beerwerth, B., Proton and deuteron magnetic resonance relaxation of benzene adsorbed on alumina and on a platinum/alumina catalyst. *Journal of Physical Chemistry* **1989,** *93*, 1440-1447.
177. Dachs, J., Conformation entropy drives slow sorption of organic chemicals into fractal sorbents. *Langmuir* **2002,** *18*, 7089-7091.

178. Dachs, J.; Eisenreich, S. J., Effects of adsorbate/adsorbate interactions and surface fractality on diffusion- and reaction-limited adsorption. *Langmuir* **1999,** *15*, 8686-8690.
179. Hennrich, F.; Krupke, R.; Lebedkin, S.; Arnold, K.; Fischer, R.; Resasco, D. E.; Kappes, M. M., Raman spectroscopy of individual single-walled carbon nanotubes from various sources. *Journal of Physical Chemistry B* **2005,** *109*, 10567-10573.
180. Li, M.; Deng, K.; Yang, Y.-L.; Zeng, Q.-D.; He, M.; Wang, C., Electronically engineered interface molecular superlattices: STM study of aromatic molecules on graphite. *Physical Review B* **2007,** *76*.
181. Macomber, R., *A Complete Introduction to Modern NMR Spectroscopy*. John Wiley & Sons: New York, 1998; p 382.
182. Torchia, D. A.; Szabo, A., Spin-lattice relaxation in solids. *Journal of Magnetic Resonance* **1982,** *49*, 107-121.
183. Boddenberg, B.; Beerwerth, B., Proton and deuteron magnetic resonance spectra of benzene adsorbed on alumina and on a platinum/alumina catalyst. *Journal of Physical Chemistry* **1989,** *93*, 1435-1440.
184. Dubinin, M. M.; Vartapetian, R. S.; Voloshchuk, A. M., NMR study of translational mobility of molecules adsorbed on active carbons. *Carbon* **1988,** *29*, (4), 515-520.
185. Sanders, J. K. M.; Hunter, B. K., *Modern NMR Spectroscopy: a Guide for Chemists*. Oxford University Press: New York, 1987; p 308 p.
186. Levitt, M. H., *Spin Dynamics: Basics of Magnetic Resonance*. John Wiley & Sons: West Sussex, England, 2001; p 686 p.
187. Duer, M. J., *Introduction to Solid-State NMR Spectroscopy*. Oxford Press: Oxford, U.K., 2004.
188. Xiong, J.; Maciel, G. E., Deuterium NMR studies of local motions of benzene adsorbed on Ca-montmorillonite. *Journal of Physical Chemistry B* **1999,** *103*, 5543-5549.
189. Nishikiori, S.-I.; Soma, T.; Iwamoto, T., In-plane and out-of-plane motion of benzene trapped in $Cd(py)_2\{Ag(CN)_2\}_2$ host as studied by deuterium NMR. *Journal of Inclusion Phenomena and Molecular Recognition in Chemistry* **1997,** *27*, 233-243.
190. Greenfield, M. S.; Ronemus, A. D.; Vold, R. L.; Vold, R. R.; Ellis, P. D.; Raidy, T. E., Lineshapes of deuterium quadrupole echoes. *Journal of Magnetic Resonance* **1989,** *72*, 89-107.
191. Griffin, R. G.; Beshab, K.; Ebelhauser, R.; Huang, T. H.; Olejniczak, E. T.; Rice, D. M.; Siminovitch, D. J.; Wittebort, R. J., Deuterium NMR studies of dynamics in solids. In *The Time Domain in Surface and Structural Dynamics*, Long, G. J. a. G., F., Ed. Kluwer Academic Publishers: 1988; pp 81-105.
192. Ok, J. H.; Vold, R. R.; Vold, R. L.; Etter, M. C., Deuterium nuclear magnetic resonance measurements of rotation and libration of bezene in a solid-state cyclamer. *Journal of Physical Chemistry B* **1989,** *93*, 7618-7624.
193. Spiess, H. W., Molecular dynamics of solid polymers as revealed by deuteron NMR. *Colloid & Polymer Science* **1983,** *261*, 193-209.

194. Auerbach, S. M.; Bull, L. M.; Henson, N. J.; Metin, H. L.; Cheetham, A. K., Behavior of benzene in Na-X and Na-Y zeolites: comparative study by ^{2}H NMR and molecular mechanics. *Journal of Physical Chemistry* **1996,** *100*, 5923-5930.
195. Eastman, M. A.; Nanny, M. A., Fitting of deuterium quadrupole echo spectra with multiple motional models. *Journal of Magnetic Resonance* **2007,** *184*, 302-314.
196. Sato, T.; Kunimori, K.; Hayashi, S., Dynamics of benzene, cyclohexane and *n*-hexane in KL zeolite studied by ^{2}H NMR. *Physical Chemistry Chemical Physics* **1999,** *1*, (3839-3843).
197. Nishikiori, S.-I., Out-of-plane motion of the guest benzene molecule trapped in a $[Cd(dmen)_2(CN)]_2[Cd(CN)_4]$ host as studied by ^{2}H-NMR. *Journal of Inclusion Phenomena and Macrocyclic Chemistry* **1999,** *34*, 331-343.
198. Chopra, N.; Chapman, R. G.; Chuang, Y.-F.; Sherman, J. C.; Burnell, E. E., Guest dynamics in carceplexes: a ^{2}H NMR study. *J Chem Soc Faraday Trans* **1995,** *91*, (21), 4127-4131.
199. Viani, A.; Gualtieri, A., F.; Arioli, G., The nature of disorder in montmorillonite by simulation of X-ray powder patterns. *American Mineralogist* **2002,** *87*, 966-975.
200. Chipera, S. J.; Bish, D. L., Baseline studies of the Clay Minerals Society source clays: powder X-ray diffraction analyses. *Clays and Clay Minerals* **2001,** *49*, 398-409.
201. Villanueva-Garibay, J. A.; Muller, K., Solid-state ^{2}H NMR studies of cyclophosphazene inclusion compounds: order and dynamics of the benzene guests. *Journal of Physical Chemistry B* **2004,** *108*, 15057-15068.
202. Schwartz, M.; Duan, D.; Berry, R. J., Molecular dynamics study of anisotropic translational and rotational diffusion in liquid benzene. *J. Phys. Chem. A* **2005,** *109*, (38), 8637-8641.
203. Silbernagel, B. G.; Garcia, A. R.; Newsam, J. M.; Hulme, R., Molecular motion of benzene, *n*-hexane, and cyclohexane in potassium zeolite studied by deuterium NMR. *Journal of Physical Chemistry* **1989,** *93*, 6506-6511.

CHAPTER 2. EXPERIMENTAL

2.1. SAMPLES AND PREPARATION

2.1.1. Black carbon (BC) solid phases

Eight diverse and well-characterized (Table 2.1) BC samples were used in

Table 2.1. Properties of black carbon samples

Sample[a]	wt % Carbon	% Other	[Ca] (ppm)[b]	Surface Area (m^2/g)	Pore Size Range (nm)	Pore Size Mode (nm)
Diesel Soot NIST SRM #2975[c] (SOOT)	87.2[d]	1.3 % H 7.0 % O[d]	249	91[c]	4-35[c,e]	20[c]
Nanocarbon particles[f] (CNP)	≥ 99	≤1	767	100	5-50[g]	10[g]
Graphite[h] (GRAPH)	> 99.99	-	< 194	4.5	5-50[g]	10,30[g]
Nanocarbon tubes, multiwalled, smaller i.d..[i] (CNS)	≥ 95	≤5	< 154	115	5-10	10,30[g]
Nanocarbon tubes, multiwalled, larger i.d.[j] (CNW)	> 95	<5	< 172	218	5-40	-
Nanocarbon tubes, single-walled[k] (SWCNT)	> 99.99	-	-	est > 600[l]	0.7-0.9[m]	-
Activated carbon[n] (AC)	87.6[o]	0.9 % H 7.9 % O[o]	467	776[o] 798[g]	0.4-50[o,g]	0.6[o,g]
Maple wood char[p] (MWC)	71.97[q]	2.83% H 0.51% N 2.03% ash[q]	3200	430[q]	0.5-5[q]	0.5,0.8[q]

[a]All samples, except as noted in text, were loaded at 1% w/w with benzene, and all values shown above which are not specifically referenced were purchased from Aldrich Chemical Co.; [b]analysis was performed by Galbraith Laboratories using inductively coupled plasma; [c]NIST Certificate of Analysis [1]; [d]Nguyen et al. [2]; [e]reported independently in Nguyen and Ball [3] to contain > 55% of pores with dia. > 35 nm; [f]amorphous, laser technique [4]; [g]this work; [h]325 mesh; [i]outer dia. 60-100 nm, inside dia. 5-10 nm, length 5-50 μm; [j]outside dia. 40-70 nm, inside dia. 5-40 nm, length 5-2 μm; [k]sample prepared by CoMoCAT technique [5], provided by Dr. Daniel E. Resasco; [l]estimate based on measurements on similar samples by Arai et al. [6]; [m]Bachilo et al. [5]; [n]Darco G60, 100 mesh; [o]Chun et al. [7]; [p]prepared from maple wood chips which were heated at 673K for 2 hours in a 15-cm watchglass-covered crucible, ground gently, and sieved to ≤ 150 mm [8]; [q]Braida et al. [8].

study: a standard reference material (SRM #2975) diesel soot from the National Institutes of Standards (NIST), maple wood char (provided by Dr. Joseph J. Pignatello of the Connecticut Agricultural Experiment Station in New Haven, Connecticut), single-walled carbon nanotubes (provided by Dr. Daniel E. Resasco of the University of Oklahoma in Norman, Oklahoma), and five commercially available BC materials purchased from Aldrich, specifically, graphite, carbon nanoparticles, two different multi-walled carbon nanotubes, and an activated carbon. The benzene-d_6 was purchased from Cambridge Isotope Laboratories and stored in a vial with a silicone/PFTE-lined septum placed into the freezer section of the refrigerator. All BCs were used as received without degassing or other treatment prior to sample sealing. Results listed in Table 2.1 which were obtained from our N_2 gas adsorption analysis will be discussed in the Chapter 3.

2.1.2. Sample Preparation

The solid phases were used as received and were not degassed exhaustively prior to the addition of benzene-d_6 vapor for complete removal of adsorbed water molecules (for example, vacuum evacuation to 1×10^{-6} torr and/or duration of vacuum for several days, or heating to 300°C) for two reasons. First, the hydrophobic nature of the black carbon surfaces is unlikely to be strongly affected by a small amount of adsorbed water molecules [9-11]. Second, the samples were deliberately prepared in the same manner as humic and fulvic acid samples used in a related study and, for those samples, excessive removal of adsorbed water can lead to structural collapse [12]. To load the samples of benzene-d_6 on BCs into NMR tubes for static solid-state ^{2}H NMR analysis, first, an accurately weighed amount of

BC solid phase was placed into a specially modified NMR tube. The tubes were attached to a custom-designed vacuum manifold, described in detail Appendix A1, evacuated to 0.001 torr at room temperature, and then an amount of benzene-d_6 vapor equivalent to 1% w/w (or other) loading was condensed onto the liquid N_2-cooled BC. The sample tube was then backfilled with N_2 gas, and, finally, the NMR tube was flame-sealed, keeping the BC and condensed benzene submerged in liquid N_2. The sample preparation process and details of the vapor deposition manifold system are explained in great detail in Appendix A1, along with the benzene-d_6 quantitation and calibration procedures.

2.2. STATIC SOLID-STATE ^{2}H NMR EXPERIMENTS

2.2.1 Instrumental Parameters

Static, solid-state deuterium NMR spectra were acquired at 46.20525 MHz on a Chemagnetics CMX-II 300 MHz instrument with a quadrupole-echo sequence, $90^o_x - \tau_1 - 90^o_y - \tau_2 -$ acquire, where τ_1 and τ_2 are the echo delays. The length of the acquisition delay was determined by the relaxation time of the sample: NMR spectra for samples which possibly contained benzene in the liquid state (T_1 1.5 s) were observed with relaxation delays of 10 s, but most of the BC samples were collected with relaxation delays of 0.25-0.5 s because the T_1 values measured at 25°C were less than 50 ms. The specific values of these T_1 values are stated in Chapters 4-8. The 90° pulse was 2.25 μs and was determined from the maximum signal intensity for a polymethyl methacrylate (PMMA) sample according the manufacturer's recommended procedures. A spectral width of 0.5 MHz (dwell time of 2 μs) was used to obtain the ^{2}H spectra, which was collected with 1024, 4096 or

8192 data points to give digital resolution of 488, 122, or 61 Hz, respectively. Spectral files collected with lesser digital resolution (1024) were zero-filled during processing as needed to obtain good fits. The probe temperature was controlled through the VT stack by a temperature controller with a temperature stability of $\pm 0.1^{o}$C. The static solid-state ^{2}H probe included coils for both 5 mm and 10 mm dia. sample tubes, and the coils were oriented within the magnet such that the long dimension of the tube was perpendicular to static magnetic field (i.e., the samples were not oriented as the magic angle because no sample spinning was utilized). All BC sample spectra were collected with 10 mm dia. sample tubes and, thus, also the 10 mm dia. coil.

2.2.2. Lineshape Analysis of ^{2}H Static Solid-State NMR Spectra

Using the group of computer programs entitled Deuterium Fitting Program (DFP), Library Creation Program (LCP) and Deuterium Motional Simulation (DMS) [13], libraries of calculated spectra for isotropic (ISO), small-angle wobble (SAW), and large-angle wobble (LAW) motional models were constructed, using different spinning rates and wobble angles, defined in the Introduction Chapter. Sample Library Creation input for two motional models for benzene are provided within the program: SAW motion, which is based on a spinning top model of rotational motion, and an ISO motion, which models a spherical distribution of molecular orientations over the NMR sampling time using 32 sites of the faces and vertices of a dodecahedron. Other desired motional models can be constructed by the user by identifying Euler angles sites which the molecule will occupy as it executes the motion in mind. A sample library creation input, modified from Eastman and Nanny [13] which is included in the DFP software, can be found in

Appendix A2. The library creation input file includes, among other parameters, a list of the Euler angle sites which describe a large-angle wobble motion combined with an independent C_6 rotation, the ranges of jump rates between these positions of the benzene molecule, and the number of increments of jump rates to be simulated. Sample simulated spectra which were output from the Library Creation Program along with stereonet projections for the *x-y-z* axes of the benzene molecule, including the principle axis systems, defined in the Introduction Chapter, at the positions that are described by the Euler angles can also be found in Appendix A2 for the large-angle wobble motion.

After the creation of the desired libraries, the DFP fitting program finds combinations of the spectra from these libraries which fit experimental spectra. In the systematic DFP fitting method, the simulated spectra within a library are compared to the experimental spectrum on a point-by-point basis, and the match is given to that simulated spectra which has the lowest sum of the square of the differences between individual simulated amplitudes and experimental amplitudes averaged over each frequency. Further, combinations of motional models (fitting of an experimental spectrum to spectra from more than one library) can be accomplished, using least squares fitting to determine a coefficient for the simulated spectra from each library which is contributing to the experimental spectrum. Examples of spectra fit from Additional information regarding the fitting program can be found in Eastman and Nanny [13].

2.3. X-RAY DIFFRACTION AND N_2 ADSORPTION EXPERIMENTAL PARAMETERS

A Rigaku Gigaflex XRD spectrometer was employed; the 2Θ scan was

performed from 5.0-70.0^{o} in 0.05^{o} increments resulting in 200 data points per degree; the dwell time was 0.5 s. The copper anode was employed with a Ni filter, providing a Cu-Kα wavelength of 1.54Å. Nitrogen isotherm analysis was performed at 77K over pressure ranges from 2x10^{-6} torr to 760 torr and equilibration time of 1 minute using a Quantachrome Corporation Autosorb 1C instrument. Samples were exhaustively degassed (at least overnight) at 300°C, and completion of degassing was verified by an outgassing test over a 3 minute interval recommended by the manufacturer.

References

1. Certificate of Analysis - Standard Reference Material 2975 - Diesel Particulate Matter (Industrial Forklift). **2001**.
2. Nguyen, T. H.; Brown, R. A.; Ball, W. P., An evaluation of thermal resistance as a measure of black carbon content in diesel soot, wood char, and sediment. *Organic Geochemistry* **2004,** *35*, 217-234.
3. Nguyen, T. H.; Ball, W. P., Absorption and adsorption of hydrophobic organic contaminants to diesel and hexane soot. *Environmental Science & Technology* **2006,** *40*, 2958-2864.
4. Aldrich Catalog. In Sigma-Aldrich Chemical Company.
5. Bachilo, S. M.; Balzano, L.; Herrera, J. E.; Pompeo, F.; Resasco, D. E.; Weisman, R. B., Narrow (*n,m*)-Distribution of single-walled carbon nanotubes grown using a solid supported catalyst. *Journal of the American Chemical Society Communications* **2003,** *125*, 11186-11187.
6. Arai, M.; Kanamaru, M.; Matsumura, T.; Hattori, Y.; Utsumi, S.; Ohba, T.; Tanaka, H.; Yang, C. M.; Kanoh, H.; Okino, F.; Touhara, H.; Kaneko, K., Pore characterization of assembly-structure controlled single wall carbon nanotube. *Adsorption* **2007,** *13*, 509-514.
7. Chun, Y.; Sheng, G.; Chiou, C. T.; Xing, B., Compositions and sorptive properties of crop residue-derived chars. *Environmental Science & Technology* **2004,** *38*, 4649-4655.
8. Braida, W. J.; Pignatello, J. J.; Lu, Y.; Ravikovitch, P. I.; Neimark, A. V.; Xing, B., Sorption hysteresis of benzene in charcoal particles. *Environmental Science & Technology* **2003,** *37*, 409-417.
9. Li, L.; Quinlivan, P. A.; Knappe, D. R. U., Predicting adsorption isotherms for aqueous organic micropollutants from activated carbon and pollutant properties. *Environmental Science & Technology* **2005,** *39*, (9), 3393-3400.

10. Fletcher, A. J.; Uygur, Y.; Thomas, K. M., Role of surface functional groups in the adsorption kinetics of water vapor on microporous activated carbons. *Journal of Physical Chemistry C* **2007,** *111*, 8394-8399.
11. Bornemann, L. C.; Kookana, R. S.; Welp, G., Differential sorption behaviour of aromatic hydrocarbons on charcoals prepared at different temperatures from grass and wood. *Chemosphere* **2007,** *67*, 1033-1042.
12. Schwarzenbach, R. P.; Gschwend, P. M.; Imboden, D. M., *Environmental Organic Chemistry, 2nd ed.* John Wiley and Sons Inc.: New York, NY, 2003.
13. Eastman, M. A.; Nanny, M. A., Fitting of deuterium quadrupole echo spectra with multiple motional models. *Journal of Magnetic Resonance* **2007,** *184*, 302-314.

CHAPTER 3. BLACK CARBON MATERIALS CHARACTERIZATION USING X-RAY DIFFRACTION (XRD) AND N_2 ADSORPTION

3.1 INTRODUCTORY SUMMARY

As the benzene-d_6 interacts with the black carbon (BC) surfaces, the benzene molecules' motion is directly affected by the surface forces of the graphenic moieties and by confinement within micro- and mesopores [1-4]. It was hypothesized that these motional influences would be observable in the ^{2}H NMR spectrum. It is well known that the adsorptive energy of the benzene-graphene interactions involves π-π interactions between benzene and the aromatic graphene functionalities on the surface and that the surface energy of the graphene π electrons is enhanced by contributions from the electrons of the crystalline graphene sheets below the surface layer [1, 2]. However, there are no studies which compare differences in pore structure and graphite crystallinity to differences in the motion of adsorbed benzene. In this chapter, the surfaces and pores of seven BC samples are characterized by N_2 adsorption analysis and their degrees of graphitic crystallinity are measured using X-ray diffraction (XRD). The samples are a low-surface-area graphite (LSAG), amorphous carbon nanoparticles (CNP), two different multi-walled carbon nanotubes (CNT), an activated carbon (ActC), and maple wood char (MWC). In addition, this is the first reported X-ray diffractogram of NIST SRM #2975 diesel soot.

Several important theoretical models of benzene/graphite interactions during adsorption include contributions due to crystalline order and/or the presence of an irregular surface [2, 3]. Smaller amounts of face-to-face contact between the benzene and the aromatic graphenes due to surface irregularity favors lowered

adsorption energies, increased rate of molecular rotation (both in-plane and out-of-plane), and lower E_a values for surface diffusivity relative to an ideal planar graphite surface . Irregularity in the graphenic surface, depicted schematically in Figure 3.1, can occur as, for instance, pits or irregularly shaped grains, and this can influence the configuration of adsorbed benzene, possibly preventing a face-to-face planar orientation [3-5]. Similarly, chemical

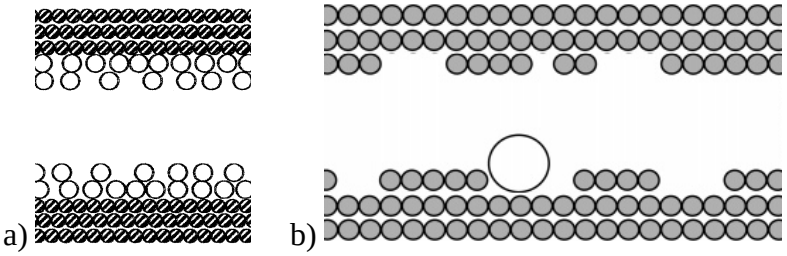

Figure 3.1. Schematic depiction of adsorption in slit-shaped graphitic pores used for DFT modeling of isotherms from Do and Do [3]; open circles are sorbate molecules; colored circles indicate the sorbent: a) the effect of decreasing surface potential toward the centers of pores on sorbate concentration profile [3]; b) the effect of surface irregularity on sorbate/surface orientation [6]

inhomogeneity of the surface, in the form of non-graphene carbon functional groups at crystallite edges and/or noncarbon functional groups, such as hydroxyls, carboxylic acids, or heteroatoms, can also affect the nature of the benzene/black carbon sorption interaction. Both vapor and aqueous phase isotherm studies have been performed by previous workers on carbonaceous sorbents to measure their sorptive activities and capacities, and these results were interpreted in light of solid phase characterizations, e.g., amount of acidic or functional groups, carbon fraction of elemental composition, pore size distributions, total porosity. Most of these studies concluded that the parameter most important for sorption of benzene in

carbonaceous solids is pore size, and that the effectiveness of activated carbons is primarily due to the predominance of micropores in their structures [7, 8]. Surface chemistry is the other primary parameter, and, although benzene is known to H-bond by electron donation through its aromatic π electron system, many workers have concluded that, except in very dry systems, the presence of water molecules out-competes benzene for polar sites on the carbon surface and effectively deactivates the surface with respect to H-bonding with benzene [9]. Illustrating this effect is the improvement in the sorption characteristics of carbon black after graphitization, in which the original carbon black is heated to high temperatures (3000°C) under anaerobic conditions, producing a material with a greater graphitic crystalline order and fewer "impurities", such as oxygen or nitrogen [10-12]. Recent studies have further established this correlation between higher degrees of graphitic crystallinity, as measured by XRD or Raman spectroscopy, with increased adsorption potentials in black carbons. A notable study of this type is that of Kruk et al. [4] comparing graphite crystallinity to results obtained with application of model Dubinin- Radushkevich isotherms on graphitized carbon black.

Previous XRD studies of BC's include work on soot, carbon nanotubes, oxidized exfoliated graphite, and activated carbon [5, 13-17]. A well crystallized graphite displays a sharp narrow peak for the basal plane (d_{002}) at a 2θ value of 26.5^{o} (d=0.335 nm) and a prominent d_{100}-d_{101} peak near .21 nm (2θ 44°) [12, 18, 19]. Broad, low-intensity XRD peaks near a 2θ 24° are common for activated carbon, low-grade coals, nongraphitized carbon blacks and similar samples [5, 13, 17, 20, 21]. Deviations from a value of 0.335 nm for d_{002} indicates structural

disorder in the crystals, such as in turbostratic graphites [21], and such disorder is also indicated by wide peaks [22]. Exfoliated, oxidized graphites also contain a characteristic peak at 10° 2θ [1].

Numerous adsorption analyses using N_2 isotherms at 77K have been performed on BC compounds [8, 23], and the development of isotherm models for analyzing pore size distributions and for general understanding of sorbate/BC interactions from this data remains an active area of research, particularly for carbon nanotubes [14, 24]. Mesoporous carbons typically display an S-shaped isotherm (like the Type II isotherm in Figure 3.2), with the initially steep slope (a large increase in the amount adsorbed with a

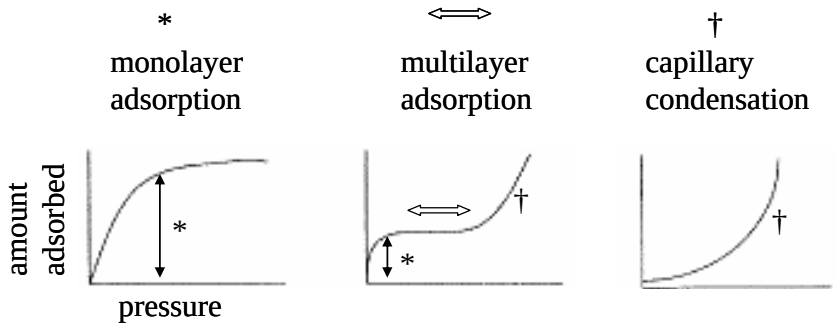

Figure 3.2. Idealized isotherms, showing different IUPAC classifications and the nature of the adsorption that occurs at different regions of the isotherm: (left) Type I, (middle) Type II, (right) Type III.

small change in the gas pressure) attributable to filling of the monolayer capacity, followed by a gentle flattening of the curve as multilayer deposition occurs, and, as the pressure approaches the vapor pressure of the sorbate gas, P_0, the slope again becomes very steep as liquid N_2 undergoes capillary condensation in the macropores [25]. The height of the initial steep-slope section is indicative of the volume of micro-and mesopores. Activated carbons, dominated by microporosity, consist only

of the initially steep-sloped portion of the S-curve described above, because the pores are so small, in some cases, that little more than a monolayer can occupy each pore. On the other hand, carbons with very low surface areas have an almost negligible initial steep-sloped segment.

3.2 EXPERIMENTAL

Powder XRD analysis was performed to measure the degree of graphitic crystalline ordering in the black carbon materials. A Rigaku Gigaflex XRD spectrometer was employed; the 2Θ scan was operated from 5.0-70.0^{o} in 0.05^{o} increments resulting in 200 data points per degree; the dwell time was 0.5 s. The copper anode was fitted with a Ni filter, providing a Cu-Kα wavelength of 1.54 Å. The sample was applied as a small swatch smeared onto a microscope slide.

Nitrogen isotherm analyses were performed at 77K over pressure ranges from 2x10^{-6} torr to 760 torr with a Quantachrome Corporation Autosorb 1C instrument, and up to 1 minute equilibration time was used for each data point. Samples were degassed at 300°C overnight, and the degassing completion was monitored using the default instrumental settings. The cross-sectional area of a N_2 molecule used in calculating the specific surface area from the Brunauer-Emmet-Teller (BET) equation was 16.2 Å^2. Pore-size distributions were calculated using Quantachrome Corporation software, with both nonlocalized density functional theory (NLDFT), which is strongly recommended for micropore analysis [26], and the Dollimore-Heal (DH) algorithm, which is one of several recommended by Quantachrome Corporation for spherical or cylindrical pores [26]. The Dollimore-Heal method has been shown to produce accurate pore size distributions, similar to

values obtained with the Barrett-Joyner-Halenda method which is also very commonly applied [27]. Both methods are based on the Kelvin equation (Eqn. 1.1) which relates the size of a droplet of condensed liquid to the vapor pressure [25, 27].

3.3 RESULTS

3.3.1 X-Ray Diffraction

The X-ray diffractograms for the BC samples are displayed in Figure 3.3.

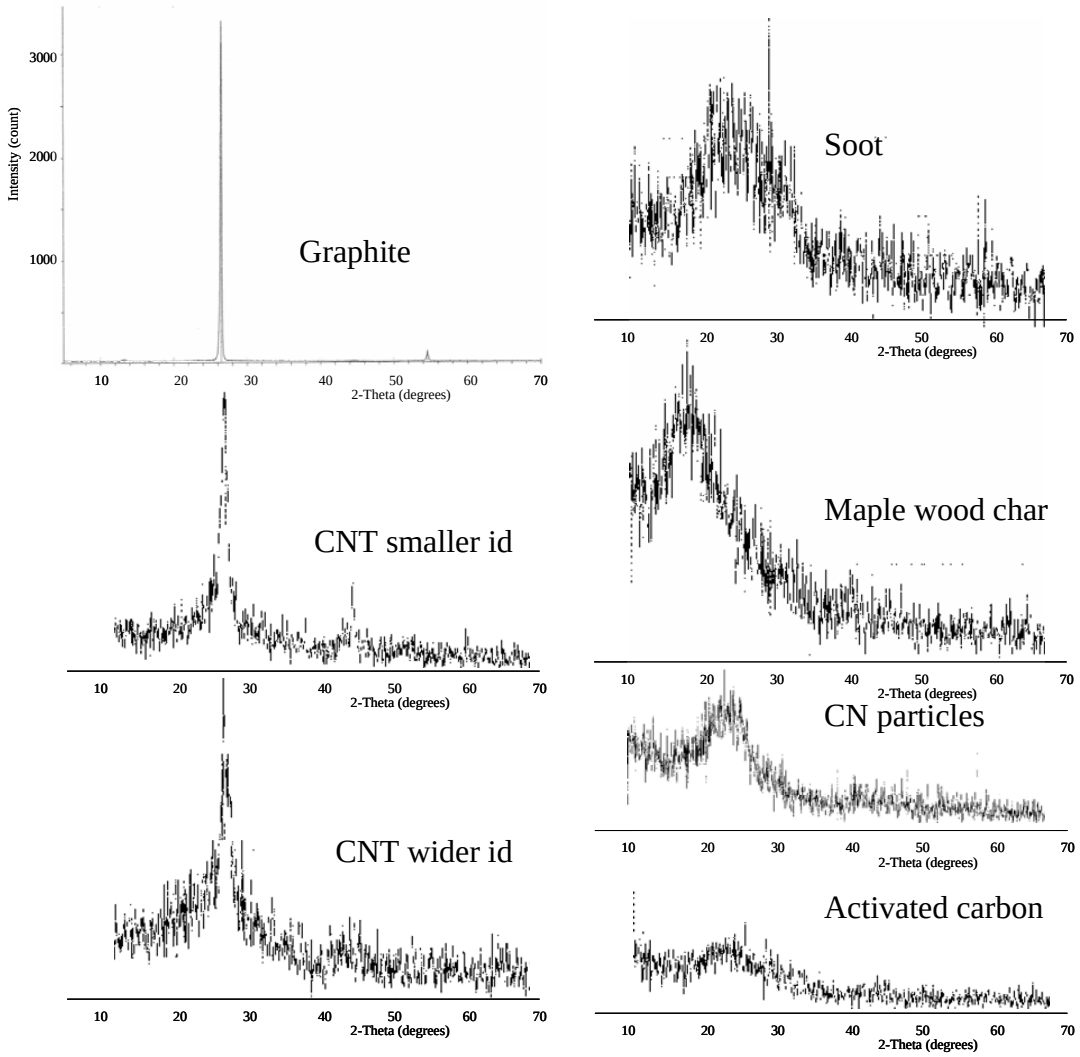

Figure 3.3. Powder X-ray diffractograms for black carbon materials. See Table 3.1 heights and text for details.

The pure crystalline graphite sample employed in this study displays peaks for d_{002} at 0.337 nm (2θ 26.5°) and d_{004} at 0.168 nm (2θ 54.5°), which is in phase with the d_{002} plane. The value of d_{002} is very slightly shifted from the ideal 0.335 nm, probably due to the small crystallite sizes [22]. The occurrence of only d_{002} and d_{004} peaks (lacking the d_{100} peak at 2θ 43° found in natural graphites [18]) has been mentioned by some authors as characteristic of small grain-size graphites [22]. While all of 0.338 nm, is also very close to ideal (Table 3.3), although the d-spacing

Table 3.1. Summary of XRD results for BC samples

Sample	d_{002} (nm)	Intensity	FWHM [β (θ)] in degrees	L_c (nm)[a]	n[b]
Low-Surface-Area Graphite	0.337±.001	3300	0.2±0.05	770	1800
Carbon Nanotubes (wider id)	0.338±0.005	120	1+0.1	15	150
Carbon Nanotubes (smaller id)	0.344±0.005	70	1+0.1	8	80
Carbon Nanoparticles	0.35±0.01	50	2±0.3	6	60
Activated Carbon	0.37±0.01	25	3±0.3	3	10
Soot	0.37+0.01	35	5±0.3	2	10
Maple wood char	0.49±0.3	60	2.5+0.3	3	8

[a] L_c (also called D, the Scherrer crystallite size) = 0.9 λ / (β_{002} cos θ_{002}), where λ = 1.54Å, the incident CuKα radiation, β = FWHM in radians, and θ (radians) is from the Bragg equation (λ = 2 d sinθ); values include a correction for instrumental broadening, B, of 0.17°; actual equation used is $L_c = 0.9\,\lambda / [(\beta^2 - B^2)^{1/2} \cos\theta]$; [b] $n = L_c / d_{002}$ [12].

of the large i.d. carbon the BC samples do contain a d_{002} peaks, the peaks for CNP, soot, activated carbon and maple wood char are very broad and of low intensity, indicating a poor crystallographic ordering of the graphitic functions. The d_{002} value for the small i.d. carbon nanotubes, nanotubes, which was calculated to be 0.344 nm, indicates lesser crystalline order. In general, the samples with larger d_{002} values also have wider peaks, as expected, since both are related to the degree of crystallinity. For samples with poorly developed crystallinity, the degree of

crystalline ordering may be related to the average crystal size for samples, and this has been calculated with the Scherer equation [28]:

$$L_c = 0.9\,\lambda / (\beta_{002} \cos \theta_{002}) \qquad \textbf{(Eqn.3.1)}$$

where L_c is the Scherer crystallite size, 0.9 is a shape factor, λ the wavelength of Cu Kα radiation, 1.54Å, β_{002} the peak width at half height (FWHM) in radians of the 002 reflection, and θ_{002} is from the Bragg equation [28],

$$\lambda = 2\, d_{002} \sin \theta_{002}. \qquad \textbf{(Eqn. 3.2)}$$

The pure crystalline graphite particles are 44μm in diameter, according to the Aldrich specification [29], but, the average diameter of the crystallites is calculated to be nearly 50 times smaller. Small grain sizes usually contain more crystal defects [22], and these defects would affect the peak width at half-height, skewing the results of the L_c calculation towards smaller grains. Of the other samples, only the carbon nanotubes contain even moderately sharp d_{002} peaks, the others meriting the adjective nongraphitized, which is applied to activated carbon and other synthetic carbon black samples which have not been subjected to high temperatures required for graphitization. For comparison, L_c values for poorly graphitized carbons and carbon blacks have reported values from 8-25 nm and activated carbon fibers from 6.7-8.8 nm [11, 12, 19, 30]. Yoon et al. (2008) calculated the Scherer width of 6.3 nm for the graphite domains of a graphitized pitch-based activated carbon, which the authors refer to as an ordered nanoporous carbon [21]. The 2θ value for the maple wood char sample is close to 15° (d-spacing 0.49 nm). This is intermediate between the 2θ 10° value for oxidized graphite and the 2θ 24° for graphite.

3.3.2 N_2 adsorption isotherms

The N_2 isotherm for the low-surface-area graphite (Figure 3.4) has a BET

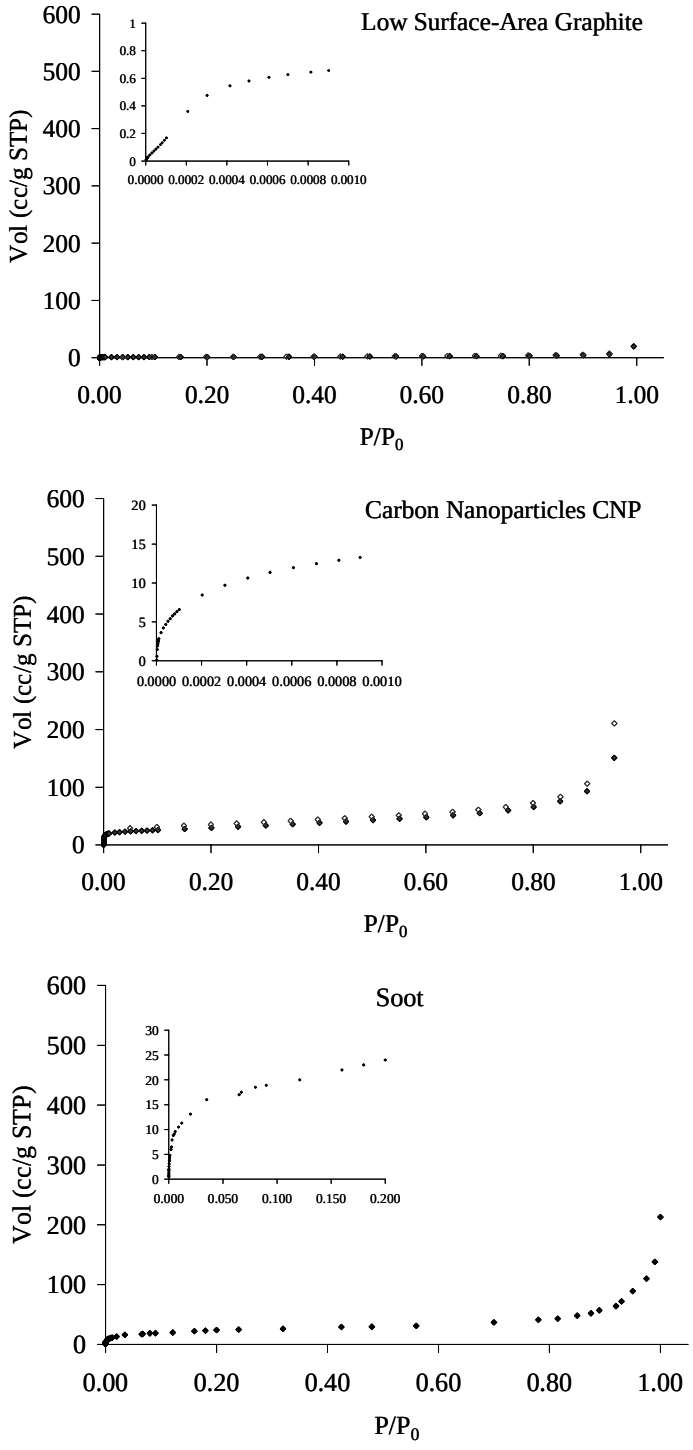

Figure 3.4. N_2 adsorption isotherms at 77K for the indicated black carbons; soot values extrapolated from the Supporting Information from Nguyen and Ball [31]; solid symbols - adsorption data points; open symbols - desorption points.

specific surface area of 4.5 m^2/g and minimal pore space, and these are indicated by the very small region of steep slope at the beginning of isotherm. The carbon nanoparticles and the soot (also shown in Figure 3.4) have higher surface areas, 100 m^2/g and 91 m^2/g, respectively, and these samples also have higher maximum values on the isotherm's *y*-axis and a more pronounced early region of steep slope. The low-surface-area graphite particles display a very small amount of hysteresis, in which by definition the *desorption* isotherm differs from the *adsorption* isotherm. Figure 3.5, in comparison, shows the CNT samples, which are BC that contain higher porosity, and all of these show a pronounced initial region of large slope (large monolayer value). The multi-walled carbon nanotubes also show well-defined hysteresis (Figure 3.5). In their studies of N_2 isotherm on carbon nanotubes, Inoue et al. [13, 32] explained that hysteresis requires that the tubes be open on both ends. This is well-developed theoretically by Greg and Sing [25] and stems from the fact that condensation in a closed tube starts at the end of the tube, creating a hemispherical meniscus, and this step is followed by condensation in the rest of the tube length across the same meniscus, and evaporation exactly reverses this path (no hysteresis). However, for tube which has no end, the condensation path occurs all along capillary simultaneously across a cylindrical meniscus, and after some time the capillary is filled, whereas the evaporation path, the same as for the closed tube, follows the retreating hemispherical meniscus (different path = hysteresis). Because multilayer adsorption fills small pores (less than 3.5-4.0 nm), hysteresis is not observed at the very low relative pressure region of an isotherm [25, 32-34]. In their study, Inoue et al. [13], by calculating the adsorbed thickness for CNT with one end closed (no hysteresis), were able to measure the amount of N_2 adsorbed on

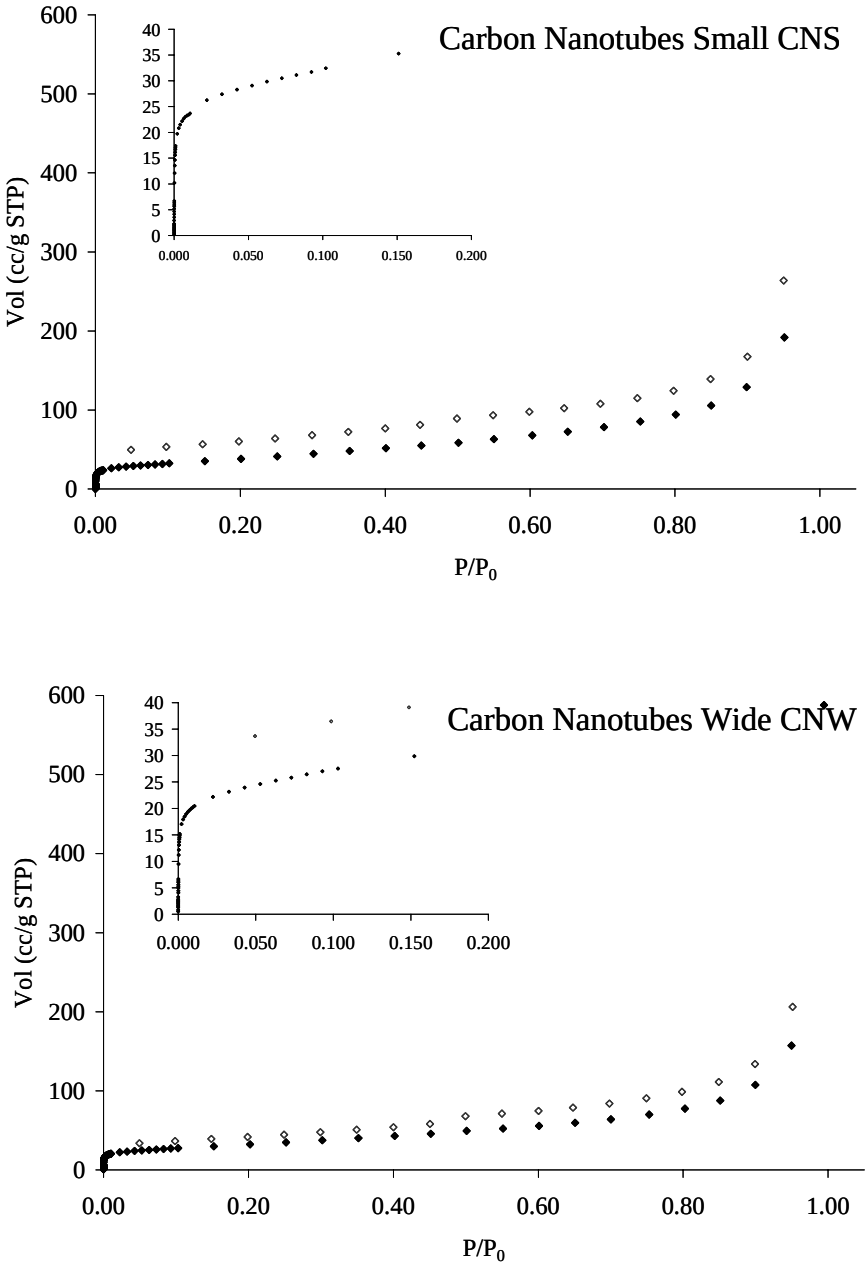

Figure 3.5. N_2 adsorption isotherms at 77K for the carbon nanotubes (CNS and CNW); solid symbols are adsorption and open symbols desorption.

the inside and the outside of the tube separately and concluded that the inner surface filled first.

The N_2 isotherms of the activated carbon and maple wood char (Figure 3.6 on the next page) contain a very pronounced initial steep slope which, displaying a

classic Type V isotherm [35] continues to rise steeply until it levels off. This adsorption behavior is indicative of sole monolayer capacity as one would expect for a microporous material with high surface area (BET SSA values of 798 and 467 m^2/g for activated carbon and maple wood char, respectively). Also, the maple wood char shows significant hysteresis, which, different from the CNT case, was attributed to swelling of the solid phase, also observed in gas and aqueous adsorption studies by Braida et al. on this material [36].

Pore size distributions for the BC materials (Table 3.2), which will be used in the following chapters along with the molecular rotational jump rate measured with ^2H NMR to calculate surface diffusivity values, were determined from the isotherms using appropriate model equations as recommended by the Autosorb manufacturer) (Quantachrome), namely, density functional theory (DFT) for micropores and Dollimore-Heal (DH) for spherical mesopores. Figure 3.7 displays pore size distribution over the micropore and mesopore ranges for the low-surface-area graphite and the CNP. The pore size distributions for soot and maple wood char were provided by other researchers, and the values only are listed in Table 3.2 with the summary distributions for all of the BCs. The low-surface-area graphite and CNP both contain predominantly micropores with size modes near 1Å and a range from 25-50Å. For the activated carbon (Figure 3.8), approximately 70% of the slit-shaped micropores are smaller than10Å in diameter, and 35% of the pore diameters are below the largest dimension for benzene, 7.7Å [38], so that at very low 4% monolayer loading of benzene-d_6 on the activated carbon sample examined in this study, it is likely that a large fraction of the adsorbed benzene molecules would be

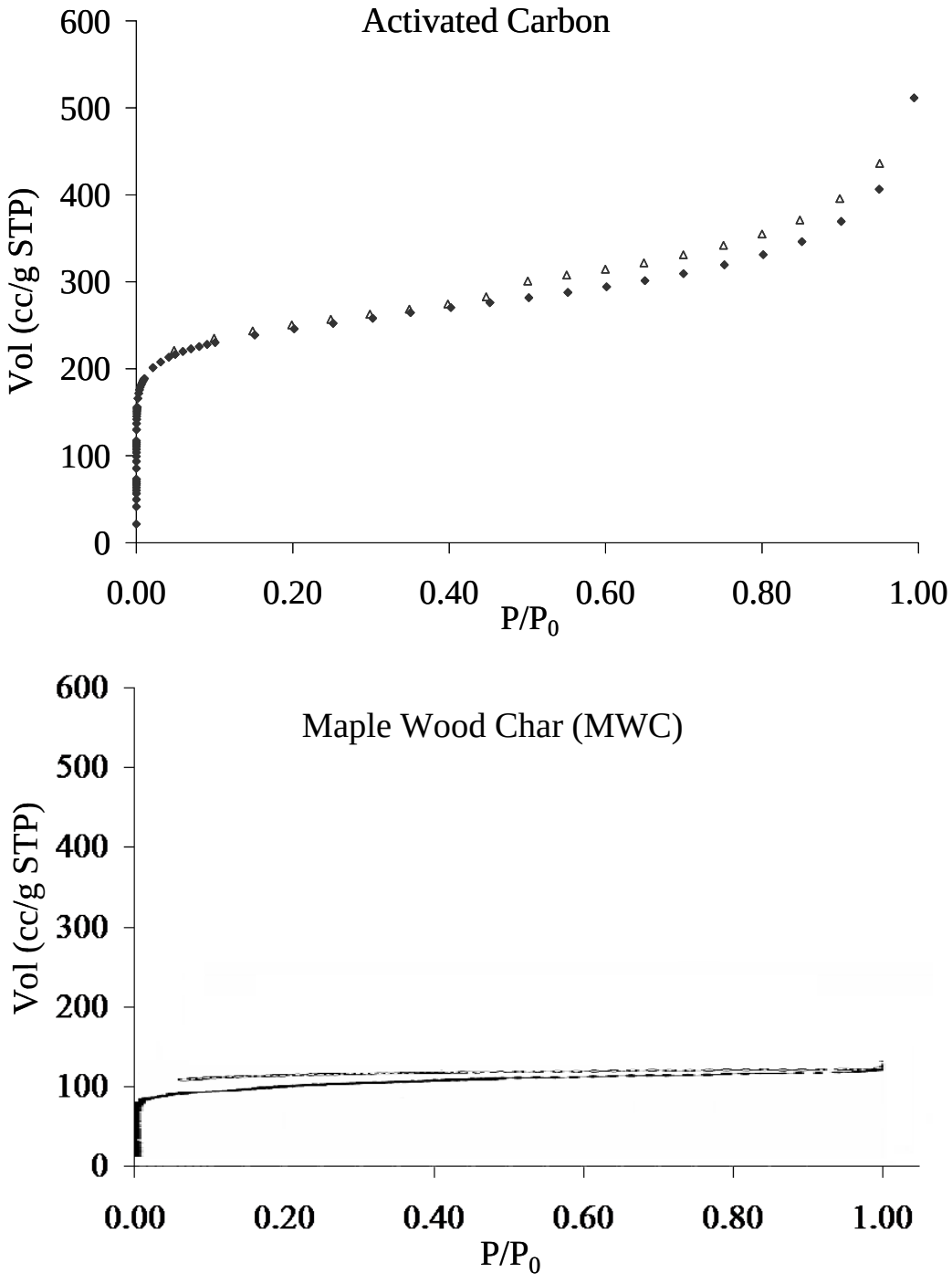

Figure 3.6. N_2 adsorption isotherms at 77K for the indicated black carbons; maple wood char isotherm (desorption is "upper" branch) modified from Braida et al. [36].

Table 3.2 Pore sizes (ml pore volume per gram solid phase) from N_2 isotherms (from this work unless specified otherwise).

	DFT Pore Diameter[a]			
Sample	< 2nm	2-5 nm	5-50 nm	Total < 5 nm
LSAG	0.001	0.003		0.003
CNP	0.025	0.050		0.074
CNS	0.031	0.073		0.104
CNW	-	-		-
Act C	0.315	0.123		0.438
Soot[c]	0.006	0.067		0.073
Maple wood char[d]	0.120	0.030	0.006	0.150

	DH Pore Diameter[b]					
Sample	< 2nm	2-5 nm	5-50 nm	Total < 5 nm	> 5 nm	Total
LSAG	0.005	0.002	0.027	0.007	0.027	0.034
CNP	0.080	0.026	1.084	0.106	1.084	1.190
CNS	0.000	0.011	0.043	0.054	1.816	1.870
CNW	0.013	0.039		0.052	0.366	0.884
Act C	-	-	-	-	-	-
Soot[c]	0.000	0.135			0.120	0.255
Maple wood char[d]	-	-	-	-	-	-

[a]Nonlocalized density functional theory used to calculate these values with fittings errors of 2-4%; [b]Dollimore-Heal algorithm used to calculate these values; [c]per Nguyen and Ball [37]; [d]estimated from Braida et al. [36].

unable to execute a full rotation. The pore size distributions for the carbon nanotubes, CNS and CNW, both look surprisingly alike (Figure 3.9). As specified in the Aldrich catalog [39], the CNS samples have internal pores which are 5-10 nm in diameter, but the DH plot is showing peaks at 2.5 nm and 4.5 nm. The size discrepancy between the measured value and the catalog value is relatively small, but, for the CNW samples, the discrepancy is much larger. The Aldrich catalog [29] describes the CNW samples as having internal diameters from 5-40 nm [39], but the DH plot also shows 2.5 nm and 4 nm. It is possible that the interiors of these tubes were clogged with residual catalyst or amorphous carbon. Similar to the results here, a related 2007 study [40] reported that a sample of MWCNTs contained an

average pore size of 38 nm as measured with the scanning electron microscope, but, by nitrogen adsorption analysis, the mean pore size was only 2.67 nm. The authors

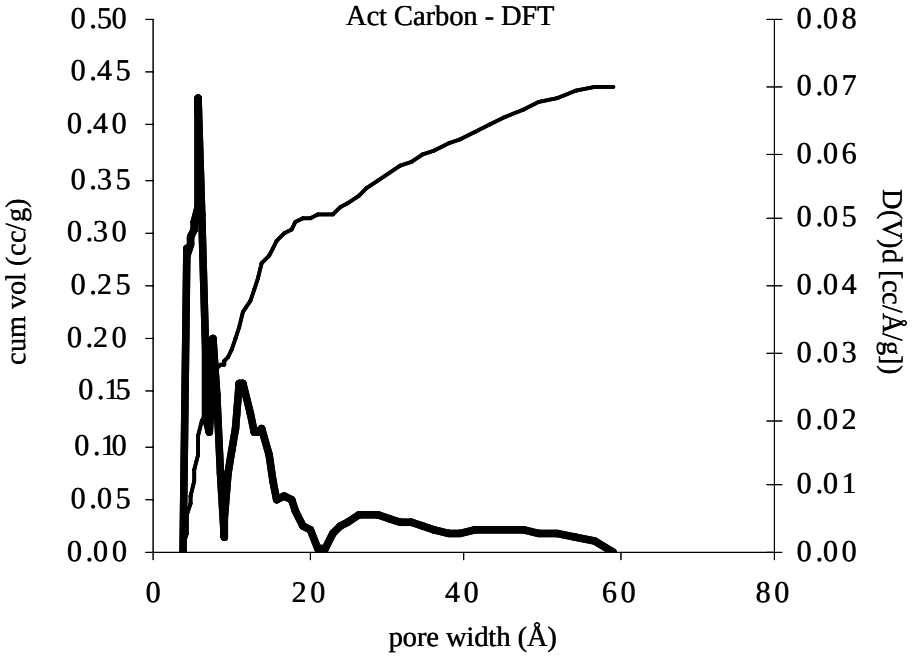

Figure 3.7. Pore size distributions from N_2 adsorption isotherms at 77K for the indicated black carbons, bold line is differential pore volume (right axis); fine line is cumulative pore volume (left axis); DFT refers to density functional theory method (recommended for slit-shaped carbon micropores); DH refers to Dollimore-Heal method (for spherical mesopores).

concluded that the visually open 38 nm pores were probably filled by material to an actual size of 2.67 nm, but the filling material was not accessible for imaging. A nitrogen isotherm was not collected for the SWCNT.

Finally, the Frankel-Halsey-Hill (FHH) equation was applied to this isotherm data to calculate the fractal dimension. As reviewed in the Introduction Chapter, the fractal dimension is a measure of the surface roughness and is thought to be connected to the distribution of high-energy adsorption sites on surfaces [41]. Rigby [42-45] in a series of papers has demonstrated a correlation between the

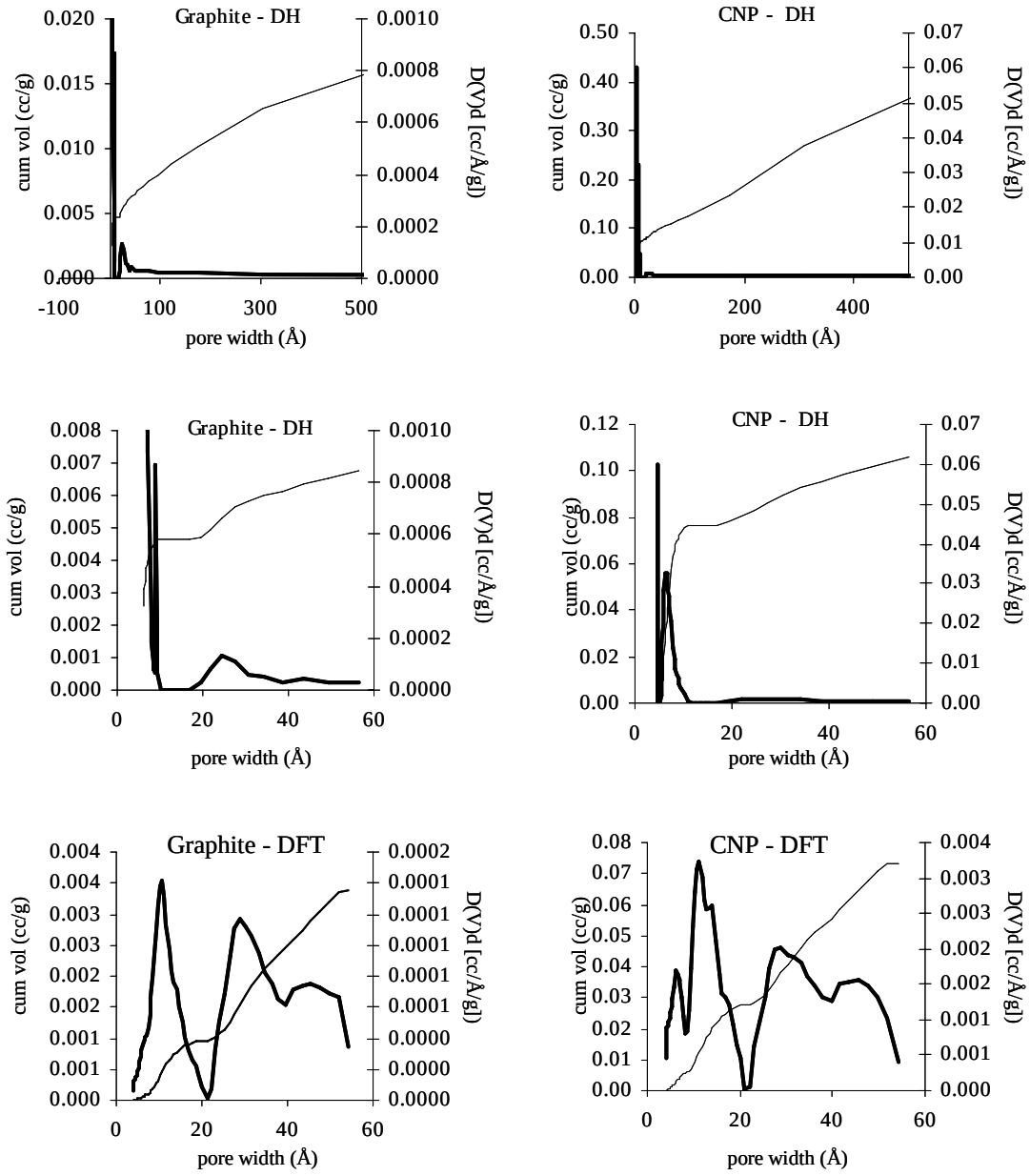

Figure 3.8. Pore size distributions from N_2 adsorption isotherms at 77K for activated carbon calculated with DFT, left axis is cumulative pore volume, right axis is differential pore volume (bold line).

fractal dimension calculated using the FHH equation on N_2 isotherms and diffusion coefficients measured using solid-state NMR. The FHH equation is:

$$\ln (V / V_m) = C + S \ln (P_0 / P) \qquad \textbf{(Eqn. 3.3)}$$

where V is volume of N_2 adsorbed, Vm is the volume of N_2 in one monolayer, P_0 is

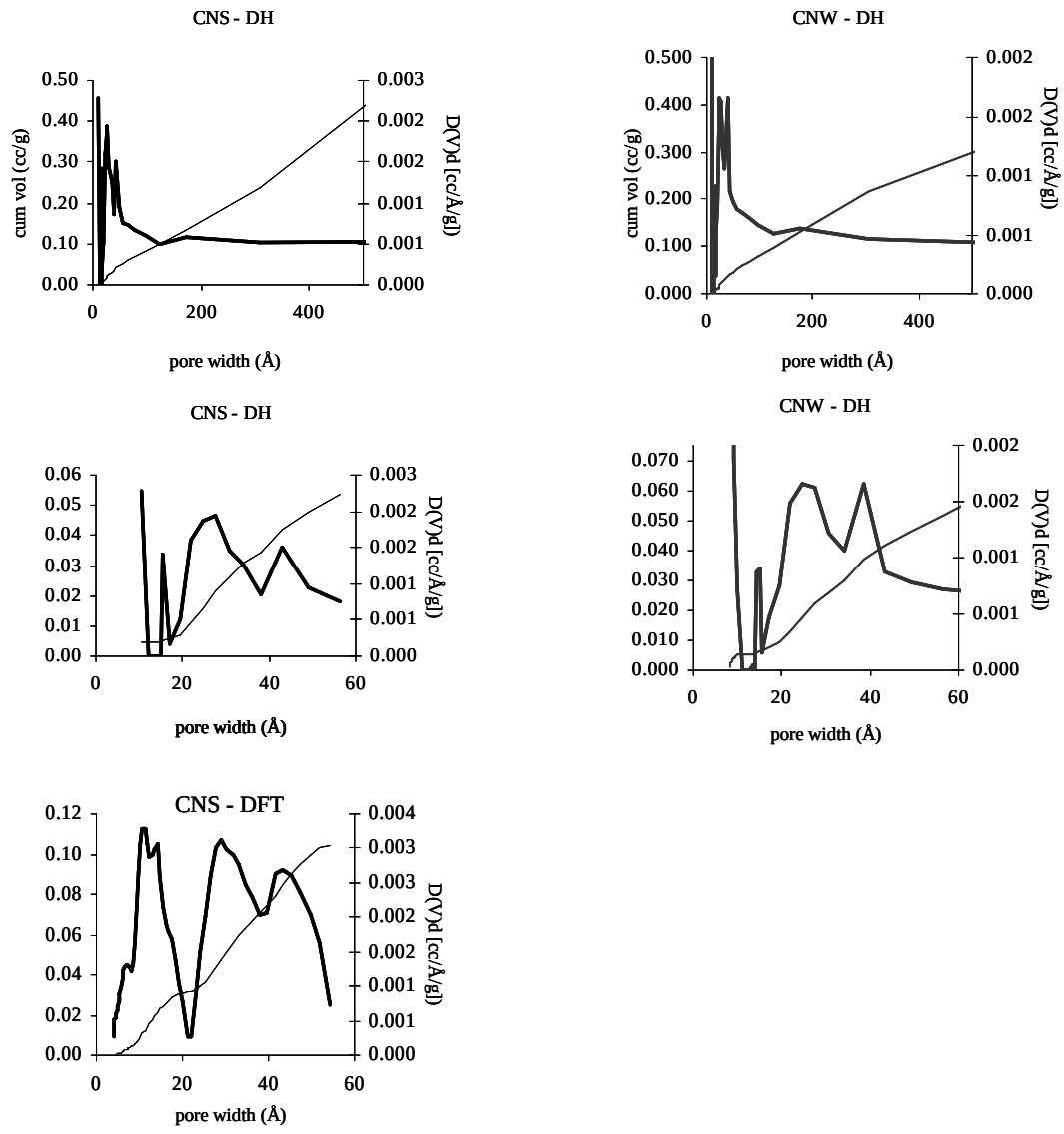

Figure 3.9. Pore size distributions from N_2 adsorption isotherms at 77K for the indicated multi-walled carbon nanotubes: bold line is differential pore volume (right axis); fine line is cumulative pore volume (left axis); DFT refers to density functional theory method (recommended for slit-shaped carbon micropores); DH refers to Dollimore-Heal method (for spherical mesopores).

the saturation pressure of N_2, P is the vapor pressure of N_2 for the given V, C is a constant, and S is a constant related to the fractal dimension, D_s, through one of the following two equations:

$$D_s = 3S + 3 \quad \text{or} \quad D_s = S + 3. \qquad \textbf{(Eqn.} \text{ 3.4, a and b)}$$

The value of the fractal dimension, by definition, must fall between 2 and 3 [46], and, if d is calculated from both equations, generally only one will be in that range. Similarly, there are two regions on the FHH plot (Figure 3.10) which, if linear, can be used to calculate a fractal dimension, one in the multilayer region (toward the left hand side) and another in the monolayer region, which is just to the right of the bend

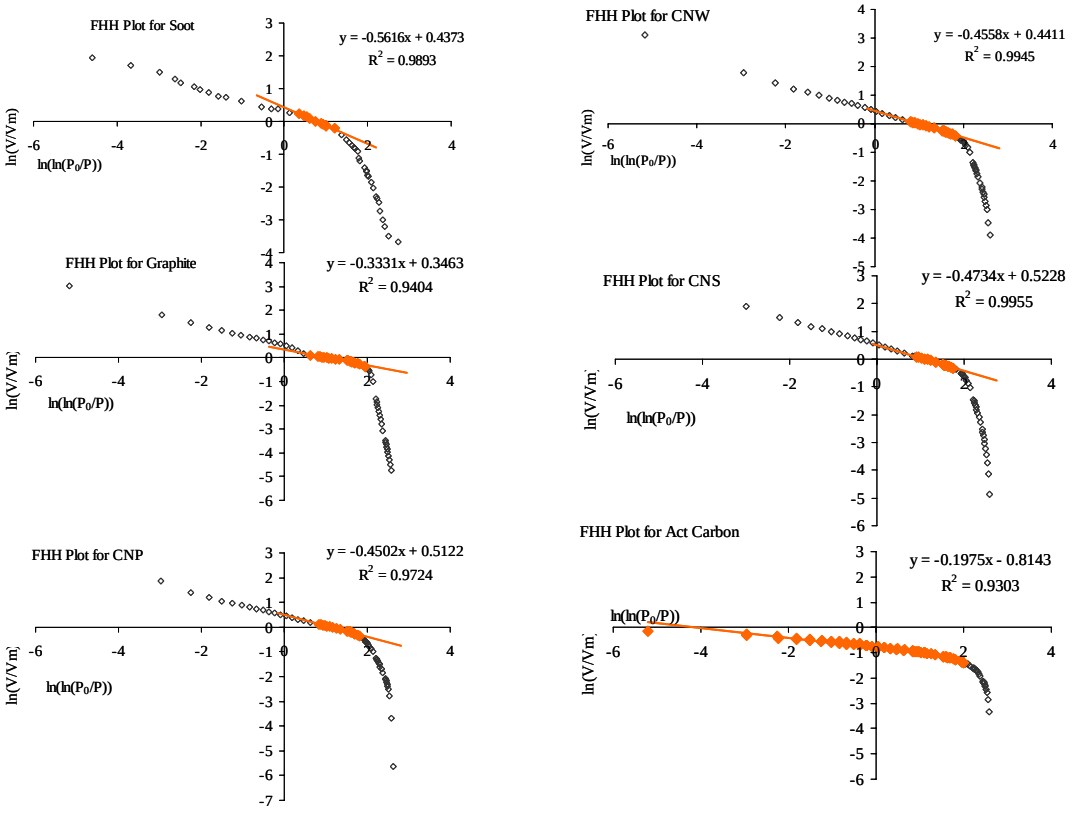

Figure 3.10. Frankel-Hill-Halsey (FHH) plots for black carbons, orange symbols with the best fit line indicate the slope for this function at an approximate monolayer. See text for discussion.

in the plot before the slope "falls off" and becomes steeply negative in the submonolayer region. While there has been some controversy as to which fractal equation (Eqn. 3.4a or 3.4b) is most applicable for a given application, and which region of the plot is most theoretically correct [47, 48], expanding the original work by [49], explains that using the monolayer region of pressures is most accurate and

that Eqn. 4(a) is applicable for van der Waals' sorption interactions and Eqn. 4(b) for sorption influenced by surface tension (cooperative adsorption or lateral interactions). Eqn. 4(a) is especially pertinent for very low coverages or for very planar, homogeneous surfaces (indicated by values for S of near -1/3).

For the fractal dimensions listed in Table 3.3, this work adhered to the above guidelines. Rigby also selected the monolayer region for calculating D_s, and he applied Eqn. 3.2b. The FHH plots (Figure 3.10) were constructed from N_2 isotherm

Table 3.3 Fractal dimensions with σ (standard deviation) for BC's measured from FHH form of the N_2 adsorption isotherm.

Solid Phase	Fractal Dimension, D_s	σ
LSAG	2.007	$\pm$0.019
CNP	2.550	$\pm$0.019
CNS	2.527	$\pm$0.010
CNW	2.544	$\pm$0.008
ActC	2.803	$\pm$0.007
Soot	2.438	$\pm$0.029

pressure data, and the monolayer volume was calculated from the BET specific surface area (SSA):

$$V_m = [SSA / (N_A * 16.2\ Å^2/\text{molecule})] * 22414\ \text{ml/mol}, \quad \textbf{(Eqn. 3.5)}$$

where 16.2 $Å^2$ is the area of one N_2 molecule, and 22414 ml/mol is the molar volume of the adsorbed gas. Except for the low-surface-area graphite, all S values were more negative than -1/3, and Eqn. 3.4(b) was used to calculate D_s. The S value for the low-surface-area graphite was -0.3331; therefore, Eqn. 3.2(a) was used; and, as one would expect for graphite, the D_s value was 2.007 ($\pm$0.01),

indicating a very planar homogeneous surface. Comparison of the fractal dimensions results above to the ^{2}H NMR correlation times in light of Rigby's results, which were mentioned above and in the Introduction Chapter, first requires presentation and discussion of the ^{2}H NMR spectra and analysis. Therefore, this discussion will be presented in Chapter 9, "Comparison of the Motion of the Benzene on the Surface of Different Black Carbons".

3.4 SUMMARY

The X-ray diffractograms of the BC materials in this study showed three samples with ordered crystalline graphitic structures: the low-surface-area graphite and the two carbon nanotube samples. The X-ray diffractograms of the other samples indicated disordered graphitic domains. The N_2 isotherms were mainly S-shaped, except the activated carbon and maple wood char samples, which were almost entirely concave down in shape, indicating a predominance of microporosity. The low-surface-area graphite contained very little porosity (0.034 ml pore space/g solid), predominantly (90%) mesoporous in size and presumably entirely intergranular. The carbon nanoparticles contained micropores (30%) and mesopores, and the multi-walled carbon nanotubes had pore size maxima at 2.5 nm and 4 nm (small mesopores). The FHH plots of the N_2 adsorption isotherms all presented linear slopes in the monolayer adsorption region, and, while the low-surface-area graphite sample had a fractal dimension of 2.007 ($\pm$0.019), the other samples displayed intermediate values. The results of the characterization experiments presented in this chapter will be used to interpret the motion of benzene molecules on these phases, as observed with ^{2}H NMR solid-state spectroscopy, in succeeding chapters.

References

1. Hristea, G.; Budrugeac, P., Characterization of exfoliated graphite for heavy oil sorption. *Journal of Thermal Analysis and Calorimetry* **2008,** *91*, (3), 817-823.
2. Fodi, B.; Hentschke, R., Molecular dynamics simulation of a binary hydrocarbon mixture near an adsorbing wall: benzene/I-heptane on graphite. *Langmuir* **1998,** *14*, 429-437.
3. Do, D. D.; Do, H. D., Characterization of micro-mesoporous carbonaceous materials. Calculations of adsorption isotherm of hydrocarbons. *Langmuir* **2002,** *18*, 93-99.
4. Kruk, M.; Li, Z.; Jaroniec, M., Nitrogen adsorption study of surface properties of graphitized carbon blacks. *Langmuir* **1999,** *15*, 1435-1441.
5. Chakarova-Kack; Schroder, S. D.; Lundqvist, E.; I, B.; Langreth, D. C., Application of van der Waals density functional to an extended system: adsorption of benzene and naphthalene on graphite. *Physical Review Letters* **2006,** *96*, 146107.
6. Do, D. D.; Do, H. D., Modeling of adsorption on nongraphitized carbon surface: GCMC simulation studies and comparison with experimental data. *Journal of Physical Chemistry B* **2006,** *110*, 17531-17538.
7. Dubinin, M. M.; Polyakov, N. S.; Kadlez, O.; Kataeva, L. I.; Petukhova, G. A., Heterogeneous microporous structures and adsorption properties of carbon adsorbents. 12.* Porous structure and adsorption properties of active carbons. *Russian Chemical Bulletin* **1993,** *42*, (8), 1304-1308.
8. Jaroniec, M.; Madey, R., A comprehensive theoretical description of physical adsorption of vapors on heterogeneous microporous solids. *Journal of Physical Chemistry* **1989,** *93*, 5225-5230.
9. Fletcher, A. J.; Uygur, Y.; Thomas, K. M., Role of surface functional groups in the adsorption kinetics of water vapor on microporous activated carbons. *Journal of Physical Chemistry C* **2007,** *111*, 8394-8399.
10. Yoon, T. H.; Benzerara, K.; Ahn, S.; Luthy, R. G.; Tyliszczak, T.; Brown, G. E., Jr., Nanometer-scale chemical heterogeneities of black carbon materials and their impacts on PCB sorption properties: soft X-ray spectromicroscopy study. *Environmental Science & Technology* **2006,** *40*, 5923-5929.
11. Schaeffer, W. D.; Smith, W. R.; Polley, M. H., Structure and properties of carbon black. *Industrial and Engineering Chemistry* **1953,** *45*, (8), 1721-1725.
12. Krishnankutty, N.; Vannice, M. A., Effect of pretreatment on surface area, porosity and adsorption properties of a carbon black. *Chemistry of Materials* **1995,** *7*, 754-763.
13. Inoue, S.; Ickikuni, N.; Suzuki, T.; Uematsu, T.; Kaneko, K., Capillary condensation of N_2 on multiwall carbon nanotubes. *Journal of Physical Chemistry B* **1998,** *102*, 4689-4692.
14. Nguyen, T. X.; Bhatia, S. K., Probing the pore wall structure of nanoporous carbons using adsorption. *Langmuir* **2004,** *20*, 3532-3535.
15. Mordkovich, V. Z., The observation of large concentric shell fullerenes and fullerene-like nanoparticles in laser pyrolysis carbon blacks. *Chem. Mater.* **2000,** *12*, 2813-2818.
16. Wang, G.; Yang, J.; Park, J.; Gou, X.; Bei, W.; Liu, H.; Yao, J., Facile synthesis and characterization of graphene nanosheets. *Journal of Physical*

Chemistry C **2008,** *112*, 8192-8195.
17. Diaz, E.; Ordonex, S.; Vega, A., Adsorption of volatile organic compounds onto carbon nanotubes, carbon nanofibers, and high-surface-area graphites. *J. Colloid and Interface Science* **2007,** *305*, 7-16.
18. Wang, J.; Yin, G.; Shao, Y.; Wang, Z.; Gao, Y., Investigation of further improvement of platinum catalyst durability with highly graphitized carbon nanotubes support. *Journal of Physical Chemistry C* **2008,** *112*, (15), 5784-5789.
19. Kaneko, K.; Suzuki, T.; Kakei, K., Phase transition of N_2 molecules filled in micropores of micrographitic carbons. *Langmuir* **1989,** *5*, 879-881.
20. Vix-Guterl, C.; Couzi, M.; Dentzer, J.; Trinquecost, M.; Delhaes, P., Surface characterizations of carbon multiwall nanotubes; comparison between surface active sites and Raman spectroscopy. *Journal of Physical Chemistry B* **2004,** *108*, 19361-19367.
21. Yoon, S. B.; Chai, G. S.; Kang, S. K.; Yu, J.-S.; Gierszal, K. P.; Jaroniec, M., Graphitized pitch-based carbons with ordered nanopores synthesized by using colloidal crystals as templates. *Journal of the American Chemical Society Communications* **2005,** *127*, 4188-4189.
22. Connan, H. G.; Reedy, B. J.; Marshall, C. P.; Wilson, M. A., New nanocarbons: rod milling and annealing of graphite in the presence of yttrium. *Energy and Fuels* **2004,** *18*, 1607-1614.
23. Isirikyan, A. A.., Kiselev, A. V., The absolute adsorption isotherms of vapors of nitrogen, benzene and *n*-hexane, and the heats of adsorption of benzene and *n*-hexane on graphitized carbon blacks. I. graphitized thermal blacks. *Journal of Physical Chemistry* **1962,** *65*, (4), 601-607.
24. Furmaniak, S.; Terzyk, A. P.; Gauden, P. A.; Rychlicki, G., Simple models of adsorption in nanotubes. *Journal of Colloid and Interface Science* **2006,** *295*, 310-317.
25. Gregg, S. J.; Sing, K. S. W., *Adsorption, Surface Area, and Porosity*. Academic Press: New York, NY, 1982.
26. Quantachrome, *Users Manual*.
27. Choma, J.; Jaroniec, M.; Burakiewicz-Mortka, W.; Kloske, M., Critical appraisal of classical methods for determination of mesopore size distributions of MCM-41 materials. *Applied Surface Science* **2002,** *196*, 216-223.
28. Sakintuna, B.; Yurum, Y., Evolution of carbon microstructures during the pyrolysis of Turkish Elbistan lignite in the temperature range 700-1000°C. *Energy and Fuels* **2004,** *18*, 883-888.
29. Sigma-Aldrich Chemical Company Online Catalog: http://www.sigmaaldrich.com/technical-service-home/product-catalog.html, (2009).
30. Sanyal, S. K.; Samantaray, B. K.; Mitra, G. B., X-ray diffraction studies on the arrangement of atoms in carbon blacks. I. Results of radial distribution analysis. *Acta Crystallographica* **1982,** *A38*, 333-336.
31. Nguyen, T. H.; Brown, R. A.; Ball, W. P., An evaluation of thermal resistance as a measure of black carbon content in diesel soot, wood char, and sediment. *Organic Geochemistry* **2004,** *35*, 217-234.
32. Inoue, S.; Hanzawa, Y.; Kaneko, K., Prediction of hysteresis disappearance in the adsorption isotherm of N_2 on regular mesoporous silica. *Langmuir* **1998,** *14*, 3079-3081.

33. Ustinov, E. A.; Do, D. D., Modeling of adsorption in finite cylindrical pore by means of density functional theory. *Adsorption* **2005,** *11*, 455-477.
34. Mackie, E. B.; Wolfson, R. A.; Arnold, L. M.; Lafdi, K.; Migone, A. D., Adsorption studies of methane films on catalytic carbon nanotubes and on carbon filaments. *Langmuir* **1997,** *13*, 7197-7201.
35. Adamson, A.; Gast, A. P., *Physical Chemistry of Surfaces*. John Wiley & Sons: New York, 1997; p 784.
36. Braida, W. J.; Pignatello, J. J.; Lu, Y.; Ravikovitch, P. I.; Neimark, A. V.; Xing, B., Sorption hysteresis of benzene in charcoal particles. *Environmental Science & Technology* **2003,** *37*, 409-417.
37. Nguyen, T. H.; Ball, W. P., Absorption and adsorption of hydrophobic organic contaminants to diesel and hexane soot. *Environmental Science & Technology* **2006,** *40*, 2958-2864.
38. Webster, C., Edwin; Drago, R. S.; Zerner, M. C., Molecular dimensions for adsorptives. *Journal of the American Chemical Society Communications* **1998,** *120*, 5509-5516.
39. Sigma-Aldrich Chemical Company Online Catalog: http://www.sigmaaldrich.com/technical-service-home/product-catalog.html, (2009).
40. Smajda, R.; Kukovecz, A.; Konya, Z.; Kiricsi, I., Structure and gas permeability of multi-wall carbon nanotube buckypapers. *Carbon* **2007,** *45*, 1176-1184.
41. Avnir, D.; Farin, D.; Pfeifer, P., Chemistry in noninteger dimensions between two and three. II. Fractal surfaces of adsorbents. *Journal of Chemical Physics* **1983,** *79*, (7), 3566-3571.
42. Rigby, S. P., Fractal theory for the compensation effect observed in a surface diffusion process studied using deuteron NMR. *Langmuir* **2002,** *18*, 1613-1618.
43. Rigby, S. P., A model for the surface diffusion of molecules on a heterogeneous surface. *Langmuir* **2003,** *19*, 364-376.
44. Rigby, S. P., NMR and modelling studies of structural heterogeneity over several length scales in amorphous catalyst supports. *Catalysis Today* **1999,** *53*, 207-223.
45. Rigby, S. P., Predicting surface diffusivities of molecules from equilibrium adsorption isotherms. *Colloids and Surfaces A: Physicochem. Eng. Aspects* **2005,** *262*, 139-149.
46. Pfeifer, P.; Avnir, D., Chemistry in noninteger dimensions between two and three. I. Fractal theory of heterogeneous surfaces. *Journal of Chemical Physics* **1983,** *79*, (7), 3558-3565.
47. Jaroniec, M., Evaluation of the fractal dimension from a single adsorption isotherm. *Langmuir* **1995,** *11*, 2316-2317.
48. Tang, P.; Chew, N. Y. K.; Chan, H.-K.; Raper, J. A., Limitation of determination of surface fractal dimension using N2 adsorption isotherms and modified Frenkel-Halsey-Hill theory. *Langmuir* **2003,** *19*, 2632-2638.
49. Ismail, M. K. I.; Pfeifer, P., Fractal analysis and surface roughness of nonporous carbon fibers and carbon blacks. *Langmuir* **1994,** *10*, 1532-1538.

CHAPTER 4. THE MOTION OF BENZENE-d_6 MOLECULES DIFFUSING ON THE SURFACE OF DIESEL SOOT AT VARIABLE TEMPERATURES AND LOADINGS

4.1 INTRODUCTION

Diesel soot is a key black carbon (BC) in the environment in both atmospheric and aqueous settings [1-3], comprising, for example, over 20% of the particulate carbon in Los Angeles [2], and acting as (1) a transport agent for sorbed environmental contaminants, such as polyaromatic hydrocarbons (PAHs) [4, 5], a (2) catalyst for atmospheric reactions, such as those involving NO_x [6], (3) an agent of both global warming (by enhanced infrared radiation at the surface) and global cooling (by radiation dampening) [7, 8], and (4) a biological toxin in itself [9, 10]. Sorption to the soot surface, which can be a function of aging [2, 11, 12], is an important, but poorly understood, step in any of these processes [13-16], and this study will focus on benzene-d_6 vapor sorbed to a diesel soot surface. The soot examined in this study, the National Institutes of Standards (NIST) Standard Reference Material (SRM) #2975 diesel soot, is the most frequently used referenced material by researchers on BC in the environment [5, 13, 17-20].

Sorbate/sorbent interactions can be studied in the vapor phase without effects from hydrophobicity and solvent interactions [21, 22], and, further, for soot, in particular, vapor phase sorption is an important atmospheric process [3, 7, 23]. Because diesel soot is the result of the incomplete oxidation of hydrocarbon vapors [24], newly condensed soot particles would be formed in close association with aromatic hydrocarbons in the vapor phase, which, upon sorption to the soot surface, could subsequently be transported across environmental settings by wind or water

[7, 16, 24]. Important recent work on the vapor phase sorption of benzene to soot includes (1) an inverse gas chromatographic analysis by Schwarzenbach's group [25] that measured the Henry's law constant on Soot #2975 to be $10^{-5.23}$ m^3/m^2, and also (2) the measurement by Aubin and Abbatt [16] of 37.5 kJ/mol for the $\Delta H_{adsorption}$ of benzene on *n*-hexane soot by from variable temperature isotherm measurements collected with a mass spectrometer fitted with a custom inlet probe. Both of these studies interpreted the results in terms of existing linear free energy relationship (LFER) frameworks, based on the assumption that benzene-soot interactions involved primarily dispersion forces between the aromatic π-electrons of benzene and the aromatic π-electrons of graphite as the model solid phase [20, 26-33], as reviewed in Chapter 1.

Adsorption interactions can be studied by analyzing the motion of the benzene sorbate molecules by spectroscopic observation of the rotation of adsorbed benzene molecules [34-41]. While this is the first such study of benzene on soot, the motion of benzene adsorbed to a graphitized carbon black, has been observed by Boddenberg's group using ^{2}H NMR, ^{1}H NMR, and pulsed-field gradient NMR [30, 38, 42]. Even at temperatures well below the freezing point of benzene (5.5^{o}C), a rapid isotropic reorientation of benzene molecules was indicated by the Lorentzian shape of the observed spectra [38, 43]. The Boddenberg group interpreted their results by assuming that the benzene was adsorbed in a planar configuration on the surface of the graphite (which would allow π-π interaction and a rapid C_6 rotation) and moved laterally (surface diffusion) across the spherically shaped grains and pores of the graphite solid [38, 44, 45]. Therefore, they hypothesized that the

spherical shape of the solid grains or pores guided the translational motion of the benzene molecule to produce a pseudoisotropic peak within the laboratory frame of reference of the NMR detector [38, 42].

In this chapter, the results of static solid-state ^{2}H NMR spectra of benzene-d_6 adsorbed at submonolayer loadings on NIST #2975 diesel soot at temperatures from 50°C to -75°C will be presented and compared with the results for graphitized carbon black in order to characterize the molecular motion of benzene on the surface on soot, measure the activation energy (E_a) for comparison with the motion of benzene adsorbed on other solid phases, and to confirm the validity of graphite as a model for BC's. In addition, by examining variations E_a and pre-exponential factor (D_0) for surface diffusivity at different loadings, these experiments probed the surface heterogeneity of the soot and provided insight into the adsorption interactions and molecular orientations of the benzene on the soot surface. Also, by examining one of the samples at different ages over a period of approximately one year, possible effects of aging were monitored.

4.2 EXPERIMENTAL

4.2.1 Materials and Sample Preparation

The soot material examined was NIST SRM #2975 diesel soot. As detailed in the NIST Certificate of Analysis [46], the soot was collected by filtering the exhaust from diesel-powered forklifts. The soot has been extensively characterized previously [16, 17, 19, 20, 24], and the physical and chemical characteristics are detailed in Table 4.1. The specific surface area was determined using the Brunauer-Emmett-Teller (BET) equation, and the pore size distributions were determined using the Barrett-Joyner-Halenda (BJH) equation applied to N_2 adsorption isotherm

Table 4.1. Characteristics of diesel soot (NIST SRM #2975)

wt % Carbon[a]	wt % Other[a]	[Ca] (ppm)[b]	Surface Area (m^2/g)[c]	Pore Size Range (nm)[c]	Pore Size Mode (nm)[c]	Particle Size Mean Dia. (μm) Vol Distr[c]	L_c (nm)[d]	Fractal Dimension, d[d]
87.2	1.3 % H 7.0 % O	249	91	4-35	20	31.9	2	2.3895

[a][17]; [b]Galbraith Laboratories; [c][47], [d]Chapter 3.

data [18, 47]. The fractal dimension shown in Table 4.1 was calculated by application of the Frenkel-Hill-Halsey equation to the N_2 isotherm data of Nguyen et al. [18], as detailed in Chapter 3. Additional characterization of the chemistry of the soot was accomplished by obtaining the X-ray diffraction (XRD) spectra, also detailed in Chapter 3. The XRD spectrum revealed that the soot contains poor graphitic crystallinity, as indicated by the broad peak in the graphite region (Figure 3.1) at $d_{002} = 0.37 \pm 0.01$ nm, and the small value of L_c, the crystallite dimension (Tables 3.1 and 4.1).

The molecular motion of benzene-d_6 adsorbed onto soot was observed using static solid-state ^2H NMR at three different submonolayer loadings. Four individual samples of Soot #2975 were loaded with benzene-d_6 at submonolayer coverages, 4%, 35% (in duplicate), and 68% , as detailed in Table 4.2.

4.2.2 NMR Analysis and Quantitative Calibration for Soot Samples

The samples were flame-sealed as outlined in the Chapter 2, and then they were taken to the Oklahoma Statewide NMR Facility at Stillwater, Oklahoma, and analyzed with the 300-MHz Chemagnetics solid-state NMR instrument. Briefly, the procedure was performed as follows. The solid phase was placed into a preweighed specially necked 10 mm dia. NMR tube, which was subsequently attached to a

Table 4.2. Samples of Benzene-d_6 on NIST #2975 Soot

Sample Name	Mass of Soot[a] (mg)	Volume of Benzene[b] (μl)	% load (w/w)	% loading (monolayer coverage)[c,d]
Soot1	54.8±0.1	0.59±0.01	1.0[e]	35±1
Soot2	61.9±0.1	0.09±0.09[f]	0.1[f]	4±4[f]
Soot3	55.0±0.1	1.16±0.02	2.1[e]	68±2
Soot4	68.7±0.1	0.74±0.01	1.0[e]	35±1

[a]Uncertainty noted is the smallest increment on the balance; [b]uncertainty in the amount of benzene loaded is 1.7%, as detailed in Chapter 2; [c]value of cross-sectional area of a benzene molecule used to calculate a monolayer is 43Å^2 [48]; [d]uncertainty in monolayer loading is the uncertainty shown for the % w/w loading plus an additional uncertainty in the surface area measurement as reported by NIST, which is estimated to display a variability of 1%, based on our experience with the Autosorb Surface Analysis instrument; [e]uncertainty is 1-2 orders of magnitude less than the rounded value shown; [f]see text for explanation of Soot2 % loading calculations.

vapor deposition manifold using an 6 mm Ultra-torr connection. After initial evacuation of gases and vapor in the sample to 0.001 torr, a precise amount of benzene-d_6 was quantitatively condensed into the NMR tube, which was submerged in liquid nitrogen. The sample was subsequently backfilled with N_2 gas to 300 (±100) torr and flamed-sealed so that the final dimensions of the sample were 10 mm dia. x 2.2 cm long in order to fit into the coil of the NMR.

Variable-temperature spectra solid-state ^{2}H NMR spectra of the Soot1 sample were collected over a period of almost one year to assess the effect of aging on the molecular motion of the soot-sorbed benzene-d_6. Spectra of the other samples were all collected within a few days after sealing. Solid-state ^{2}H NMR spectra were collected with a quadrupole echo sequence ($\pi/2 - \tau_{echo} - \pi/2 - \tau_{echo}$ – acquire) at 46.20525 MHz using both 20 μs and 40 μs τ_{echo} values. Except for those spectra collected for the benzene-d_6 NMR quantitation procedure in Chapter 2,

relaxation delays were 0.25 s or 0.5 s. Spectra were collected with either 1024 or 8192 data points and processed without line broadening, zero filling to 8192 data points as needed. The experimental spectra were fit using the Deuterium Fitting Program (DFP) to libraries of simulated spectra constructed over the reorientational jump rate range of 1 x 10^5 rad/s to 1 x 10^7 rad/s with 400 increments created with the Library Creation Program (LCP) and Deuterium Motional Simulation (DMS) for isotropic jump motions between the 32 faces and vertices of an icosahedron (all-sites-exchange) [49].

NMR quantitation for the amount of benzene-d_6 on each sample was examined in greater detail for the soot samples than for the other BC solid sample sets. Therefore, instead of relying on the standard calibration curve, described in the Chapter 2, which used 10.0 s relaxation delays and only 20 scans, an NMR quantitation plot was prepared exclusively for the soot samples from spectra collected with short 0.25-0.50 s relaxation delays and 3600 scans (Table 4.3) The use of these shorter relaxation delays was possible because the T_1 value for the soot-sorbed benzene on the Soot1 sample was measured to be 0.37ms, much less than 20% of the relaxation delays. The T_1 measurement was performed using inversion recovery with the quadrupole pulse echo sequence used to observe the signal. The quantitation plot of the benzene-d_6 loaded on the soot samples vs. NMR signal area (Figure 4.1) is linear, and this, along with an acceptable position of the Soot1 NMR Table 4.3. NMR quantitation for soot samples at different temperatures quantitation on the more general NMR calibration plot in Chapter 2 (Figure A1.4), provides assurance that the loading values calculated for the samples are accurate. Soot2 was originally loaded with 1.32 μl, but the low NMR signal intensity indicated that most

Table 4.3. NMR Quantitation for Soot Samples at Different Temperatures, 40μs-tau Spectra[a]

Sample	Vol of Benzene (μl)	% loading (w/w) / % nominal monolayer (ML)	estimate of minimal % benzene-d_6 on soot surface[b]	Temperature of Spectrum (^oC)[c]	NMR Area[d] (Arbitrary Units)	Number of Scans	Age of Sample (days)
Soot2	0.09±0.09	0.1% w/w	92%	5	13.2±0.7	28800	1
Soot2		4% ML	100%	-25	13.1±0.7	28800	1
Soot2			100%	-35	12.5±0.6	28800	1
Soot1	0.59±0.01	1.0%	95%	15	4.8±0.2	3600	306
Soot1		34% ML	98%	-5	4.5±0.2	3600	306
Soot1			99%	-15	4.4±0.2	3600	306
Soot1			100%	-25	4.7±0.2	3600	291
Soot1			100%	-35	4.5±0.2	3600	291
Soot4	0.74±0.01	1.0%	92%	25	7.7±0.4	3600	1
Soot4		34% ML	95%	15	7.6±0.4	3600	1
Soot4			98%	0	7.6±0.4	3600	1
Soot4			98%	-5	7.7±0.4	3600	1
Soot4			99%	-15	7.7±0.4	3600	1
Soot4			100%	-25	7.6±0.4	3600	1
Soot3	1.16±0.02	2.1%	92%	25	11.2±0.6	3600	1
Soot3		68% ML	99%	-15	12.3±0.6	3600	1
Soot3			100%	-35	11.8±0.6	3600	1

[a]All spectra were collected with 40μs echo spacing and 0.25-0.50s relaxation delay, which is greater than 5 times measured T_1 of 0.37ms, ensuring that no deuterons remained unobserved due to signal oversaturation; [b]see text for explanation; [c]uncertainty in temperature ±0.1°C; [d]uncertainty in NMR area estimated at 5%.

of the sample benzene-d_6 was apparently lost, presumably during sealing. Therefore, the volume of benzene in that sample was estimated by comparing the signal-to-noise ratio (S/N) of a ^{2}H NMR spectrum of Soot 1 (which had been quantified on Figure 2.4, as mentioned above) to the S/N of a ^{2}H NMR spectrum of Soot2 collected under the same conditions, namely, 7200 scans at 25°C using a 40μs τ_{echo} spacing. The S/N of the Soot1 spectrum was 6.3 times the S/N of the Soot2 spectrum, and, thus, Soot1 contains 6.3 times as much benzene as Soot2, thus estimated to be 0.09 ml (±100%).

Table 4.3 also lists the percentage of benzene adsorbed onto the soot surface for each sample at the indicated temperature. These values were calculated with the

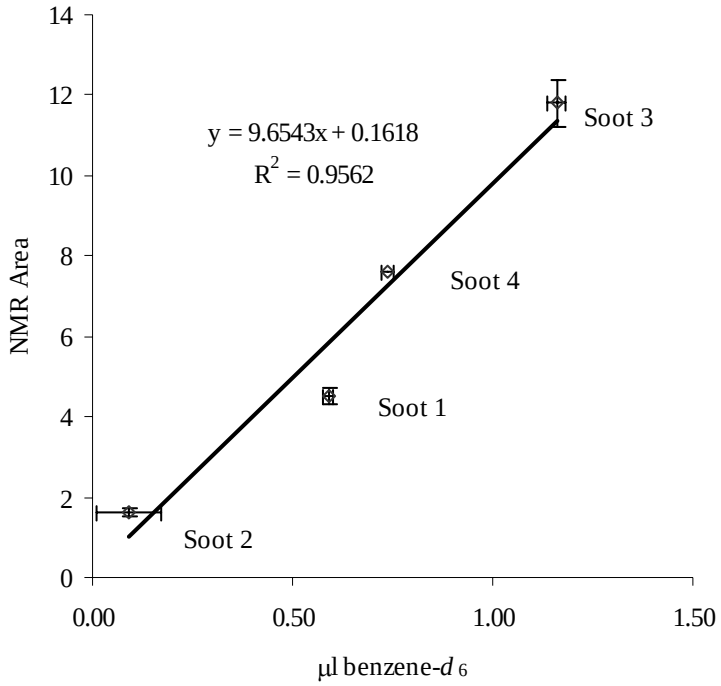

Figure 4.1. NMR quantitation plot for benzene-d_6 on soot samples from 3600-scan spectra (variable loaded samples).

experimentally measured Henry's law constant, $K_{soot/air}$, at 15°C of $10^{-5.23}$ m^3/m^2 [19] for benzene on #2975 diesel soot and Eqn. 4.1:

$$K_{soot//air} = (C_{soot} / C_{air}) = (M_{soot} / SA_{soot}) / (M_{air} / V_{air}) \qquad \textbf{(Eqn. 4.1) [19].}$$

C represents the concentration of benzene-d_6, *M* moles of benzene, *SA* soot surface area in m^2, *V* volume of air in m^3 (actually N_2 gas in these samples), and the sum of M_{soot} and M_{air} is the total number of moles of benzene-d_6 loaded at the time of sealing. Even estimating that the soot itself occupies zero volume and disregarding possible sorption to the surface of the glass tube, at least 95% of the benzene is sorbed to the soot surface at 15°C. The surface percentages at temperatures other than 15°C were calculated per Goss and Schwarzenbach [50], using a modified van't Hoff equation:

$$\ln K_{soot\text{-}air}(T_2) = \ln K_{soot\text{-}air}(288K) + (\Delta H_{adsorption\text{-}soot/air} + RT_a / R)$$

x (1/288K $1/T_2$) (**Eqn.** 4.2) [50].

The value of $\Delta H_{adsorption\text{-}soot/air}$ (which is assumed to be constant over the range of temperatures and loadings) inserted into this equation when compiling Table 4.3 was calculated using the authors' LFER (**Eqn.** 4.2a below), obtained by them from regression analysis of mineral and organic surfaces, which related adsorption enthalpy to the Henry's law constant:

$$\Delta H_{adsorption\text{-}soot/air} = -4.17 \ln K_{soot/air} - 88.1 \quad \text{(Eqn. 4.2a) [50].}$$

The value obtained with Eqn 4.2a for $\Delta H_{adsorption\text{-}soot/air}$ is 37.9 ($\pm$2.6) kJ/mol, which is very close to the value of 37.5 ($\pm$2.2) kJ/mol obtained experimentally by Aubin and Abbatt for benzene on *n*-hexane soot [16].

4.3 ^{2}H NMR SPECTRA AND SIMULATED FIT RESULTS

The samples of soot loaded with 1% w/w benzene-d_6 were examined in greater detail than the other two loadings. The 1%-loaded Soot1 sample was examined for motional changes of the sorbed benzene-d_6 molecules with aging by collecting variable temperature spectra at three different ages over the period of approximately one year. Also, a duplicate 1% sample (Soot4) was prepared and analyzed at age 1-2 days with variable temperature spectra. Therefore, the results for the 1% loaded samples will be examined in detail before considering, in Section 4.3.3, the other two samples (Soot2 and Soot3), which were prepared at different loadings of benzene-d_6.

4.3.1 ^{2}H NMR spectra for 1% w/w loading

4.3.1.1. Type of motion

The ^{2}H NMR spectra of benzene-d_6 adsorbed at 1% w/w loading on sample

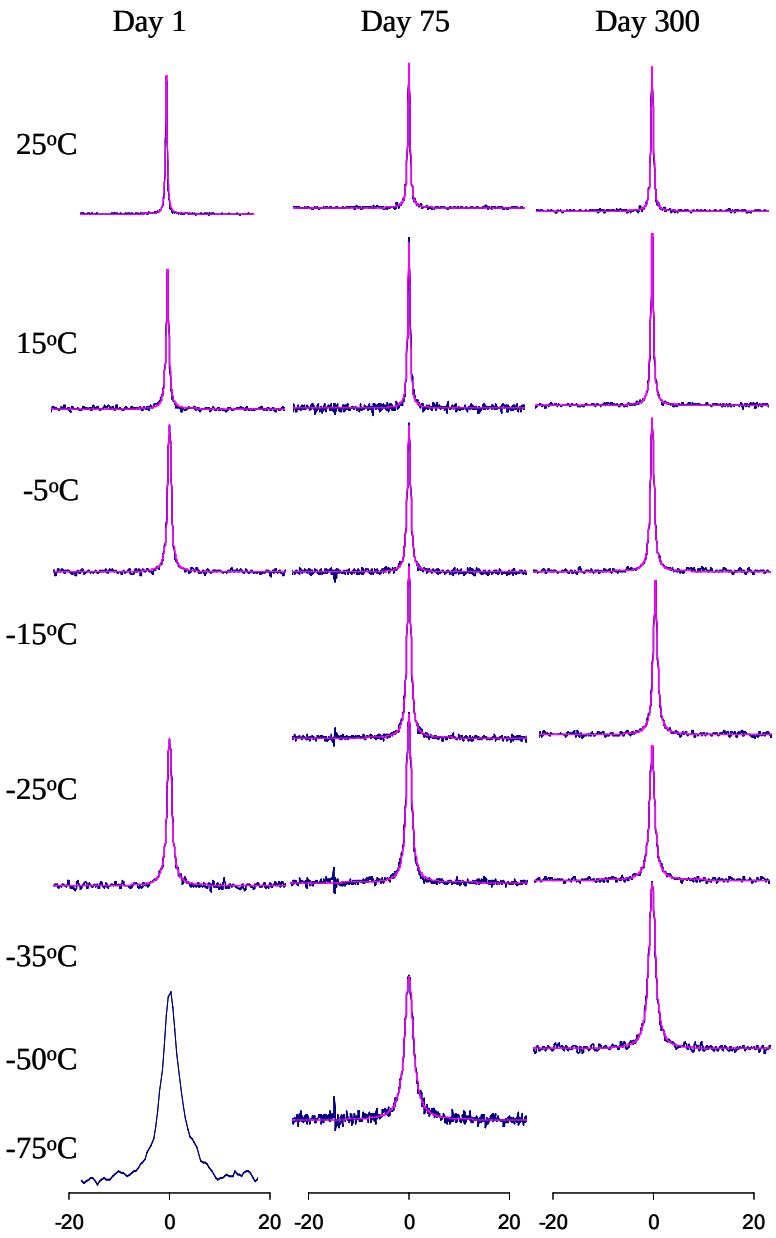

Figure 4.2. Soot1 (35% monolayer coverage, 1% w/w benzene/soot) variable-temperature experimental ^{2}H static solid-state NMR spectra (blue line) collected at different ages using 40μs echo spacing, overlain by DFP simulated spectra (pink line). The maximum intensity of each spectrum has been normalized to one. Number of scans and δν values are detailed in Table 4.4.

Soot1 displays a single Lorentzian peak which broadens with decreasing temperature (Figure 4.2). Lorentzian peaks are the result of motional-averaged isotropic orientations [51, 52], such as would occur in liquid samples. This pattern

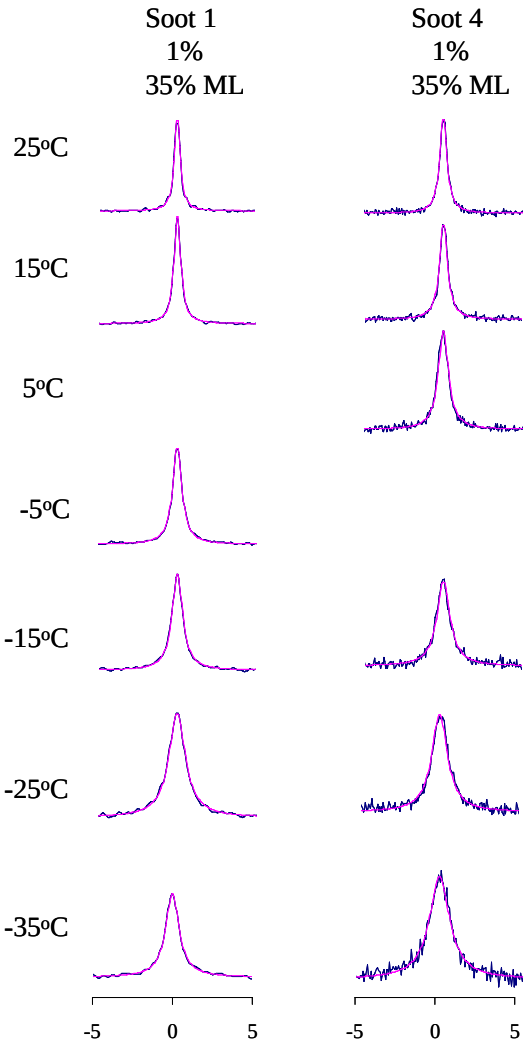

Figure 4.3. Variable-temperature static solid-state ^{2}H NMR spectra of 1% w/w loaded samples, 35% monolayer (ML), of benzene-d_6 on soot. All spectra were collected with 40μs echo spacing, and simulated spectra (pink) overlay the experimental (blue), which have all been normalized to peak height of one. Number of scans is listed in Tables 4.3.

can also be seen spectra from Soot4 (Figure 4.3). The occurrence of such spectra for these samples at temperatures well below the freezing point of bulk benzene, 5°C [53], constitutes a substantial freezing point depression. Freezing point depression has been observed in ^{2}H NMR studies of benzene adsorbed to silicates and attributed to disruption of crystallization by surface forces [37]. Further, the

lowered freezing point is consistent with the behavior of two-dimensional liquid benzene, which has been shown on various solid phases (silicates, zeolites, graphitized carbon black) to under a transition from 2D liquid to 2D solid at between 130-150K [30, 34, 35, 42, 43]. At these low loadings, according to computer simulations, the most favorable orientation for the benzene molecule on the graphene surface was calculated to be that of a face-to-face planar orientation in register with the aromatic rings on the graphenic soot surface, centered over the graphite's carbon atoms [54-56], and these computational studies were supported by results from low-energy-electron diffraction and neutron scattering experiments [28, 31]. This limited conformation for benzene in the sorbed phase would appear to favor limited sorbate mobility and result in a Pake pattern in a ^{2}H static spectrum [44, 45], especially since the benzene exists dominantly in the sorbed phase in these samples (Table 4.3). The small contribution of benzene molecules isotropically moving in the gas phase would not dominate the NMR spectrum and could not account for the observed Lorentzian peak shape or width. Close association of benzene-d_6 with the soot surface in these samples is further confirmed in these spectra by the substantial freezing point depression, mentioned above, and by the very short measured T_1 value of 0.37 ms at 25°C. Shortened T_1's of adsorbed or confined molecules have been attributed to surface relaxation processes, in particular, the influence of paramagnetic impurities on the surface and the increased collision frequency of the sorbed molecule with the surface [57]. The 0.37 ms T_1 measured for the deuterons in benzene-d_6 sorbed onto Soot1 at room temperature is intermediate between the 1.5 s T_1 for neat liquid benzene [58] and an estimated 5ms T_1 for solid benzene at -50°C [40]. Thus, the results here support the interpretation

of Grundke and Boddenberg [38], mentioned above, in their study of benzene-d_6 on Carbopack B, which originally hypothesized that the apparent isotropic reorientation of the benzene molecule is due to benzene moving across the surface of the spherical particles, resulting in an isotropic reorientation of the C_6 axis relative to the laboratory frame of reference. This motion has been labeled pseudoisotropic [59] to differentiate it from the motion of a molecule which is isotropically spinning around the molecule's *own* center (rather than around a coordinate-system centered within the solid particle to which the molecule is adsorbed).

4.3.1.2. Aging

Peak widths at half-height ($\delta\nu$) of the experimental spectra (Table 4.4) do not exhibit broader or narrower peaks with time. Further support for this lack of aging is the constant value over time of the NMR area for spectra collected under the same conditions (scan number, echo delay, etc.), shown in Figure 4.6. For over 300 days, the NMR area under the curve for spectra of Soot1 averages within 5.3% of 4.5 arbitrary NMR intensity units. The lack of motional change with aging indicates that different ages and temperatures for Soot1 were measured. Importantly, with respect to sample aging, Figures 4.4 and 4.5 show that there is no systematic trend of the system is at equilibrium, with respect to surface-to-vapor equilibria, with respect to diffusion into micropores which may alter the molecular motion, and with respect to alteration of the soot solid phase in response to the presence of sorbed benzene (i.e., no swelling).

Figure 4.6 not only shows a constant peak area with time, but is also constant for each temperature over the range 50°C to -75°C. This is evidence that the benzene exists as one motional phase over this temperature range [40, 52]. As

Table 4.4 $\delta\nu^{a,b}$ (Hz) of the Soot1 aparent isotropic peak at different ages

Temp (^{o}C)	$\delta\nu$ (Hz) from Days 1-5	$\delta\nu$ (Hz) from Day 75	$\delta\nu$ (Hz) from Days 291-306	Average $\delta\nu$ (Hz) All Ages	$\pm$ %
25	467 7200 scans	407 7200 scans	465 3600 scans	446 ± 34^{c}	$\pm$7.6%
15	553 1912 scans	487 1800 scans	545 3600 scans	528 ± 36^{c}	$\pm$6.8%
-5	735 1808 scans	664 3600 scans	719 3600 scans	706 ± 37^{c}	$\pm$5.3%
-15	-	810 7200 scans	850 3600 scans	830 ± 20^{d}	$\pm$2.4%
-25	1000 1872 scans	1005 7200 scans	1047 3600 scans	1017 ± 17^{d}	$\pm$1.7%
-35			1245 3600 scans	1245	
-50		1803 7000 scans		1803	
-75	4121 3600 scans			4121	

[a]Spectral peak width at half-height; [b]all spectra collected with 40ms echo spacing and processed without line broadening; [c]standard deviation; [d]difference between the high and the average value.

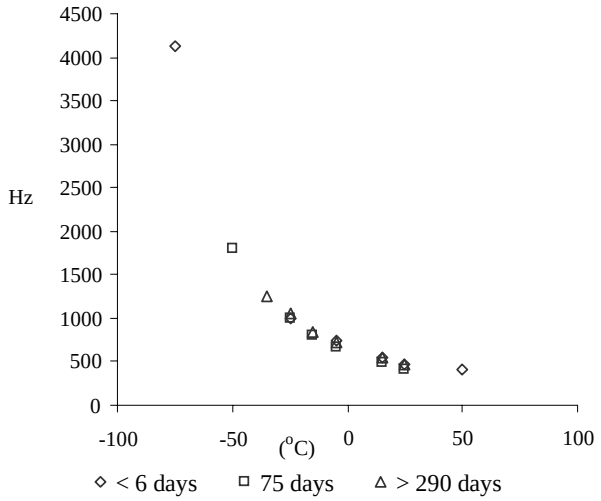

Figure 4.4. Soot1 peak widths at half-height ($\delta\upsilon$) vs. temperature (^{o}C) for different ages; peak width uncertainties listed in Table 4.4; temperature $\pm$0.1^{o}C.

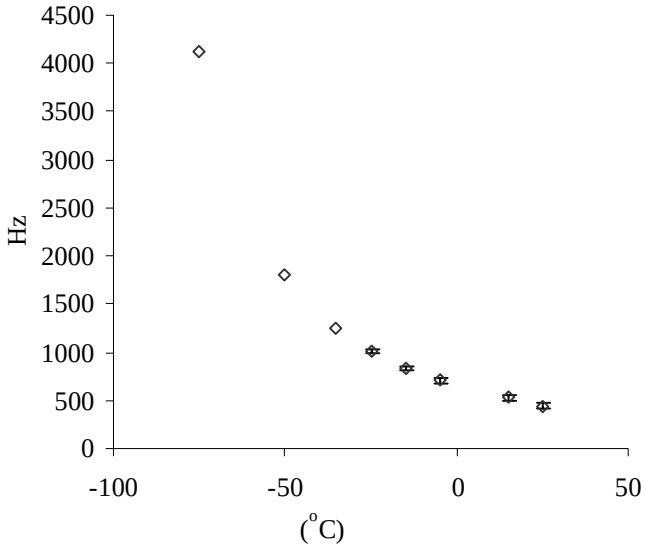

Figure 4.5. Soot1 peak widths at half-height (δν) vs. temperature (°C) averaged from spectra collected at different ages and scan lengths; peak width uncertainties listed in Table 4.4; temperature ±0.1°C.

explained by Duer [52] and by Spiess [60], when two motional populations exist at the same temperature, each population will have a unique dephasing (T_2) constant, and these coexisting dephasing rates cause destructive interference of the signal. The result of this interference is a decrease in signal amplitude (peak area), which reaches a characteristic minimum at a certain distribution of the two motional populations. The constant area value over a range of temperatures is evidence that the entire ensemble of benzene molecules is executing a single type of motion, and that a valid measurement for the Arrhenius constant can be obtained from this data.

4.3.2 Arrhenius data for the pseudoisotropic reorientational motion of 1% w/w loading

The experimental spectra were fitted (Figure 4.7) to simulated spectra using DFP [49] in order to obtain the reorientational jump rates,. A library for isotropic motion was created, based on the molecular reorientation to the 32 faces and

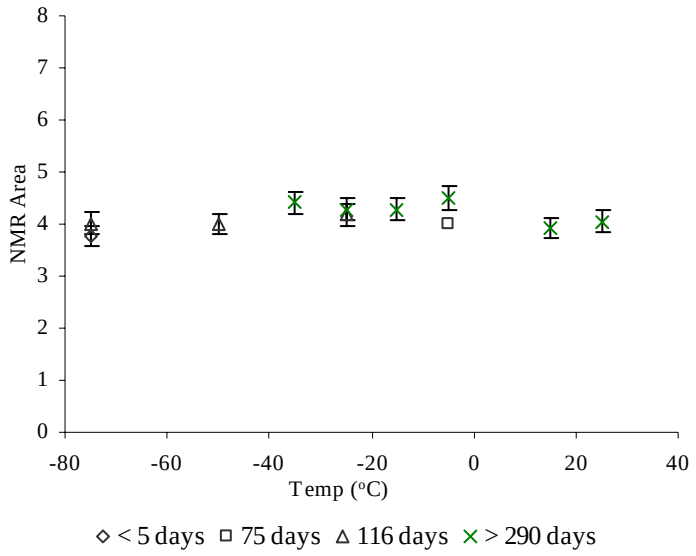

Figure 4.6. Soot1 NMR area for spectra collected with 3600 scans and 40μs echo spacing at variable temperatures for different ages; temperature uncertainty is $\pm$0.1°C; average area is 4.5$\pm$5.3%.

vertices of a dodecahedron with rates from 10^{-5} rad/s to 10^{-7} rad/s. The library consisted of 200 spectra each for 20 μs and 40 μs τ_{echo} values, so that the jump rates were fit to $\pm$1.2%. For the set of spectra collected on days 291-306, data was collected with both 20 μs and 40 μs echo spacings, but otherwise identical instrumental parameters. This method of comparing fits to spectra with different echo delays helps to confirm the particular motional model in use. The jump rates for the fits of the 20 μs spectra differ by less than 4% from the jump rates obtained from fits of the 40 μs spectra. Qualitatively, the 20 μs and 40 μs spectra look nearly identical, differing only in amplitude. The greater loss of amplitude for spectra collected with longer echo spacings occurs with any motion and is due to the greater amount of dephasing which occurs during the longer echo tau [52, 60]. Also, this slight variability in the jump rates obtained from fits of spectra collected with 20 μs

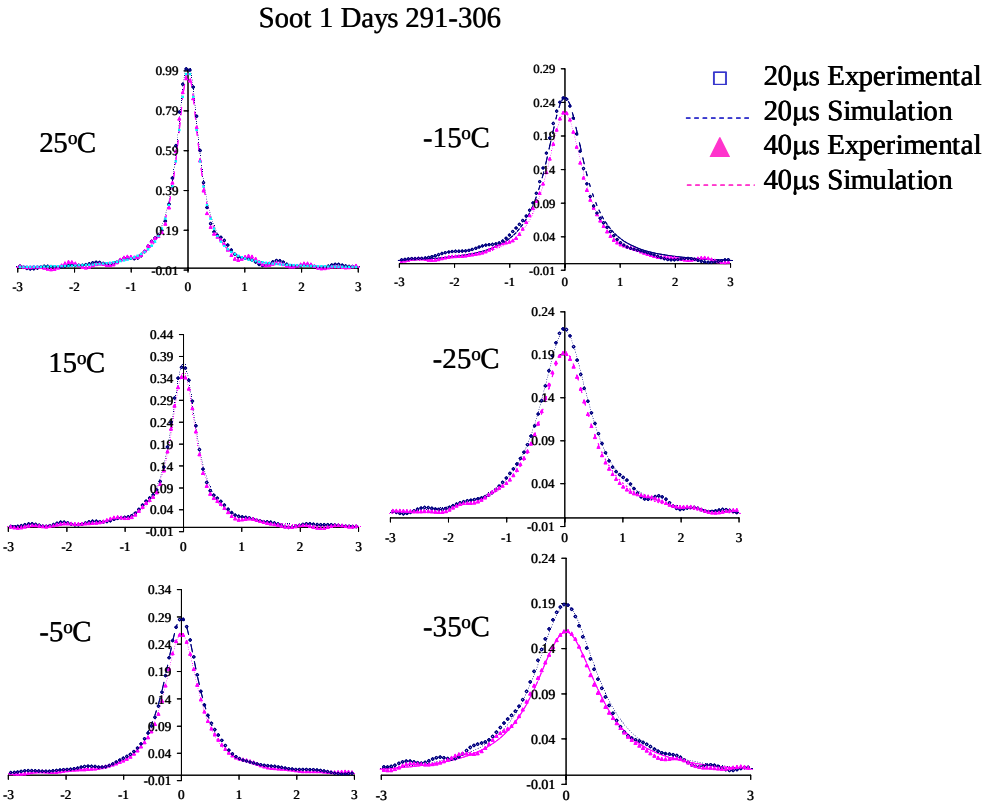

Figure 4.7. Soot1 spectra collected on the same day with 20µs and 40µs echo spacings, experimental spectra overlain with the simulated.

echo spacing relative to spectra collected with 40 µs echo spacing indicates that the motional process may not strictly conform to the assumption of rapid jumps between deep energy wells with steep walls, but may proceed as a more continuous rotational diffusion model [60]. Because the adsorption of benzene on soot is a physisorption process ($\Delta H < 40$ kJ/mol), as opposed to a chemisorption process ($\Delta H > 40$ kJ/mol) [13, 16, 27], it is logical that the adsorption sites are not deep energy wells, but are more like gentle valleys. Thus, the slight variability in fitted jump rates between 20 µs and 40 µs echo-spacing spectra is consistent with the motion of a physisorbed molecule, and, in short, the model of isotropic reorientation is confirmed by the fitting of spectra with different echo spacings.

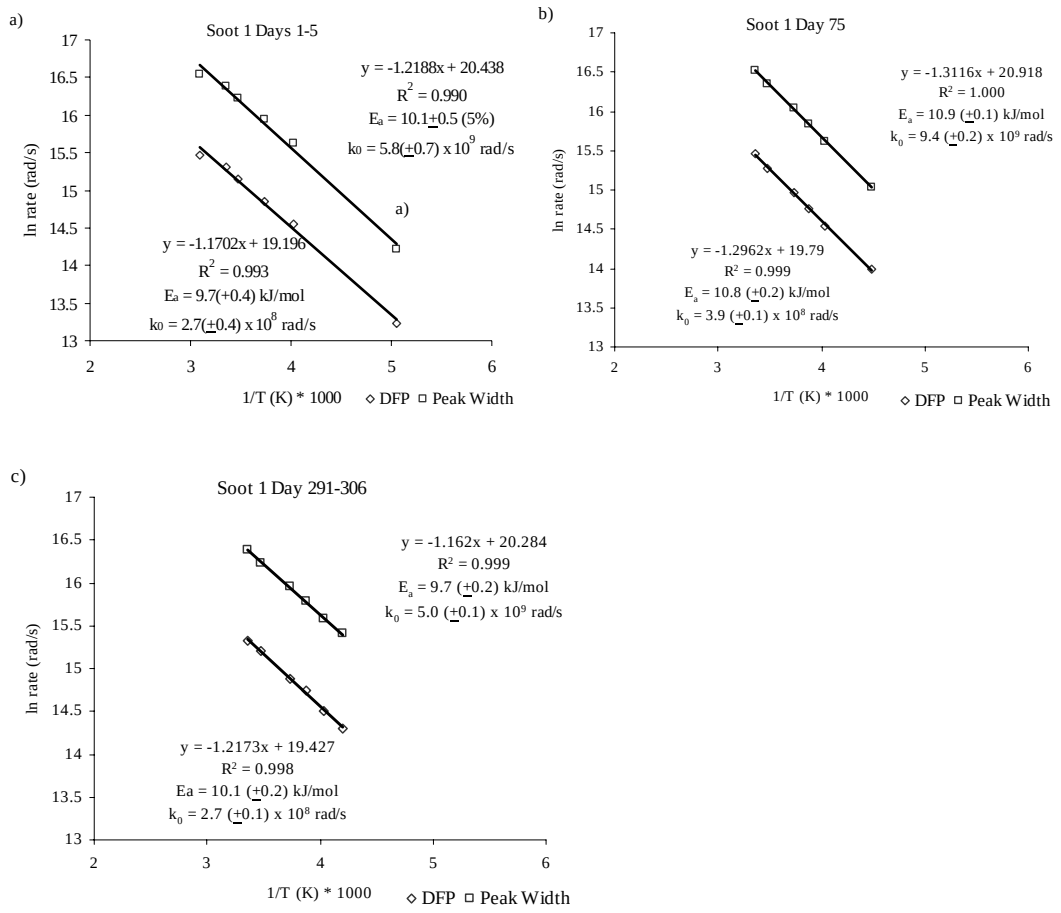

Figure 4.8. Arrhenius plots of reorientational rates of benzene-d_6 on 1% w/w loaded Soot1 at different ages, using Eqn. 4.3 (squares) and DFP (diamonds); a) days 1-5, b) day 75, c) days 291-306.

Arrhenius plots of the 1% w/w loaded Soot1 sample at three different ages (Figure 4.8 a, b, c) confirm the lack of a change in benzene motion with aging, as discussed previously. The high values for the Pearson correlation coefficient (R^2 near 1) indicate minimal scatter in the data, and the values) for the E_a of the pseudoisotropic jump rates from different ages cluster around 10.0 kJ/mol (Table 4.5), which is the value of E_a computed using all 24 individual rate values from the DFP fits (Figure 4.9a).

In addition to calculating the pseudoisotropic jump rates using DFP, the rates

Table 4.5. Arrhenius plots of benzene-d_6 on Soot1 at different ages using DFP and peak width from Equation 4.5.

Temp Range	Method	Age	E_a (kJ/mol)	E_a rel uncer (% kJ/mol)	R^2	k_0 (rad/s)	k_0 rel uncer (% rad/s)
50°C to -75°C	peak width	1-5 days	10.1±0.5	5.0%	0.990	5.8±0.7 x 10^9	12.0%
50°C to -75°C	DFP	1-5 days	9.7±0.4	4.0%	0.993	2.7±0.4 x 10^8	15.0%
25°C to -50°C	peak width	75 days	10.9±0.1	1.0%	1.000	9.3±0.2 x 10^9	2.5%
25°C to -50°C	DFP	75 days	10.8±0.2	1.4%	0.999	3.9±0.1 x 10^8	3.4%
25°C to -35°C	peak width	291-306 days	9.7±0.2	1.7%	0.999	5.0±0.1 x 10^9	2.8%
25°C to -35°C	DFP	291-306 days	10.1±0.2	2.0%	0.998	2.7±0.1 x 10^8	3.5%
50°C to -75°C	peak width	all	10.2±0.3	3.2%	0.984	8.2±0.6 x 10^8	7.6%
50°C to -75°C	DFP	all	10.0±0.2	2.3%	0.988	2.5±0.2 x 10^8	6.0%

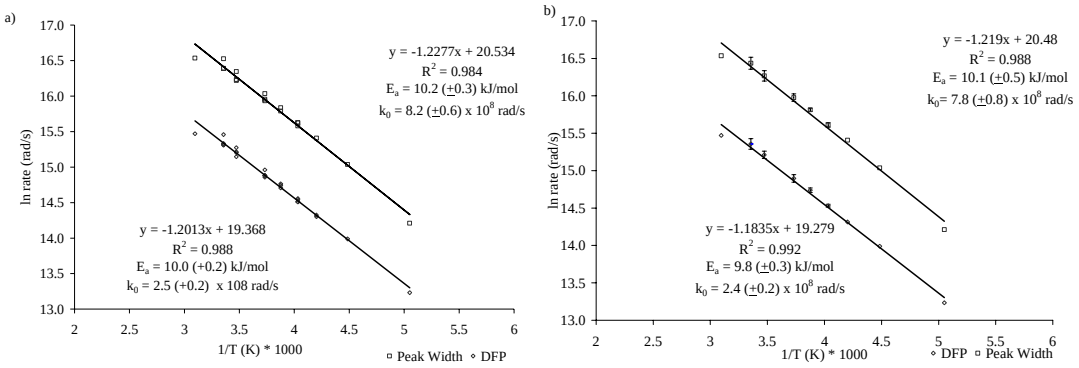

Figure 4.9. Arrhenius plots for all ages of reorientational rates of benzene-d_6 on 1% w/w loaded Soot 1, using Eqn. 4.3 (squares) and DFP (diamonds) for a) all values individually, and b) each temperature age-averaged; temperature uncertainty ±0.1°C.; error bars represent the standard deviation and, for single measurements, the uncertainty is 1.2% for DFP rates (Table 4.5) and less than 8% for peak width measurements (Table 4.4).

have been calculated independently from the peak width, using the following equation taken here from Grundke and Boddenberg [38].

$$\delta\upsilon = (9\pi/20)\, QCC^2\, \tau_C, \qquad \textbf{(Eqn. 4.3)}$$

where $\delta\nu$ is the peak width at half-height for the spectrum, *QCC* is the motionally averaged value of the quadrupole coupling constant, 93 kHz, and τ is the reorientational correlation time,

$$\tau_C = 1/k, \qquad \textbf{(Eqn. 4.4)}$$

where *k* is the jump rate (rad/s) for the reorientational motion. Jump rates calculated with the peak width method are, on average for the values of Soot 1 between 25°C and 25°C, larger than those determined with DFP by a factor of 2.9. The plots in Figures 4.8 and 4.9, reveal that the two methods of rate calculation, using DFP and using Eqn 4.3, give the same values for E_a because the slopes of the lines are parallel. Therefore, the offset is a constant value, and inspection of Eqn. 4.3 reveals that the *QCC* is a constant in this equation, but its value does, as stated above, varies with temperature. The value of 93 kHz used by Grundke and Boddenberg [38] is the maximum value of the *QCC* for a benzene-d_6 molecule undergoing C_6 (hexad) rotation at any rate, but this value can become smaller as the rate of rotation increases or as a wobble is introduced. Gedat et al. [37], in their simulations of a benzene on Na-zeolites at the fast jump rate limit (-66.4°C), have determined a *QCC* value of 90.3 kHz. Using this *QCC* value, the jump rates calculated with DFP are only a little closer (2.7 times more rapid). While the difference could indicate the occurrence of a wobbling motion, it seems equally like that the difference may be due to an error in the equation constants, such as including or excluding a factor of π, especially since, in two of the papers by the Boddenberg group, the constants used are different [35, 38]. At present, however, the exact source of this difference remains unclear.

As explained in Chapter 1, the E_a for surface diffusion represents the energy required for the molecule to overcome the energy barrier between its present conformation and an adjacent conformation while remaining within the field of surface forces from the solid phase. This would include local surface energy variations (sorbate-substrate interactions) and repulsive lateral interactions with

neighboring sorbate or gas phase molecules. The 10.0 kJ/mol E_a we have obtained for benzene on soot at 35% monolayer loading is higher than the 3.8 kJ/mol obtained by Grundke and Boddenberg on Carbopack B, a graphitized carbon black. For comparison, reorientational E_a values for neat benzene have been measured with NMR T_1 analysis as 6.1 kJ/mol for overall tumbling measured [61] and 4.5 and 8.1 kJ/mol for diffusional rotation perpendicular and parallel to the molecular plane, respectively [58]; reorientational E_a values of benzene associated strongly with a solid phase include ^{2}H static solid-state NMR measurements of benzene-d_6 on Na-zeolites, 30.0 kJ/mol [37], and benzene-d_6 in a clathrate compound, 24.9 kJ/mol [40]; and additional values are shown in Table 1.2. The higher E_a value of benzene-d_6 on soot relative to the graphitized carbon black may indicate the influence of strong adsorption sites on the surface of the soot which are absent in the homogeneous Carbopack grains. However, there is reason to question the value measured by Grundke and Boddenberg [38] on the Carbopack B as representative of benzene on graphite. First, the ratio of E_a to $\Delta H_{adsorption}$ for benzene on graphite is much lower than expected: The value of the E_a for surface diffusion is related to the isosteric heat of adsorption, usually by a factor of about 1/3 to ½ [62, 63], and the E_a value of 3.8 kJ/mol listed by Grundke and Boddenberg is only 1/12th of the isosteric heat for graphitized carbon black reported experimentally, 43 kJ/mol, (the median value from Table 1.1), and lower even than the reorientational E_a of neat liquid benzene cited above. The E_a value for surface diffusion on soot measured here is 27% of the heat of adsorption for benzene on soot measured by Aubin and Abbatt [16] and 24% of the heat of adsorption for benzene on graphite. Because Grundke and Boddenberg [38] extrapolated the value of the pseudoisotropic peak

width into low temperatures for which the peak shape was not fully isotropic, the measured E_a value was possibly too low.

The pre-exponential factor, k_0, is determined from the *y*-intercept of the Arrhenius plot and constitutes the fundamental and most rapid jump rate of the molecule reorienting on the surface and would correspond to the jump rate for a lattice gas in the absence of adsorption affected only by interactions with nearest neighbors and temperature [64]. The adsorption of benzene on soot is a mobile adsorption as categorized by Choi et al [36], and the motion observed with the NMR is surface diffusion. As detailed by Grundke and Boddenberg [38], in assuming the diffusion distance, *a*, over which the molecule travels during time τ_C to be the radius of the sphere or pore around which the molecule is diffusing, one can then apply the Einstein diffusion equation [30, 38, 65],

$$D = a^2/6\tau_C, \qquad \textbf{(Eqn. 4.5)}$$

to convert reorientational jump rates to rates of surface diffusion and obtain the diffusion constant, D_0, of benzene-d_6 on soot. Whereas the energy of activation depends upon the enthalpic contribution of the adsorption interaction to a large extent, the pre-exponential factor represents generally the contribution of entropy to the diffusion process [66]. A complete discussion of the D_0 values and comparison of the values between different BC phases will be presented in Chapter 9.

4.3.3 ^{2}H NMR spectra for variable-loaded samples

Static solid-state ^{2}H NMR spectra (Figure 4.10) were collected at different temperatures from 25°C to -35°C of benzene-d_6 on soot at 0.1% and 2% w/w loading, in addition to the 1% w/w loaded samples already discussed. The pseudoisotropic spectra are overlain with the simulated spectra to which they were

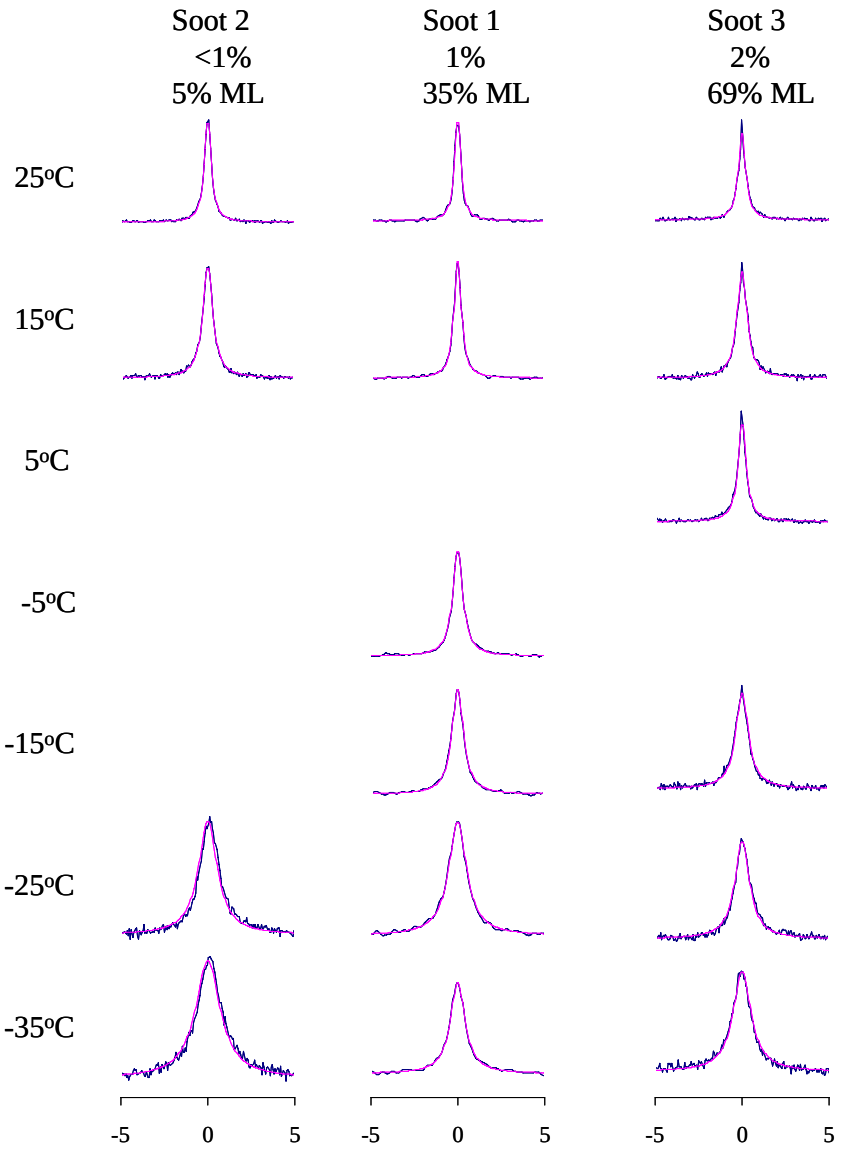

Figure 4.10. Variable-temperature spectra of samples with three different submonolayer loadings of benzene-d_6. All spectra were collected with 40μs echo spacing, and simulated spectra (pink) overlay the experimental (blue), which have all been normalized to peak height of one.

fit with DFP using the same library discussed previously. Table 4.6 lists the spectral data and results of the fitting. Arrhenius plots were constructed (Figure 4.11 a, b, c) and the resulting values of the E_a and k_0 are shown in Table 4.6 and D_0 values in Table 4.7.

Table 4.6. Jump rates and peak widths for Arrhenius plots of variable loaded samples

Loading	Temp (^{o}C)	No Scans	δυ (Hz)	rate (x 10^6) rad/s[a]
< 0.1% w/w	25	28800	500	4.20±0.05
5%ML	5	28800	736	2.83±0.03
Soot2	-25	28800	1360	1.52±0.02
	-35	28800	1782	1.18±0.01
1% w/w	50	7200	403	5.23±0.06
35% ML	25	-	446[b]	4.67±0.06
Soot1	15	-	528[b]	4.04±0.05
	-5	-	706[b]	2.94±0.04
	-15	-	830[b]	2.51±0.03
	-25	-	1017[b]	2.04±0.02
	-35	3600	1245	1.64±0.02
	-50	7000	1803	1.19±0.01
	-75	3600	4121	0.56±0.01
1% w/w	25	3600	559	3.74±0.04
35% ML	15	3600	627	3.33±0.04
Soot4	0	3600	777	2.67±0.03
	-15	3600	1020	2.03±0.02
	-25	3600	1250	1.70±0.02
	-35	3600	1539	1.19±0.01
2% w/w	25	3600	517	4.06±0.05
68% ML	15	3600	583	3.57±0.04
Soot3	0	3600	723	2.90±0.03
	-15	3600	905	2.30±0.03
	-25	3600	1080	1.96±0.02
	-35	3600	1294	1.63±0.02

[a]Fitted spectra for the above are displayed in Figure 4.13; uncertainty in the rates obtained from these fits is 1.2%; [b]values are averages from spectra taken at different ages.

The E_a values become larger for lower loadings (Figure 4.12), and this is consistent with adsorption on a heterogeneous solid on which the strongest adsorption sites are occupied first. Figure 4.13, a plot of the pre-exponential factor vs. the energy of activation for different loadings, displays a linear relationship, evidence of the existence of a compensation effect in the sorption process. A

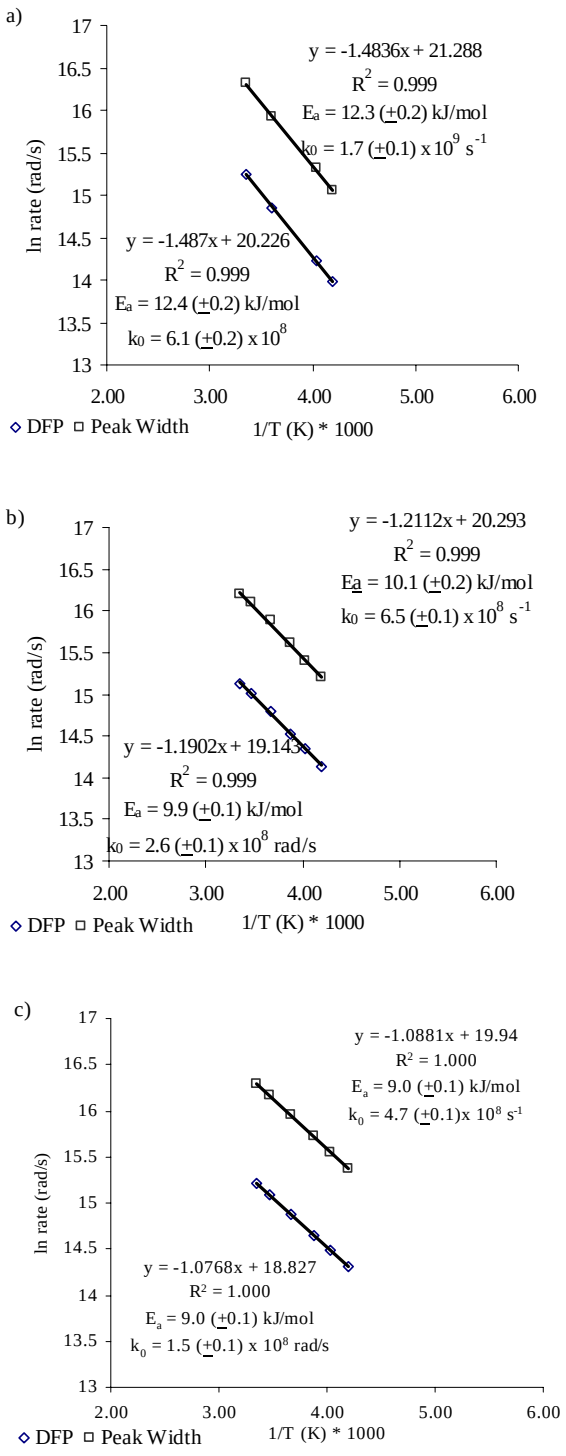

Figure 4.11. Arrhenius plots of variable-loaded soot samples fitted with DFP a) Soot 2 0.1% w/w loading, b) Soot4 1.0% w/w loading (duplicate to Soot1), c) Soot3 2.0% w/w loading; uncertainty in temperature is $\pm 0.1^{o}$C and uncertainty in rate as fit by the DFP library constructed is 1.2%.

Table 4.7. Arrhenius data for benzene-d_6 on soot at different loadings using DFP and peak width Eqn. 4.5.

Temp Range	Method	Sample	Loading (w/w)	E_a (kJ/mol)	R^2	k_0 (rad/s)	D_0 (m^2/s)
25°C to -35°C	Peak Width	Soot2	0.1%	12.3 (±0.2)	0.999	1.7 (±0.1) x 10^9	2.8 (±0.5) x 10^{-10}
25°C to -35°C	DFP	Soot2	0.1%	12.4 (±0.2)	0.999	6.1 (±0.1) x 10^8	
50°C to -75°C	Peak Width	Soot1[a]	1.0%	10.1 (±0.5)	0.988	7.8 (±0.8) x 10^8	3.9 (±0.3) x 10^{-9}
50°C to -75°C	DFP	Soot1[a]	1.0%	9.8 (±0.3)	0.992	2.4 (±0.2) x 10^8	
25°C to -25°C	Peak Width	Soot4	1.0%	10.1 (±0.2)	0.999	6.5 (±0.1) x 10^8	3.3 (±0.6) x 10^{-9}
25°C to -25°C	DFP	Soot4	1.0%	9.9 (±0.1)	0.999	2.6 (±0.2) x 10^8	
25°C to -35°C	Peak Width	Soot3	2.0%	9.00 (±0.1)	1.000	4.6 (±0.1) x 10^8	7.7 (±0.2) x 10^{-9}
25°C to -35°C	DFP	Soot3	2.0%	9.00 (±0.1)	1.000	1.5 (±0.1) x 10^8	

[a]Arrhenius calculation shown used age-averaged rates.

compensation effect is observed when entropy and enthalpy values offset each other as conditions are changed so that the ratio of the two remains constant [67]. Compensation effects are commonly observed between enthalpic and entropic contributions to the energy of adsorption and of surface diffusion [21, 36, 67]. In

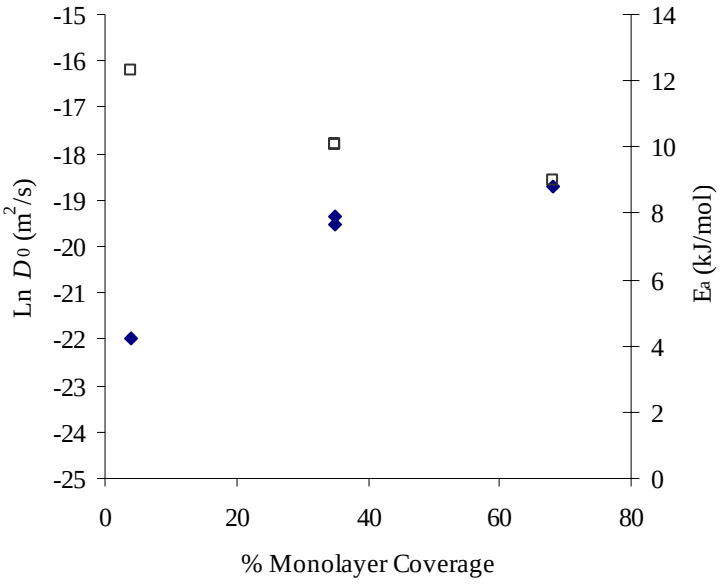

Figure 4.12. Plot of the variation with surface coverage of D_0 (solid diamond) and E_a (open squares).

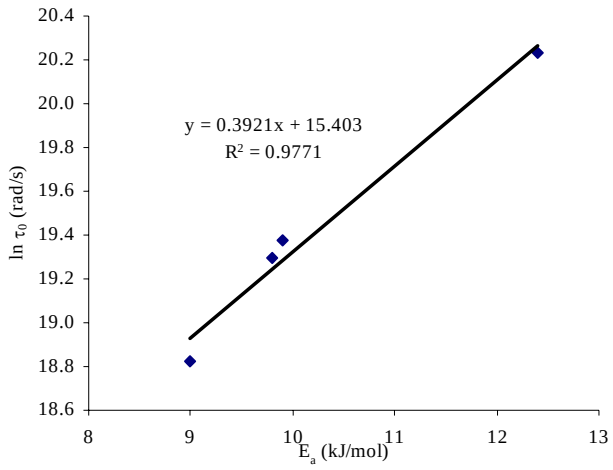

Figure 4.13. Plot of pre-exponential factors vs energy of activation, demonstrating an enthalpy/entropy compensation effect.

this case, at low loadings, the benzene molecule adsorbs onto the strongest adsorption sites, which are relatively few in number and with a greater number possible number of available sites (higher entropy), but at higher loadings, the available adsorption sites are weaker, but the entropy is also reduced because of crowding from adjacent molecules [66, 68, 69].

4.4 CONCLUSIONS

The surface diffusion of benzene-d_6 on SRM #2975 diesel soot has been measured by line shape analysis of the ^{2}H solid-state NMR spectra collected at variable temperatures, ages, and submonolayer loadings. Arrhenius plots of the data have produced E_a and D_0 values for 4%, 35%, and 68% nominal monolayer loaded samples of 12.3 ($\pm$0.2), 10.0 ($\pm$0.3), and 9.0 ($\pm$0.1) kJ/mol, respectively, and 2.8 ($\pm$0.1) x 10^{-8} m^2/s, 1.2 ($\pm$0.1) x 10^{-8} m^2/s, and 7.7 ($\pm$0.1) x 10^{-8} m^2/s, respectively. There was no apparent effect of sample aging on the molecule motion of the

benzene-d_6. The data was compared with results from similar experiments performed on a graphitized carbon black (a model soot substance) and discussed in light of adsorption data from other workers on hexane soot and SRM #2975 diesel soot and found to support conclusions from these studies that the benzene-d_6 molecules is likely to be oriented either parallel with the solid surface or at a slight acute angle. Further, a compensation effect was observed in the data over different loadings, and this, combined with the inverse correlation of E_a with loading, indicates that the soot surface may contain a heterogeneous distribution of adsorption sites energies (possibly oxygen-containing acidic functions at the surface).

References

1. Cornelissen, G.; Gustafsson, O.; Bucheli, T. D.; Jonker, M. T. O.; Koelmans, A. A.; van Noort, P. C. M., Extensive sorption of organic compounds to black carbon, coal, and kerogen in sediments and soils: mechanisms and consequences for distribution, bioaccumulation, and biodegradation. *Environmental Science & Technology* **2005,** *39*, (18), 6881-6895.
2. Schauer, J. J.; Wolfgang, F. R.; Hildemann, L. M.; Mazurek, M. A.; Cass, G. R., Source apportionment of airborne particulate matter using organic compounds as tracers. *Atmospheric Environment* **1996,** *30*, (22), 3837-3855.
3. Lohmann, R.; Lammell, G., Adsorptive and absorptive contributions to the gas-particle partitioning of polycyclic aromatic hydrocarbons: state of knowledge and recommended parameterization for modeling. *Environmental Science & Technology* **2004,** *38*, (14), 3793-3803.
4. Bucheli, T. D.; Gustafsson, O., Quantification of the soot-water distribution coefficient of PAH's provides mechanistic basis for enhanced sorption observations. *Environmental Science & Technology* **2000,** *34*, 5144-5151.
5. Cornelissen, G.; Gustafsson, O., Sorption of phenanthrene to environmental black cabon in sediment with and without organic matter and native sorbates. *Environmental Science & Technology* **2004,** *38*, 148-155.
6. Aubin , D. G.; Abbatt, J. P., Adsorption of gas-phase nitric acid to n-hexane soot: thermodynamics and mechanism. *Journal of Physical Chemistry A* **2003,** *107*, 11030-11037.
7. Ramanathan, V.; Feng, Y., Air pollution, greenhouse gases and climate change: global and regional perspectives. *Atmospheric Environment* **2009,** *43*, 37-50.

8. Jacobson, M. Z., Strong radiative heating due to the mixing state of black carbon in atmospheric aerosols. *Nature* **2001,** *409*, 695-697.
9. Murr, L. E.; Garza, K. M., Natural and anthropogenic environmental nanoparticulates: their microstructural characterization and respiratory health implications. *Atmospheric Environment* **2009,** *43*, 2683-2692.
10. Su, D. S.; Serafino, A.; Muller, J.-O.; Jentoft, R. E.; Schlogl, R.; Fiorito, S., Cytotoxicity and inflammatory potential of soot particles of low-emission diesel engines. *Environmental Science & Technology* **2008,** *42*, 1761-1765.
11. Abu, A.; Smith, S., Assessing sequestration of selected polycyclic aromatic hydrocarbons by use of adsorption modeling and temperature-programmed desorption. *Environmental Science & Technology* **2005,** *39*, 7585-7591.
12. Jonker, M. T. O.; Hawthorne, S. B.; Koelman, A. A., Extremely slowly desorbing polycyclic aromatic hydrocarbons from soot and soot-like materials: evidence by supercritical fluid extraction. *Environmental Science & Technology* **2005,** *39*, (20), 7889-7895.
13. Accardi-Dey, A.; Gschwend, P. M., Assessing the combined roles of natural organic matter and black carbon as sorbents in sediments. *Environmental Science & Technology* **2002,** *36*, 21-29.
14. Goss, K.-U., Conceptual model for the adsorption of organic compounds from the gas phase to liquid and solid surfaces. *Environmental Science & Technology* **1997,** *31*, 3600-3605.
15. Arp, H. P. H.; Schwarzenbach, R. P.; Goss, K.-U., Ambient gas/particle partitioning. 2: The influence of particle source and temperature on sorption to dry terrestrial aerosols. *Environmental Science & Technology* **2008,** *42*, (16), 5951-5957.
16. Aubin , D. G.; Abbatt, J. P., Laboratory measurements of thermodynamics ofadsorption of small aromatic gases to *n*-hexane soot surface. *Environmental Science & Technology* **2006,** *40*, 179-187.
17. Nguyen, T. H.; Sabbah, I.; Ball, W. P., Sorption nonlinearity for organic contaminants with diesel soot: method development and isotherm interpretation. *Environmental Science & Technology* **2004,** *38*, 3595-3603.
18. Nguyen, T. H.; Ball, W. P., Absorption and adsorption of hydrophobic organic contaminants to diesel and hexane soot. *Environmental Science & Technology* **2006,** *40*, 2958-2864.
19. Roth, C. M.; Goss, K.-U. a. S., Rene P., Sorption of a diverse set of organic vapors to diesel soot and road tunnel aerosols. *Environmental Science & Technology* **2005,** *39*, 6632-6637.
20. Braun, A.; Mun, B. S.; Huggins, F. E.; Huffman, G. P., Carbon speciation of diesel exhaust and urban particulate matter NIST standard reference materials with C(1s) NEXAFS spectroscopy. *Environmental Science & Technology* **2007,** *41*, 173-178.
21. Miyabe, K.; Shigeya, T., Analysis of surface diffusion phenomena in liquid phase adsorption. *Journal of Physical Chemistry B* **1997,** *101*, 7773-7779.
22. Manes, M.; Hofer, L. J. E., Application of the Polanyi adsorption potential theory to adsorption from solution on activated carbon. *Journal of Physical Chemistry* **1969,** *73*, 584-590.

23. Sachdeva, K.; Attri, A. K., Morphological characterization of carbonaceous aggregates in soot and free fall aerosol samples. *Atmospheric Environment* **2008,** *42*, 1025-1034.
24. Nguyen, T. H.; Brown, R. A.; Ball, W. P., An evaluation of thermal resistance as a measure of black carbon content in diesel soot, wood char, and sediment. *Organic Geochemistry* **2004,** *35*, 217-234.
25. Schwarzenbach, R. P.; Gschwend, P. M.; Imboden, D. M., *Environmental Organic Chemistry, 2nd ed.* John Wiley and Sons Inc.: New York, NY, 2003.
26. Adamson, A.; Gast, A. P., *Physical Chemistry of Surfaces*. John Wiley & Sons: New York, 1997; p 784.
27. Do, D. D.; Do, H. D., Adsorption of benzene on graphitized thermal carbon black: reduction of the quadrupole moment in the adsorbed phase. *Langmuir* **2006,** *22*, 1121-1128.
28. Bardi, U.; Magnanelli, S.; Rovida, G., LEED study of benzene and naphthalene monolayers adsorbed on the basal plane of graphite. *Langmuir* **1987,** *3*, 159-163.
29. Tabony, J.; White, J. W.; Delachaume, J. C.; Coulon, M., Nuclear magnetic resonance studies of the melting and orientation of benzene adsorbed upon graphite *Surface Science* **1980,** *95*, L282-L288.
30. Boddenberg, B.; Grosse, R., A deuteron NMR study on a benzene multilayer on graphite. *Z. Naturforsch* **1987,** *421*, 272-274.
31. Meehan, P.; Rayment, T.; Thomas, R. K.; Guillermo, B.; White, J. W., Neutron diffraction from benzene adsorbed on graphite. *J.C.S. Faraday 1* **1980,** *76*, 2011-2016.
32. Kruk, M.; Li, Z.; Jaroniec, M., Nitrogen adsorption study of surface properties of graphitized carbon blacks. *Langmuir* **1999,** *15*, 1435-1441.
33. Fodi, B.; Hentschke, R., Molecular dynamics simulation of a binary hydrocarbon mixture near an adsorbing wall: benzene/I-heptane on graphite. *Langmuir* **1998,** *14*, 429-437.
34. Auerbach, S. M.; Bull, L. M.; Henson, N. J.; Metin, H. L.; Cheetham, A. K., Behavior of benzene in Na-X and Na-Y zeolites: comparative study by ^{2}H NMR and molecular mechanics. *Journal of Physical Chemistry* **1996,** *100*, 5923-5930.
35. Boddenberg, B.; Burmeister, R., ^{2}H n.m.r. study on the rotation and diffusion kinetics of propene and benzene in NaX and AgNaX zeolites. *Zeolites* **1988,** *8*, 488-494.
36. Choi, J.-G.; Do, D. D.; Do, H. D., Surface diffusion of adsorbed molecules in porous media: monolayer, multilayer, and capillary condensation regimes. *Ind. Eng. Chem. Res.* **2001,** *40*, 4005-4031.
37. Gedat, E.; Schreiber, A.; Albrecht, J.; Emmler, T.; Shenderovich, I.; Findenegg, G. H.; Limbach, H.-H.; Buntknowsky, G., ^{2}H solid-state NMR study of benzene-d_6 confined in mesoporous silica SBA-15. *Journal of Physical Chemistry B* **2002,** *106*, 1977-1984.
38. Grundke, V.; Boddenberg, B., One and two component adsorption layers of *n*-hexane and benzene on graphite studied by ^{2}H NMR spectroscopy. *Molecular Physics* **1993,** *79*, (6), 1215-1226.
39. Nishikiori, S.-I.; Soma, T.; Iwamoto, T., In-plane and out-of-plane motion of benzene trapped in $Cd(py)_2\{Ag(CN)_2\}_2$ host as studied by deuterium NMR. *Journal*

of Inclusion Phenomena and Molecular Recognition in Chemistry **1997,** *27*, 233-243.
40. Ok, J. H.; Vold, R. R.; Vold, R. L.; Etter, M. C., Deuterium nuclear magnetic resonance measurements of rotation and libration of bezene in a solid-state cyclamer. *Journal of Physical Chemistry B* **1989,** *93*, 7618-7624.
41. Xiong, J.; Maciel, G. E., Deuterium NMR studies of local motions of benzene adsorbed on Ca-montmorillonite. *Journal of Physical Chemistry B* **1999,** *103*, 5543-5549.
42. Voss, V.; Boddenberg, B., Anisotropic reorientation dynamics of benzene molecules adsorbed on graphite, alumina, and zeolite Y. *Surface Science* **1993,** *298*, (241-250).
43. Boddenberg, G.; R., H.; Opperman, G., NMR spin echo studies on mobility and diffusion of benzene adsorbed on silica. *Journal of Colloid and Interface Science* **1972,** *38*, 210-216.
44. Boddenberg, B.; Beerwerth, B., Proton and deuteron magnetic resonance relaxation of benzene adsorbed on alumina and on a platinum/alumina catalyst. *Journal of Physical Chemistry* **1989,** *93*, 1440-1447.
45. Boddenberg, B.; Beerwerth, B., Proton and deuteron magnetic resonance spectra of benzene adsorbed on alumina and on a platinum/alumina catalyst. *Journal of Physical Chemistry* **1989,** *93*, 1435-1440.
46. Technology, N. I. o. S. a., Certificate of Analysis - Standard Reference Material #2975 - Diesel Particulate Matter (Industrial Forklift). In Gaithersburg, MD, 2001.
47. Certificate of Analysis - Standard Reference Material 2975 - Diesel Particulate Matter (Industrial Forklift). **2001**.
48. Webster, C., Edwin; Drago, R. S.; Zerner, M. C., Molecular dimensions for adsorptives. *Journal of the American Chemical Society Communications* **1998,** *120*, 5509-5516.
49. Eastman, M. A.; Nanny, M. A., Fitting of deuterium quadrupole echo spectra with multiple motional models. *Journal of Magnetic Resonance* **2007,** *184*, 302-314.
50. Goss, K.-U.; Schwarzenbach, R., Empirical prediction of heats of vaporization and heats of adsorption of organic compounds. *Environmental Science & Technology* **1999,** *33*, (19), 3390-3393.
51. Sanders, J. K. M.; Hunter, B. K., *Modern NMR Spectroscopy: a Guide for Chemists*. Oxford University Press: New York, 1987; p 308 p.
52. Duer, M. J., *Introduction to Solid-State NMR Spectroscopy*. Oxford Press: Oxford, U.K., 2004.
53. NMR Solvent Reference Chart. *Cambridge Isotope Laboratories*.
54. Do, D. D.; Do, H. D., Characterization of micro-mesoporous carbonaceous materials. Calculations of adsorption isotherm of hydrocarbons. *Langmuir* **2002,** *18*, 93-99.
55. Vernov, A.; Steele, W. A., Computer simulations of benzene adsorbed on graphite. 1. 85K. *Langmuir* **1991,** *7*, 3110-3117.
56. Vernov, A.; Steele, W. A., Computer simulations of benzene adsorbed on graphite. 2. 298K. *Langmuir* **1991,** *7*, 2817-2820.
57. Korb, J.-P.; Xu, S.; Jonas, J., Confinement effects on dipolar relaxation by translational dynamics of liquids on porous silica glasses. *J. Chem. Phys.* **1993,** *98*,

(3), 2411-2422.
58. Schwartz, M.; Duan, D.; Berry, R. J., Molecular dynamics study of anisotropic translational and rotational diffusion in liquid benzene. *J. Phys. Chem. A* **2005,** *109*, (38), 8637-8641.
59. Bull, L. M.; Henson, N. J.; Cheetham, A. K.; Newsam, J. M.; Heyes, S. J., Behavior of benzene in siliceous faujasite: a comparative study of deuteron NMR and molecular dynamics. *J. Phys. Chem.* **1993,** *97*, 11776-11780.
60. Spiess, H. W., Molecular dynamics of solid polymers as revealed by deuteron NMR. *Colloid & Polymer Science* **1983,** *261*, 193-209.
61. Wakai, C.; Nakahara, M., Attractive potential effect on the rotational correlation times for benzene-d_6 in organic solvents. *Bulletin of the Chemical Society of Japan* **1996,** *69*, 853-860.
62. Gilliland, E. R.; Baddour, R. F.; Perkinson, G. P.; Sladek, K. J., Diffusion on surface. I. Effect of concentration on the diffusivity of physically adsorbed gases. *Ind. Eng. Chem.; Fundam.* **1974,** *13*, 95-99.
63. Miyabe, K.; Guiochon, G., Thermodynamic characteristics of surface diffusion in reversed-phase liquid chromatography
Journal of Physical Chemistry B **1999**, (103), 11086-11097.
64. Anton, A. B., Mechanism, configurational degeneracy, and mass action in transition-state rate functions for adsorption-desorption reactions. *J. Phys. Chem.* **1993,** *97*, (1942-1951), 1942-1951.
65. Giddings, C. J., *Unified Separation Science*. John Wiley & Sons, Inc.: New York, NY, 1991; p 320 p.
66. Suarez, M. P.; Palermo, A.; Aldao, C. M., The compensation effect revisited. *Journal of Thermal Analysis* **1994,** *41*, 807-816.
67. Bond, G. C.; Keane, M. A.; Kral, H.; Lercher, J., Compensation phenomena in heterogeneous catalysis: general principles and a possible explanation. *Catalysis Reviews* **2000,** *42*, (3), 323-383.
68. Rigby, S. P., A model for the surface diffusion of molecules on a heterogeneous surface. *Langmuir* **2003,** *19*, 364-376.
69. Arena, M. V.; Deckert, A. A.; J.L., B.; George, S. M., Surface diffusion and desorption of pentane isomers on Ru(001)
Journal of Physical Chemistry **1990,** *94*, 6792-6797.

5. THE MOTION OF BENZENE-d_6 MOLECULES ON AMORPHOUS CARBON NANOPARTICLES OBSERVED WITH STATIC SOLID-STATE ^{2}H NMR SPECTRA

5.1 INTRODUCTION

In order to understand the contribution of graphenic carbon functionalities to the sorption interactions of benzene with the surface of black carbon (BC), a comparison of those interactions can be made to the interactions of benzene with the surfaces of a sample of carbon which lacks crystalline organization. For this purpose, carbon nanoparticles (CNP) were selected as a model amorphous black carbon: their surface chemistry is lacking in contributions from heteroatoms (99.9% carbon) and is not dominated by a graphitic crystalline structure (Chapter 3) [1]. In order to assess the benzene-amorphous carbon surface interactions, the molecular motion of adsorbed benzene-d_6 molecules was measured with solid-state ^{2}H NMR at different temperatures and contrasted with the motion of benzene molecules interacting with related surfaces.

Key properties of CNPs are listed in Table 5.1. They are similar in particle size and surface area to soot, 31.9 nm dia. and 91 m^2/g, respectively, for soot, and < 30 nm. dia. and 100 m^2/g, respectively, for CNP [1] . Some differences exist in the pore structure, however, with CNPs having less pore volume than NIST #2975 soot

Table 5.1. Characteristics of carbon nanoparticles[a]

wt % Carbon[a]	% Other	[Ca] (ppm)[a]	Surface Area[a,c] (m^2/g)	Pore Size[c] (nm)	Particle Size dia[a] (nm)
$\geq$ 99	$\leq$1	767	100	0.5-5	30

[a]Amorphous carbon particles produced by laser ablation [1]; [b]Galbraith Laboratories; [c]verified with N_2 adsorption analysis, this work (Chapter 3).

(0.105 and 0.163 g/ml, respectively), and a higher fraction of microporosity (24% and 3%, respectively), as calculated from N_2 isotherms using the Quantachrome DFT algorithm (Chapter 3, Table 3.2, Figure 3.2). Prepared from laser ablation of graphite rods, carbon nanoparticles used in this study can be expected to be similar in chemistry and structure to "carbon soots" [2] synthesized from the same technique. As discussed in the Introduction, research on laser-ablated carbon nanoparticles have examined them using Raman, X-ray reflectivity techniques and transmission electron microscopy, and these studies revealed the presence of disordered graphite domains, which were linked by sp^3 bonds, included some fullerene configurations, and contained some dangling bonds (-C:) and edges [2-5]. The graphitic crystallinity of both CNP and NIST #2975 soot is measurable, but small (Table 3.1), although the CNPs contain slightly larger average graphite crystals as measured by X-ray diffraction (L_c = 6 nm and 2 nm for CNP and soot, respectively). However, the internal particle structure of condensed graphitic layers surrounding an inner polyaromatic core, which is observed in diesel soot (Figure 1.5a [6]), is absent from CNPs produced by laser ablation, according to the studies cited above [2]. Thus, CNPs are similar in size and shape to the NIST #2975 diesel soot examined in the previous chapter, but differ in internal particle structure and surface chemistry.

As stated above, CNPs are closely related to graphite itself because they both have the same elemental composition (carbon only), but they differ chemically in the variety of carbon functionalities and degree of crystallinity. However, the CNPs also differ from the low-surface-area graphite samples physically: in grain size ($\geq$30 nm and 44 μm dia., for CNP and low-surface-area graphite grains,

respectively) and in grain shape. Whereas CNPs display spherical or cubic particle morphology in the scanning electron micrographs from the studies mentioned above [2], graphite has a platey crystal habit [7, 8]. In any case, all three of these BCs (soot, CNP, low-surface-area graphite) are similar to each other in having *only inter*particulate porosity, in contrast to the carbon nanotubes, char and activated carbon BC samples.

In this chapter, the sorption interaction of benzene on CNP, with its amorphous carbon chemistry, is assessed by observing the rotational motion of benzene in vapor/solid adsorption equilibrium using static solid-state ^{2}H NMR, and these results allow comparison of benzene's motion on CNP to benzene's motion on other BCs, which do not have amorphous carbon. Spectra of the benzene were collected over a range of temperatures (25°C to -125°C) and ages (from 1 to 318 days), and the rotational jump rate was determined by fitting the experimental spectra to simulations, using the Deuterium Fitting Program (DFP) of Eastman and Nanny [9]. Jump rates were also calculated using Eqn. 4.3 and the width of the spectra at half-height ($\delta\upsilon$) as the only fitting variable, just as was done for the diesel soot samples. Arrhenius analysis of the variable-temperature data provided energies of activation and pre-exponential values for the reorientational jump motion and the diffusivity. Examination of the data provided information about changes in the molecular motion of benzene-d_6 on the CNP samples with aging, and comparison of the measured rates, activation energies, and pre-exponential factors to those obtained for other BCs provided insight into the nature of the chemical interactions that affect the motion and adsorption of benzene with the surface of BCs

5.2 EXPERIMENTAL

5.2.1 Materials Characterization

The XRD spectrogram of the CNP (displayed in Figure 3.1) displayed a rather wide, low intensity peak and 0.35 nm *d*-spacing, shifted from the pure graphite position at 0.335 nm for d_{002} [10], with the half-width measuring 2 ($\pm$0.3)^{o} (Table 3.1). These data indicated the presence of graphitic functions with poor crystalline ordering, confirming the chemical description for amorphous carbon mentioned above [4, 7]. However, as mentioned above, the amount of crystalline order, as indicated by the L_c parameter calculated from the half-width of the XRD intensity peak, in this "amorphous" carbon sample is twice that of the soot, activated carbon or char, and only a little below one of the carbon nanotubes (CNS). So, some amount of graphene stacking/ordering is present.

The pore size distribution, obtained from the N_2 isotherms (Figure 3.4, Table 3.2), displayed a total porosity of 0.105 ml of pore volume per gram of solid. This is lower than the total porosity for the diesel soot (0.16-0.25 ml pore space per gram of solid), but with a much higher amount of micropores (0.025 g/ml; 24% of the total porosity). Relative to the graphite sample, the CNP pore volume is larger by a factor of 10 and the fraction of microporosity by a factor of 4.

5.2.2 Sample Preparation

Duplicate samples of CNP/benzene-d_6 (Table 5.2) were prepared according to the procedure outlined in the Experimental Section. Briefly, the solid phase was placed into a specially-necked 10 mm NMR tube which was attached to a vapor deposition manifold. A precise amount of benzene-d_6 was condensed into the NMR tube, which was submerged in liquid nitrogen, and the sample was subsequently

Table 5.2. Samples of benzene-d_6 on carbon nanoparticles

Sample Name	Mass of CNP (mg)	Deposited Volume of Benzene (μl)	Volume of Benzene per NMR Quantitation Plot (μl)	% load (w/w)[a]	% loading (monolayer coverage)[a]
CNP1	147.1 (±0.1)	1.5 (±0.1)	1.3 (±0.3)	1.0 (±0.1)%	35 (±2)
CNP2	144.3 (±0.1)	1.5 (+0.1)	1.0 (+0.3)	1.0 (±0.1)%	35 (±2)

[a]Per original volume calculated with the manifold, i.e., 1.5μl.

backfilled to 200-400 torr with N_2 gas, flamed-sealed, and transported to the Oklahoma Statewide NMR Facility at Stillwater, Oklahoma, for collection of the variable-temperature solid-state ^{2}H NMR spectra on the Chemagnetics 300 MHz instrument. A quadrupole echo sequence ($\pi/2 - \tau_{echo} - \pi/2 - \tau_{echo}$ – acquire) at 46.20525 MHz was used to collect all spectra. In order to verify the quantities of benzene-d_6 loaded into both samples, an NMR spectrum was collected with standard parameters (10 s delay time, 128 scans, 25°C, 20 μs echo tau, 1024 data points, and 1 kHz line broadening), and the NMR spectral areas were plotted against the volume loaded in comparison to a quantitation line prepared from the areas of NMR spectra of sealed liquid benzene-d_6 collected with those same parameters, as described in the Appendix A1 (Figure A1.3). The quantities of benzene-d_6 on CNP1 and CNP2 predicted from the NMR area calibration curve (Table 5.2, Figure A1.4) are below the quantities measured on the vapor deposition system, but within a range deemed acceptable (Dr. Margaret A. Eastman, personal communication, 2006). For collecting static solid-state ^{2}H NMR spectra at variable temperatures for curve-fitting and jump rate determination, parameters used were 1800-7200 scans (Table 5.3), delay times of either 0.50 s or 0.25 s, both 20 μs and 40 μs echo spacing taus,

either 1024 or 8196 data points, and were processed with zero filling (if necessary) to 8196 points without line broadening. The experimental spectra were fit using the Deuterium Fitting Program (DFP) [9] from ISO libraries constructed over the jump rate range of 1 x 10^5 rad/s to 1 x 10^7 rad/s with 400 increments to give a minimum uncertainty of 1.2% in the jump rate obtained from the fit.

5.3 RESULTS: ^{2}H STATIC SOLID-STATE NMR SPECTRA

The ^{2}H solid-state NMR experimental spectra for samples CNP1, which were collected at several ages and variable temperatures, are shown in Figure 5.1, and, for sample CNP2, in Figure 5.2, overlain with the simulated spectra to which they were fit by DFP. All are Lorentzian, even at temperatures well below the 5°C freezing point of benzene, illustrating a very large freezing point depression [11]. As was detailed when discussing the spectra on soot (Chapter 4), the freezing point depression indicates an intimate association of benzene molecules with the surface of the carbon nanoparticles [11, 12]. In further support for the existence of a close association between the benzene-d_6 and the CNP1 surface, the T_1 value was measured experimentally by inversion-recovery at 32.4 ms, which is close to the value of 37.0 ms observed on the soot and well below the 1.5 s T_1 published for neat liquid benzene [12]. Thus, just as with the soot samples (Chapter 4), this data is in accord with the pseudoisotropic motional model suggested by Boddenberg's group in which the benzene molecule is oriented face-to-face with respect to the grain surface, but 2D liquid flow around the spherical surface of the CNP pores or grains results in a isotropic distribution of molecular orientations. This interpretation is brought into some question for these samples because the original supposition of Boddenberg's group that the benzene is oriented face-to-face with the grain surface

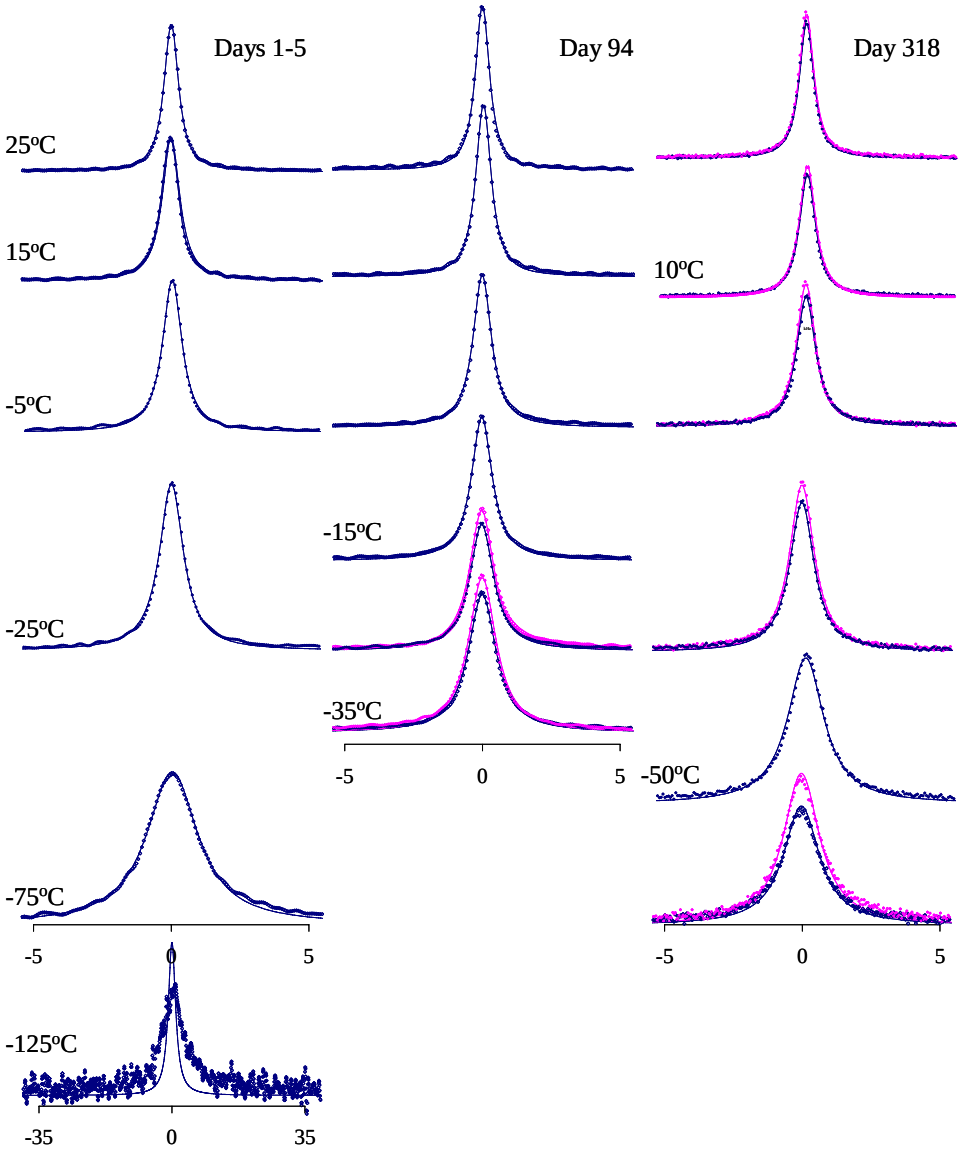

Figure 5.1. ^{2}H static solid-state NMR spectra of benzene-d_6 on CNP1 at different ages and temperatures with both 20 μs (pink)and 40 μs (blue) τ_{echo}, overlain by simulated spectra from DFP ISO library; open - experimental data point; lines – simulation

stemmed from the likelihood of π-π sorption interactions. However, because CNP is amorphous and, therefore, is likely to have a lesser amount of graphenic functionalities on the surface than does Boddenberg's graphitized carbon black, the supposition of face-to-face interactions with surface graphenes is less

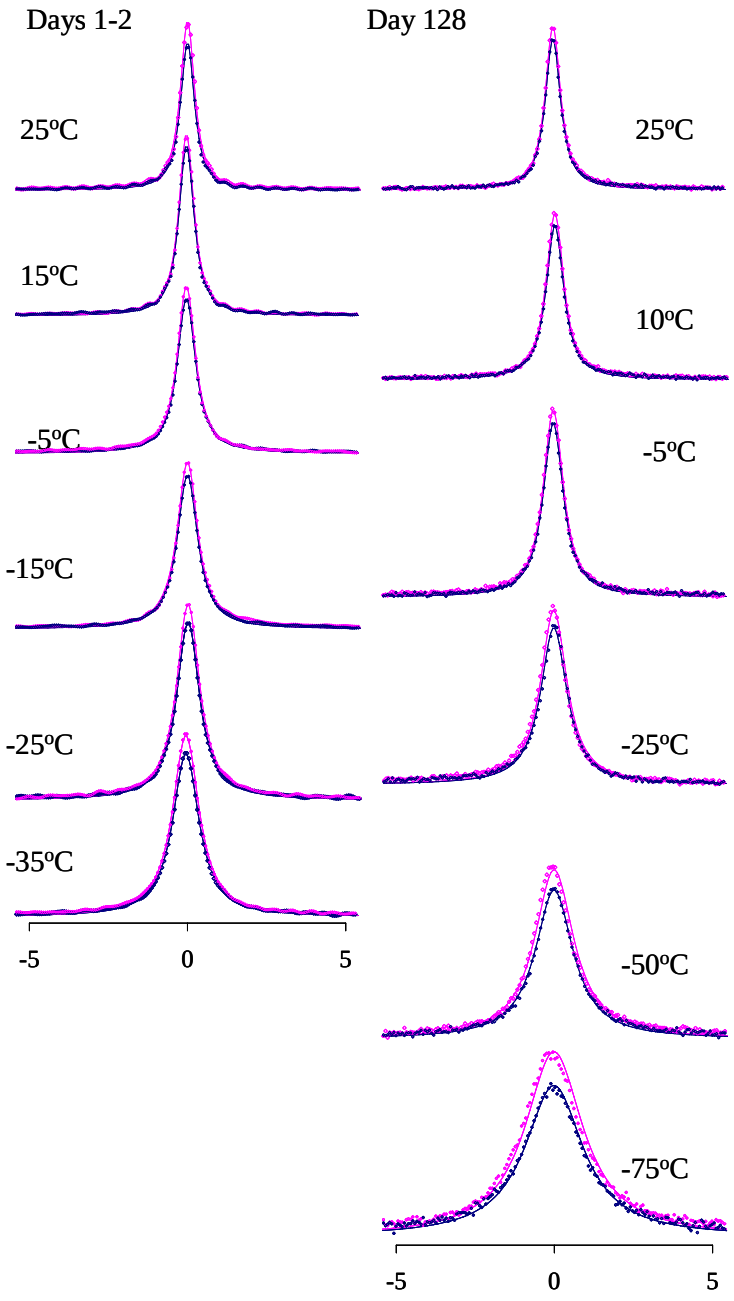

Figure 5.2. ^{2}H static solid-state NMR spectra of benzene-d_6 on CNP2 at different ages and temperatures with both 20 μs (pink) and 40 μs (blue) τ_{echo}, overlain by simulated spectra from DFP ISO library; open - experimental data point; lines - simulation.

straightforward. Therefore, it remains possible that the benzene molecules are more weakly sorbed to the CNP and could execute in-place isotropic motions within the pores or in proximity to the CNP surfaces.

Table 5.3. $\delta\nu$[a] (Hz) of the ^{2}H NMR spectra of benzene-d_6 on CNP samples at different ages and temperatures.

Sample	Temp (^{o}C)	Ages		
CNP1		Days 1-5	Day 94	Days 318
	25	585 Hz	571 Hz	591 Hz
		7200 scans	3600 scans	3600 scans
	15	713 Hz	621 Hz	
		1752 scans	3600 scans	
	10			673 Hz
				7200 scans
	-5	814 Hz	755 Hz	775 Hz
		1704 scans	3600 scans	7200 scans
	-15		856 Hz	
			3600 scans	
	-25	991 Hz	1003 Hz	1000 Hz
		2168 scans	3600 scans	7200 scans
	-35		1152 Hz	
			3600 scans	
	-50			1521 Hz
				7200 scans
	-75	2285 Hz		2485 Hz
		3600 scans		7200 scans
	-125	9352 Hz		
CNP2		Days 1-2	Day 128	
	25	540 Hz	553 Hz	
		3600 scans	7200 scans	
	15	550 Hz[b]		
		3600 scans		
	10		628 Hz	
			7200 scans	
	-5	654 Hz[b]	731 Hz	
		3600 scans	7200 scans	
	-15	732 Hz[b]		
		3600 scans		
	-25	817 Hz[b]	951 Hz	
		3600 scans	7200 scans	
	-35	946 Hz[b]		
		3600 scans		
	-50		1400 Hz	
			7200 scans	
	-75		2292 Hz	
			7200 scans	

[a]Peak widths at half-height, 40 μs echo delay, 1024 data points, no line broadening, zero-filled to 8192 data points; [b]peak widths by manual extrapolation; other peak from Spinsight software; manual and Spinsight values differed by <3% from 25°C to -35°C; peak width uncertainty $\pm$30 Hz, temperature uncertainty $\pm$0.1^{o}C.

The peak widths at half height, $\delta\nu$, for each of the 40μs spectra are listed in Table 5.3. There appears to be a mild increase in peak widths for the same

identical amounts of solid material and benzene-d_6. Nevertheless, although there was an increase in peak width at the same temperature with increasing age, which was particularly observable for Sample CNP2 (day 128). It is unclear why there is a 10-15% difference between the initial peak widths at the same temperature (25°C, 15°C, -5°C) for these two samples (Table 5.3), because the samples contain nearly may be a slight change in peak width with aging for the ^{2}H NMR spectra of benzene-d_6 on CNP (Figure 5.3), there is *no* change in the NMR peak area at

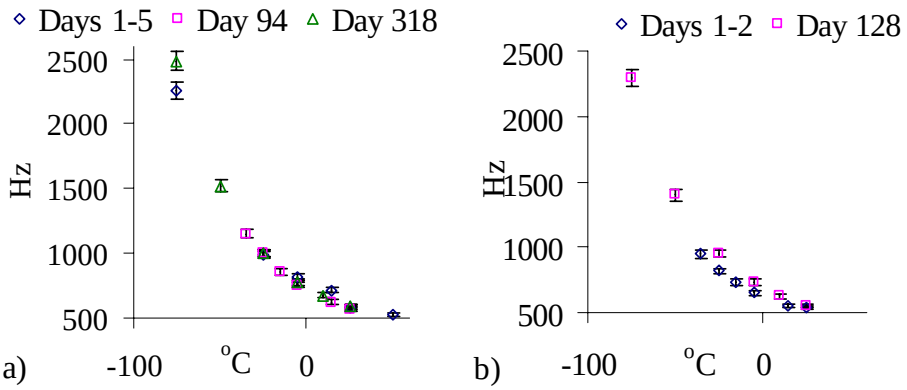

Figure 5.3. δν (spectral peak width at half-height) vs. temperatures for ^{2}H NMR spectra of benzene-d_6; a) CNP1; b) CNP2; uncertainty estimated at 3% for δν; temperature uncertainty $\pm$0.1°C.

different ages or at different temperatures (Figure 5.4), and this lack of change of signal intensity with temperature indicates that a constant motional regime is maintained. Therefore, an Arrhenius constant can be calculated from the jump rates as it was for the soot.

Arrhenius plots were prepared for different ages using jump rates calculated from DFP and from the peak width equation (Eqn. 4.3), provided below,

$$\delta\nu = (9\pi/20)\, QCC^2\, \tau. \qquad \textbf{(Eqn. 4.3)}$$

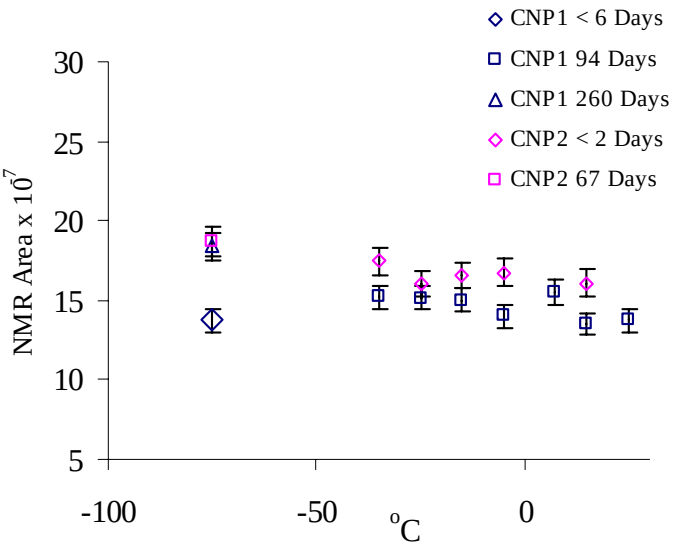

Figure 5.4. NMR areas under the spectral curve for data collected with 3600 scans on two CNP samples loaded with 1.5 (±0.1) µl benzene-d_6, as detailed in Table 5.2, for different ages and temperatures; error bars indicate estimated 5% variance for NMR areas; average area for CNP1 is 15.5 (±1.5), for CNP2 is 16.9 (±1.0).

The variables are defined as: $\delta\nu$, the peak width at half-height for the spectrum; *QCC*, the motionally averaged value of the quadrupole coupling constant; and τ_C, the reorientational correlation time and the reciprocal of the jump rate, *k*. Arrhenius values were calculated for each sample at each age, and using both sets of jump rates (DFP and Eqn. 4.3). As was observed for the Arrhenius plots of the soot sample and discussed in Chapter 4, the Arrhenius plots at different ages (Figure 5.5) result in parallel best fit lines for the data using DFP jump rates and the data obtained using peak width values, indicating that the energy of activation value is the same value as calculated by either method.

Figure 5.6 is the Arrhenius plot for CNP2. Figure 5.7 plots the E_a values over time for both samples. The average E_a value for the earliest ages of both samples, CNP1 (days 1-5) and CNP2 (days 1-2), is 6.2 (±0.4) kJ/mol, and, for all

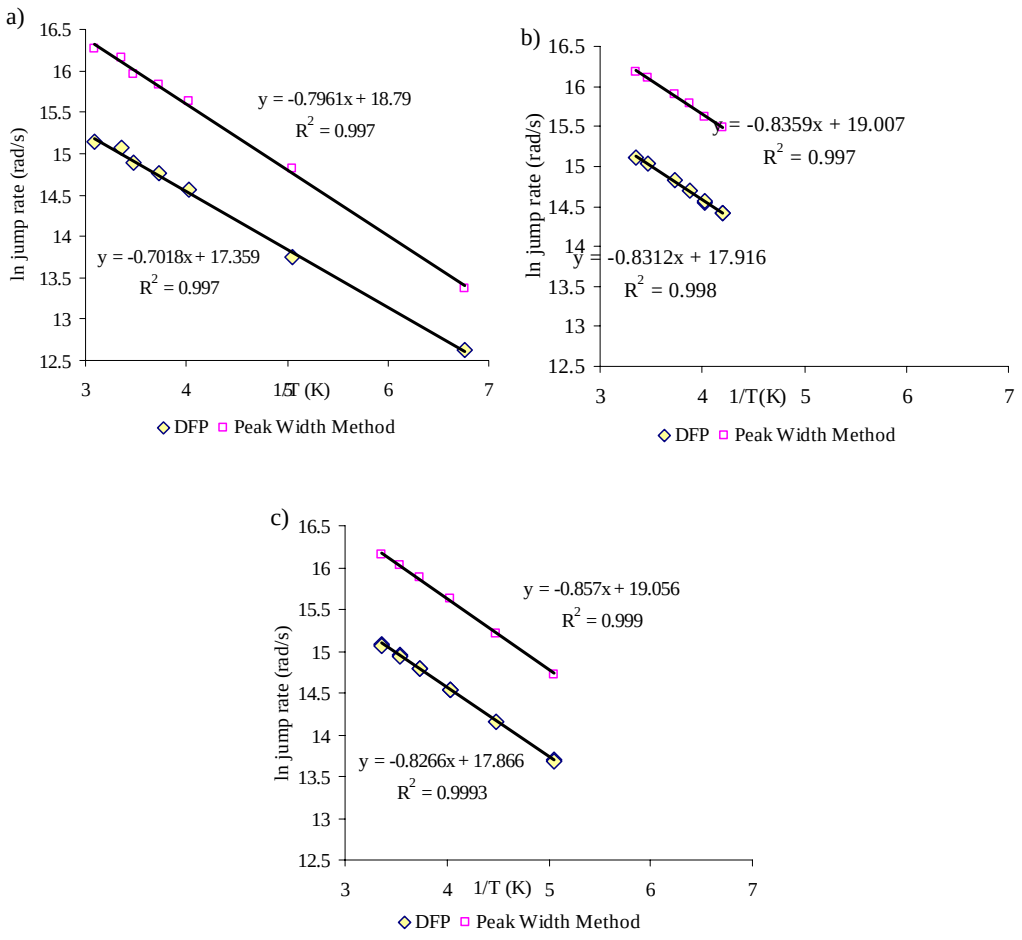

Figure 5.5. Arrhenius plots for CNP1 from jump rates based on DFP fits using ISO library (diamonds) and peak widths (pink squares): a) 1-6 days old, b) 94 days old, c) 318 days old.

the later ages, 7.0 (±0.1) kJ/mol. Therefore, despite the fact that the peak widths for the spectra on CNP1 and CNP2 show different peak widths for the same temperature at their respective early ages, the energies of activation for the variable-temperature spectra at that age matches. At later ages, the peak widths and the activation energies for both samples are very close to each other, 7.0 (±0.1) kJ/mol, and both of the samples show a small increase in the E_a with aging (Figure 5.7).

If, as Boddenberg's group [12, 13] did and as applied in this work to the soot

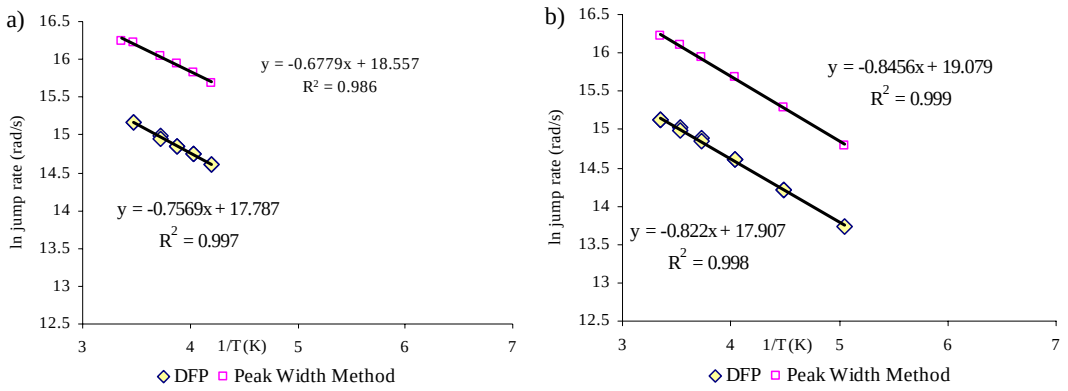

Figure 5.6. Arrhenius plots for CNP2 from jump rates using an ISO library from both DFP (diamonds) and Eqn. 4.3 (pink squares): a) 1-2 days old, b) 128 days old.

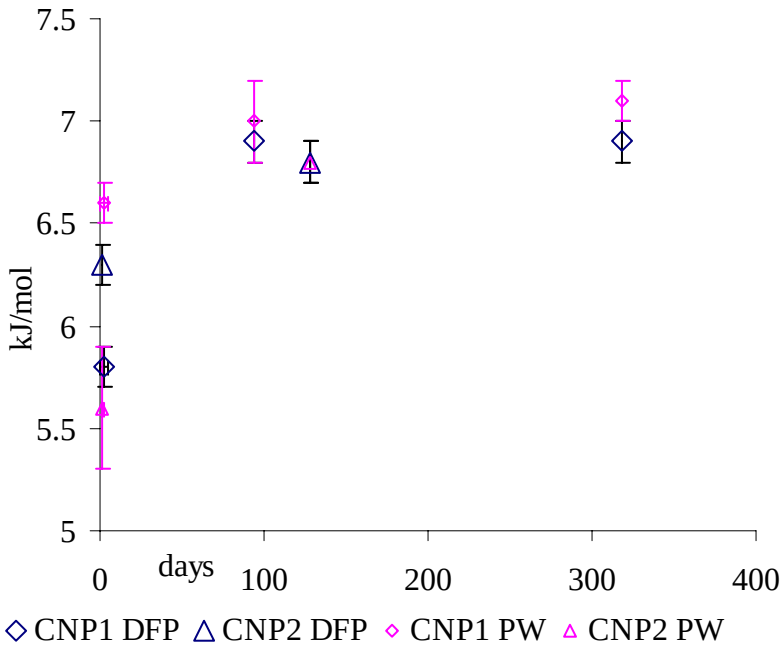

Figure 5.7. Energies of activation of the pseudoisotropic jump motion of benzene-d_6 on duplicate CNP samples at different ages.

samples (Chapter 4), the Einstein diffusion equation

$$D_0 = a^2 / 6\,\tau_0, \qquad \textbf{(Eqn. 4.5)}$$

is used to calculated D_0, it is necessary to determine τ_0, and a. When calculating D_0

Table 5.4. Arrhenius data for benzene-d_6 on CNP at different ages using both DFP and the peak width equation

Sample	Temperatures	Method	Age	E_a (kJ/mol)	R^2	k_0 (rad/s)
CNP1	50°C to -75°C	peak width	1-5 days	6.6 (±0.2)	0.997	1.4 (±0.1) x 10^8
	50°C to -75°C	DFP	1-5 days	5.8 (±0.1)	0.997	3.4 (±0.2) x 10^7
	25°C to -35°C	peak width	94 days	7.0 (±0.2)	0.997	1.8 (±0.1) x 10^8
	25°C to -35°C	DFP	94 days	6.9 (±0.1)	0.998	6.0 (±0.1) x 10^7
	25°C to -75°C	peak width	318 days	7.1 (±0.1)	0.999	1.9 (±0.1) x 10^8
	25°C to -75°C	DFP	318 days	6.9 (±0.1)	0.999	5.7 (±0.1) x 10^7
	50°C to -75°C	peak width	all	6.7 (±0.1)	0.998	1.5 (±0.1) x 10^8
	50°C to -75°C	DFP	all	6.0 (±0.1)	0.994	3.8 (±0.2) x 10^7
CNP2	50°C to -75°C	DFP	1-2 days	6.3 (±0.1)	0.997	5.3 (±0.1) x 10^7
	25°C to -75°C	peak width	128 days	7.0 (±0.1)	0.998	1.9 (±0.1) x 10^8
	25°C to -75°C	DFP	128 days	6.8 (±0.1)	0.998	6.0 (±0.1) x 10^7
	25°C to -75°C	peak width	all	7.1 (±0.4)	0.982	2.2 (±0.2) x 10^8
	50°C to -75°C	DFP	all	6.9 (±0.4)	0.980	6.6 (±0.5) x 10^7

for Carbopack B, Grundke and Boddenberg [13] assumed that the area traveled by the molecule around the surface of the particle, and, therefore, *a* is the particle radius. However, Boddenberg and Beerwerth [14] and Voss and Boddenberg [15] have also mentioned that the area traveled by the molecule could be the surface of the pore itself, making a is the *pore* radius (rather than the *particle* radius). The CNP has enough microporosity to accommodate the 1.5 μl of benzene-d_6 on the sample. Therefore, the pore size distribution curves for CNP from Chapter 3 (Figure 3.6, Table 3.2) can be used to approximate an average pore radius for calculation of the surface diffusivity. The loading of benzene-d_6 on graphite was 1.0% w/w, which, because the density of benzene-d_6 is 0.95 g/ml, was approximately 0.01 cc/g, and on the cumulative pore volume curves, one can read

that at 0.01 cc/g of pore-filling, the pore diameter is 10 Å or 1 nm, and thus the radius is 0.5 nm. Inserting this value and the τ_0 obtained from the Boddenberg peak width line, then the surface diffusion rate is:

$$D_0 = a^2 * k_0 / 6 \qquad \textbf{(Eqn. 5.1)}$$

$$= (0.5 \times 10^{-9}\ \text{m})^2 * 1.9 \times 10^8\ \text{rad/s} / 6$$

$$D_0 = 7.9\ (\pm 0.8) \times 10^{-12}\ \text{m}^2/\text{s}$$

The energy of activation for the motion of benzene adsorbed onto CNP, 7.0 ($\pm$0.1) kJ/mol, is much lower than on soot, 10.0 ($\pm$0.2) kJ/mol, and is closer to the energy of activation for the isotropic reorientational motion of neat liquid benzene, 6.5 kJ/mol [16]. Comparing the two-dimensional liquid motion of the benzene to its three-dimensional motion as a neat liquid, the C_6 rotation of benzene molecules in a neat liquid involves π-π interactions as does C_6 rotation of benzene adsorbed to aromatic carbon groups on graphite, and the rate of diffusion along the plane (which would correspond to along the surface for a flat, adsorbed molecule) is twice as fast as diffusion perpendicular to the plane in the neat liquid [17]. Therefore, if benzene on CNP executes translational motion across the surface while spinning about its C_6 axis, the Ea for this is only 2.5 kJ/mol above the same motion in the neat liquid, and tumbling end-over-end in the neat liquid has a higher activation energy (8.1 kJ/mol [17]) than does surface diffusion on CNP. The above discussion implies that, because the E_a for surface diffusion is directly related to the energy of adsorption [18], a benzene molecule appears not to be as strongly adsorbed to the surface of CNP as it is to the surface of soot and only slightly more attracted to the surface of CNP as it is to other benzene molecules.

A second important difference between the behavior of benzene on soot vs. CNP was that the E_a for CNP does show an increase over time (Figure 5.7, Table 5.4). Because the CNP contains a significant fraction of micropores (24% total porosity), and the soot contains only minimal (2%) microporosity, it seems likely that the increase in E_a of the rotational jump of benzene-d_6 indicates that the benzene has diffused over time into the micropores, where the adsorption potential from the pore walls is greater or where there are fewer opportunities to escape.

5.4 CONCLUSIONS

The motion of benzene-d_6 on amorphous carbon nanoparticles was examined as a reference material for the interaction of benzene with carbon which contains minimal graphenic functional groups on the surface with which to interact. In general, the low energy of activation, 7.0 ($\pm$0.1) kJ/mol, for the pseudoisotropic motion of benzene-d_6 on the surface of the CNP, as compared with E_a value of 10.1 ($\pm$0.2) kJ/mol on soot, did point away from a dominant π-π interaction between benzene-d_6 and CNP aromatic rings and may indicate that the benzene does not occupy a face-to-face configuration on the plane on the CNP surface, despite its close association with the surface as evidenced by the lowered freezing point and short T_1. However, the mere existence of a lowered E_a does not definitively indicate a nonplanar orientation of the sorbed benzene with respect to the surface because this could simply be the result of weaker surface interactions with the amorphous carbon. Therefore, this material could be considered a reasonable reference point for the minimal amount of benzene-graphene interaction to a nanocarbon surface for comparison with other BCs. Importantly, it did display a change with aging in the

motional activation energy which is attributable to slow diffusion into micropores, from which escape possibilities are limited.

References

1. Sigma-Aldrich Chemical Company Online Catalog: http://www.sigmaaldrich.com/technical-service-home/product-catalog.html, (2009).
2. Iijima, S.; Wakabayashi, T.; Achiba, Y., Structures of carbon soot prepared by laser ablation. *Journal of Physical Chemistry* **1996,** *100*, 5839-5843.
3. Ferrari, A. C.; Robertson, J., Interpretation of Raman spectra of disordered and amorphous carbon. *Physical Review B* **2000,** *61*, (20), 14,095-14,107.
4. Scilletta, C.; Servidori, M.; Orlando, S.; Cappelli, E.; Barba, L.; Ascarelli, K. P., Influence of substrate temperature and atmosphere on nano-graphene formation and texturing of pulsed Nd YAG laser-deposited carbon films. *Applied Surface Science* **2005,** *252*, 4877-4881.
5. Murr, L. E.; Bang, J. J.; Esquivel, E. V.; Guerrero, P. A.; Lopez, D. A., Carbon nanotubes, nanocrystal forms, and complex nanoparticle aggregates in common fuel-gas combustion sources and ambient air. *Journal of Nanoparticle Research* **2004,** *6*, 241-251.
6. Muller, J.-O.; Su, D. S.; Jentoft, R. E.; Wild, U.; Schlogl, R., Diesel engine exhaust emission: oxidative behavior and microstructure of black smoke soot particulate. *Environmental Science & Technology* **2006,** *40*, 1231-1236.
7. Connan, H. G.; Reedy, B. J.; Marshall, C. P.; Wilson, M. A., New nanocarbons: rod milling and annealing of graphite in the presence of yttrium. *Energy and Fuels* **2004,** *18*, 1607-1614.
8. Pimenta, M. A.; Dresselhaus, G.; Dresselhaus, M. S.; Cancado, L. G.; Jorio, A.; Saito, R., Studying disorder in graphite-based systems by Raman spectroscopy. *Physical Chemistry Chemical Physics* **2007,** *9*, 1276-1291.
9. Eastman, M. A.; Nanny, M. A., Fitting of deuterium quadrupole echo spectra with multiple motional models. *Journal of Magnetic Resonance* **2007,** *184*, 302-314.
10. Sanyal, S. K.; Samantaray, B. K.; Mitra, G. B., X-ray diffraction studies on the arrangement of atoms in carbon blacks. I. Results of radial distribution analysis. *Acta Crystallographica* **1982,** *A38*, 333-336.
11. Gedat, E.; Schreiber, A.; Albrecht, J.; Emmler, T.; Shenderovich, I.; Findenegg, G. H.; Limbach, H.-H.; Buntknowsky, G., ^{2}H solid-state NMR study of benzene-d_6 confined in mesoporous silica SBA-15. *Journal of Physical Chemistry B* **2002,** *106*, 1977-1984.
12. Boddenberg, B.; Grosse, R., A deuteron NMR study on a benzene multilayer on graphite. *Z. Naturforsch* **1987,** *421*, 272-274.
13. Grundke, V.; Boddenberg, B., One and two component adsorption layers of *n*-hexane and benzene on graphite studied by ^{2}H NMR spectroscopy. *Molecular Physics* **1993,** *79*, (6), 1215-1226.
14. Boddenberg, B.; Beerwerth, B., Proton and deuteron magnetic resonance spectra of benzene adsorbed on alumina and on a platinum/alumina catalyst. *Journal of Physical Chemistry* **1989,** *93*, 1435-1440.

15. Voss, V.; Boddenberg, B., Anisotropic reorientation dynamics of benzene molecules adsorbed on graphite, alumina, and zeolite Y. *Surface Science* **1993,** *298*, (241-250).
16. Wakai, C.; Nakahara, M., Attractive potential effect on the rotational correlation times for benzene-d_6 in organic solvents. *Bulletin of the Chemical Society of Japan* **1996,** *69*, 853-860.
17. Schwartz, M.; Duan, D.; Berry, R. J., Molecular dynamics study of anisotropic translational and rotational diffusion in liquid benzene. *J. Phys. Chem. A* **2005,** *109*, (38), 8637-8641.
18. Gilliland, E. R.; Baddour, R. F.; Perkinson, G. P.; Sladek, K. J., Diffusionon surface. I. Effect of concentration on the diffusivity of physically adsorbed gases. *Ind. Eng. Chem.; Fundam.* **1974,** *13*, 95-99.

CHAPTER 6. THE MOTION OF BENZENE-d_6 MOLECULES ON LOW-SURFACE-AREA GRAPHITE (LSAG) OBSERVED WITH STATIC SOLID-STATE ^{2}H NMR SPECTRA

6.1 INTRODUCTION

The mineral graphite is a common, naturally occurring form of graphene [1, 2], in which the graphene sheets are all planar and exist in a stacked three-dimensional (3D) configuration (Figure 6.1) [3, 4]. Therefore, the behavior of

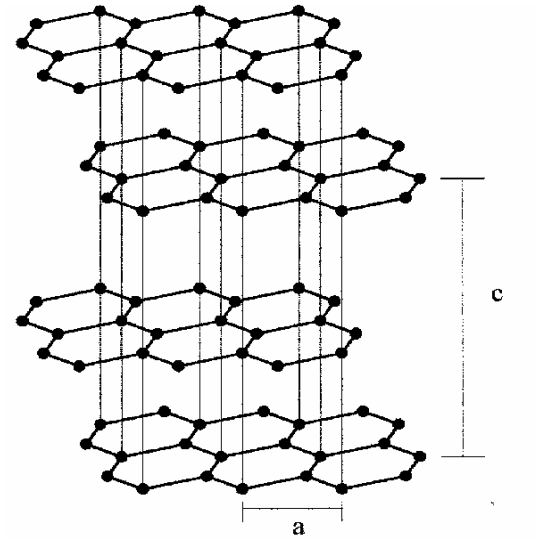

Figure 6.1 (also Figure 2.1) Crystallographic structure of graphite, a (2.46 Å) and c (7.71 Å) indicate the dimensions of the hexagonal unit cell [3, 4]

benzene-d_6 on its surface was chosen as an important reference standard with which to compare the behavior of benzene on other graphitic configurations. As discussed in the Introduction Chapter, adsorption theory predicts that the most energetically favored configuration of benzene on graphite is a face-to-face planar orientation which lines up the aromatic π bonds of benzene to the aromatic π bonds of graphite [5-7]. Further, the surface energy of the graphite is enhanced [8] by electron-donating contributions from lower graphene layers. Therefore, a well-ordered

crystalline graphite, such as this sample, should exhibit the maximum available energy for π-π interactions from a planar surface with adsorbing benzene molecules, as evaluated by the activation energy of the reorientational motion of benzene adsorbed on the LSAG surface, and test the utility of the graphite model for BC interactions with benzene.

6.2. EXPERIMENTAL – MATERIALS AND SAMPLE PREPARATION

The low surface-area graphite sample was purchased from Aldrich Chemical Company and its physical characteristics are outlined in Table 6.1. As detailed in

Table 6.1. Characteristics of low surface-area graphite

wt % Carbon[a]	% Other	[Ca] (ppm)[b]	Surface Area[a,c] (m^2/g)	Pore Size[c] (nm)	Particle Size dia[a] (μm)
≥ 99.99	-	< 194	4.5	0.5-50	44

[a]Aldrich catalog [9]; [b]Galbraith Laboratories; [c]from N_2 adsorption analysis, this work.

Chapter 3, the X-ray diffraction (XRD) analysis reveals diffraction peaks only from the 002 and 004 planes and lacks reflections from 100 and 110 planes which are commonly present in natural graphite samples. Such limited XRD reflections have been observed in graphite samples by others workers for very small grain sizes [10]. With regard to pore sizes, because graphite contains no *intra*granular porosity (for example, no zeolitic cages), the only pores were *inter*granular, due to the packing arrangements of the platey grains of crystalline graphite. Because of such a platey geometry, the assumption of slit-shaped pores by the Quantachrome nonlocalized density functional theory (DFT) pore size analysis program is justifiable for the low-

surface-area graphite [11], but the DFT analysis only applies for pores smaller than 6 nm (60Å) in diameter [12]. The sample exhibits local peaks in the pore size distributions with maxima at 1 nm and 3 nm, but these peaks account for less than 10% of the total pore volume, which was 0.034 ml/g according to the Dollimore-Heal (DH) calculation method. The remaining 90% of the pores are more or less randomly distributed in size, showing a gradual increase in the cumulative pore volume curve without the peaks visible in the smaller pore-size range (Figure 3.5). For each of the samples in Table 6.2, the volume of benzene-d_6 exceeds the volume of micro- and mesopores (0.70, 0.34, and 0.38 μl for GRAPH1, 2 and 3, respectively), but is less than half of the total pore volume (7.05, 3.45, and 3.83 μl, respectively). Thus, for all of the LSAG samples, the amount of benzene-d_6 exceeds not only one monolayer, but exists as a multilayer (or even a bulk) phase within micro-, meso-, and macropores.

Table 6.2 Samples of benzene-d_6 on low-surface-area graphite

Sample Name	Mass of Graphite (mg)	Deposited Volume of Benzene (μl)	Volume of Benzene per NMR Quantitation Plot	% load (w/w)	% loading (monolayer coverage)
GRAPH1	207.3 (±0.1)	2.2 (±0.1)	1.5 (±0.3)	1.0 (±0.1)%	735 (±2)%
GRAPH3	101.4 (±0.1)	1.1 (±0.1)	1.0 (±0.3)	1.0 (±0.1)%	756 (±2)%
GRAPH4	112.5 (±0.1)	0.6 (±0.1)	0.4 (±0.1)	0.5 (±0.1)%	372 (±2)%

The three samples, each at different loadings, (Table 6.2) were prepared according to the procedure outlined in the Experimental Chapter (Chapter 2). The solid phase was placed into a specially necked 10 mm NMR tube which was attached to a vapor deposition manifold. A precise amount of benzene-d_6 was

condensed into the NMR tube, which was submerged in liquid nitrogen, and the sample was subsequently backfilled with N_2 gas to 200-400 torr, flamed-sealed, and removed to the Oklahoma Statewide NMR Facility at Stillwater, Oklahoma, for collection of the variable-temperature solid-state ^{2}H NMR spectra on the Chemagnetics 300 MHz instrument. A quadrupole echo sequence ($\pi/2 - \tau_{echo} - \pi/2 - \tau_{echo}$ – acquire) at 46.20525 MHz was used to collect all spectra. The excitation frequency used was that which provided the maximum signal intensity and was the same for benzene-d_6 on all BC solid phases in the study. In order to verify the quantities of benzene-d_6 loaded into both samples, an NMR spectra was collected with standard parameters (10 s delay time, 128 scans, 25°C, 20 μs echo tau, 1024 data points, and 1 kHz line broadening), and the curve areas compared to a quantitation curve prepared from NMR spectra of sealed liquid benzene-d_6 collected with those same parameters, as described in the Appendix A1 (Figure A1.3). The quantities of benzene-d_6 predicted from the NMR area calibration curve (Figure 2.4) are acceptably close to the quantities measured with the vapor deposition system (Dr. Margaret A. Eastman, personal communication, 2006). The NMR predicted values for benzene-d_6 on the LSAG samples are slightly lower than measured with the manifold system, although much closer to the calibration curve than for most of the other BC samples in this study (Figure A1.4). For collecting solid-state ^{2}H NMR spectra at variable temperatures for jump rate determination, the instrumental parameters were 1800-7200 scans, delay times ranging from 0.50-10.0 s, either 20 μs or 40 μs τ_{echo} values, either 1024 or 8196 data points, and the spectra were processed with zero filling (if necessary) to 8196 points without line broadening.

Because these samples contained multilayer quantities and included a separate liquid benzene-d_6 phase (more than 4 monolayers) [11], longer relaxation delays were required to quantitatively observe the liquid phase, with its T_1 value of 1.5 s at 25°C. Also, the spectra did not consist solely of a powder pattern, and thus were not amenable to fitting with DFP. However, the peak width value was available for calculating jump rates, as described below.

6.3 ^{2}H NMR SPECTRA AND RESULTS FOR LOW SURFACE-AREA GRAPHITE

6.3.1 ^{2}H NMR static solid-state spectra, 25°C

The spectrum of benzene-d_6 loaded at 1% w/w on Sample GRAPH1, displayed in Figure 6.2 a), displays two Lorentzian peaks, one with a negative offset positive offset. These two peaks are due to the deuterium quadrupole coupling,

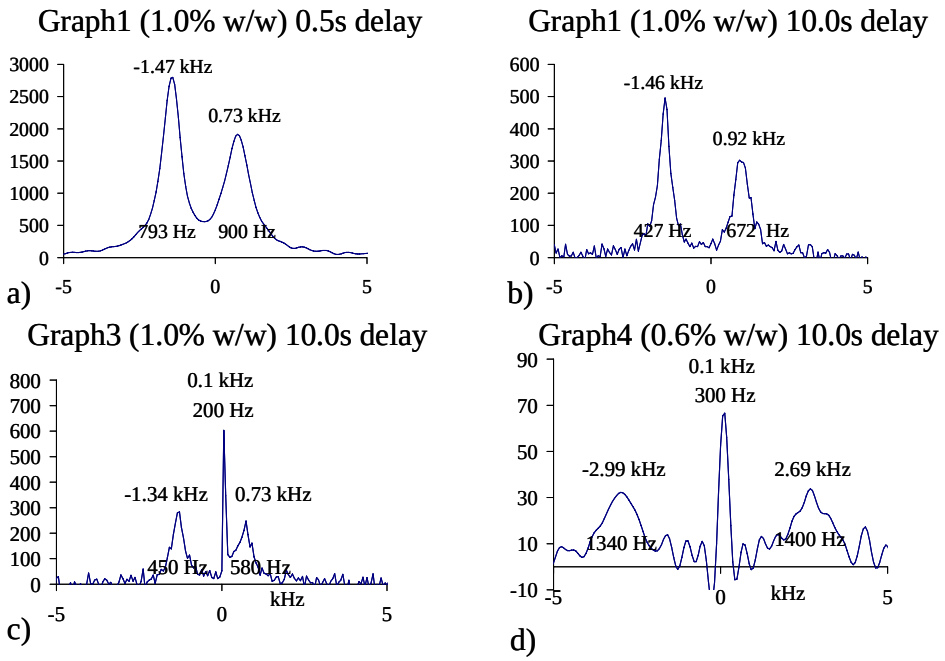

Figure 6.2. ^{2}H NMR spectra of benzene-d_6 on graphite at 25°C with loadings and relaxation delay times as specified in the figure; each peak is labeled with the shift from the spectrum's center (kHz) and the δν (Hz); the central peak in c) and d) is attributed to gaseous benzene; see text for explanation.

from the central deuterium resonance and another smaller amplitude peak with a which is revealed by the orientational ordering effect of the graphite planar surface acting as a director on the benzene-d_6 molecules as they exchange between the bulk and the surface adsorbed phases. Such an effect has previously been observed and described in oriented sol gels [13] and on clay platelets [14] and, although two phases are present, each peak does *not* indicate a separate phase with a separate chemical shift. Rather, the amount of the splitting is function of the exchange motion of the benzene-d_6 between the two phases, and, thus, lower loadings have a slower rate of exchange and wider splitting, as well as wider peak widths. The reason the positive peak is shorter and wider is due to the effect of the magnetic anisotropy of graphite, which was also observed by Boddenberg's group [15, 16] to produce a slight distortion of the Pake patterns of a two-dimensional (2D) solid benzene-d_6 adsorbed on Carbopack B graphitized carbon (Introduction Chapter, Figure 24a, 112K spectrum). Lower loading of benzene-d_6 on the graphite (0.6% w/w) results in a greater fraction of the benzene-d_6 molecules existing in the adsorbed phase and causes a larger separation of the two peaks, as seen in Figure 6.2d.

Another interesting feature of these spectra was the central narrow peak displayed for Sample GRAPH3, a 1% w/w loaded sample, and Sample GRAPH4, a 0.6% loaded sample, in Figure 6.2c and d. This central peak can be explained as follows: it is known that the effect of the surface on a liquid commonly extends out to only three or four molecular layers [17], and, consequently, a sample which contained over seven nominal monolayers of benzene-d_6, such as GRAPH1 and GRAPH3, would contain liquid benzene-d_6 as a separate phase, which would also

be in equilibrium with a separate gaseous benzene-d_6 phase. Further, it can be deduced that this peak observed in the spectrum of GRAPH3 was indeed in the gas phase by its very narrow peak width (200-300 Hz) and by the reduction in peak height which was observed when the temperature was lowered by 3°C to 22°C. In order to estimate the possible amount of gaseous benzene present in the GRAPH1 sample, one can begin by estimating the volume inside the sample tube at 1.62 ml, deducting the volume of graphite which has a density of 2.1 g/ml, the number of moles of benzene in the vapor phase can be estimated at 6.3×10^{-6} moles from the ideal gas law and the vapor pressure of benzene, 70 torr (CRC). The total amount of benzene in the sample is known to be 2.5×10^{-5} moles, so that as much as 25% of the sample benzene-d_6 could exist in the gas phase at 25°C. However, although GRAPH1 and GRAPH3 contained the same loading level of benzene-d_6, only GRAPH3 displayed a central peak. It may be suspected that, because many of the spectra of GRAPH1 were collected using a 0.5 s relaxation delay, possibly the gaseous benzene nuclei were saturated and thus not detected. Yet a spectrum of GRAPH1 at 25°C using a 10 s delay is shown in Figure 6.2c, and the spectrum still did not display a central gaseous peak. Therefore, it must be concluded that capillary condensation within the pores of the graphite in GRAPH1 prevented a detectable amount of benzene-d_6 from existing in the gas phase in this sample. This hypothesis is supported by the fact that the two samples which did show a central gaseous peak, GRAPH3 and GRAPH4, contained approximately half the amount of graphite which was present in GRAPH1, and so would have had fewer pores available for vapor pressure reduction. However, inhomogeneity of the magnetic field from the probe coils can also affect the detection of the gaseous peak, and this

is noticeable if the sample is placed at different positions within the coil [18]. However, all three of these sample tubes were sufficiently large as to restrict variability of placement within the coil.

With respect to aging, the GRAPH1 sample did not appear to experience changes with aging, although because of a lack of spectra which were collected at identical conditions at different ages, the changes in peak width and peak area over time could not be evaluated in the same manner as was done for the other samples. However, the offsets from spectral center and quadrupolar splittings had the same value at 15°C, -5°C, and -25°C for spectra collected at different ages, discussed below, and this indicates a lack of motional change with aging.

6.3.2 ^{2}H static solid-state NMR spectra at variable temperatures

The two Lorentzian peaks described at 25°C remain in the spectra as the temperature is lowered (Figure 6.3), even at a temperature as low as 100°C, and their relative heights did not change with temperature (Table 6.3), although their peak separation did. This was a significant freezing point depression, recalling that neat benzene freezes at 5.5^{o}C, and indicated the presence of a 2D adsorbed liquid phase [15, 16, 19-22]. The spectrum at -5°C and at lower, also displays a Pake component at $\pm$34 kHz, which is the quadrupole splitting value expected for bulk solid benzene-d_6. Therefore, one may conclude that the bulk liquid benzene-d_6 with which the adsorbed benzene-d_6 molecules were exchanging at 25°C has solidified into separate individual crystallites. As the temperature decreased from -5°C to -100°C, the fraction of benzene molecules in the adsorbed phase can be seen to decrease, based upon the relative areas of the inner Lorentzian peaks to the Pake peaks. The right side of Figure 6.3 shows the detail of the inner Lorentzian peaks,

and these can be seen to increase their separation as the temperature is decreased (Table 6.4), just as the separation increased with lower loadings at 25°C. In both

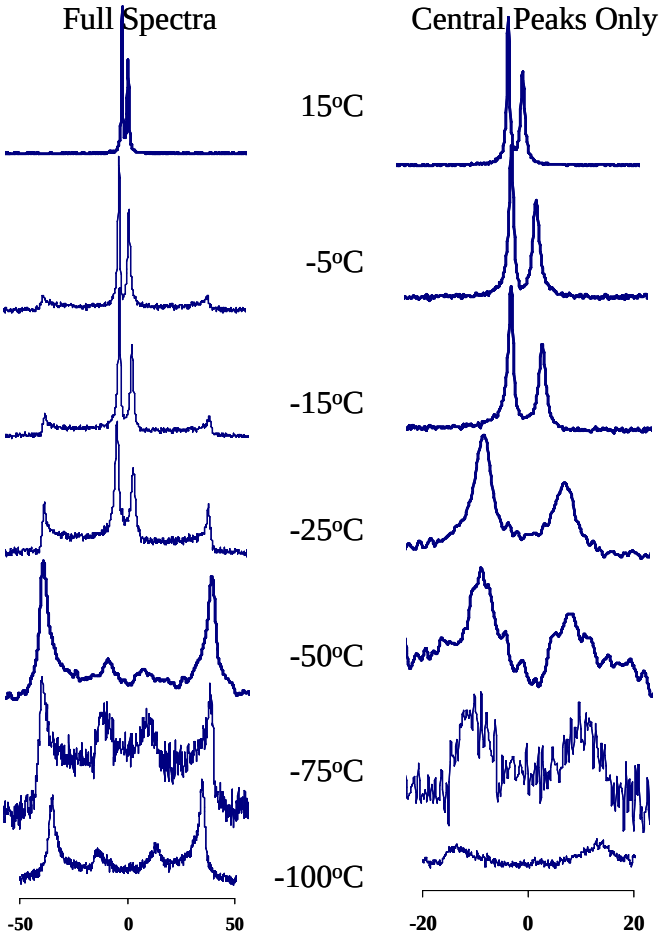

Figure 6.3. Variable-temperature ^{2}H static solid-state NMR spectra of benzene-d_6 on LSAG (1% w/w loading), sample GRAPH1; see Table 6.3 for spectral data.

cases, this is the result of the lower amount of adsorbed phase and lower rate of exchange with the bulk, and, additionally, it can be seen that there is no effect of aging on the amount of this splitting. Therefore, spectra from different ages can be used to calculate the Arrhenius value, and the peak width equation was used to

Table 6.3. Spectral data from the ^{2}H NMR spectra of benzene-d_6 on low-surface-area graphite at different temperatures.

Sample	Age (days)	Number of scans	Pulse Delay (s)	Temp (^{o}C)[a]	$\Delta\upsilon$ (kHz)[b,c]	Shift from Spectral Center (kHz)		
						Positive Peak	Negative Peak	Center Peak
GRAPH1								
	1	3600	0.50	25.0	1.9	0.2	-1.7	[d]
	396	256	10.00	25.0	2.4	0.9	-1.5	[d]
	111	7200	0.50	22.5	2.4	0.5	-1.9	[d]
	1	1800	0.50	15.0	2.4	0.7	-1.7	[d]
	103	7200	0.50	15.0	2.4	0.7	-1.7	[d]
	1	1824	0.50	-5.0	3.9	1.3	-2.6	[d]
	103	7200	0.50	-5.0	3.9	1.2	-2.7	[d]
	103	7200	0.50	-15.0	5.4	2.2	-3.2	[d]
	1	7200	0.50	-25.0	7.4	3.2	-4.2	[d]
	103	7200	0.50	-25.0	6.9	2.7	-4.2	[d]
	287	3600	1.25	-35.0	8.3	3.7	-4.6	[d]
	349	4800	0.50	-50.0	14.6	6.1	-8.5	[d]
	1	3600	0.50	-75.0	18.5	9.5	-9.0	[d]
	349	4800	0.50	-100.0	26.5	13.6	-12.9	[d]
	204	3600	0.50	-115.0	29.3	14.4	-14.9	[d]
GRAPH3	1	256	10.00	25.0	2.0	0.7	-1.3	-0.2
GRAPH4	1	256	10.00	25.0	5.9	2.7	-3.2	0.0

[a]Uncertainty in temperature measurement $\pm$0.1^{o}C; [b]peak separation between positive and negative peaks due to quadrupolar splitting; [c]uncertainty in frequency $\pm$0.06 kHz; [d]central peak not present.

determine the jump rate based on the peak widths at half-height ($\delta\nu$), listed in Table6.4. It was not possible to use DFP to fit these spectra because the program was not designed to simulate split Lorentzian peaks. The E_a and pre-exponential values from the Arrhenius plots of the jump rate of benzene-d_6 on graphite are (1) 10.4 ($\pm$1.1) kJ/mol and 6.4 ($\pm$1.2) x 10^8 rad/s, (2) 9.8 ($\pm$0.6) kJ/mol and 3.7 ($\pm$0.4) x 10^8 rad/s, (3) 10.1 ($\pm$1.1) kJ/mol and 4.8 ($\pm$1.2) x 10^8 rad/s, for (1) the negative peak, (2) the positive peak, and (3) their average, respectively (Figure 6.4).

Table 6.4. δν (Hz)[a] of the static solid-state ^{2}H NMR spectra of benzene-d_6 on low surface-area graphite samples at different temperatures.

Sample	Temp (°C)	Age	δυ (kHz)[a]	
GRAPH1			Positive Peak	Negative Peak
	25	1	0.73 (+0.06) kHz	0.49 (+0.06) kHz
	15	103	0.86 (+0.06) kHz	0.61 (+0.06) kHz
	-5	103	1.47 (+0.06) kHz	0.92 (+0.06) kHz
	-15	103	1.65 (+0.06) kHz	1.10 (+0.06) kHz
	-25	103	2.03 (+0.06) kHz	1.71 (+0.06) kHz
	-50	349	7.3 (+2.0) kHz	4.7 (+2.0) kHz
	-75	1	6.2 (+2.0) kHz	5.6 (+2.0) kHz

[a]Peak width at half-height collected manually; [b]noisy spectra did not allow for measurement precision better than 2 kHz.

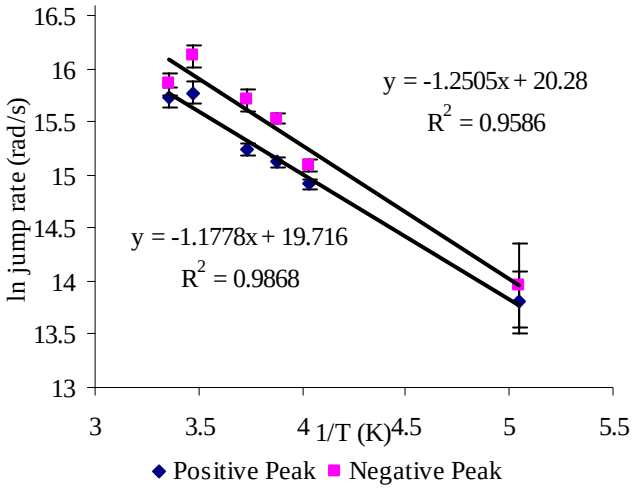

Figure 6.4. Arrhenius plot of jump rates calculated using the peak width method from the spectra in Figure 2 of samples GRAPH1. Error bars represent the uncertainty in the peak width measurement.

However, this evaluation must be applied with some caution for several reasons. First, the peak widths were measured from spectra collected with a 0.50 s relaxation delay, but, because of the long T_1 value for liquid benzene, a 10.0 s delay would have been preferable. Second, the basic assumption that the molecule was actually behaving as a solid on the surface [16] has clearly been violated by the occurrence

of a separate liquid benzene phase contributing to these peaks. Third and last, for these samples, the radius of spherical motion from the Einstein equation could not be taken as the radius of the particles because the particles was too large (22 μm radius) to be considered near the molecular dimensions of benzene, which was also important assumption underlying the peak width formula [16]. Consequently, as was done for the soot and the CNP, a value for the mean pore radius explored by the benzene-d_6 molecules can be obtained from the pore size distribution in Chapter 3 (Figure 3.4, Table 3.2). Following the cumulative pore volume curve to 0.01 cc/g loading, the maximum pore size is indicated to be approximately 25 nm (250Å), making the radius 13 nm. Using this value for a in the diffusion equation (Eqn. 4.5) and $1/k_0$ from the average value above, then the surface diffusivity, D_0, was 4.8 ($\pm$0.8) x 10^{-8} m^2/s, which was close to the 2 x 10^8 m^2/s determined by Grundke and Boddenberg [16], although the E_a values differ considerably (3.8 kJ/mol vs. 10.1($\pm$1.1) kJ/mol for Grundke and Boddenberg [16] and this work, respectively). As discussed with respect the to soot results in Chapter 4, the value of 3.8 kJ/mol would appear to be too low, especially since it is lower than the value for neat benzene, 6.5 kJ/mol [23]. This would imply that benzene is more attracted to other benzene molecules than to graphite, in which case, it would be expected than benzene would not spread on the graphite surface, but would pool into droplets, and the contact angle between benzene and graphite would be negative [17]. Since this behavior is not observed, the 10.1($\pm$1.1) kJ/mol value measured here, although it represents a more complicated motion of exchange between two phases, was considered to be a more supported measurement for the actual E_a of the surface diffusion of benzene on graphite.

6.4. CONCLUSIONS

The molecular motion of benzene-d_6 diffusing on the surface of planar graphite grains and exchanging between this adsorbed phase and a bulk liquid phase has been observed with ^{2}H solid-state NMR. A director for the benzene's motion revealed peaks split by quadrupole coupling at temperatures above the bulk freezing point of benzene attributable to exchange between the two phases. The occurrence of a minor separate gas phase was also observed at 25°C in one of the samples. The surface diffusivity/phase exchange rate was calculated from variable temperature experiments, and a value of 10.1($\pm$1.1) kJ/mol was measured for the E_a of this motion. This value slightly exceeds that measured for the carbon nanoparticles (Chapters 4 and 5), as is expected for a more ordered solid phase.

References

1. Mauter, M. S.; Elimelech, M., Environmental applications of carbon-based nanomaterials. *Environmental Science & Technology* **2008,** *42*, (16), 5843-5859.
2. Keiluweit, M.; Kleber, M., Molecular-level interactions in soils and sediments: the role of aromatic #-systems. *Environmental Science & Technology* **2009**.
3. Pan, B.; Xing, B., Adsorption mechanisms of organic chemicals on carbon nanotubes. *Environmental Science & Technology* **2008,** *42*, (24), 9005-9013.
4. Sun, G.; Kurti, J.; Kertesz, M.; Baughman, R. H., Variations of the geometries and band gaps of single-walled carbon nanotubes and the effect of charge injection. *Journal of Physical Chemistry B* **2003**, (107).
5. Do, D. D.; Do, H. D., Adsorption of benzene on graphitized thermal carbon black: reduction of the quadrupole moment in the adsorbed phase. *Langmuir* **2006,** *22*, 1121-1128.
6. Vernov, A.; Steele, W. A., Computer simulations of benzene adsorbed on graphite. 1. 85K. *Langmuir* **1991,** *7*, 3110-3117.
7. Vernov, A.; Steele, W. A., Computer simulations of benzene adsorbed on graphite. 2. 298K. *Langmuir* **1991,** *7*, 2817-2820.
8. Fodi, B.; Hentschke, R., Molecular dynamics simulation of a binary hydrocarbon mixture near an adsorbing wall: benzene/I-heptane on graphite. *Langmuir* **1998,** *14*, 429-437.

9. Sigma-Aldrich Chemical Company Online Catalog: http://www.sigmaaldrich.com/technical-service-home/product-catalog.html, (2009).
10. Connan, H. G.; Reedy, B. J.; Marshall, C. P.; Wilson, M. A., New nanocarbons: rod milling and annealing of graphite in the presence of yttrium. *Energy and Fuels* **2004,** *18*, 1607-1614.
11. Gregg, S. J.; Sing, K. S. W., *Adsorption, Surface Area, and Porosity*. Academic Press: New York, NY, 1982.
12. Quantachrome, *Users Manual*.
13. Fukasawa, J.-i.; Poon, C.-D.; Samulska, E. T., Deuterium NMR investigation of benzene adsorbed on boehmite glass. *Langmuir* **1991,** *7*, 1727-1733.
14. Delville, A.; Grandjean, J.; Laszlo, P., Order acquisition by clay platelets in a magnetic field. NMR study of the structure and microdynamics of adsorbed water layer. *Journal of Physical Chemistry* **1991,** *95*, 1383-1392.
15. Boddenberg, B.; Grosse, R., A deuteron NMR study on a benzene multilayer on graphite. *Z. Naturforsch* **1987,** *421*, 272-274.
16. Grundke, V.; Boddenberg, B., One and two component adsorption layers of *n*-hexane and benzene on graphite studied by ^{2}H NMR spectroscopy. *Molecular Physics* **1993,** *79*, (6), 1215-1226.
17. Adamson, A.; Gast, A. P., *Physical Chemistry of Surfaces*. John Wiley & Sons: New York, 1997; p 784.
18. Eastman, M. A.; Brothers, L. A.; Nanny, M. A., **in press**.
19. Tabony, J.; White, J. W.; Delachaume, J. C.; Coulon, M., Nuclear magnetic resonance studies of the melting and orientation of benzene adsorbed upon graphite. *Surface Science* **1980,** *95*, L282-L288.
20. Tabony, J.; White, J. W., Nuclear magnetic resonance from a quasi two dimensional fluid: Neopentane adsorbed upon graphite. *Molecular Physics* **1980,** *40*, (5), 1209-1225.
21. Boddenberg, B.; Beerwerth, B., Proton and deuteron magnetic resonance relaxation of benzene adsorbed on alumina and on a platinum/alumina catalyst. *Journal of Physical Chemistry* **1989,** *93*, 1440-1447.
22. Boddenberg, B.; Beerwerth, B., Proton and deuteron magnetic resonance spectra of benzene adsorbed on alumina and on a platinum/alumina catalyst. *Journal of Physical Chemistry* **1989,** *93*, 1435-1440.
23. Wakai, C.; Nakahara, M., Attractive potential effect on the rotational correlation times for benzene-d_6 in organic solvents. *Bulletin of the Chemical Society of Japan* **1996,** *69*, 853-860.

CHAPTER 7. THE MOTION OF BENZENE-d_6 MOLECULES ON CARBON NANOTUBES OBSERVED WITH STATIC SOLID-STATE ^{2}H NMR SPECTRA

7.1 INTRODUCTION

Understanding the sorption interactions of benzene and related compounds with carbon nanotubes is important for designing carbon nanotube (CNT) sorbents for hydrophobic organic contaminants (HOCs) in both analytical and environmental remediation applications [1-4], for functionalization reactions that involve benzene or related compounds to modify CNTs as sensors or catalysts [5], and for predicting the transport behavior of benzene through hydrophobic cylindrical pores for separations and biochemical applications [6-10]. Because CNTs are ideally composed of tubes of single, double or multiple graphene layers, held to each other by the same van der Waals' forces that hold together layers of planar graphite [1, 11, 12], the adsorption interactions of benzene with CNTs could be expected to involve π-π and dispersive interactions, very similar to those observed with graphite. This hypothesis can be tested by examining the molecular motion of benzene in vapor/solid equilibrium diffusing on the CNT surface because the motional orientations and jump rates can serve as a probe for the types of interactions and the chemical functionalities on the CNT surface with which the benzene is interacting [13-17].

Because it is difficult to synthesize and isolate structurally ideal CNTs, a great scientific effort is currently underway to discover techniques that will result in minimal impurities and defects and to functionalize the CNTs for specific applications [5, 18, 19]. Consequently, an extremely wide range of CNT structures

in various stages of purification have been presented in the literature, e.g. [11, 12, 19, 20], and a brief mention of the chemical bonds and functionalities at the surface of CNTs is warranted at this point. Single-walled carbon nanotubes (SWCNTs) have been synthesized with diameters in the micropore to small mesopore range, with specific chiral angles (See Introduction Chapter, Figure 1.12), and with either armchair or zigzag configurations (Fig 7.1) parallel to the tube axis [19, 21, 22]. Multi-walled carbon nanotubes

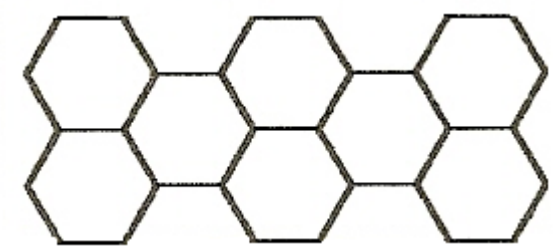

Figure 7.1. Diagrammatic illustration of armchair (top and bottom edges) and zigzag (side edges) of graphene [23].

(MWCTNs) can be thought of as consisting of an outer surface of a SWCNT, with the same surface chemical functionalities. These linear, ideal structural configurations are accompanied by the presence of suspected Stone-Wales defects, which are 5-7-7-5 ring configurations (Figure 7.2), and associated with the growth of fullerenes, onions, and

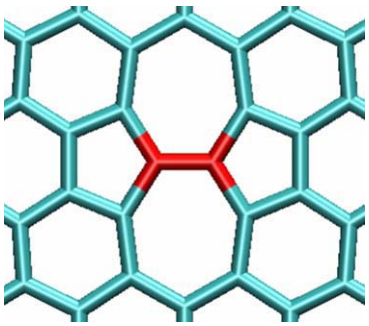

Figure 7.2. Diagrammatic illustration of a Stone-Wales defects from Ma et al. [24]

amorphous carbon particles (Introduction Chapter, Figure 1.11) [25, 26]. Lastly, CNTs are subject to the same kinds of edge defects, point defects and dislocation defects that occur in other graphites [27], illustrated in Figure 7.3. However, the location of the edges (Figure 7.4) is important for functionalizing CNTs [28].

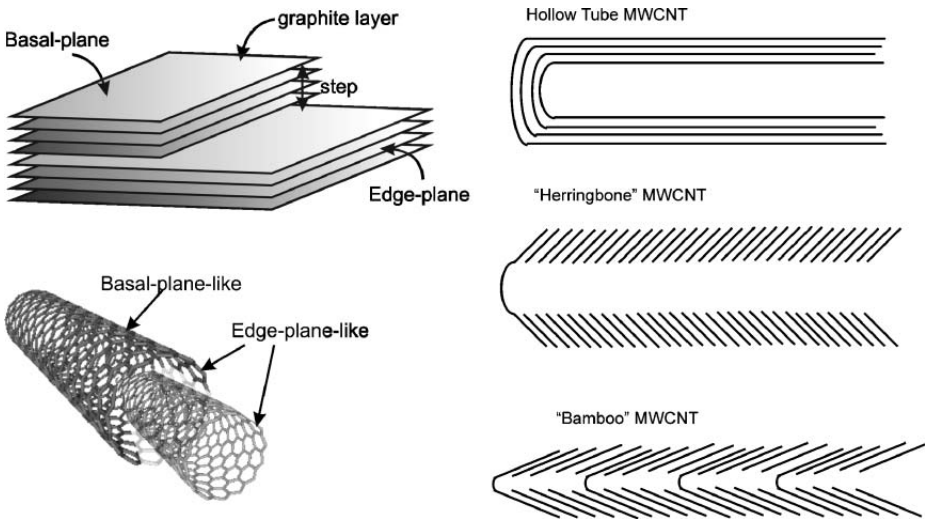

Figure 7.3. Diagrammatic illustration of edge-associated defects in CNTs [28].

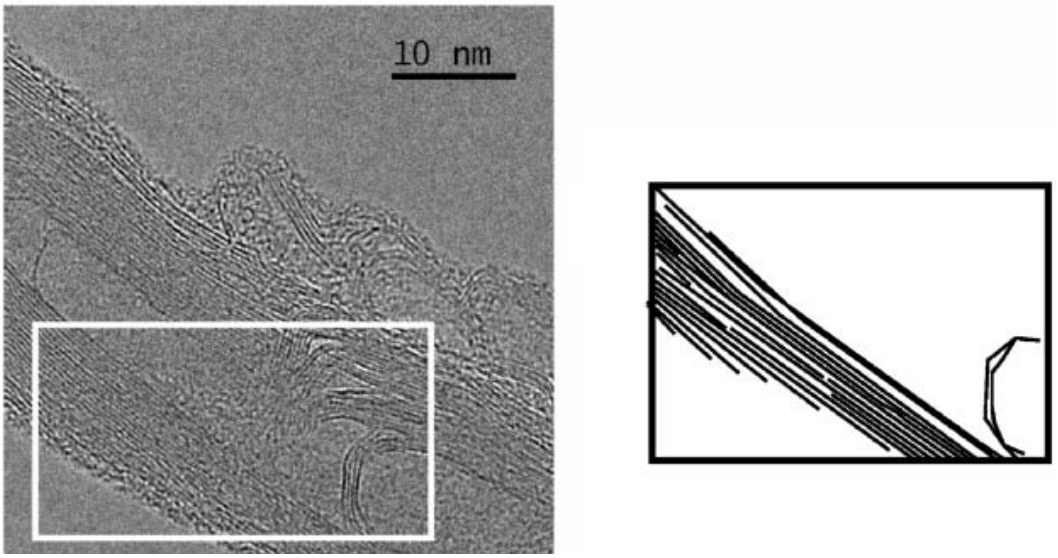

Figure 7.4. Transmission electron microscopy image of bamboo-MWCNT (left) and a trace of the carbon walls for the highlighted regions, which shows the graphene plane terminal edges [28].

Double and multi-walled CNTs are also subject to structural complications resulting from interlayer stacking of the tubes such as the presence of turbostratic graphite layers, in which there is no stacking order between adjacent graphene planes [23, 29-31]. These above-described defects and structural irregularities provide sites for epoxide formation with molecular oxygen in the air or oxygen in acidic purifying agents [20, 32] and for free radical attack by nucleophilic derivatizing agents, e.g. anthraquinone-1-diazonium chloride, which produces teardrop structures (Figure 7.5) [28].

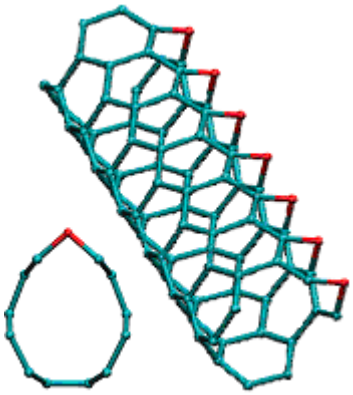

Figure 7.5. Teardrop structure (upper) in CNTs from attachment to oxygen on CNT exterior from Kutana and Giapis [33].

While it is unknown whether the MWCNTs used in this study are predominantly hollow tube, herringbone, or bamboo structures, the above configurations of carbon surface functionalities on CNT shown in Figure 7.3 present two different types of possible interaction sites for a benzene sorbate molecule: (1) “edge-plane like” or (2) “basal-plane-like” [28]. Because the samples prepared in this study were not exhaustively degassed, it is likely that some water molecules remained adsorbed to the surface, and this water adsorption most commonly occurs

at edge or defect sites and results in an acidic proton at that site REF. Benzene, which can act as a hydrogen acceptor [5, 27, 34, 35], could therefore interact with these acidic protonated defect sites, and the expected adsorption enthalpies, $\Delta H_{adsorption}$, would be in the chemisorption region (greater than approximately 40 kJ/mol) [15, 36, 37], and, thus, expected surface diffusion energy of activation (E_a) values would be greater than approximately ½ of that value, or 20 kJ/mol [38]. If, however, instead of a site-specific chemisorption interaction, the benzene interacts with the "basal plane", then van der Waals and dispersion interactions are like to be more important [8, 17], and the surface diffusion E_a values would be less than approximately 20 kJ/mol.

Moreover, the interacting aromatic graphene π electrons of benzene adsorbed onto a graphenic surface also experiences electrostatic π-π quadrupolar [39] interactions (also referred to as electron donor/acceptor interactions [10, 14]), although electron donor/acceptor interactions are reported to have a major effect only on the adsorption of more polar aromatic compounds, such a nitrobenzene, on CNTs [10]. An additional consideration with CNTs is the bond strain experienced by the graphene as it is curved away from its planar, aromatically-stabilized configuration[3]. A few recent studies have looked at the thermodynamics of benzene vapor on CNTs [40, 41], notably Diaz et al. [17], who showed that the $\Delta H_{adsorption}$ is slightly lower on MWCNTs (34.7 kJ/mol) than on planar graphite ~40 kJ/mol (Table 1.1), and Crespo and Yang [42] who report 54 kJ/mol on SWCNTs. Diaz et al. [17] attributed this to the lowered adsorption energy of the nonplanar aromatic rings in MWCNT, and the higher value for the SWCNT implies that

adsorption is occurring inside the tube. Theoretical studies of the adsorption of benzene on CNTs indicate two favorable sites: the first is with the benzene ring centered above the carbon atoms in the CNT, similar to its position on graphite; the next most energetically favorable site appears to be the bridge position; and the position with the π bonds aligned directly was calculated to be least favored (Figure 7.6) [3, 43].

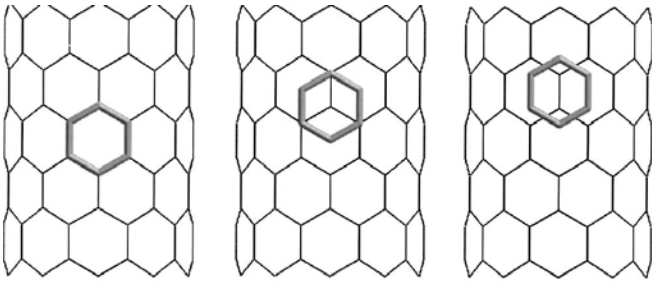

Figure 7.6 Modeled adsorption sites; graphite-like position is the center; bridge position is on the right [44].

Finally, the enhanced adsorption potential within a pore creates another category of adsorption "sites" (Figure 7.7). The molecular motion of benzene within

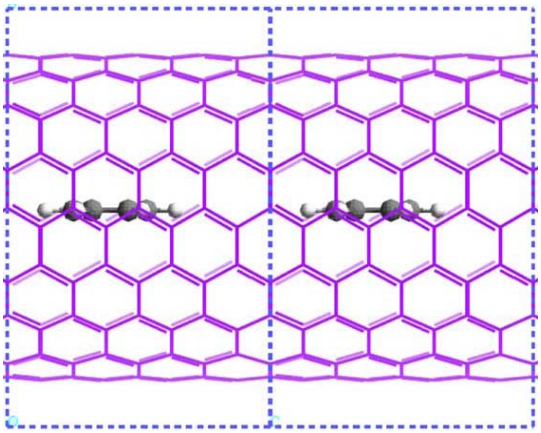

Figure 7.7. Computational model of the optimized position of benzene adsorbed to a 9,9 SWCNT (in the center of the tube) [5].

a nanotube has been modeled theoretically as most stable in the center, a position which would correspond conceptually to a Polanyi-Dubinin-Manes (PDM) model of a benzene model equilibrated with symmetrical surface forces extending out from the cylindrical tube walls. In addition, CNTs not only contain pore space in the tube interior, but also are known to aggregate (sorb to other CNTs) and thus form *inter*tubular pore spaces[7].

However, experimental verification of these adsorption models is lacking and will be explored in this chapter. This is the first reported study of the molecular motion of benzene adsorbed on CNTs using ^{2}H NMR. The molecular motion of the benzene on CNTs will be discussed in light of the pore size distribution determined from the N_2 adsorption and X-ray diffraction (XRD) analyses presented in Chapter 3. As discussed above, small pore sizes enhance adsorption on solid phases, and this effect may be observable in the jump rate or the orientation of the benzene molecule. Also, as mentioned in the introductory section of Chapter 3, adsorption on microporous and mesoporous BCs is enhanced by well developed graphitic crystallinity [11], an effect which is attributed by isotherm modelers to facilitation of the face-to-face orientation of the benzene molecule to the aromatic graphenic functions [45, 46].

In this chapter, the motion of benzene as it interacts with adsorption sites on a CNT surface will be examined for indications of preferred adsorption sites. Specifically, the ^{2}H NMR signal for a benzene molecule diffusing around the inner or outer circumference of a CNT would be expected to produce a Lorentzian peak, similar to the spectra observed for benzene on soot or carbon nanoparticles. (Even

though the tube axis has a preferred orientation, translation across the tube would ideally occur as ~60° site-to-site jumps in *either* direction (backwards or forwards), and thus the preferred orientation of the tube axis is removed.) On the other hand, a benzene molecule localized by chemisorption to the proton associated with an oxidized defect site would be expected to produce only a large-angle wobble (LAW) or a small-angle-wobble (SAW) and would require higher energy to activate a jump from site to site. Therefore, the static solid-state ^{2}H NMR spectra can distinguish between these two general types of interactions by virtue of (1) the shape of the peak (Lorentzian or Pake) and (2) the magnitude of the E_a. This information will be useful for design of surface functionalization syntheses, and the knowledge of the associated rates of surface diffusivity enables prediction of CNT performance as chromatographic media.

7.2 EXPERIMENTAL

7.2.1 Materials Characterization

The MWCNTs were purchased from Aldrich Chemical Company and the single-walled carbon nanotube sample was provided by Dr. Daniel E. Resasco of the School of Engineering at the University of Oklahoma, Norman, Oklahoma. Chemical and physical parameters of the CNTs are summarized in Table 7.1. Powder X-ray diffraction analysis (Chapter 3: Table 3 1 and Figure 3.3) shows a d_{002} graphitic spacing of 0.338 nm for the larger diameter MWCNTs and 0.344 nm for the smaller i.d. MWCNT sample, indicating graphitic crystalline ordering with minor disorder [46]. Based on the peak width, the Scherer crystallite size is calculated to be 15 nm for the larger diameter tubes and 8 nm for the smaller

diameter tubes.

The pore size distribution (Chapter 3, Table 3.2, Figure 3.9), calculated using the Dollimore-Heal algorithm for cylindrical pores [47] provided with the

Table 7.1. Characteristics of CNTs

Sample	wt % Carbon	[Ca] (ppm)[a]	Inside Diameter (nm)[b]	Outside Diameter (nm)[b]	Length[b]	Specific Surface Area (m^2/g)[c]	Estimated surface area ratio of inner to outer tube surface[d]
CNW, carbon nanotubes multiwalled[b]	> 95	< 172	5-40	40-70	0.5-2 mm	163	0.3
CNS, carbon nanotubes multiwalled[b]	> 95	< 154	5-10	60-100	0.5-50 μm	125	0.1
SWCNT, single-walled carbon nanotubes[e]	> 99	-	0.6-1.0[f]	0.8-1.3[f]		7300[f]	0.6

[a]Galbraith Labs; [b]Aldrich Chemical Co.[48]; [c]from N_2 adsorption analysis, this work; [d]calculated using the ratio of the median radii per the specified range of tube diameters; [e]provided by Daniel E. Resasco, University of Oklahoma; [f]Bachilo et al. [19]

.Quantachrome Chemisorb 1A Surface Analyzer [49], has a bimodal distribution, which was also reported for other MWCNT by Diaz et al. [17]. The mesopore size distribution for the CNS samples showed peaks at 2 nm and 4 nm, close to the 5-10 nm range listed in the Aldrich catalog for this sample. However, the CNW sample showed a similar size pore size distribution, although the Aldrich catalog [48] listed the sample as containing pores up to 40nm in inner diameter. It is likely that the CNW sample contained residual catalyst or carbon particles in the pores, as has been reported by other workers [50] to affect the pore size distribution measured by N_2 adsorption analysis. For the CNS sample, the pore size distribution showed a volume of microporosity (using the DFT algorithm recommended by Quantachrome for micropores in carbon materials [49]) equal to approximately one-third of total

porosity. It is possible that the slit-shaped microporosity occurs in spaces between agglomerated carbon nanotubes. The SWCNT sample was not analyzed with N_2 adsorption, but its size was well-characterized by fluorescence during synthesis [19]. The N_2 isotherms themselves for the MWCNT both displayed hysteresis (a difference in the pressure curve during adsorption vs. desorption), and, as discussed in Chapter 3, this is due to a difference in the mechanism of the vapor/liquid transition between the condensation step and the evaporation step [51], and indicates (1) the occurrence of pore sizes larger than 3.6 nm in diameter in order to accommodate more than 3-4 monolayers of N_2 adsorbate [52] and the presence of tubes that are open at both ends because tube that are closed at one end have identical condensation and evaporation paths [11, 53, 54].

7.2.2 Sample Preparation

Samples were prepared according to the procedure outlined in the Experimental Section. Briefly, the solid phase was placed into a specially necked 10 mm NMR tube which was attached to a vapor deposition manifold. A precise amount of benzene-d_6 was condensed into the NMR tube, which was submerged in liquid nitrogen, and the sample was subsequently backfilled to 200-400 torr with N_2 gas, flamed-sealed, and transported to the Oklahoma Statewide NMR Facility at Stillwater, Oklahoma, for collection of the variable-temperature solid-state ^{2}H NMR spectra on the Chemagnetics 300 MHz instrument. The loading of each sample is specified in Table 7.2. In order to verify the quantities of benzene-d_6 loaded into each sample, an NMR spectrum was collected with particular parameters (10 s delay time, 128 scans, 25°C, 20 μs echo tau, 1024 data points, and 1 kHz line broadening),

Table 7.2. Samples of benzene-d_6 on CNTs

Sample Name	Mass of CNT (mg)[a]	Deposited Volume of Benzene (μl)[b]	NMR Quantitation Volume Predicted(μl)[c]	% load (w/w)[d]	% loading (monolayer coverage)[d,e]
CNW2	131.2±0.1	1.4±0.1	0.4±0.3	1.0±0.1	19±2
CNW4[f]	169.5±0.1	1.8±0.1	0.5±0.3	1.0±0.1	19±2
CNW5	136.3±0.1	1.4±0.1	0.7±0.3	1.0±0.1	19±2
CNS1	111.1±0.1	1.2±0.1	0.5±0.3	1.0+0.1	24±2
CNS3	105.0±0.1	1.1±0.1	0.4±0.3	1.0±0.1	25±2
SWCNT1	48.7±0.1	1.0±0.1	0.7±0.3	2.0±0.1	1±1
SWCNT2	37.6±0.1	0.9±0.1	0.7±0.3	2.0±0.1	1±1

[a]Uncertainty noted is the smallest increment on the balance; [b]uncertainty in the amount of benzene deposited as calculated from the pressure difference in the manifold is rounded from 0,05μl listed in the Experimental Chapter; [c]based on the NMR quantitation plots for individual samples (Figure 2.4) in the Experimental Chapter; [d]per the original volume calculated with the manifold pressure difference; [e]uncertainty in monolayer loading is the uncertainty shown for the % w/w loading plus an additional uncertainty in the surface area measurement as reported by NIST, which is estimated to display a variability of 1%, based on our experience with the Autosorb Surface Analysis instrument; value of cross-sectional area of a benzene molecule used to calculate a monolayer is 43Å^2 [55]; [f]this sample was not backfilled with N_2 gas.

and the NMR spectral area was plotted against the volume loaded in comparison to a quantitation line prepared from the areas of NMR spectra of sealed liquid benzene-d_6 collected with those same parameters, as described in the Appendix A1 (Figure A1.3). For collecting solid-state ^{2}H NMR spectra at variable temperatures for line shape analysis and jump rate determination, the instrumental parameters were 3600-86400 scans, delay times ranging of 0.5 s, either 20 μs or 40 μs echo spacing, either 1024 or 8196 data points, and the spectra were processed with zero filling (if necessary) to 8196 points with 1 kHz line broadening.

7.2.3. Quantitation

All of the ^{2}H NMR spectra of benzene-d_6 on CNTs required a large number of scans to attain an adequate signal-to-noise ratio (S/N). For example, for the carbon nanoparticles and soot sample, 3600 scans would provide S/N in excess of

20, but for the CNS samples, 21600 scans provided S/N of nearly 20, for the CNW spectra, less than 20. Similarly, the signal intensity was very low in comparison with the liquid benzene-d_6 NMR quantitation curve (Table 7.2), and, this apparent signal loss was a sample-dependent phenomenon (Appendix A3). The volume of benzene-d_6 predicted from the NMR calibration line for the other BC samples was approximately 80% of the volume loaded, but, for CNS and CNW, the value was approximately 33% and 25%, respectively. Its most likely cause was exchange between two phases with different dephasing rates over the temperature ranges under investigation [56], as addressed in Appendix A3. The interpretation is supported by the similarity in shape of these spectra to that of benzene-d_6 on NaX and NaAgX zeolites in the region of motional transition [57], also observed by Grundke and Boddenberg for benzene-d_6 on Carbopack B [58]. Another possibility is the existence of unusual magnetic properties of carbon nanotubes which may affect the NMR signal [59, 60], although this has not been reported for other graphitic carbon phases [61]. However, the electrical and magnetic properties of carbon nanotubes remain poorly understood [12, 62]. Similarly, the presence of residual paramagnetic catalyst could reduce the signal, but such an effect is much less significant for quadrupolar nuclei than dipolar nuclei [63]. Boddenberg and Beerwerth relied on this when comparing ^{2}H to ^{1}H NMR spectra [64, 65].

7.3 RESULTS

7.3.1 ^{2}H solid-state NMR spectra of benzene-d_6 on CNTs

Experimental ^{2}H solid-state spectra of benzene-d_6 adsorbed to the CNTs for less than 5 days consisted of very broad, nearly isotropic peaks (Figure 7.8). The

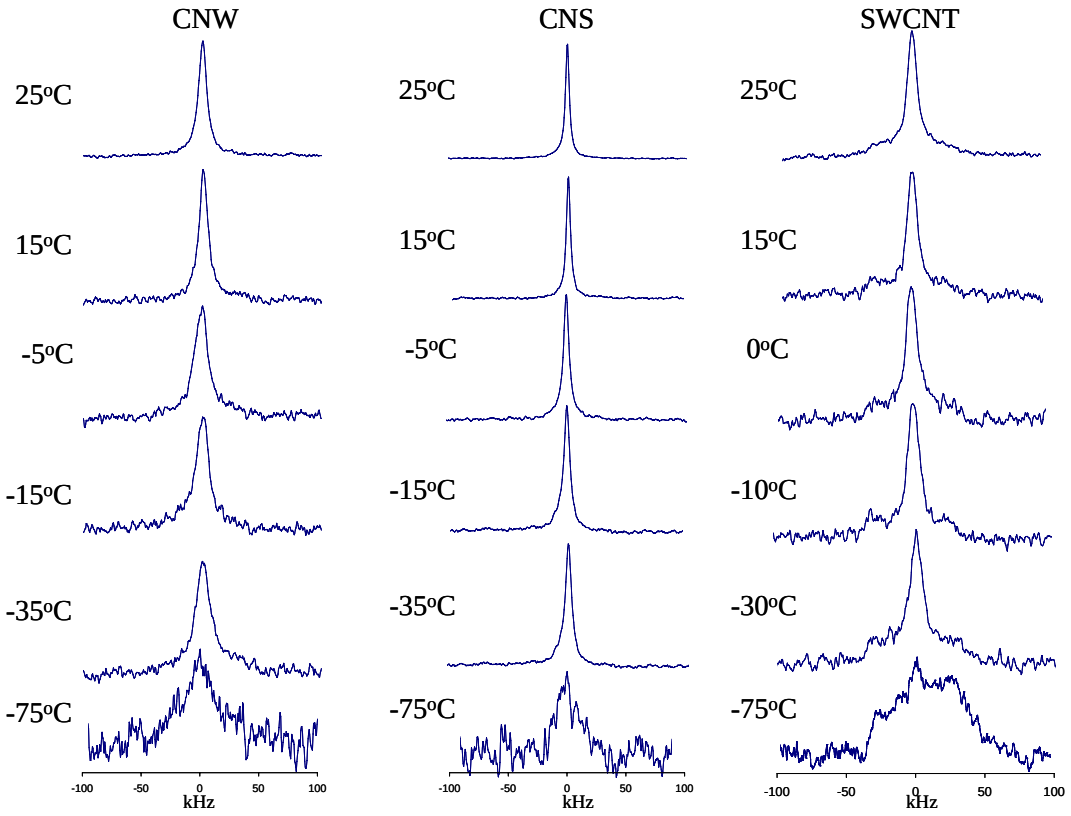

Figure 7.8. ^{2}H NMR solid-state experimental spectra of benzene-d_6 on carbon nanotubes; *y*-axis is arbitrary NMR intensity units, normalized to one for each spectrum.

peaks appeared to have a large-angle wobble (LAW) contribution near the base, although the Pake outline was barely distinguishable by eye, except for the spectra on the SWCNT. Because the experimental spectra had low S/N, as discussed above, and somewhat indistinct features, fitting of the spectra using DFP was unsatisfactory (See Appendix A3), but jump rates were calculated at several temperatures using the peak width, according to the equation [58]:

$$\delta\upsilon = (9\pi/20)\, QCC^2\, \tau_C. \qquad \textbf{(Eqn. 4.3)}$$

The variables are defined as: $\delta\nu$, the peak width at half-height for the spectrum;

QCC, the motionally averaged value of the quadrupole coupling constant; and τ_C, the reorientational correlation time and the reciprocal of the jump rate, *k*.

If the reduction in signal discussed in the previous section was due to the existence of two exchanging phases at nearly equal concentrations, then an Arrhenius plot of jump rate vs. temperature would not be strictly valid because the spectra would be recording two ensembles of molecules executing different motions with (possibly) different Arrhenius behaviors. However, the peak widths did display a consistent increase with lowered temperature (Figure 7.9), so the

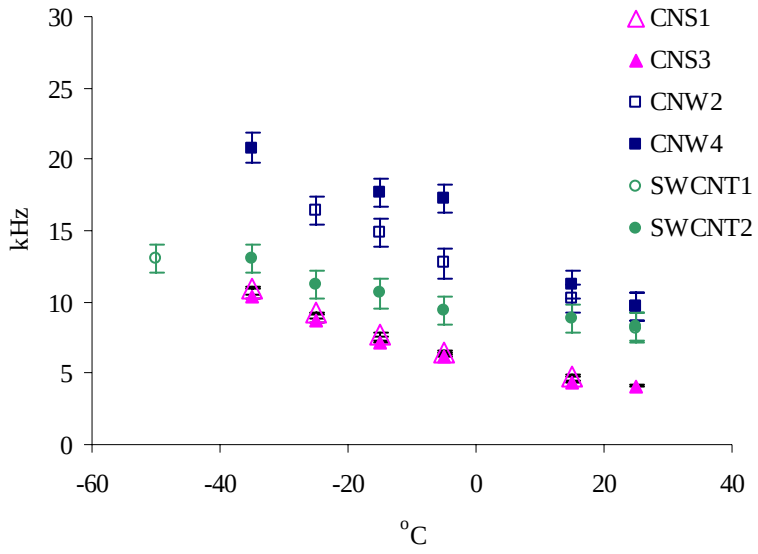

Figure 7.9. Peak width values for spectra of benzene-d_6 on CNT samples less than 5 days old; error bars indicate uncertainty in peak width measurement.

Arrhenius analysis will be undertaken, using the peak widths listed in Table 7.3, despite the fact that the results might be unreliable. Because the plots of peak width vs. temperature for all of the different CNTs (Figure 7.9) reveal linear trends offset

Table 7.3. Peak widths at half-height, δν (kHz)[a], for pseudoisotropic peaks at early ages[b] for benzene-d_6 on CNT samples

Temp (°C)[d]	CNS1	CNS3	CNW2	CNW4	SWCNT1	SWCNT2[c]
25		4.1 7200 scans	9.7[e] 21,600 scans	9.7 21,600 scans	8.2 86,400 scans	8.3 3600 scans
15	4.8 21,600 scans	4.4 7200 scans	10.2 21,600 scans	11.2 21,600 scans		8.8 3600 scans
-5	6.5 21,600 scans	6.2 7200 scans	12.7 21,600 scans	17.2[f] 21,600 scans		9.4[g] 3600 scans
-15	7.7 21,600 scans	7.2 7200 scans	14.9 21,600 scans	17.7[h] 21,600 scans		10.6[g] 3600 scans
-25	9.2 14,400 scans	8.7 7200 scans	16.4			11.2[g] 3600 scans
-35	11.0 7200 scans	10.4 7200 scans		20.8 21,600 scans		13.0[g] 5120 scans
-50					13.0[i] 15,776 scans	
-75		38.5[j] 3600 scans		58.1[i] 3600 scans	70.0[i] 21,600 scans	
-115				61.0[i] 7200 scans		

[a]40μs echo spacing and 1kH line broadening for all spectra and estimated uncertainty in δν is ±0.1 kHz, ±1 kHz, and ±1kHz for CNS, CNW, and SWCNT samples, respectively; [b]all spectra were collected at less than 5 days old, except as noted; [c]spectra of SWCNT2 used 20 μs echo delays; [d]uncertainty in temperature measurements was ±0.1°C, [e]22.5°C; [f]day 28; [g]temperature 5°C less than listed; [h]day 21; [i]peak displays some Pake appearance; [j]day 11.

from each other, there could be a relationship between CNT diameter and jump rate. If these are pseudoisotropic peaks caused by the diffusion of benzene around molecular-sized particles, then the offsets of these linear trends might be expected for different particle sizes. Because this would be expected for different sized CNTs, this pattern was also an indication that the Arrhenius values obtained from these data had validity.

7.3.2 Aging

Further loss of signal intensity over time could indicate an effect of aging on the motion of benzene-d_6 associated with the carbon nanotubes. In particular, the

CNW2 sample lost 32% of its signal area for spectra taken under identical conditions between day 5 and day 79, although there was no change in peak width during this time (Table 7.4). Directly comparable spectra for CNW4 are not

Table 7.4. Peak widths at half-height, δν (Hz)[a], for pseudo-isotropic peaks from different ages for benzene-d_6 on CNW2

Temp (°C)[b]	Ages			
	Days 1-4		Day 80	Day 156
25	9.7[c]		10.7	10.6[c]
	21,600 scans		21,600 scans	86,400 scans
15	10.2	Lost	10.6	
	21,600 scans	68%	21,600 scans	
-5	12.7	of		
	21,600 scans	signal		
-15	14.9	intensity	13.4	
	21,600 scans		21,600 scans	
-25	16.4		18.1[d]	
	13,096 scans		21,600 scans	
-35			22.9	
			21,600 scans	
-75				49.3[e]
				3600 scans

[a]All spectra collected with 40μs echo spacing and processed with 1 kHz line broadening; estimated uncertainty in δν was ±1kHz; [b]uncertainty in temperature measurement was ±0.1°C, [c]22.5°C; [d]average value for duplicate samples (18.4 and 17.7 kHz, respectively on days 80 and 81); [e]peak displays some Pake appearance.

available to test whether or not the duplicate CNW sample also lost signal over time. Spectra of benzene-d_6 on CNS1 at different ages also suffer from a lack of comparable conditions, although there is one indication of signal loss: The area of the 20 μs tau, -15°C spectra is much lower than the 40 μs, -15°C spectra collected at Day 1, both with 21,600 scans (Appendix A2). Such a loss in signal area over time (if due to some reason other than leakage of benzene from the sample tube) could be attributable to a change in motion of some of the benzene molecules. Such a change in motion could occur by diffusion over time of the benzene onto sites with higher

adsorption energies, and the interaction with these new sites inducing more restricted motion. If such high energy sites exist on the CNTs (e.g., adsorbed water with acidic hydrogens at edge sites or on the catalyst itself), then these may account for the transitional appearance of the spectrum by contributing a second motional ensemble moving in a different mode than the graphene-adsorbed molecules. However, there was no noticeable change in peak width over time at the same temperature (Table 7.4). Further, a change in motion with aging would be expected to produce a change in the ratio of the area for the spectra taken with 40 μs echo spacing to the area for spectra taken with 20 μs echo spacing. However, this is not observed either: this ratio for the CNW spectra at 15°C is 0.5 (including CNS1 day 5, CNS1 day 77, and CNW4, day2), and, for CNW, it is 0.7 (including CNS1 day2, CNS1 day 77, and CNW4, day 2). Unfortunately, because of the amount of time required to collect these low S/N spectra, only two spectra were collected at identical conditions at different ages. In summary, although there is insufficient data to draw conclusions for this sample as to why its spectra displayed an initially low signal intensity and continued to lose signal intensity over time, careful monitoring of the areas for spectra collected under identical conditions over time may prove a good indicator for changes in the motion of the benzene with time for future studies. If samples could be prepared with improved S/N (such as with higher benzene loading or by collecting data at higher temperatures), then a set of Arrhenius parameters for several days after initial preparation of the sample may show a change in peak width and/or area that would indicate diffusive equilibration from intertube sites to intratube sites (behavior suggested by the work of

Kondratyuk et al. [7]) or from lower energy sites to higher energy sites, such as positions in the grooves between tubes which are sorbed to each other.

7.3.3 Arrhenius data for the pseudoisotropic reorientational motion

Attempts were made to fit the spectra using an ISO library, but acceptable visual fits were not obtained. Because, qualitatively, the spectra appear to contain a LAW Pake component near the base of an otherwise broad Lorentzian peak, attempts were also made to fit the spectra to simulations of different benzene populations moving in separate motional modes, specifically, combinations of ISO, SAW, and LAW. However, satisfactory visual fits were not obtained in many cases, and, in the cases where fits looked reasonable (especially ISO and LAW combination), the results either (1) contained large disparities in the rates calculated for the 20μs and 40μs tau spectra at the same temperature, (2) showed no trend, and/or (3) were illogical, such as indicating an increase of ISO component at colder temperatures. Unsuccessful fitting could be due to several reasons, including excessive noise within the spectrum itself, the complexity of the molecular motion, the effect of site symmetry on the benzene's motion [66], or a Gaussian distribution of jump rates by benzene molecules executing the same motion [37]. Ideally, the activation energy calculated from an Arrhenius plot should be obtained over a temperature range in which the relative concentrations of different motions present remained constant [67], as indicated by a constant value for the ratio of spectral areas collected with different echo spacings, a condition which holds for the SWCNT (Table 7.5).

Table 7.5. NMR peak areas[a,b], normalized to the value at 15°C, for benzene-d_6 on CNT samples from spectra with 40 μs τ_{echo} and 1 kHz line broadening.

Temp (°C)[d]	CNS1 (21,600 scans)	CNS3 (7200 scans)	CNW2 (21,600 scans)	CNW4 (21,600 scans)	SWCNT2[c] (3600 scans)
25		1.07	0.95[e]	1.00	
15	1.00	1.00	1.00	1.00	1.00
-5	0.87	0.93	0.86	0.86[f]	0.90
-15	0.75	0.83	0.86	0.84[g]	0.95
-25		0.78			0.97
-35		0.77		0.82	1.11

[a]Estimated uncertainty in the area values was ±5%; [b]all spectra were collected at less than 5 days old, except as noted; [c]spectra of SWCNT2 used 20 μs echo delays; [d]uncertainty in temperature measurements was ±0.1°C; [e]22.5°C; [f]day 28; [g]day 21.

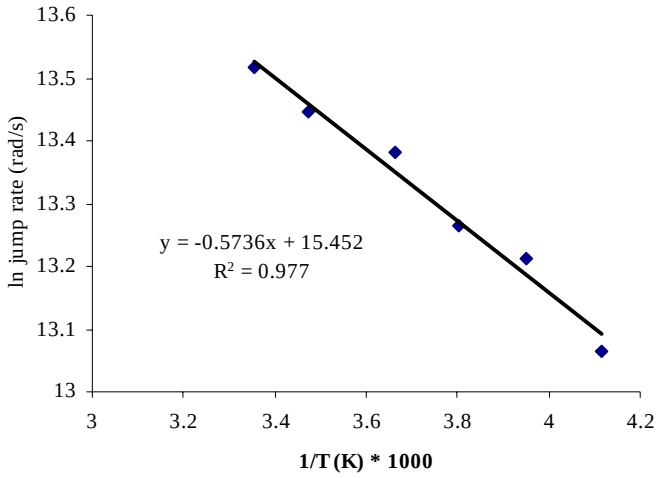

Figure 7.10. Arrhenius plot for benzene-d_6 on SWCNT2 using jump rates calculated from the peak width; peak widths listed in Table 7.3; E_a = R * slope and k_0 is the preexponential factor..

The Arrhenius plot of benzene-d_6 on SWCNTs (Figure 7.10) using jump rates calculated from the peak width equation (Eqn. 4.3) indicates a low value for the energy of activation for the pseudoisotropic motion, 4.8 (±0.4) kJ/mol. The accuracy of this value depends upon the assumption of pseudoisotropic motion, but

the LAW/SAW type of Pake hump visible in the spectrum indicated the presence of an additional type of motion, such as LAW or SAW. For the MWCNT, a hint of a Pake pattern along the base of the spectrum could be seen, but the definition of such a solid-type spectra was better in the SWCNT spectra. Of the ISO/LAW/SAW combination fits, the ISO/LAW gave the best visual fit, but the LAW rates showed no trends, and the slope from the ISO rates formed a slope approximately the same value as the pseudoisotropic rates in Figure 7.10. If another type of motion were present for some of the molecules, then a separate set of Arrhenius constants would exist for each motion. This could be the case, even if the temperature region is not transitional (as indicated by the constant area), if this temperature region maintains a constant proportion of the different types of motion, with each motion occurring faster at higher temperatures. One other possibility is that the all of the molecules are moving as a single ensemble, but are not moving around the surface of the SWCNT in a pseudoisotropic fashion, but are executing a completely different motion (for example, a sterically hindered motion in the tube interior) for which the peak width equation (Eqn. 4.3) does not apply.

For the MWCNT samples, the areas of the 40 μs spectra relative to 20 μs areas listed in Table 7.5 become smaller as the temperature is lowered. Nevertheless, the Arrhenius plots (Figure 7.11), calculated using the peak width as above, provide values comparable to those observed for other black carbons (Chapter 1, Table 1.2, and Chapter 4, 5, and 6). The Arrhenius values at different ages and over different temperature ranges for both CNW samples show more scatter than soot, carbon nanoparticles, or low-surface-area graphite, although

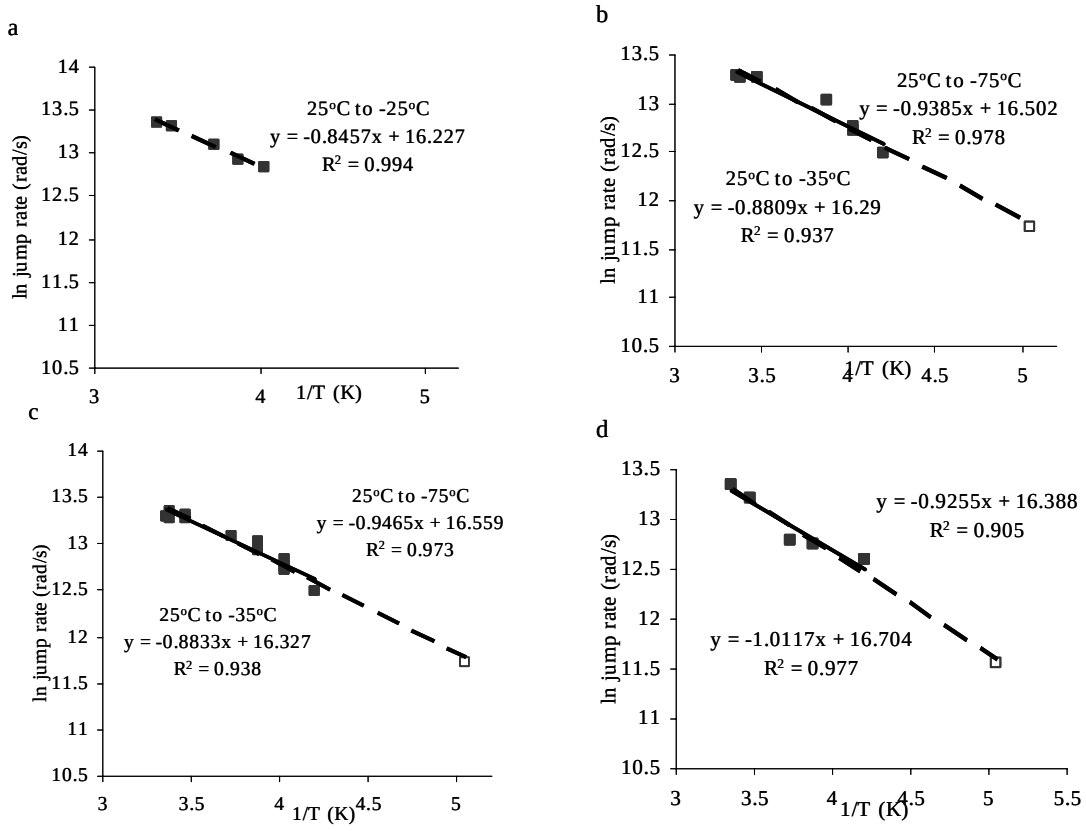

Figure 7.11. Arrhenius plots for benzene-d_6 on CNW using jump rates calculated from the peak width equation: a) CNW2 1-4 days old; b) CNW2 79-156 days old; c) CNW2 all ages; d) CNW4 1-29 days old; peak widths listed in Tables 7.3 and 7.4; solid lines from 25°C to -35°C and dashed lines from 25°C to -75°C; E_a = R * slope and k_0 is the pre-exponential factor..

within that scatter, the values for different ages are similar. The Arrhenius plot of the CNS samples (Figure 7.12) for different samples and temperature ranges show less scatter than the CNW sample, although some changes with aging cannot be excluded, as mentioned earlier. For CNS, the E_a values for the pseudo-isotropic jump motion for CNS1 does decrease from a younger age to an older age. However, this change was in the opposite direction to the very small change in the older CNW2 sample s or on the carbon nanoparticles, which both were larger in

magnitude at older ages than younger. Therefore, even though it was of interest whether or not the molecular motion of benzene associated with black carbon changes over time, because it may have indicated diffusing into more sequestered regions of the solid phase, these data confirmed the previous discussion regarding NMR area of these samples that the set was too small and too noisy to answer this question definitively. The energy of activation and pre-exponential jump rates are summarized for all of the carbon nanotubes samples in Table 7.6.

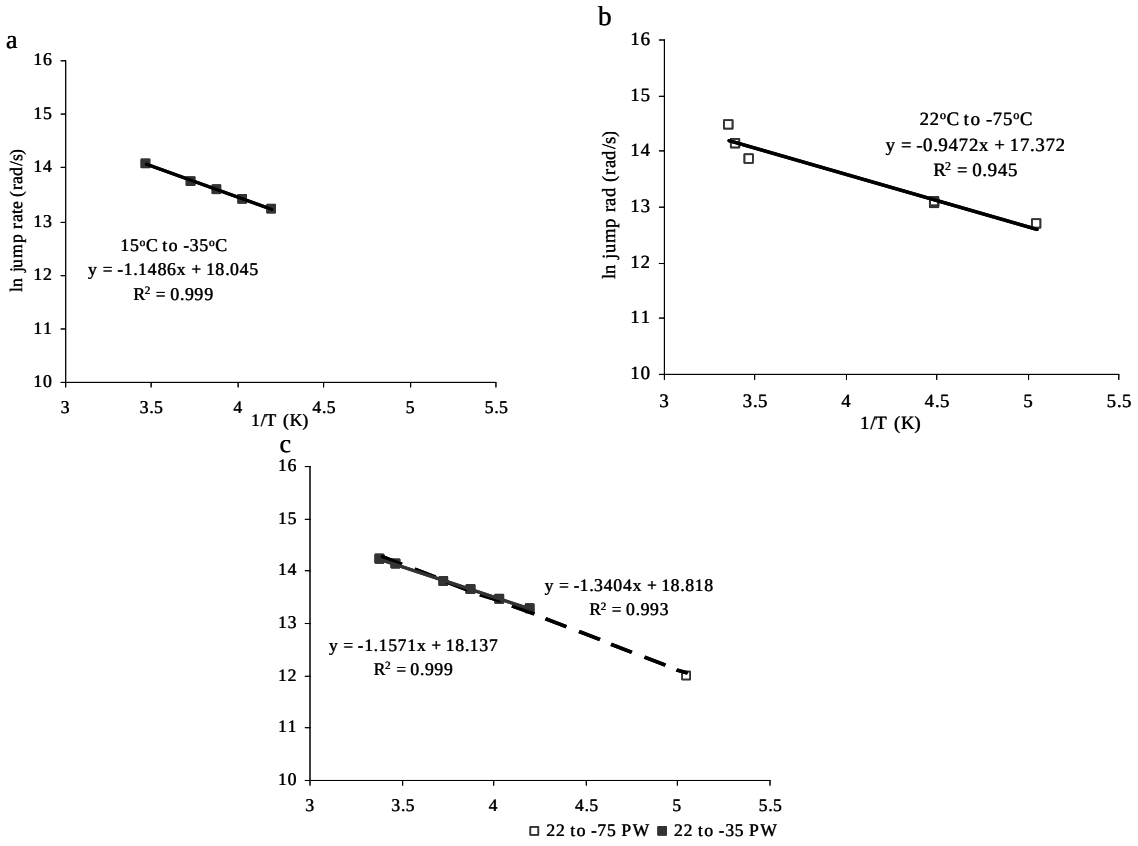

Figure 7.12. Arrhenius plots for benzene-d_6 on CNS using jump rates calculated from the peak width: a) CNS1 2-3 days old; b) CNS1 77-259 days old; c) CNS3 days 1-11; error bars (not shown) would be smaller than the symbols; solid lines from 25°C to -35°C and dashed lines from 25°C to -75°C; E_a = R * slope and k_0 is the pre-exponential factor.

The magnitude of the E_a values falls into the range of physisorption (less than the 15.8 kJ/mol for benzene in neat crystals), indicating that most of the interaction was between the aromatic π bonds of benzene and graphene, as expected. This indicates that chemisorption to surface defect sites is *not* a major

Table 7.6. Arrhenius data for benzene-d_6 on CNTs obtained from plots of jump rate[a], *k*, vs. 1/T.

Sample	Temp Range	Age	E_a (kJ/mol)	R^2	k_0 (rad/s)
SWCNT2[b]	25°C to -30°C	1 day	4.8 (±0.4)	0.977	5.1 (±0.1) x 10^6
CNW2	25°C to -25°C	1-4 days	7.0 (±0.3)	0.994	1.1 (±0.1) x 10^7
	25°C to -35°C	79 days	7.3 (+0.9)	0.937	1.1 (±0.1) x 10^7
	25°C to -35°C	all	7.3 (±0.6)	0.938	1.2 (±0.1) x 10^7
	25°C to -75°C	79 days	7.8 (±0.5)	0.978	1.5 (±0.1) x 10^7
	25°C to -75°C	all	7.9 (±0.4)	0.973	1.6 (±0.1) x 10^7
CNW4	25°C to -35°C	< 29 days	7.7 (±1.4)	0.905	1.3 (±0.2) x 10^7
	25°C to -75°C	< 29 days	8.4 (±0.6)	0.977	1.8 (±0.2) x 10^7
CNW average			7.6 (±0.5)		1.3 (±0.3) x 10^7
CNS1	25°C to -35°C	2-3 days	9.5 (+0.2)	0.999	6.9 (+0.1) x 10^7
	25°C to -75°C	77-259 days	7.9 (+1.0)	0.945	3.5 (+0.7) x 10^7
CNS3	25°C to -35°C	< 12 days	8.5 (+0.5)	0.999	4.5 (+0.3) x 10^7
	25°C to -75°C	< 12 days	11.1 (+0.4)	0.993	1.5 (+0.1) x 10^8
CNS average			9.3 (+1.4)		7.5 (+5.2) x 10^7

[a]Jump rates, *k*, calculated from peak width using Eqn. 4.3; [b]SWCNT peak widths taken from 20 μs spectra; all other peak widths taken from 40 μs spectra listed in Tables 3,4, and 5.

component of the benzene vapor/CNT surface interactions in systems which are relatively dry with respect to water. Further, the MWCNT E_a values are

intermediate between the low-surface-area graphite (10.4 kJ/mol) and the amorphous carbon nanoparticles (6.9 kJ/mol), and these values correlate with the degree of graphitization. The effect of the graphitic crystallinity on surface energy is known to be an important parameter in modeling the adsorption behavior of benzene on graphite [68, 69]. However, there is not a linear correlation between graphite crystallinity, as measured by X-ray diffraction crystallite size, L_c, and d-spacing (Table 3.1 in Chapter 3), and the E_a or k_0 values for the rotational motion of benzene-d_6 measured with ^{2}H NMR and listed in Table 7.5.

In addition to measuring the Arrhenius parameters of the pseudoisotropic jump motion, surface diffusivity constants, D_0, were calculated, as in previous chapters, according to the Einstein diffusion equation (Chapter 4, Eqn. 4.5),

$$D = a^2/6\tau_C \qquad \textbf{(Eqn}.\ 4.5),$$

However, the value of *a* presents several possibilities. If, as Boddenberg's group did, you assume that *a* is equal to the radius of the particle, then *a* would equal the tube diameter, and could be either the inner or the outer diameter. D_0 is the pre-exponential factor in the activation equation for surface diffusivity (below)

$$D = D_0 \exp(-E_a/RT), \qquad \textbf{(Eqn}.\ 7.1)$$

and is directly related to the k_0 values calculated in the last section by

$$D_0 = (a^2/6) * k_0. \qquad \textbf{(Eqn}.\ 7.2)$$

D_0 values (Table 7.7 on the next page) were calculated for the possible inner and from the 0.01 ml/g loading on the cumulative pore volume distributions determined from the N_2 adsorption data in Chapter 3 (Figure 3.9, Table 3.2). If the benzene-d_6 molecules (3.3Å x 43 Å^2) were able to occupy the same pore sizes that the smaller

N_2 molecules (3.0Å x 16.2 Å^2) occupy, then these smallest available pores would account for all of the benzene-d_6 volume loaded onto the CNT samples. As shown in the table, smaller pores result in smaller rates of diffusivity, as would be expected. With respect to the other BCs, the D_0 values for benzene-d_6 on the surfaces of the carbon nanotubes are at least an order of magnitude smaller than for outer diameters and also for 1.3 nm wide pores, which was based on the pore sizes a comparably loaded soot, 1.3 ($\pm$0.1) x 10^{-8} m^2/s, or carbon nanoparticle, 7.1 ($\pm$0.1)

Table 7.7. D_0[a] values for CNTs diffusion on inner or outer surfaces

	CNW	CNS	SWCNT
interstices	1.3 nm	1.3 nm	1.3 nm
D_0 (m^2/s)	9.2 ($\pm$2.1) x 10^{-13}	5.3 ($\pm$3.7) x 10^{-13}	3.6 ($\pm$0.1) x 10^{-13}
smallest i.d.[b]	5 nm	5 nm	0.8 nm
D_0 (m^2/s)	1.4 ($\pm$0.3) x 10^{-11}	7.8 ($\pm$5.4) x 10^{-11}	1.4 ($\pm$0.1) x 10^{-13}
largest i.d.[b]	40 nm	10 nm	
D_0 (m^2/s)	8.7 ($\pm$2.0) x 10^{-10}	3.1 ($\pm$2.2) x 10^{-10}	
smallest o.d.[b]	40 nm	60 nm	1.3 nm
D_0 (m^2/s)	8.7 ($\pm$2.0) x 10^{-10}	1.1 ($\pm$0.8) x 10^{-8}	3.6 ($\pm$0.1) x 10^{-13}
largest o.d.[a]	70 nm	100 nm	
D_0 (m^2/s)	2.7 ($\pm$0.6) x 10^{-9}	3.1 ($\pm$2.2) x 10^{-8}	

[a]Calculated using the Einstein diffusion equation, where $\tau_0 = 1/k_0$, reported in Table 7.5, and a = ½ of the indicated diameter; uncertainty reported was associated with k_0 values; [b]i.d. = inside diameter and o.d. = outside diameter, according to the nanotube dimension reported in Table 7.1.

x 10^{-9} m^2/s, but closer to that calculated for graphite, 3.7 ($\pm$0.9) x 10^{-10} m^2/s. It is evident from Eqn. 4.5, however, that he magnitude of the D_0 value is highly dependent on the selected value for the time-averaged jump distance, which is a direct function of pore or particle size. This will be addressed in further detail in the Chapter 9.

Compensation effects (a correlation of enthalpy with entropy for a given reaction or process) for surface processes have been observed by other researchers [70-76] including CNTs [17], and, for surface diffusion, the effect is defined as a plot of E_a (enthalpic component) vs. k_0 (entropic component) . Compensation effects have been the object of some controversy, but, for surface diffusion, the effect results from site heterogeneity, adsorbate-adsorbate interactions, and pore structure [71, 73, 74, 77]. One explanation is as follows: at low loadings, the adsorbate is attracted to the sites with higher adsorption energies, and entropy is also high because of a higher number of possible sites to which it can jump; at higher loadings, only lower adsorption sites are available, and entropy is reduced due to adsorbate-adsorbate crowding [78]. Rigby has suggested that the compensation effect observed in surface diffusion as measured with static solid-state ^2H NMR is directly related to the surface fractal dimension [79-82]. The fractal dimension, which was calculated in Chapter 3 for all BC samples from the Frenkel-Halsey-Hill (FHH) equation for N_2 adsorption data, is a measure of surface roughness [77, 82]. It seems reasonable that the fractal dimension, which occurs as an exponent from a slab model of a gaseous adsorbed layer (which is the basis for the FHH equation) [83] would also be related to surface roughness and motion of adsorbed molecules along that surface.

A compensation effect trend of E_a vs. k_0 for the CNT data can be observed (Figure 7.13), and a best fit line was constructed for the MWCNTs. Adding the SWCNT to the plot changes the slope significantly (to 0.55) and reduces the R^2 value from 0.927 to 0.880, and not including it with the MWCNTs is consistent with

the idea that the benzene molecules are executing a different motion on the SWCNTs. The MWCNTs differ from the SWCNTs in two particular ways: (1) The porosity in the SWCNTs was entirely in the microporous range, and (2) the MWCNT contain three-dimensional graphitic crystallinity. Microporosity would be like to affect the motion, and the lack of graphitic layers could be expected to reduce the strength of the π-π interaction to give a smaller E_a. However, surface forces are magnified in micropores because the forces extend from both walls. It is less clear

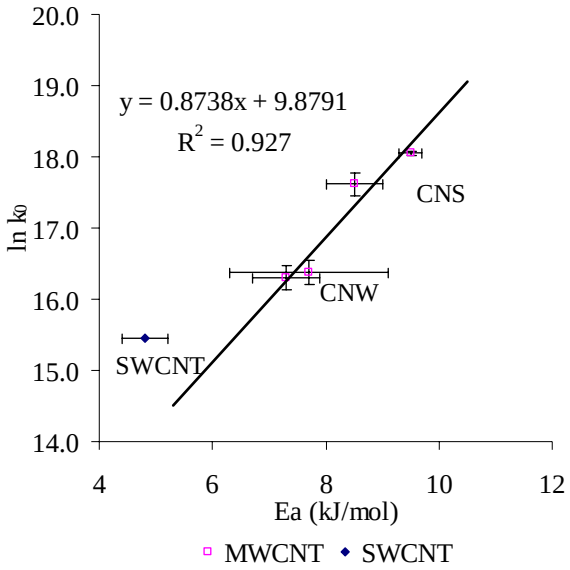

Figure 7.13 Compensation effect plot for CNT samples; best fit line shown for MWCNTs only.

why CNW would have such a smaller E_a than CNS, almost as low as the amorphous carbon nanoparticles. The walls are thinner, but this was not reflected in the L_c value from the X-ray diffractogram, for which CNW is larger. The CNW are nearly three orders of magnitude longer than the CNS, but it is unclear how this would affect the motion. The compensation effect for surface diffusion of physisorbed benzene molecules and its to the fractal dimension of the BC solid phases will be

discussed in detail in Chapter 9 for all the BCs in this study.

7.4 CONCLUSIONS

The molecular motion of benzene-d_6 was observed spectroscopically for the first time at multiple temperatures as it diffused in submonolayers on multi-walled and single-walled carbon nanotubes. The E_a for the surface-diffusion of benzene-d_6 on CNS, 9.3 ($\pm$1.4) kJ/mol, is only a little lower than on the low-surface-area graphite, 10.2 ($\pm$1.1) kJ/mol, which would be expected for a graphenic solid with a slight distortion of the π bonds due to surface curvature. The E_a for benzene-d_6 on the CNW was 7.6 ($\pm$0.5) kJ/mol, lower than on the CNS, which could be attributed to thinner tube walls, to increased bond distortion from a more tightly curved outer surface, or to contributions from impurities associated with the CNW which interacted weakly with benzene-d_6. However, the general Lorentzian appearance of the peak indicates that benzene-d_6 is executing pseudoisotropic motion, similar to the soot and CNP, and, thus, is closely associated with the surface and the translation path guided by the shape of the pores. This does not exclude a significant population of the benzene-d_6 having occupied the interstices between the CNTs. The dominance of mesopores, with pore-size-distributions from the N_2 isotherm data showing peaks at 2 nm and 4 nm, but including a significant contribution from micropores, supports the above interpretation of the ^{2}H NMR spectral results. Thus, the motion appeared to be pseudoisotropic, although, qualitatively, the spectra also contain some Pake appearance which may indicate a minor component of benzene localized on acidic surface sites with high adsorption energies. The loss of NMR signal over time may be due to benzene diffusing into

pores (interstices or tube interior) which either have a different magnetic environment or induce a different motion which produces signal interference with the motion of the remaining benzene molecules. The SWCNT, in particular, appears to have a localized component; however, fitting of the spectra to such a more complicated model was not achieved at this time. The MWCNTs demonstrate a compensation effect which could be related to the fractal dimension, as observed for surface diffusion in numerous studies reviewed in the Introduction Chapter, but the value of diffusivity depended upon a choice of pore size within which the benzene was diffusing.

References

1. Mauter, M. S.; Elimelech, M., Environmental applications of carbon-based nanomaterials. *Environmental Science & Technology* **2008,** *42*, (16), 5843-5859.
2. Sone, K.; Fugetsu, B.; Tsukada, T.; Endo, M., Affinity-based elimination of aromatic VOC's by highly crystalline multi-walled carbon nanotubes. *Talanta* **2008,** *74*, 1265-1270.
3. Gotovac, S.; Honda, H.; Hattori, Y.; Takahashi, K.; Kanoh, H.; Kaneko, K., Effect of nanoscale curvature of single-walled carbon nanotubes on adsorption of polycyclic aromatic hydrocarbons. *Nanoletters* **2007,** *7*, (3), 583-587.
4. Yuan, L.-M.; Ren, C.-X.; Li Li, P. A.; Yan, Z.-H.; Zi, M.; Li, Z.-Y., Single-walled carbon nanotubes used as stationary phase in GC. *Anal. Chem.* **2006,** *78*, 6384-6390.
5. Irving, D. L.; Sinnot, S. B.; Lindner, A. S., Interaction of functionalized benzene molecules with carbon nanopores. *Chemical Physics Letters* **2004,** *389*, 96-100.
6. Murr, L. E.; Bang, J. J.; Esquivel, E. V.; Guerrero, P. A.; Lopez, D. A., Carbon nanotubes, nanocrystal forms, and complex nanoparticle aggregates in common fuel-gas combustion sources and ambient air. *Journal of Nanoparticle Research* **2004,** *6*, 241-251.
7. Kondratyuk, P.; Wang, Y.; Liu, J.; Johnson, J. K.; Yates, J. T., Jr., Inter- and intratube self-diffusion in *n*-heptane adsorbed on carbon nanotubes. *Journal of Physical chemistry* **2007,** *111*, 4578-4584.
8. Chen, W.; Duan, L.; Zhu, D., Adsorption of polar and nonpolar organic chemicals to carbon nanotubes. *Environmental Science & Technology* **2007,** *41*, 8295-8300.
9. Bhatia, S. K.; Jepps, O. G.; Nicholson, D., Adsorbate transport in nanopores. *Adsorption* **2005,** *11*, 443-447.

10. Shih, Y.-h.; Li, M.-s., Adsorption of selected volatile organic vapors on multiwall carbon nanotubes. *Journal of Hazardous Materials* **2008,** *154*, 21-28.
11. Inoue, S.; Ickikuni, N.; Suzuki, T.; Uematsu, T.; Kaneko, K., Capillary condensation of N_2 on multiwall carbon nanotubes. *Journal of Physical Chemistry B* **1998,** *102*, 4689-4692.
12. Bandow, S.; Numao, S.; Jinno, M.; Hirahara, K.; Iijima, S., Correlation between diamagnetic susceptibility and electron spin resonance feature for various multi-walled carbon nanotubes. *Applied Physics A: Materials Science & Processing* **2007,** *87*, 13-16.
13. Pan, B.; Xing, B., Adsorption mechanisms of organic chemicals on carbon nanotubes. *Environmental Science & Technology* **2008,** *42*, (24), 9005-9013.
14. Schwarzenbach, R. P.; Gschwend, P. M.; Imboden, D. M., *Environmental Organic Chemistry, 2nd ed.* John Wiley and Sons Inc.: New York, NY, 2003.
15. Adamson, A.; Gast, A. P., *Physical Chemistry of Surfaces*. John Wiley & Sons: New York, 1997; p 784.
16. Yang, K.; Zhu, L.; Xing, B., Adsorption of polycyclic aromatic hydrocarbons by carbon nanomaterials. *Environmental Science & Technology* **2006,** *40*, (6), 1855-1861.
17. Diaz, E.; Ordonex, S.; Vega, A., Adsorption of volatile organic compounds onto carbon nanotubes, carbon nanofibers, and high-surface-area graphites. *J. Colloid and Interface Science* **2007,** *305*, 7-16.
18. Wang, J.; Yin, G.; Shao, Y.; Wang, Z.; Gao, Y., Investigation of further improvement of platinum catalyst durability with highly graphitized carbon nanotubes support. *Journal of Physical Chemistry C* **2008,** *112*, (15), 5784-5789.
19. Bachilo, S. M.; Balzano, L.; Herrera, J. E.; Pompeo, F.; Resasco, D. E.; Weisman, R. B., Narrow (*n*,*m*)-Distribution of single-walled carbon nanotubes grown using a solid supported catalyst. *Journal of the American Chemical Society Communications* **2003,** *125*, 11186-11187.
20. Li, F.; Chou, S. G.; Ren, W.; Gardecki, J. A.; Swan, A. K.; unlu, M. S.; Goldberg, B. B.; Cheng, H.-M.; Dresselhaus, M. S., Identification of the constituents of double-walled carbon nanotubes using Raman spectra taken with different laser-excitation energies. *Journal of Materials Research* **2003,** *18*, (5), 1251-1258.
21. Torrens, O. N.; Milkie, D. E.; Ban, H. Y.; Zheng, M.; Onoa, G. B.; Gierke, T. D.; Kikkawa, J. M., Measurement of chiral-dependent magnetic anisotropy in carbon nanotubes. *Journal of the American Chemical Society Communications* **2007,** *129*, (2), 252-253.
22. Hennrich, F.; Krupke, R.; Lebedkin, S.; Arnold, K.; Fischer, R.; Resasco, D. E.; Kappes, M. M., Raman spectroscopy of individual single-walled carbon nanotubes from various sources. *Journal of Physical Chemistry B* **2005,** *109*, 10567-10573.
23. Pimenta, M. A.; Dresselhaus, G.; Dresselhaus, M. S.; Cancado, L. G.; Jorio, A.; Saito, R., Studying disorder in graphite-based systems by Raman spectroscopy. *Physical Chemistry Chemical Physics* **2007,** *9*, 1276-1291.
24. Ma, J.; Alfe, D.; Michaelides, A.; Enge, W., Stone-Wales defects in graphene and other planer sp^2-bonded materials. *Physical Review B* **2009,** *80*.

25. Sun, G.; Kurti, J.; Kertesz, M.; Baughman, R. H., Variations of the geometries and band gaps of single-walled carbon nanotubes and the effect of charge injection. *Journal of Physical Chemistry B* **2003**, (107).
26. Yudasaka, M.; Fan, J.; Miyawaki, J.; Iijima, S., Studies on the adsorption of organic materials inside thick carbon nanotubes. *Journal of Physical Chemistry B* **2005,** *109*, 8909-8913.
27. Vix-Guterl, C.; Couzi, M.; Dentzer, J.; Trinquecost, M.; Delhaes, P., Surface characterizations of carbon multiwall nanotubes; comparison between surface active sites and Raman spectroscopy. *Journal of Physical Chemistry B* **2004,** *108*, 19361-19367.
28. Masheter, A. T.; Abiman, P.; Wildgoose, G. G.; Wong, E.; Xiao, L.; Rees, N. V.; Taylor, R.; Attard, G. A.; Baron, R.; Crossley, A.; Jones, J. H.; Compton, R. G., Investigating the reactive sites and the anomalously large changes in surface pK_a values of chemically modified carbon nanotubes of different morphologies. *Journal of Materials Chemistry* **2007,** *17*, 2616-2626.
29. Giusca, C. E.; Tison, Y.; Stolojan, V.; Borowiak-Palen, E.; Silva, S. R. P., Inner-tube chirality determination for double-walled carbon nanotubes by scanning tunneling microscopy. *Nanoletters* **2007,** *7*, (5), 1232-1239.
30. Zhu, Z.; Su, D.; Weinberg, G.; Schlogl, R., Supermolecular self-assembly of graphene sheets; formation of tube-in-tube nanostructures. *Nanoletters* **2004,** *4*, 2255-2259.
31. Wildgoose, G. G.; Wilkins, S. J.; Williams, G. R.; Frances, R. T.; Carnahan, D. L.; Jiang, L.; Jones, T., G.J.; Compton, R. G., Graphite powder and multi-walled carbon nanotubes chemically modified with 4-nitrobenzylamine. *ChemPhysChem* **2005,** *6*, 352-362.
32. Hristea, G.; Budrugeac, P., Characterization of exfoliated graphite for heavy oil sorption. *Journal of Thermal Analysis and Calorimetry* **2008,** *91*, (3), 817-823.
33. Kutana, A.; Giapis, K. P., First-principles study of chemisorption of oxygen and aziridine on graphitic nanostructures. *Journal of Physical Chemistry C* **2009,** *113*, 14721-14726.
34. Komarneni, M.; Sand, A.; Lu, M.; Burghaus, U., Adsorption kinetics of small organic molecules on thick and thinner layers of carbon nanotubes. *Chemical Physics Letters* **2009,** *470*, 300-303.
35. Holloway, A. F.; Wildgoose, G. G.; Compton, R. G.; Shao, L.; Green, M. L. H., The influence of edge-plane defects and oxygen-containing surface groups on the voltammetry of acid-treated, annealed and "super-annealed" multi-walled carbon nanotubes. *Journal of Solid State Electrochemistry* **2008,** *12*, 1337-1348.
36. Gregg, S. J.; Sing, K. S. W., *Adsorption, Surface Area, and Porosity*. Academic Press: New York, NY, 1982.
37. Gedat, E.; Schreiber, A.; Albrecht, J.; Emmler, T.; Shenderovich, I.; Findenegg, G. H.; Limbach, H.-H.; Buntknowsky, G., ^{2}H solid-state NMR study of benzene-d_6 confined in mesoporous silica SBA-15. *Journal of Physical Chemistry B* **2002,** *106*, 1977-1984.
38. Gilliland, E. R.; Baddour, R. F.; Perkinson, G. P.; Sladek, K. J., Diffusion on surface. I. Effect of concentration on the diffusivity of physically adsorbed gases. *Ind. Eng. Chem.; Fundam.* **1974,** *13*, 95-99.
39. Do, D. D.; Do, H. D., Effects of quadrupole moments of graphite surface on

adsorption of simple gases on graphitized thermal carbon black. *Colloids and Surfaces A: Physicochem. Eng. Aspects* **2007,** *300*, 50-59.
40. Gauden, P.; Terzyk, A. P.; Rychlicki, G.; Kowalczyk, P.; Lota, K.; Raymundo-Pinero, E.; Frackowiak, E.; Beguin, F., Thermodynamic properties of benzene adsorbed in activated carbons and multi-walled carbon nanotubes. *Chemical Physics Letters* **2006,** *421*, 409-414.
41. Hilding, J.; Grulke, E. A.; Sinnott, S. B.; Qian, D.; Andrews, R.; Jagtoyen, M., Sorption of butane on carbon multiwall nanotubes at room temperature. *Langmuir* **2001,** *17*, (24), 7540-7544.
42. Crespo, D.; Yang, R. T., Adsorption of organic vapors on single-walled carbon nanotubes. *Ind. Eng. Chem Res* **2006,** *45*, (16), 5524-5530.
43. Tournus, F.; Latil, S.; Heggie, M. I.; Charlier, J.-C., π-stacking interaction between carbon nanotubes and organic molecules. *Physical Review B* **2005,** *72*.
44. Zhao, J.; Lu, J. P.; Han, J.; Yang, C.-K., Noncovalent functionalization of carbon nanotubes by aromatics organic molecules. *Applied Physics Letters* **2003,** *82*, (21), 3746-3748.
45. Do, D. D.; Do, H. D., Characterization of micro-mesoporous carbonaceous materials. Calculations of adsorption isotherm of hydrocarbons. *Langmuir* **2002,** *18*, 93-99.
46. Kruk, M.; Li, Z.; Jaroniec, M., Nitrogen adsorption study of surface properties of graphitized carbon blacks. *Langmuir* **1999,** *15*, 1435-1441.
47. Choma, J.; Jaroniec, M.; Burakiewicz-Mortka, W.; Kloske, M., Critical appraisal of classical methods for determination of mesopore size distributions of MCM-41 materials. *Applied Surface Science* **2002,** *196*, 216-223.
48. Sigma-Aldrich Chemical Company Online Catalog: http://www.sigmaaldrich.com/technical-service-home/product-catalog.html, (2009).
49. Quantachrome, *Users Manual*.
50. Smajda, R.; Kukovecz, A.; Konya, Z.; Kiricsi, I., Structure and gas permeability of multi-wall carbon nanotube buckypapers. *Carbon* **2007,** *45*, 1176-1184.
51. Ustinov, E. A.; Do, D. D., Modeling of adsorption in finite cylindrical pore by means of density functional theory. *Adsorption* **2005,** *11*, 455-477.
52. Inoue, S.; Hanzawa, Y.; Kaneko, K., Prediction of hysteresis disappearance in the adsorption isotherm of N_2 on regular mesoporous silica. *Langmuir* **1998,** *14*, 3079-3081.
53. Ustinov, E. A.; Do, D. D., Application of density functional theory to capillary phenomena in cylindrical mesopores with radial and longitudinal density distributions. *Journal of Chemical Physics* **2004,** *120*, (20), 9769-9781.
54. Mackie, E. B.; Wolfson, R. A.; Arnold, L. M.; Lafdi, K.; Migone, A. D., Adsorption studies of methane films on catalytic carbon nanotubes and on carbon filaments. *Langmuir* **1997,** *13*, 7197-7201.
55. Webster, C., Edwin; Drago, R. S.; Zerner, M. C., Molecular dimensions for adsorptives. *Journal of the American Chemical Society Communications* **1998,** *120*, 5509-5516.
56. Duer, M. J., *Introduction to Solid-State NMR Spectroscopy*. Oxford Press: Oxford, U.K., 2004.

57. Boddenberg, B.; Burmeister, R., ^{2}H n.m.r. study on the rotation and diffusion kinetics of propane and benzene in NaX and AgNaX zeolites. *Zeolites* **1988,** *8*, 488-494.
58. Grundke, V.; Boddenberg, B., One and two component adsorption layers of *n*-hexane and benzene on graphite studied by ^{2}H NMR spectroscopy. *Molecular Physics* **1993,** *79*, (6), 1215-1226.
59. Rodriguez-Manzo, J. A.; Lopez-Urias, F.; Terrones, M.; Terrones, H., Magnetism in corrugated carbon nanotori: the importance of symmetry, defects, and negative curvature. *Nano Letters* **2004,** *4*, (11), 2179-2183.
60. Wakabayashi, K.; Harigaya, K., Magnetic structure of nano-graphite Mobius ribbons. *Journal of the Physical Society of Japan* **2003,** *72*, (5), 998-1001.
61. Boddenberg, B.; Grosse, R., A deuteron NMR study on a benzene multilayer on graphite. *Z. Naturforsch* **1987,** *421*, 272-274.
62. Ferrari, A. C.; Robertson, J., Interpretation of Raman spectra of disordered and amorphous carbon. *Physical Review B* **2000,** *61*, (20), 14,095-14,107.
63. Levitt, M. H., *Spin Dynamics: Basics of Magnetic Resonance*. John Wiley & Sons: West Sussex, England, 2001; p 686 p.
64. Boddenberg, B.; Beerwerth, B., Proton and deuteron magnetic resonance relaxation of benzene adsorbed on alumina and on a platinum/alumina catalyst. *Journal of Physical Chemistry* **1989,** *93*, 1440-1447.
65. Boddenberg, B.; Beerwerth, B., Proton and deuteron magnetic resonance spectra of benzene adsorbed on alumina and on a platinum/alumina catalyst. *Journal of Physical Chemistry* **1989,** *93*, 1435-1440.
66. Nishikiori, S.-I., Out-of-plane motion of the guest benzene molecule trapped in a $[Cd(dmen)_2(CN)]_2[Cd(CN)_4]$ host as studied by ^{2}H-NMR. *Journal of Inclusion Phenomena and Macrocyclic Chemistry* **1999,** *34*, 331-343.
67. Xiong, J.; Maciel, G. E., Deuterium NMR studies of local motions of benzene adsorbed on Ca-montmorillonite. *Journal of Physical Chemistry B* **1999,** *103*, 5543-5549.
68. Fodi, B.; Hentschke, R., Molecular dynamics simulation of a binary hydrocarbon mixture near an adsorbing wall: benzene/*n*-heptane on graphite. *Langmuir* **1998,** *14*, 429-437.
69. Nguyen, T. X.; Bhatia, S. K., Probing the pore wall structure of nanoporous carbons using adsorption. *Langmuir* **2004,** *20*, 3532-3535.
70. Suarez, M. P.; Palermo, A.; Aldao, C. M., The compensation effect revisited. *Journal of Thermal Analysis* **1994,** *41*, 807-816.
71. Bond, G. C.; Keane, M. A.; Kral, H.; Lercher, J., Compensation phenomena in heterogeneous catalysis: general principles and a possible explanation. *Catalysis Reviews* **2000,** *42*, (3), 323-383.
72. Carman, P. C.; Raal, F. A., Diffusion and flow of gases and vapours through micropores. III. Surface diffusion coefficients and activation energies. *Proceedings of the Royal Society of London. Series A. Mathematical and Physical Sciences* **1951,** *209*, (1096), 38-58.
73. Choi, J.-G.; Do, D. D.; Do, H. D., Surface diffusion of adsorbed molecules in porous media: monolayer, multilayer, and capillary condensation regimes. *Ind. Eng. Chem. Res.* **2001,** *40*, 4005-4031.

74. Fletcher, A. J.; Thomas, K. M., Compensation effect for the kinetics of adsorption/desorption of gases/vapors on microporous carbon materials. *Langmuir* **2000,** *16*, 6253-6266.
75. Liu, L.; Guo, Q. X., Isokinetic relationship, isoequilibrium relationship, and enthalpy-entropy compensation. *Chemical Reviews* **2001,** *101*, 673-695.
76. Miyabe, K.; Guiochon, G., Thermodynamic characteristics of surface diffusion in reversed-phase liquid chromatography. *Journal of Physical Chemistry B* **1999,** *103*, 11086-11097.
77. Jaroniec, M., Evaluation of the fractal dimension from a single adsorption isotherm. *Langmuir* **1995,** *11*, 2316-2317.
78. Arena, M. V.; Deckert, A. A.; J.L., B.; George, S. M., Surface diffusion and desorption of pentane isomers on Ru(001)
Journal of Physical Chemistry **1990,** *94*, 6792-6797.
79. Rigby, S. P., Fractal theory for the compensation effect observed in a surface diffusion process studied using deuteron NMR. *Langmuir* **2002,** *18*, 1613-1618.
80. Rigby, S. P., A model for the surface diffusion of molecules on a heterogeneous surface. *Langmuir* **2003,** *19*, 364-376.
81. Rigby, S. P., Predicting surface diffusivities of molecules from equilibrium adsorption isotherms. *Colloids and Surfaces A: Physicochem. Eng. Aspects* **2005,** *262*, 139-149.
82. Tang, P.; Chew, N. Y. K.; Chan, H.-K.; Raper, J. A., Limitation of determination of surface fractal dimension using N2 adsorption isotherms and modified Frenkel-Halsey-Hill theory. *Langmuir* **2003,** *19*, 2632-2638.
83. Pfeifer, P.; Avnir, D., Chemistry in noninteger dimensions between two and three. I. Fractal theory of heterogeneous surfaces. *Journal of Chemical Physics* **1983,** *79*, (7), 3558-3565.

8. THE MOLECULAR MOTION OF BENZENE-d_6 ON MICROPOROUS, HETEROGENEOUS BLACK CARBONS

8.1 INTRODUCTION

The black carbons (BCs) discussed in previous chapters were similar to each other in their elemental composition, almost entirely carbon (with the exception of the NIST #2975 soot), but differing only *slightly* in the nature of the carbon aromatic structure and *significantly* in the shape and size of the grains and associated micro- and mesopores. The remaining two BCs, maple wood char (MWC) and activated carbon (AC), which are addressed in this chapter, were elementally heterogeneous (Table 8.1), although they still contained between 70-88% carbon, and the porosity (Table 8.2) was almost exclusively in the

Table 8.1 Elemental composition and polar functionalities of MWC and AC

Sample	Elemental Composition							Concentration of Functional Group			Functional Groups[b]
	wt%					ppm	ppm (mM/g)	mM/g			
	C	N	H	O	ash	Fe	Ca	carboxyl	total acid	total base	
MWC	71.97[c]	0.51[c]	2.84[c]	23[c]	-	-	3200[d] (0.18)[e]				aromatic, phenolic, carboxylic[c]
AC	87.6[f]	-	0.90[f]	7.0[f]	4.5[g]	200 max[g]	467[d] (0.03)[e]	0.1[f]	0.27[f]	0.34[f]	aromatic[f]

[a]Boehm titration; [b]NMR, FTIR; [c][1]; [d]Galbraith Laboratories; [e]based on the density of graphite, 2.26 g/ml; [f][2]; [g][3].

Table 8.2. Pore and surface area properties of AC and MWC

Sample	Surface Area (m^2/g)	Particle Size	DFT Pore Diameter[a]			
			< 2nm	2-5 nm	5-50 nm	Total < 5 nm
Activated carbon (Darco G60) AC	776[b], 798[c]	125 μm (100 mesh)[b]	0.315[c]	0.123[c]		0.438[c]
Maple wood char[d] MWC	430[e]	125 μm (100 mesh)[e]	0.120[e]	0.030[e]	0.006[e]	0.150[e]

[a]Density functional theory (nonlocalized) method; [b][2]; [c]this work; [d]sample provided by Dr. Joseph J. Pignatello of the Connecticut Agricultural Research Station; [e][1].

micropore size range. If these differences in solid phase properties resulted in different sorption interactions, then different molecular motions could be induced in the benzene sorbed on the MWC and AC than on the BCs examined in the previous chapters, and, further, these different molecular motions could be detected in their ^{2}H nuclear magnetic resonance (NMR) spectra.

The physisorption interactions of benzene with activated carbons have been considered by most researchers to consist of essentially the same dispersive and electrostatic π-π interactions with which benzene interacts with graphite, enhanced by overlapping surfaces forces from the micropore walls [4-11]. Numerous models of isotherms for activated carbon have been based on this assumption, using benzene as a reference sorbate [5, 9, 10, 12]. Activated carbon, in particular Darco G-60, has been considered a model for naturally occurring chars, and the MWC in the present study, after examination of aqueous isotherms of polyaromatic hydrocarbons, was determined by the authors to interact primarily via planar alignment of the aromatic functionality onto char's graphenic surfaces [13]. In other words, the process of adsorption of aromatics onto graphite was a good model for the adsorption of aromatics on MWC. If this assumption were correct, then the motion of benzene on MWC and AC should be very similar to that observed within the micropores of the carbon nanoparticles and the carbon nanotubes, that is, translation across the surface of the pore walls with which the benzene plane was oriented face-to-face while simultaneously executing a C_6 rotation. In the previous chapters of this dissertation, the orientational change of the benzene molecule which was detected by the nuclear magnetic resonance (NMR) of the benzene deuterons in

these BCs reflected the isotropic shapes of the BCs' pores. If this model holds for the AC and MWC, then the spectral shape should be similar, although the even smaller slit-shape pores would not provide an isotropic distribution of orientations. Additionally, the enhanced surface forces within the subnanometer micropores could increase the viscous "drag" on the rotation of benzene [14], slowing the rate of motion and widening the peak or even falling below the quadrupolar exchange coupling value to produce a Pake peak [15, 16]. On the other hand, if the ionic, noncarbon composition of heterogeneous BCs were to dominate the sorption interactions, then the acidic surface sites interacting with benzene as an electron donor would be the most important influence on the motion. The molecular motion of site-constrained chemisorbed benzene would be expected to display a small angle wobble (SAW) or large angle wobble (LAW) and generally to provide a Pake component to the ^{2}H solid-state NMR spectrum [17]. Finally, the very smallest pores could sterically constrain the benzene motion to induce a LAW, SAW or other motion [18].

The MWC and AC are heterogeneous with respect to elemental composition and contain significant oxygenated chemical functionalities (Table 8.1) [1, 2]. Both samples are predominantly aromatic carbon, with carboxyl and other oxygen-containing groups, based on NMR, FTIR, and IR [1, 2]. Although the Boehm titration analysis of the AC indicated the presence of surface basic functional groups, the pH of an equilibrated aqueous phase is 6 [3]. Comparable data was not available for the BCs in previous chapters, although the amount of carbon was > 95% for these BCs (other than soot) so that polar surface sites due to covalently

bonded H or O could only exist as minor components. With respect to the graphenic functions on the AC and MWC, the X-ray diffractograms (XRDs) indicated only minimal graphitic crystallization (Figure 3.3 and Table 3.2 in Chapter 3) because of the broad diffraction peaks at d-spacing values of 0.37 nm and 0.49 nm. As discussed in Chapter 3, the amount of shift away from the ideal value of 0.335 nm was an indicator of crystalline disorder. Thus, for both MWC and AC, although the pore walls may be dominated by graphenic functionality, the platey graphenic domains are not aligned in a commensurate arrangement to produce high crystallinity. An abundance of low-angle curved surfaces in activated carbons, which were observed in a recent high-resolution transmission electron microscopic images [8], provides a possible explanation for the lack of graphitic alignment.

Both of the samples have high surface areas (Table 8.2), evident from the steep initial slope on the Type I N_2 isotherm (Figure 3.6). Similar isotherms have been observed for benzene vapor on other activated carbons [19], and, also, an aqueous isotherm of benzene on Darco G60, displayed a Type I Langmuir shape, indicating only monolayer adsorption [20]. Further, the desorption arm of the N_2 isotherm on MWC was hysteretic (showed offset from the adsorption isotherm) by 20% for the largest separation at 0.08 relative pressure [20]. The aqueous isotherm of benzene on MWC collected by Braida et al. [1] did not adhere to either a Langmuir or Freundlich equation, although hysteresis was also observed, and the authors concluded that it was due to swelling of the pores at higher benzene concentrations during the isotherm experiment [1]. The N_2 isotherm for the activated carbon (Figure 3.6 in Chapter 3) did not display hysteresis.

The pore size distributions (Table 8.2 and, from Chapter 3, Table 3.2 and Figure 3.8), were strongly weighted toward the micropore size range. For the AC, the 0.01 cc/g cumulative pore volume curve filled pores up to 4.2Å wide, although the lower confidence limit of the DFT analysis was 5.7Å. Even at the modal pore width of 5.9Å (and 35% of all the pores were equal to or lower than this value), the 7.4Å wide benzene molecule could not perform a full rotation within the pore. Thus, it would appear to be impossible for the benzene to execute either an isotropic or a pseudoisotropic motion, and a possible alternate motion would be a sliding wobble. However, in very small pores, the benzene could be pulled equally by pore walls on both sides. For MWC, the 0.01 ml/g cumulative pore volume was also at 4Å [1], so that the pore size constraints on the motion of benzene were similar in both the MWC and the AC.

8.2 EXPERIMENTAL

The maple wood char was provided by Joseph J. Pignatello and prepared as described by Braida et al. [1]. Briefly, maple wood shavings were pyrolyzed under atmospheric conditions at 400°C for 2 hours and subsequently sieved through a 0.150 mm (#100) screen. The activated carbon was purchased from Aldrich and was selected for this study on the basis of its previous selection by Chiou's group as a standard for methodological study on the optimal separation procedures of environmental charcoal from natural samples [20]. As mentioned above, in addition to characterization by previous workers, in the present study, X-ray diffractograms, N_2 isotherm data, and pore size analyses were obtained, as well as measurement of the concentration of elemental calcium (Table 8.1). Details of the experimental

protocols for these analyses are detailed in Chapter 3.

In order to prepare samples for ^{2}H solid-state NMR analysis of the sorbed benzene, samples of the BCs were loaded with benzene-d_6 (Table 8.3), according to the procedure outlined in the Experimental Section. Briefly, the solid phase was

Table 8.3. Samples of benzene-d_6 on MWC and AC

Sample Name	Mass of Char/Carbon (mg)	Deposited Volume of Benzene (μl)	Volume of Benzene per NMR Quantitation Plot[a]	% load (w/w)	% loading (monolayer coverage)
MWC2	16.6 (±0.1)	1.7 (±0.1)	-[b]	10.0 (±0.1)%	21.5 (±1.4)
MWC3	186.2 (±0.1)	2.0 (±0.1)	0.9 (±0.2)	1.0 (±0.1)%	7.2 (±0.4)
MWC5[c]	135.5 (±0.1)	1.4 (±0.1)	1.0[d]	1.0 (±0.1)%	7.2 (±0.4)
ActC2	211.3 (±0.1)	2.2 (±0.1)	0.8 (±0.1)	1.0 (±0.1)%	3.9 (±0.2)
ActC3	190.8 (±0.1)	2.0 (±0.1)	1.4[d]	1.0 (±0.1)%	4.0 (±0.2)
ActC4	128.0 (±0.1)	1.3 (+0.1)	0.9 (+0.1)	1.0 (±0.1)%	3.9 (±0.3)

[a]The NMR quantitation plot was calibrated to the area of neat liquid benzene; [b]no quantitation spectrum was collected for this sample; [c]this sample was cannibalized froma previous sample loaded at 0.1% for which no signal was observed; [d]only one quantitation spectrum was collected for this sample.

placed into a specially-necked 10 mm NMR tube which was attached to a vapor deposition manifold. A precise amount of benzene-d_6 was condensed into the NMR tube, which was submerged in liquid nitrogen, and the sample was subsequently backfilled to 200-400 torr with N_2 gas, flamed-sealed, and transported to the Oklahoma Statewide NMR Facility at Stillwater, Oklahoma, for collection of the variable-temperature solid-state ^{2}H NMR spectra on the Chemagnetics 300 MHz instrument. In order to verify the quantities of benzene-d_6 loaded into both samples, an NMR spectra was collected with particular parameters, and the NMR spectral areas were plotted against the volume loaded in comparison to a calibration line prepared from the areas of NMR spectra of sealed liquid benzene-d_6 collected with

those same parameters, as described in Appendix A1. The quantities of benzene-d_6 on the MWC and AC predicted from the NMR area calibration curve (Table 8.3, Figure A1.4) were approximately 70% of the value calculated from the pressure difference on the vapor deposition manifold, and this was the same amount of deficit which was observed in the quantitation plots of the samples discussed in Chapters 4-7, which was deemed acceptable (Margaret Eastman, personal communication). For collecting solid-state ^{2}H NMR spectra at variable temperatures for jump rate determination, parameters used were 3600-86400 scans (Table 8.4), delay times of either 0.5 s or 0.25 s, both 20 μs and 40 μs echo spacing taus, 1024 data points, and were processed without line broadening. Longitudinal relaxation time measurements at four different temperatures were measuring with the inversion recovery technique and either 0.50 s or 5.0 s delay times.

8.3 RESULTS: ^{2}H SOLID-STATE NMR SPECTRA AT VARIABLE TEMPERATURES AND AGES

8.3.1 Distinctively broad spectra

The ^{2}H static NMR spectra of 1% benzene-d_6 on AC at 25°C (Figure 8.1, Table 8.4, both on the next page) changed with aging, initially appearing pseudoisotropic, but, by day 76, had become a broad single peak, which displays symmetric shoulders towards the base. As the temperature is reduced to 15°C, the peak broadens slightly. At -5°C, the upper part of the peak is broader and the shoulders in the lower part of the peak are more prominent. By -25°C, the spectrum is generally triangular, with straight sides at the base, but lacking the feet which are

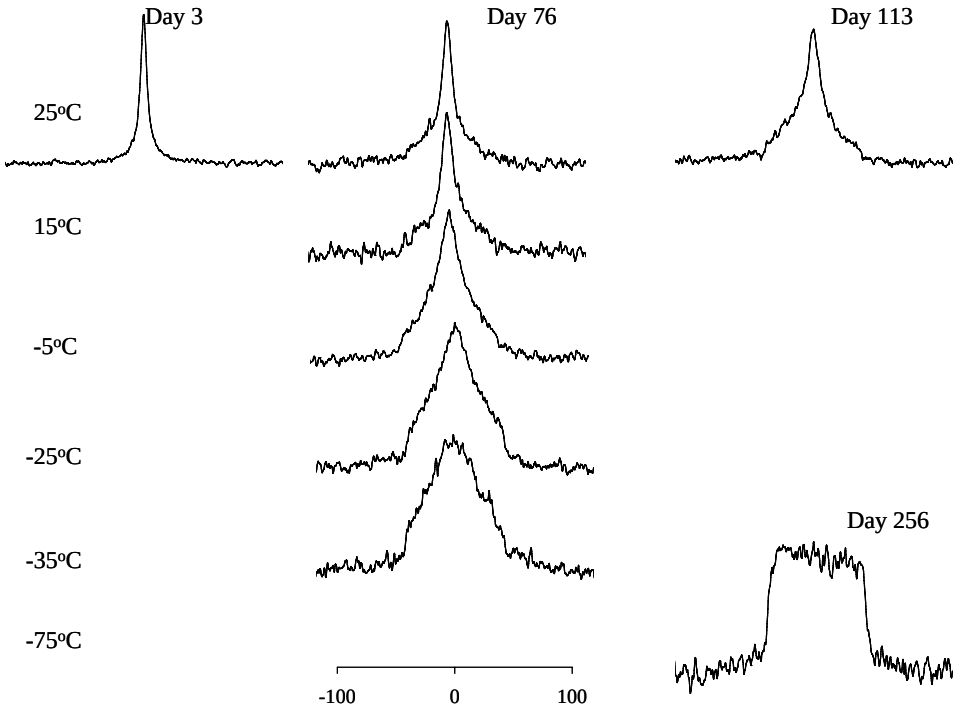

Figure 8.1. ^{2}H NMR static solid-state spectra of benzene-d_6 on AC at different temperatures and ages.

Table 8.4. Peak width at half-height ($\delta\nu^{a}$) of the static solid-state ^{2}H NMR spectra of benzene-d_6 on AC at different temperatures and ages

Sample	Temp (°C)	Ages		
ActC2		Day 3	Day 76	> Day 76
	25	6.9 kHz 3600 scans	18.1 kHz[b] 3600 scans	16 kHz[c] 21600 scans
	15		23.1 kHz[b] 3600 scans	
	-5		37.7 kHz[b] 14400 scans	
	-25		47.5 kHz[b] 14400 scans	
	-35		51.2 kHz[b] 7200 scans	
	-75			68 kHz[d] 3600 scans

[a]Peak widths at half-height from spectra collected with a 40 μs echo delay, 1024 data points, processed with 0 line-broadening function and zero-filled to 4096 data points; temperature uncertainty $\pm$0.1°C; peak width uncertainty $\pm$0.5 kHz; [b]data collected with 2048 data points; [c]day 113; [d]day 256.

common in Pake spectra. At -35°C, the top of the peak is quite curved, the lower shoulders are broader and, higher up on the peak sides, there is another, upper shoulder which is suggestive of a developing Pake horn. By -75°C on day 256, the spectrum is squared off at the top and the sides are straight.

The spectrum on maple wood char (Figure 8.2) at 25°C is a rather nondescript peak with the general appearance of a house, with peak widths

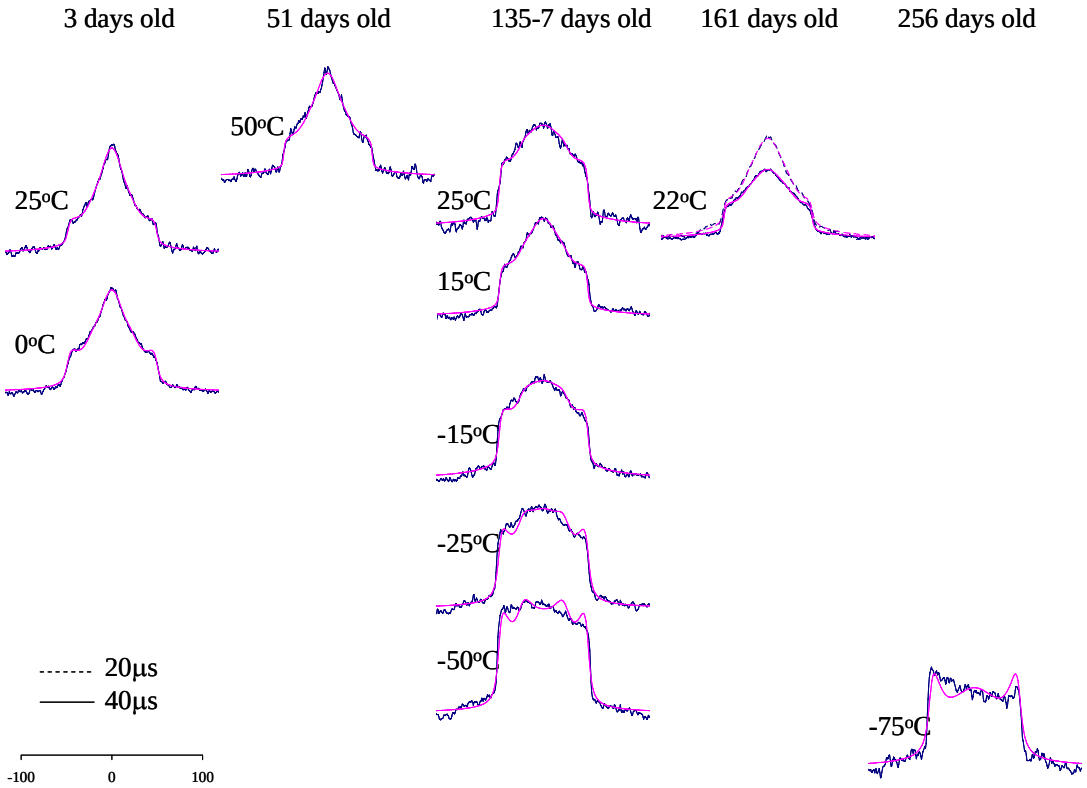

Figure 8.2. ^{2}H NMR experimental spectra (blue) overlain by simulated spectra (pink) of benzene-d_6 loaded at 1% w/w on MWC at variable temperatures and ages. See text for instrumental parameters and spectral libraries.

approaching the value of quadrupolar splitting, i.e., as wide as a SAW peak (Table 8.5 on the next page). As the temperature is decreased to -75°C, the peak of the house flattens until it becomes mesa-like. The quantitation spectra for the

samples MWC3 and ActC2 were collected at days 311 and 256, respectively, after sealing, and contained 49% and 36%, respectively, of the amount of benzene-d_6 deposited, as calculated at the time of sealing. Therefore, some of the benzene-d_6

Table 8.5. Peak width at half-height ($\delta\nu^a$) of the ^{2}H NMR spectra of benzene-d_6 on MWC at different temperatures and ages.

Sample	Temp (^{o}C)	Ages				
MWC2		Day 1				
10% load	25	8 kHz 86400 scans				
	0	9 kHz 14400 scans				
MWC3		Day 3	Day 51	Days 135-137	Day 161	Day 256
1% load	50		39 kHz 7200 scans			
	25	32 kHz		63 kHz 14400 scans	70 kHz	
	15			60 kHz 14400 scans		
	0	38 kHz				
	-15			66 kHz 14400 scans		
	-25			67 kHz 14400 scans		
	-50			69 kHz 14400 scans		
	-75					70 kHz 3600 scans

[a]Peak widths at half-height determined manually from spectra collected with a 40 μs echo delay, 1k data points, processed with 1kHz line-broadening function; temperature uncertainty $\pm$0.1^{o}C; peak width uncertainty estimated at $\pm$2kHz; [b]22°C.

which was originally loaded may have leaked slowly out of the samples over time, or may have diffused into configurations which changed its motion and led to destructive interference within the spectrum. Unfortunately, there were no directly comparable spectra of the MWC taken at different ages which could be compared for signal loss over time. However, there was a substantial increase in peak width between day 3 and day 135 for similar temperatures of the benzene on MWC3

(Table 8.5). For the ActC2 sample, there were two directly comparable spectra (25°C, 40 μs echo delay, 3600 scans) taken at different ages (days 3 and 77), and they were within 1% of the same spectral area, indicating no loss of analyte, although the peak width has increased (Table 8.4). Therefore, a loss of signal due to a change in motional mode over time and subsequent destructive interference via exchange between those motional modes may account for the apparent lack of benzene. However, it seemed reasonable nevertheless to keep in mind that the benzene loading for some of the spectra may have been lower than the original 4% of a monolayer.

8.3.2 Indicators of motional models from the character of the spectra

Both the AC and MWC contained lower amounts of carbon than the other BCs. The char was the only sample in the study for which an appreciable inorganic ionic component was measured (3200 ppm Ca), and it seemed plausible to attribute part of the motion of the benzene to localized π-cation interactions, leading to the Pake-like character of the spectrum [21]. In a related study of the molecular motion of benzene-d_6 sorbed to Ca-montmorillonite, Xiong and Maciel [17] hypothesized that the π-cation interaction was the principle sorption mechanism at low loadings levels. However, in Ca-montmorillonite, the Ca^{2+} ions are evenly distributed across the pore surface whereas the Ca in a char may exist as clumps of $CaCO_3$ (Figure 1.7). The AC, however, has a somewhat larger concentration of organic polar functional groups on the surface than the concentration of Ca in MWC, and therefore those spectra may similarly reflect the interaction of benzene undergoing π-H^+ electron donor/acceptor interactions. However, several workers on activated

carbons have concluded that, other than pore blocking with the involvement of water molecules, hydrogen functionalities at the surface are minimal in accounting for the sorption characteristics, especially with regard to hydrophobic compounds, such as benzene [22]. It should be noted at this time that the NIST #2975 soot sample contains approximately the same fraction of heteroatoms as the AC, but, as discussed in Chapter 4, the interaction of benzene with the surface is primarily with the graphenic functions. However, this does not necessarily exclude the role of surface heteroatoms as important contributors to sorption interactions because the soot heteroatoms may occur primarily within the core of the soot, as discussed in the Introduction.

As mentioned above, another unique feature of the AC and MWC which might have affected the motion of adsorbed benzene was the dominance of micropores in the MWC which effectively "trapped" the benzene molecules inside the micropores. Recalling from Chapter 3 that the 1% (0.01 ml pore/g BC) loading accounted for pore sizes only up to 4Å, in a slit-shaped pore narrower than the smallest distance across the benzene plane, which had a maximum diameter of 6.7Å, the benzene would be unable either to execute a full rotation to provide isotropic reorientation, or to move 360° around the surface of the pore for pseudoisotropic motion. Whereas the soot, carbon nanoparticles, carbon nanotubes, and the graphitized carbon black (Carbopack B) [23] had followed the surface of the spherical pores to produce pseudoisotropic motion, the slit-shape pores in MWC had a preferred surface orientation.

In comparing these spectra with samples from the literature, the closest

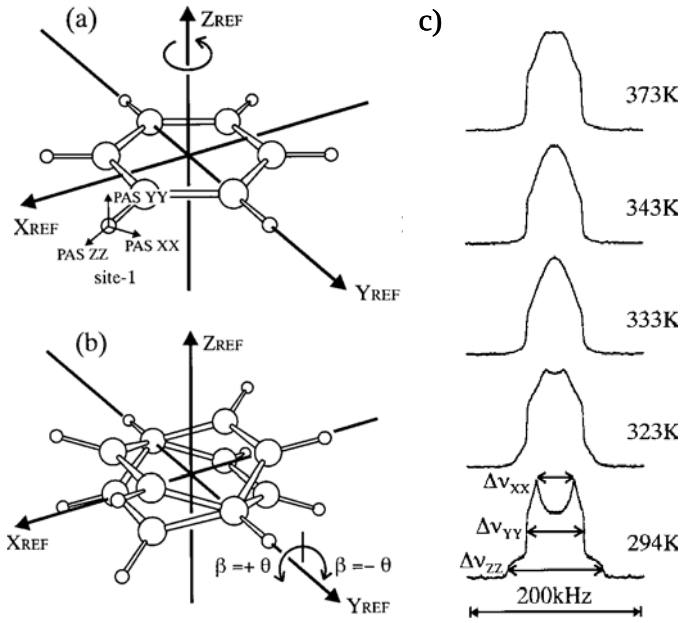

Figure 8.3. a) First motional frame; b) second motional frame; c) experimental spectra of benzene-d6 in clathrate after et al. [25] X_{REF}, Y_{REF} and Z_{REF} are axes of the benzene molecule before motion. X_{PAS}, Y_{PAS}, and Z_{PAS} are the axes of the principal axis system, which is observed relative to the laboratory frame of reference. β is the Euler angle, Δν is the quadrupolar splitting for the PAS [25].

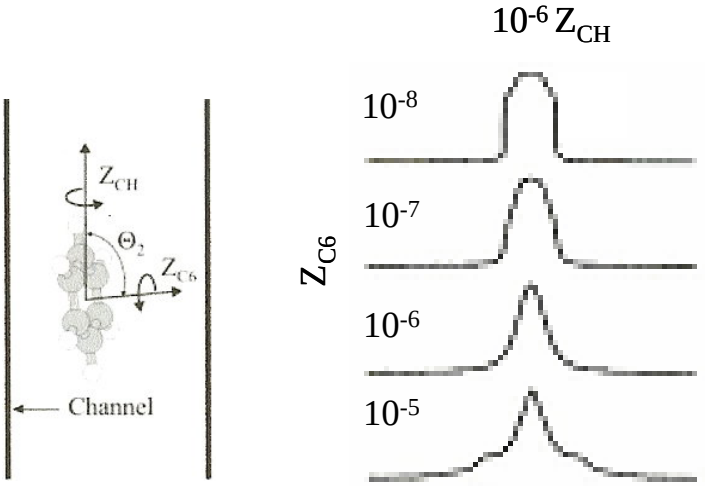

Figure 8.4 (left) motional model, showing axes of rotation, Z_{CH} is the rotation about the channel axis (benzene C_2); (right) the simulated spectra for the modeled motion at the indicated rates [26].

resemblance comes from studies of transitional regions between motional regimes

of guest benzene in clathrate compounds done by Chopra et al. [24] and Nishikiori et al. [25] (Figure 8.3), and in an inclusion compounds which forms channels by Villanueva-Garibay and Muller [26] (Figure 8.4). The last two studies, addressed in the Introduction Chapter, were able to model the motion and construct simulated spectra, and the models in both cases involved a C_6 in-plane rotation executed simultaneously with an out-of-plane motion. For the Nishkiori samples, $Cd(dmen)_2(CN)]_2[Cd(CN)_4]$, the out-of-plane motion took the form of a $\pm 30^o$ wag at low temperatures and became a full 360° rotation as the clathrate "pore" structure became more flexible at high temperatures (Figure 8.5) [25]. For the Villanueva-Garibay and Muller samples, tris(1,2-dioxyphenyl)cyclotriphosphazene, the pores are channels and the benzene plane rotated fully around its C_2 axis, and, as with most benzene motion, simultaneously performed a C_6 in-plane rotation (Figure 8.4) [26]. Both of these cases contain two motional frames around axes that are at a fixed angle to each other. This is distinguished from a wobble motion in which the angle between the two axes of rotation varies, which introduced a third axis of variability into the molecule's motion [27, 28]. Further, in both of these cases, the out-of-plane motion was influenced by the "pore" symmetry, which had diameters slightly larger than the benzene guests [25, 26].

Considering ^2H solid-state NMR peak shapes in a general way (Figure 8.3), as reviewed by Nishikiori et al. [25], the quadrupolar splitting along the axis of the electric field gradient (along the C-D bond), referred to as the $\Delta\nu_{zz}$, shows up in the widest value of the spectral feet at the base of the spectrum. The quadrupolar splitting along the perpendicular axis , $\Delta\nu_{yy}$, which corresponds to the benzene C_6,

shows up near the peak half-height, and the third dimension of the quadrupolar splitting, $\Delta\nu_{xx}$, toward the top of the peak [25]. In the MWC spectra (Figure 8.2), in particular, the decrease in the outer feet spacing ($\Delta\nu_{zz}$ splitting) and, to a lesser extent, the increase in the "pointiness" ($\Delta\nu_{xx}$ splitting) of the spectra with increasing temperature was indicative of motional narrowing in response to an increased rate of C_6 rotation, although the peak width, which is in the region of $\Delta\nu_{yy}$ splitting, is nearly constant across a range of temperatures. According to the authors, this pattern indicated a constant angle of motion in the out-of-plane direction (β Euler angle in Figure 8.5) [25]. The loss of the outer feet could be attributed (1) to interference between the signals from two difference motional populations, which is inherent in the transitional region, or (2) to the effect of weighted site populations [25]. Weighted site populations means that the molecule occupies certain motional sites more than others [25, 26, 28].

It seemed likely that motion of benzene trapped in the very narrow pores in the MWC or AC would be affected by surface forces from the pore walls [18, 22]. Because many of the pores were narrow enough to preclude full rotation, such steric hindrance should restrict the benzene's motion. Further, the surface forces would be exerted onto and interacting with the benzene molecule from both sides of the pore, as well as from cationic and protonic sites in the char matrix [18]. It would seem that a motional model similar to one of those described above for clathrates could be used to fit the MWC or AC spectra. For instance, if the pore is 4Å in diameter, then a 30° wag would be permitted, and, in a 5.9Å diameter pore, a 54° wag would be permitted. If the benzene molecule were in larger pores, it could rotate 360°, but its

rotation would not be strictly isotropic because it would favor a face-to-face orientation on the pore wall. This could be described as translating across the surface of a graphitic pore, just as described by Grundke and Boddenberg [23] and for BC samples in preceding chapters, but the surface of the pore is not isotropic, but is box-shaped. Also, if the benzene were near the mouth of the pore, it could conceivable perform an isotropic or pseudoisotropic rotation.

8.3.3 Arrhenius behavior of benzene-d_6 on maple wood char

At last, after attempting several fits using DFP of the experimental ^{2}H NMR spectra of benzene-d_6 on MWC to simulations using various combinations of wags, ISO, LAW and SAW, the most successful was an ISO/LAW combination and these simulated spectra are shown overlaying the experimental in Figure 8.1. All of the fits indicated the motional mode consisted of over 97% ISO (except 90% for the 15°C) with very slow reorientational jump rates, nearly slow enough to produce quadrupolar coupling doublets. The LAW component accounts for the Δ_{yy} constant peak width, resulting in a β Euler angle (Figure 1.17 and Figure 8.3) of 46° for all spectra. Although it would seem that the 3% LAW component of the fit is so small that a good fit could be obtained to ISO only, the resulting simulations are lacking in either feet or the abrupt peak/baseline transition displayed in the experimental spectra, but instead show very wide Lorentzian peaks with a gradual transition to baseline. The change of signal area with temperature (Figure 8.5) indicated that this temperature regime was at least beginning to enter a transition between motional modes, and this gave some concern about the validity of the Arrhenius constants measured. These values were low, but comparable to other BC samples in this

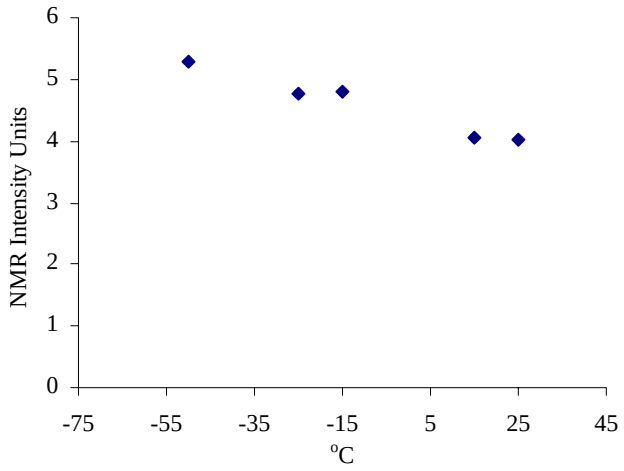

Figure 8.5. NMR area vs. temperature for days 135-7 on MWC.

dissertation. The ISO jump rates were nearly the same over the range of temperatures, 1.5 (±0.7) kJ/mol E_a and 1.2 (±0.2) x 10^5 rad/s pre-exponential, but the rate of LAW angle reorientation gives an E_a value of 8 (±3) kJ/mol and a pre-exponential value of 1.2 (±0.6) x 10^7 rad/s, comparable to the CNT (Figure 8.6). This would imply that a small fraction of the molecules exist in sites that were more localized (perhaps interacting with water molecules adsorbed to Ca^{2+} ions?). The pseudoisotropic motion with the low E_a values seemed to imply that the benzene molecules occupied pores large enough for complete rotation and rotated within those pores with minimal interaction, but considerable steric constraint as indicated by the low value of the pre-exponential. Possibly, the smaller pores, while accessible to N_2 and CO_2 molecules in the gas isotherm experiment, were less accessible to larger benzene-d_6 molecules.

The E_a value for the C_6 rotation, which shows no apparent trend with temperature from the fitted data above, was measured by collecting T_1 values at

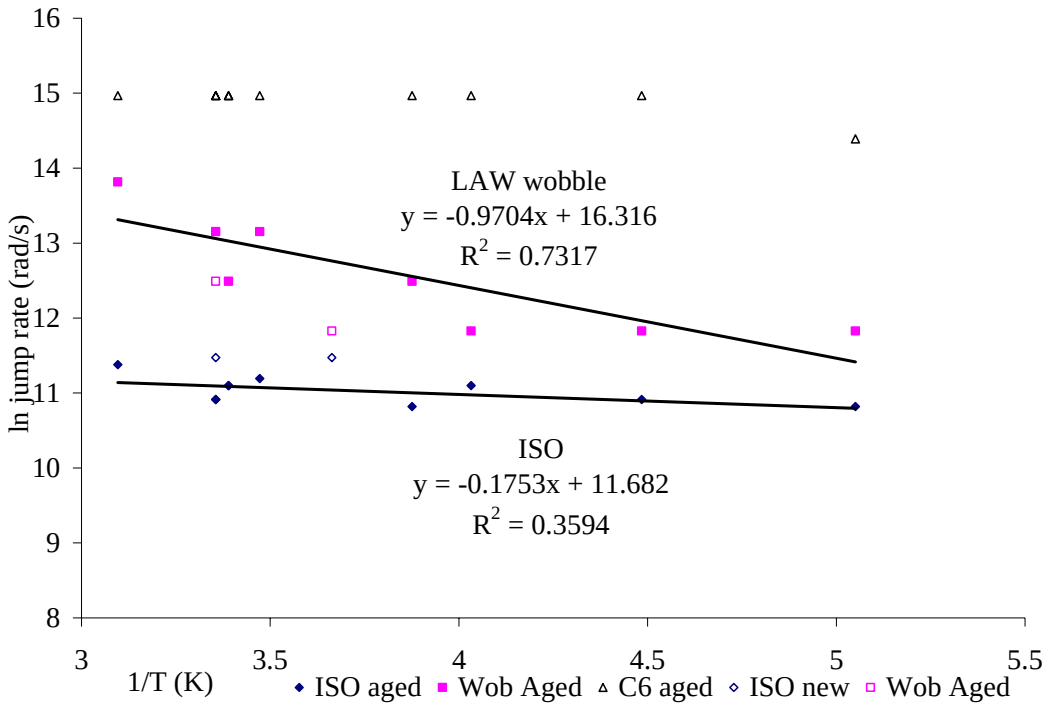

Figure 8.6 Arrhenius plots from fits of 1% w/w loaded benzene-d_6 on MWC spectra with a combination of ISO and LAW motions. The ranges of the ISO library are from 5 x 10^4 to 5 x 10^8 rad/s, for the LAW library 46° to 66°, 5 x 10^3 to 1 x 10^6 rad/s, and 1 x 10^6 to 1 x 10^8 rad/s for the wobble angle, wobble rate, and C_6 rotation rate, respectively.

different temperatures (Figure 8.7) and calculating the correlation time according to the following equation modified for power spectra, which is sensitive to the C_6 rotation as derived by Chopra [24],

$$1/T_1 = (3/32)\, QCC^2\, [g(\tau,\omega) + 4g(\tau,2\omega)], \qquad \textbf{(Eqn. 8.1)}$$

where

$$g(\tau,\omega) = \tau/[1 + (\omega\tau)^2], \qquad \textbf{(Eqn. 8.2)}$$

τ is the correlation time and ω is the Larmor precession frequency, 46,20525 MHz. [24] By solving this equation using simple iteration and the T_1 values collected on

day 135, jump rates for the C_6 rotation were calculated. The Arrhenius value for the C_6 rotation obtained (Figure 8.8, black regression line) was 2.7 kJ/mol, which is

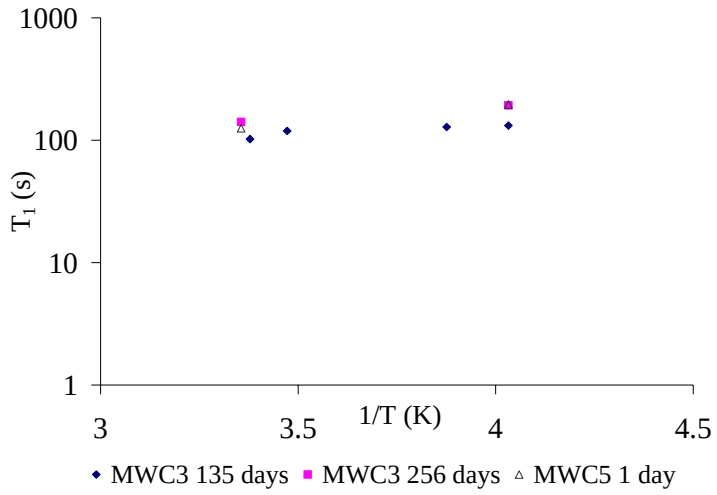

Figure 8.7. Longitudinal relaxation times for MWC at variable temperatures and ages after sealing.

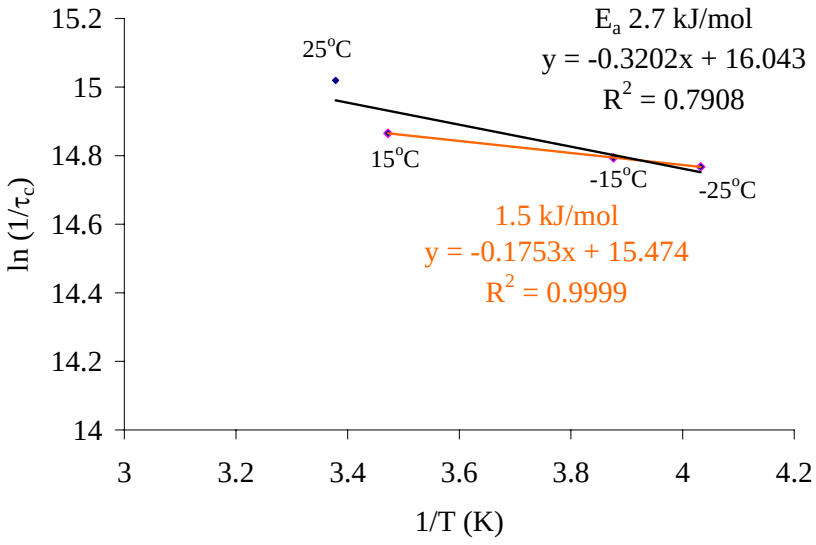

Figure 8.8. Arrhenius plot for the C_6 rotation of 1% w/w MWC samples, aged 135-7 days; black line with R^2 of 0.7908 fits all 4 points; orange line with R^2 of 0.9999 excludes 25°C point.

close to the value of 2.1 kJ/mol measured by Villanueva-Garibay and Muller in clathrate channels [26]. However, the R^2 value is only 0.7908, and, visually, the distribution appears potentially nonlinear, which indicates the possibility of more than one relaxation process. If the highest temperature, 25°C, is excluded from the fit (orange regression line), then the R^2 value improves considerable (0.9999), and the E_a is calculated to be 1.5 kJ/mol. However, additional data points would be required to select one fit over the other.

For MWC, a sample with a higher benzene-d_6 loading, 10% w/w, was examined at 25°C and 0°C. The difference in the spectra between the 10% and 1% loaded samples is striking, with the 10% sample displaying a broad Lorentzian peak in the center, flanked by a Pake base without well-developed horns. There is a slight increase in the width of the Lorentzian peak at the lower temperature. When these two spectra were fit to an ISO/LAW combination, the fits indicated the motion was mostly LAW, and the fits themselves were less visually acceptable. Therefore, the DFP fits of these samples were done using a mixture of ISO, LAW, and SAW, and the results were satisfactory. Even at a 10% loading, the pore diameters on MWC are no greater than 4.0Å [1], and thus the 1% and the 10% are similarly constrained sterically by pore size. Yet the spectra indicate greater restriction of the motion of the benzene molecules in the 10% loaded sample by virtue of the predominance of LAW and SAW over ISO motion (Figure 8.9). This restricted motion must be due to the crowding of benzene, either by benzene molecules within the same pores or by impingement of adjacent enlarged pores that also contain benzene.

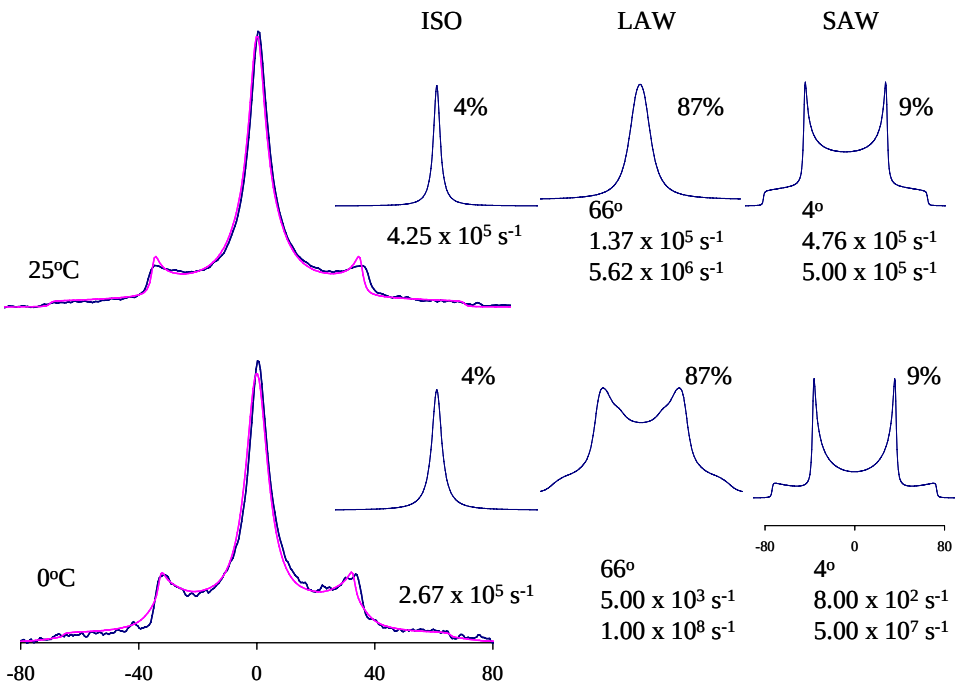

Figure 8.9. Fitted ^{2}H NMR spectra of 10% benzene-d_6 on MWC with component simulated spectra; library ranges for ISO and LAW are the same as for the 1% fit; the SAW differs from the LAW only in the wobble angle: 4°-24°.

8.3.4 Arrhenius behavior of benzene-d_6 on activated carbon

Attempts to fit the experimental ^{2}H spectra of benzene-d_6 on activated carbon were inconclusive. While fits that were visually approximate could be made, such as that with ISO, SAW, and LAW (Figure 8.10), the Arrhenius plots did not show trends and/or the results seemed illogical, such as an increase in the fraction of ISO motion as the temperature lowered. Additionally, fits to other motional models could be made which were equally good, particularly using a combination of a wag and a modified LAW (Appendix A4). In the ISO/LAW/SAW fit, the lower broader part of the spectrum was picked by DFP as mostly ISO, just as the very broad part of the MWC. It is possible that a broad apparent ISO peak with slow jump rates

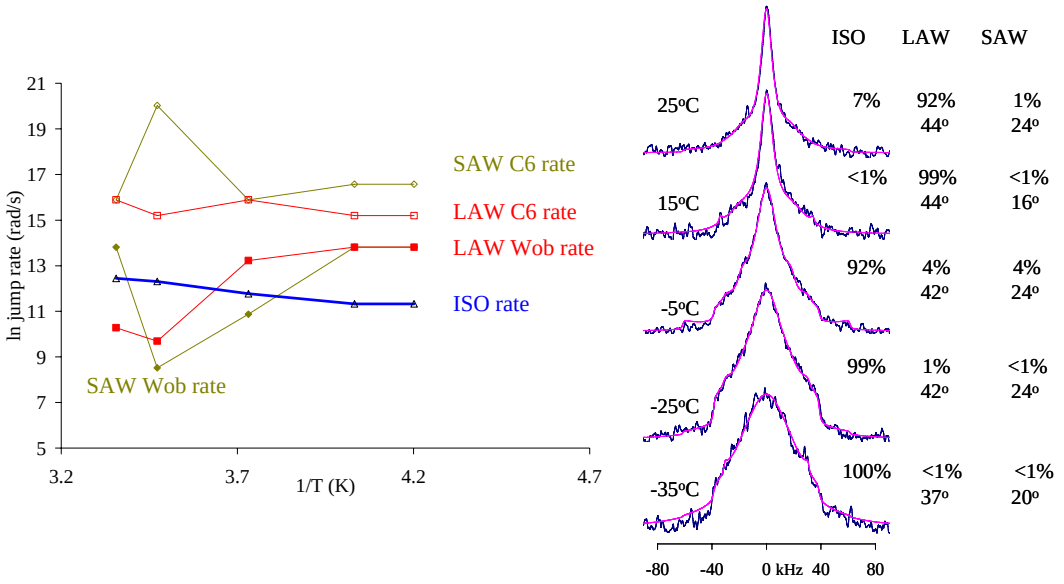

Figure 8.10. (right) Experimental ^{2}H spectra of benzene-d_6 on activated carbon on day 77 overlain by simulated spectra fitted by DFP using ISO, SAW and LAW combinations; ISO and LAW library ranges the same as those used for the MWC fits; (left) Arrhenius plots of the rates from those fits.

might indicate relatively strong adsorption which caused an enhanced viscous drag that varies randomly from pore to pore or site to site. Therefore, although the orientations of benzene as it moved within the pore might not have been averaged, rather the variations of rate from pore to pore might have caused a blurring of the individual Pake patterns as they are combined in the signal.

However, in contrast the to MWC, the peak widths for AC did show a trend with temperature, which indicated a variability in the out-of-plane angle, and, therefore, an Arrhenius plot was prepared (Figure 8.11), using the jump rates calculated according to Eqn. 4.3 after Grundke and Boddenberg [23],

$$\delta\upsilon = (9\pi/20)\, QCC^2\, \tau, \qquad \textbf{(Eqn. 4.3)}$$

where $\delta\nu$ is the peak width at half-height for the spectrum, *QCC* is the motionally

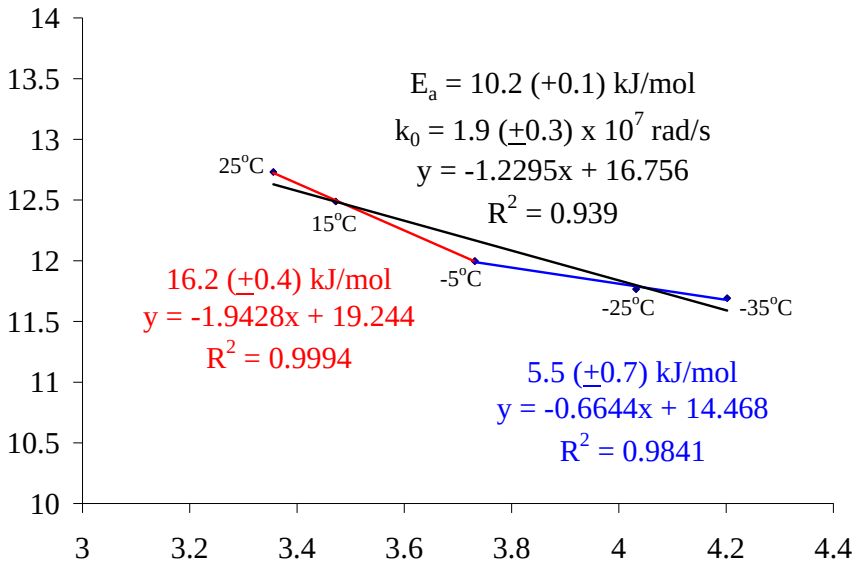

Figure 8.11. Arrhenius plot for sample ActC2; best fit line is for day 76.

averaged value of the quadrupole coupling constant, and τ is the reorientational correlation time, 1/*k* [23]. Even though it would appear that the peaks were not pseudoisotropic because they did not have ideal Lorentzian shapes, the E_a value calculated from the jump rates on day 76 was nevertheless close to that of the other BCs, 10.2(±0.1) kJ/mol, and the pre-exponential jump rate was 1.9 (±0.3) x 10^7 rad/s. If the Einstein diffusion equation,

$$D = a^2/6\tau \qquad \textbf{(Eqn. 4.5)}$$

was used to calculated the surface diffusivity [23], and if one-half of the diameter of the modal pore size was taken as *a*, the radius of diffusive path, then D_0 = 2.85 x 10^{-13} m^2/s. Because the best fit line of the day 76 data in Figure 8.11 has an R^2 value of only 0.939, and because it appears that two rate processes may occur at different temperatures, slope values were calculated for the higher temperature and the lower temperature segments of the plot. As with Figure 8.8 for the MWC,

however, it remains unclear whether one fit or another is the more accurate reflection of the Arrhenius behavior on the AC sample because the small number of data points.

One possible explanation for the difference between the AC and MWC is the affect of matrix swelling on the benzene motion. Braida et al. [1] suggested that adsorption of benzene may deform the MWC pores, as indicated by the hysteresis observed in the gas isotherm and the aqueous benzene isotherm. If (1) the narrower spectra on AC, (2) the apparent pseudoisotropic narrowing with temperature for the AC, and (3) the expected E_a value on AC for the motion of benzene on a graphenic BC were all indicators that the benzene was able to translate at higher temperatures to a pore mouth or other wider pore configuration for more complete rotation, then perhaps the swelling of MWC around the benzene molecules prevented them from occupying a position that permitted more rotational freedom. Interaction with Ca or other polar groups might have also played a role in this constraint.

8.4 CONCLUSIONS

The motion of benzene-d_6 on MWC and AC appears to be strongly influenced by the pore size of material and, to a lesser extent, by interaction with electron acceptors, such as organic acids functional groups and Ca^{2+} ions. The AC showed motional narrowing of the peak width with temperature, and the E_a of the isotropic rotational jump, 10.2 (+0.1) kJ/mol, was, within experimental error, the same value as that of benzene-d_6 on the low-surface-area graphite and the other BCs in this dissertation. However, because of the deviation from the ideal Lorentzian peak shape, this E_a value might be fortuitous. In contrast, the MWC did not show

motional narrowing with temperature, but had a width of approximately the value of quadrupolar splitting, and this is indicative of an out-of-plane motion with a constant angle with respect to the plane of the benzene. The spectra of benzene-d_6 on the MWC after 135 days yielded a good visual fit with ISO and LAW, and the E_a of the LAW motion was 8 ($\pm$3) kJ/mol and, for an associated ISO motion, the E_a was 1.5 (+0.2) kJ/mol, which is also in the range of the values obtained from the Arrhenius plot of T_1 measurements, 1.5-2.7 kJ/mol.

References

1. Braida, W. J.; Pignatello, J. J.; Lu, Y.; Ravikovitch, P. I.; Neimark, A. V.; Xing, B., Sorption hysteresis of benzene in charcoal particles. *Environmental Science & Technology* **2003,** *37*, 409-417.
2. Chun, Y.; Sheng, G.; Chiou, C. T.; Xing, B., Compositions and sorptive properties of crop residue-derived chars. *Environmental Science & Technology* **2004,** *38*, 4649-4655.
3. Norit, Datasheet Darco G-60 powdered activated carbon. In Norit Americas Inc.: 2005; Vol. 1185.
4. Chiang, Y.-C.; Chiang, P.-C.; Chang, E. E., Effects of surface characteristics of activated carbons on VOC adsorption. *Journal of Environmental Engineering* **2001**, (January, 2001).
5. Dubinin, M. M.; Polyakov, N. S.; Kadlez, O.; Kataeva, L. I.; Petukhova, G. A., Heterogeneous microporous structures and adsorption properties of carbon adsorbents. 12.* Porous structure and adsorption properties of active carbons. *Russian Chemical Bulletin* **1993,** *42*, (8), 1304-1308.
6. Do, D. D.; Do, H. D., Surface diffusion of hydrocarbons in activated carbon: comparison between constant molar flow, differential permeation and differential adsorption bed methods. *Adsorption* **2001,** *7*, 189-209.
7. Gauden, P.; Terzyk, A. P.; Rychlicki, G.; Kowalczyk, P.; Lota, K.; Raymundo-Pinero, E.; Frackowiak, E.; Beguin, F., Thermodynamic properties of benzene adsorbed in activated carbons and multi-walled carbon nanotubes. *Chemical Physics Letters* **2006,** *421*, 409-414.
8. Harris, P. J. F.; Liu, Z.; Suenaga, K., Imaging the atomic structure of activated carbon. *Journal of Physics: Condensed Matter* **2008,** *20*.
9. Jaroniec, M.; Madey, R., A comprehensive theoretical description of physical adsorption of vapors on heterogeneous microporous solids. *Journal of Physical Chemistry* **1989,** *93*, 5225-5230.
10. Terzyk, A. P.; Rychlicki, G.; Cwiertnia, M. S.; Gauden, P. A.; Kowalczyk,

P., Effect of the carbon surface layer chemistry on benzene adsorption from the vapor phase and from dilute aqueous solutions. *Langmuir* **2005,** *21*, 12257-12267.
11. Yoon, T. H.; Benzerara, K.; Ahn, S.; Luthy, R. G.; Tyliszczak, T.; Brown, G. E., Jr., Nanometer-scale chemical heterogeneities of black carbon materials and their impacts on PCB sorption properties: soft X-ray spectromicroscopy study. *Environmental Science & Technology* **2006,** *40*, 5923-5929.
12. Do, D. D.; Do, H. D., Characterization of micro-mesoporous carbonaceous materials. Calculations of adsorption isotherm of hydrocarbons. *Langmuir* **2002,** *18*, 93-99.
13. Sander, M.; Pignatello, J. J., Characterization of charcoal adsorption sites for aromatic compounds: Insights drawn from single-solute and bi-solute competitive experiments. *Environmental Science & Technology* **2005,** *39*, 1606-1615.
14. Choi, J.-G.; Do, D. D.; Do, H. D., Surface diffusion of adsorbed molecules in porous media: monolayer, multilayer, and capillary condensation regimes. *Ind. Eng. Chem. Res.* **2001,** *40*, 4005-4031.
15. Duer, M. J., *Introduction to Solid-State NMR Spectroscopy*. Oxford Press: Oxford, U.K., 2004.
16. Spiess, H. W.; Sillescu, H., Solid echoes in the slow-motion region. *Journal of Magnetic Resonance* **1981,** *42*, 381-389.
17. Xiong, J.; Maciel, G. E., Deuterium NMR studies of local motions of benzene adsorbed on Ca-montmorillonite. *Journal of Physical Chemistry B* **1999,** *103*, 5543-5549.
18. Gauden, P. A.; Terzyk, A. P.; Cwiertnia, M. S.; Rychlicki, G.; Newcombe, G.; Kowalczyk, P., Benzene adsorption on carbonaceous materials: The influence of pore structure on the state of the adsorbate. *Applied Surface Science* **2006,** *253*, 2525-2539.
19. Isirikyan, A. A.; Kiselev, A. V., The absolute adsorption isotherms of vapors of nitrogen, benzene and *n*-hexane, and the heats of adsorption of benzene and *n*-hexane on graphitized carbon blacks. I. graphitized thermal blacks. *Journal of Physical Chemistry* **1961,** *65*, (4), 601-607.
20. Chun, Y.; Sheng, G.; Chiou, C. T., Evaluation of current techniques for isolation of chars as natural adsorbents. *Environmental Science & Technology* **2004,** *38*, 4227-4232.
21. Zhu, D.; Herbert, B. E.; Schlautman, M. A.; Carraway, E. R.; Hur, J., Cation-π bonding: A new perspective on the sorption of polycyclic aromatic hydrocarbons to mineral surfaces. *J. Environ. Qual* **2004,** *32*, 1322-1330.
22. Turov, V. V.; Leboda, R.; Bogillo, V. I.; Skubiszewska-Zeiba, J., Structure of adsorption centers on a carbosil surface deduced from ^{1}H nuclear magnetic resonance spectroscopy data of adsorbed benzene and water molecules. *Langmuir* **1995,** *11*, 931-935.
23. Grundke, V.; Boddenberg, B., One and two component adsorption layers of *n*-hexane and benzene on graphite studied by ^{2}H NMR spectroscopy. *Molecular Physics* **1993,** *79*, (6), 1215-1226.
24. Chopra, N.; Chapman, R. G.; Chuang, Y.-F.; Sherman, J. C.; Burnell, E. E., Guest dynamics in carceplexes: a ^{2}H NMR study. *J Chem Soc Faraday Trans* **1995,** *91*, (21), 4127-4131.

25. Nishikiori, S.-I., Out-of-plane motion of the guest benzene molecule trapped in a $[Cd(dmen)_2(CN)]_2[Cd(CN)_4]$ host as studied by ^{2}H-NMR. *Journal of Inclusion Phenomena and Macrocyclic Chemistry* **1999,** *34*, 331-343.
26. Villanueva-Garibay, J. A.; Muller, K., Solid-state ^{2}H NMR studies of cyclophosphazene inclusion compounds: order and dynamics of the benzene guests. *Journal of Physical Chemistry B* **2004,** *108*, 15057-15068.
27. Ok, J. H.; Vold, R. R.; Vold, R. L.; Etter, M. C., Deuterium nuclear magnetic resonance measurements of rotation and libration of bezene in a solid-state cyclamer. *Journal of Physical Chemistry B* **1989,** *93*, 7618-7624.
28. Greenfield, M. S.; Ronemus, A. D.; Vold, R. L.; Vold, R. R.; Ellis, P. D.; Raidy, T. E., Lineshapes of deuterium quadrupole echoes. *Journal of Magnetic Resonance* **1989,** *72*, 89-107.

CHAPTER 9. COMPARISON OF THE MOLECULAR MOTION OF BENZENE-d_6 ON DIFFERENT BLACK CARBONS (BCs)

9.1 INTRODUCTION

In the present study, the molecular motion of benzene-d_6 sorbed onto several BCs was observed with ^{2}H solid-state NMR spectroscopy, as detailed in Chapters 4-8. The solid phase BCs represent a range of BCs with differing pore shapes, sizes and chemical composition. The hypothesis of this study is that the motion of adsorbed benzene-d_6 could be observed to be influenced (1) by the surface chemistry of the graphene functionalities and (2) by the pore shapes and sizes of the different BCs, and, in addition, that analysis of these differences could allow us to separate the factors into their component parts. From the perspective of chemical interactions, previous workers have treated the model solid-phase component for benzene-BC molecular interactions as graphene/graphite, the surface of which is composed of aromatic carbon rings [1-4]. Numerous isotherm models have been developed based on the adsorption of benzene to this surface via π-π and van der Waals interactions using hypothetical pore structures, but there are no experimental verifications of these models by spectroscopic observations of the motion of benzene under the influence of surface forces while it was adsorbed to BCs. In the previous chapters, the motion of benzene on different BCs has been examined in detail, and, in this chapter, the motional differences of adsorbed benzene across the range of BC solid phases will be compared and contrasted in order to identify how the pore shapes, pore sizes, and surface properties affected the molecular motion of adsorbed benzene.

To examine both model and natural samples with a range of ideal pores

types, variants of pure-carbon graphene were selected as sample BCs: (1) a synthetic graphite with a flat planar surface: low-surface-area graphite (LSAG); (2) an amorphous carbon with meso- and micropores in the intergranular spaces: carbon nanoparticles (CNP); and (3) meso- and microporous carbons with tube-like cylindrical pores, conceptually similar to some of the models employed for molecular flow paths through porous media [5, 6] multi-walled carbon nanotubes of smaller (CNS) and wider (CNW) internal diameters as well as single-walled carbon nanotubes (SWCNT), In addition to these pure carbon BCs, between 10-30% of noncarbon elements were present in the other samples, namely, (4) a commercial activated carbon (AC), which was used by previous workers as a reference for natural chars and which consisted almost entirely of slit-shaped microporosity [7, 8]; (5) a microporous natural maple wood char (MWC) produced from wood in a laboratory setting [9-13]; and a reference diesel soot from the National Institutes of Standards (NIST SRM #2975), which contains a very small amount of microporosity, but predominantly intergranular mesopores [14-19]. The specific details on these solid phases were explained in Chapters 2-8, and Chapter 3 focused especially on porosity and physical surface properties.

In addition to differing pore geometries and sizes, the surface roughness of the BCs were described by the fractal dimension as determined from the Frenkel-Hill-Halsey (FHH) equation (Eqn. 3.3) applied to N_2 isotherm adsorption data (Chapter 3) [20-22]. Values for the surface fractal dimension, d, have possible values which range between 2 (a fla t two-dimensional surface) and 3 (a very convoluted surface which essentially surrounds or “dissolves” the adsorbate

molecule) [20]. For the BCs in this dissertation, the lowest value was 2.007 for the LSAG and the highest 2.813 for the AC. Surface roughness does not, in general, correlate directly to chemical heterogeneity [23], but has been related to pore sizes and pore size distributions [24-27]. As explained in the Introduction Chapter, in a number of studies (and references therein), Rigby, along with other workers, has established that molecules of N_2 gas and physisorbed benzene vapor diffusing on the surface of the first monolayer of a solid phase are essentially probing the same surface features [28-31]. In addition, these researchers have derived a mathematical relationship between the correlation time, τ, of the deuterons in benzene-d_6, and the fractal dimension. The reorientational jump rate, k or $1/\tau$, can be measured by the peak width ($\delta\nu$) of the ^{2}H NMR Lorentzian peak, according to equations 4.5 and 4.6. Further, Rigby has shown that these can be predicted by comparison with a reference material according to the following equation,

$$\tau_0\ sample\ /\ \tau_0\ reference = \sigma^{(\mathrm{d}\ sample\ -\ \mathrm{d}\ reference)\ /\ 2}\ [31], \qquad (\textbf{Eqn}.\ 9.1)$$

where d is the surface fractal dimension as calculated from the FHH isotherm equation. Their equations are based on the hypothesis that the rate of hopping is related to the number of available surface sites (through k_0 or τ_0), and the number of available surface sites can be related to the fractal dimension [28]. These relationships also depend upon the existence of a compensation effect in the surface diffusivity of the adsorbate molecules, which is a correlation of the enthalpy of activation to the entropy of activation of surface diffusion [29] because it is the occurrence of a compensation effect across different solids phases which identifies that a common adsorption mechanism is operating, as discussed in the Introduction

Chapter. Compensation effects are common in adsorption thermodynamics [32], as are linear free energy relationships (LFERs), such as the frequent correlation between isosteric heat of adsorption (Q^{st}) and the energy of activation of surface diffusion (E_a/Q_0^{st}, which is 0.33-0.50 [33-36]).

Electron-donating contributions from underlayers of graphitic sheets are known to increase the surface interaction energies of aromatic π electrons with adsorbate benzene molecules [37, 38]. Similarly, microporous carbons with greater crystallinity (and thus greater numbers of stacked graphitic planes) have stronger adsorption energies [39]. Further, the enhancement of π-π interactions by alignment of planar aromatic molecules with BCs has been postulated to account for increased adsorption in several aqueous batch isotherm studies [12]. As an extension of this hypothesis, it would appear likely that the π-electrons in the curved graphenic sheets of CNTs would have less favorable interactions with the sorbate because of the lack of sorbent surface planarity. Supporting this, Diaz has demonstrated that π electrons in curved graphene sheets on multi-walled CNTs have lower enthalpies of adsorption [40]. If the surface interactions between benzene and BCs are enhanced by greater graphitic stacking, one would expect to find a correlation between graphite crystallinity and the E_a of surface diffusion, as measured by the rotational jump motion. Therefore, the graphitic crystallinity of the BCs in this work was measured with X-ray diffraction (XRD), as described in Chapter 3.

9.2 EXPERIMENTAL

Experimental details for the N_2 adsorption analysis, the XRD collection, and the ^2H solid-state NMR spectroscopy have been presented in detail in the preceding

chapters. BC solid phases were characterized with N_2 adsorption analysis for surface area and pore size distributions and with X-ray diffraction (XRD). After degassing the sample overnight at 300°C, nitrogen isotherm analysis was performed with a Quantachrome Corporation Autosorb 1C instrument at 77K over pressure ranges from 2 x 10^{-6} torr to 760 torr with an equilibration time for each data point of 1 minute. Pore size distributions were calculated using software provided by the manufacturer, using either a nonlocalized density functional theory or Dollimore-Heal algorithm. For the XRD analysis, a Rigaku Gigaflex XRD spectrometer was employed; the 2Θ scan was performed from 5.0-70.0^o in 0.05^o increments resulting in 200 data points per degree; the dwell time was 0.5 s. The copper anode was employed with a Ni filter, providing a Cu-Kα wavelength of 1.54Å.

Solid-state static ^{2}H NMR spectra were obtained with a 300MHz Chemagnetic instrument, and the specific parameters are detailed in Chapters 4-8.. Spectra were collected at different temperatures at $\pm$0.1^{o}C. Samples were prepared for NMR analysis by loading a precise amount of benzene-d_6 from a vapor manifold into an NMR tube containing the BC solid phase. The tube was then submerged into liquid nitrogen for quantitative condensation of the benzene-d_6 vapor and flame-sealed. Most samples loaded at 1% w/w. After collection of the spectra, reorientational jump rates were obtained from fits to simulated spectra generated with the DFP software [41], or from the peak width at half-height ($\delta\nu$) of the Lorentzian spectra.

9.3. RESULTS: STATIC SOLID-STATE ^{2}H NMR SPECTRA

9.3.1 Differences in ^{2}H NMR spectra for benzene-d_6 on different BCs

Most of the spectra were Lorentzian in character, indicating an isotropic molecular reorientation on the NMR timescale (10^{-4}s to 10^{-9}s for deuterons) and this was interpreted as due to the influence of the spherical orientation of the BC grains as the benzene-d_6 molecules translated across the surfaces of the molecular-sized pores, as suggested by previous workers [42]. This was also in accord with the mobile adsorption model of surface diffusion [43]. However, per Figure 9.1, the peak widths ($\delta\nu$) varied considerably from sample to sample, indicating that each of the BCs exhibit different ranges of rates of molecular reorientation, i.e., different

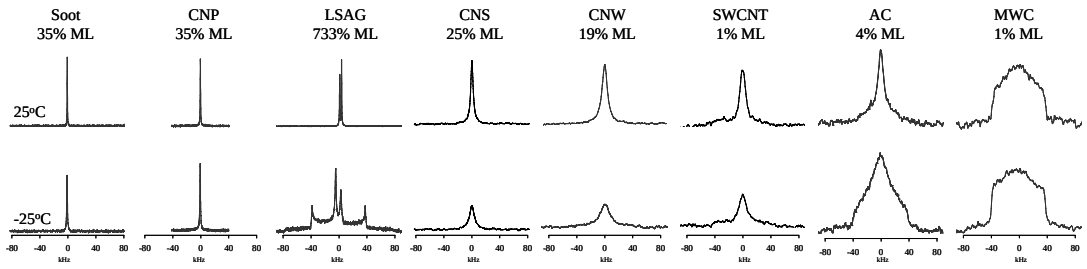

Figure 9.1. ^{2}H static solid-state NMR spectra of benzene-d_6 on the specified BCs at two temperatures, 25°C and -25°C; %ML indicates the monolayer loading of benzene.

ranges of jump rates. The samples with lower surfaces areas (and thus higher monolayer loadings) are towards the left on Figure 9.1 and display the most isotropic NMR peaks. Similarly, the spectra from samples with smaller pores (and, consequently, higher surface area and lower monolayer loadings) are towards the right-hand side. These spectra on the right display wider peaks with greater Pake

character and indicate slower and more constrained motion of the benzene-d_6 molecules. The AC, MWC and soot all contained 10-20% of heteroatoms (Chapters 4 and 8), but, for the soot, these probably constituted an inorganic core, while the soot surface remained essentially graphenic carbon [17]. For the AC and MWC, there are three factors which could restrict the motion of benzene and produce noticeably wide ^{2}H NMR peaks: (1) An abundance of micropores, even smaller than the molecular dimensions of benzene, would slow the rate of motion of benzene due to increased viscous drag from enhanced surface forces in narrow pores [43] and (2) sterically prevent full rotation of the benzene in many pores [44, 45]. Additionally, (3) protonated and cationic (particularly Ca^{2+}) sites would interact with benzene via π-cation interactions [46], and such chemisorption is more localized and motionally restrictive than the mobile physisorption interactions that benzene undergoes when adsorbed to graphenic aromatic π-electrons [47, 48].

9.3.2 Comparison of Arrhenius behavior among benzene-d_6 on different BCs

The energies of activation, E_a, and correlation times, τ_0, (Table 9.1) which were determined from Arrhenius plots using peak width measurements ($\delta\nu$) of the Lorentzian peaks as described in Chapters 4-8, display a range of values for the different BCs in this study (Figure 9.2). LSAG, AC, and soot display reorientational jump/surface diffusivity Ea values of near 10 kJ/mol (Table 9.1). Thus, since the E_a would indicate the strength of the adsorption bond, the soot and AC would interact more like the ideal planar graphite sample, LSAG, than the other BC samples. Therefore, it is hypothesized that this similarity of E_a indicates (1) that, on AC and soot, the face-to-face benzene/ graphene conformation is more

favored than on the other BC surfaces, and/or (2) that the surface chemistry of

Table 9.1. Correlation times and energies of activation for benzene-d_6 on various solid phases measured with ^{2}H NMR.

Substrate	Reference	Motion	E_a (kJ/mol)	temp range	t_0(s)
LSAG	[a]	pseudoisotropic	10.1 (±1.1)	198K-298K	2.1 (±0.5) x 10^{-9}
CNS	[b]	pseudoisotropic	9.3 (±1.4)	198K-298K	1.3 (±0.9) x 10^{-8}
CNW	[b]	pseudoisotropic	7.6 (±0.5)	198K-298K	7.7 (±1.8) x 10^{-8}
SWCNT	[b]	pseudoisotropic	4.8 (±0.4)	198K-298K	2.0 (±0.1) x 10^{-7}
CNP	[c]	pseudoisotropic	7.0 (±0.1)	198K-298K	5.3 (±0.3) x 10^{-9}
Soot	[d]	pseudoisotropic	10.1 (±0.8)	198K-298K	1.3 (±0.1) x 10^{-9}
AC	[e]	pseudoisotropic	10.2 (±0.1)	198K-298K	5.3 (±0.8) x 10^{-8}
Carbopack B	[f]	pseudoisotropic	3.8	160K-298K[g]	3 x 10^{-9}
cyclophosphazene channels	[h]	C_6	2.1 (±0.1)	190K-300K	3 x 10^{-12}
cyclophosphazene channels	[h]	tumbling along axis channel	4.2 (±0.1)	190K-300K	2 x 10^{-12}
neat liquid	[i]	C_6	4.5 (±0.6)	260K-360K	6 x 10^{-14}
alumina (h-Al_2O_3)	[j]	C_6	4.9	77K-250K	1 x 10^{-13}
SBA-15 mesoporous silica	[k]	C_6	6	20K-60K[g]	
neat liquid benzene	[l]	isotropic tumbling	6.5	278K-348K	9 x 10^{-14}
zeolite Na-Y	[j]	C_6	7.4	77K-250K	1.5 x 10^{-12}
Carbopack B	[j]	C_6	7.9	77K-250K	1 x 10^{-13}
neat liquid	[i]	tumbling perpendicular to plane	8.1 (±0.6)	260K-360K	8 x 10^{-14}
Ca-Mont 1.2% load	[m]	SAW	8.3	148K-198K	
Ca-Mont 3.8% load	[m]	ISO	8.8	173K-223K	
Zeolite, Na-X	[n]	cartwheel	14 (±0.6)	155K-350K	8.8 (±2.3) x 10^{-12}
neat solid benzene	[o]	SAW	16.5 (±0.1)	87K-252K	5 (±1)x 10^{-14}
neat solid benzene	[k]	C_6	16.8	88K-206K	5 x 10^{-14}
clathrate	[p]	C_6	18.2	123K-403K	
clathrate	[p]	out-of-plane		123K-403K	1 x 10^{-8}
K-zeolite, ZSM-5	[q]	cation hopping	20	100K-350K	
Zeolite, Na-Y	[n]	cartwheel	23.5 (±0.9)	155K-350K	9.6 (±0.4) x 10^{-13}
clathrate	[o]	SAW	24.9 (±0.4)	124K-290K	1 (±0.4) x 10^{-14}
carceplex	[r]	C_6	25.8 (±0.4)	310K-400K	2 x 10^{-12}
carceplex	[r]	C_4 (wobble symmetry ?)			10^6 - 10^7
K-zeolite, ZSM-5	[s]	cation hopping and bulk	28.0 (±1.6)	220K-373K	
SBA-15 mesoporous silica	[k]	C_6 to ISO	30.6 (±2.2)	189K-219K	3 x 10^{-6} [s]

[a]Chapter 6; [b]Chapter 7; [c]Chapter 5; [d]Chapter 4; [e]Chapter 8; [f][42]; [g]associated with a region of phase change; [h][49]; [i][50]; [j][51]; [k][52]; [l][53]; [m][46]; [n][54]; [o][55]; [p][56]; [q][57]; [r][58]; [s][59]; [t]estimated averaged.

LSAG, soot, and AC is homogenously aromatic carbon. The AC, however, is predominantly microporous, and the enhanced forces from the pore walls on the adsorbed benzene would be expected to result in an E_a larger than that for the LSAG. It is possible that a detailed motional model could provide a larger value. The different ranges of jump rates, mentioned above, translates into different values

of τ_0 for the motion of benzene-d_6 on different BCs, as can be observed in the overlay of the Arrhenius plots from previous chapters (Figure 9.2).

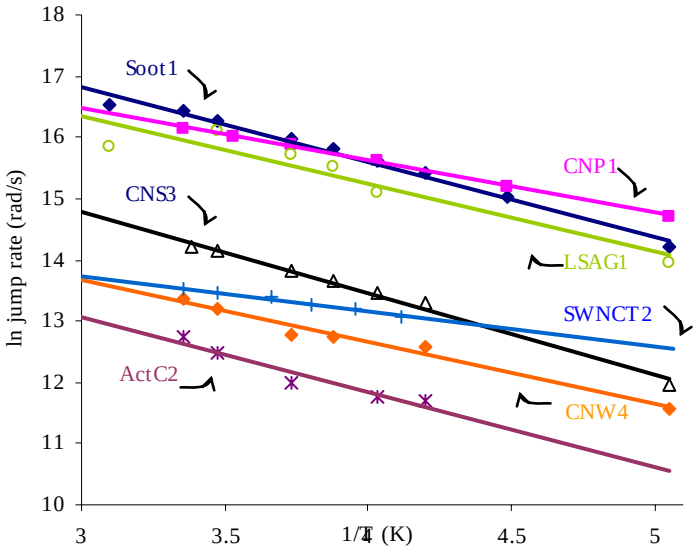

Figure 9.2. Arrhenius plots for reorientational jump rates of the indicated BC; all jump rates were calculated using δν (peak width) and Eqn. 4.5; individual plots are shown in Chapter 4-8; LSAG1 is referred to as GRAPH1 in Chapter 6.

The magnitude of the activation energy for surface diffusion is a measure of the interaction strength between adsorbate molecules and the solid phase, similar in this respect to enthalpies of adsorption [60]. In general, for benzene on various solid phases (also listed in Table 9.1), it can be seen that the highest E_a values are for benzene molecules which are chemisorbed in zeolites or strongly constrained in guest sites. Benzene existing within linear channel pores has low interaction energies. The range of E_a from 7-10 kJ/mol for the motion of benzene on BCs is lower than benzene in the guest or cationic sites, but higher than most of the tumbling values for benzene, whether in a neat liquid or within a channel. The E_a for benzene on LSAG, the most planar and homogeneous of the BC surfaces, is 10.1

kJ/mol. The E_a value for benzene's rotational jumps on the CNTs are all less than 10 kJ/mol, possibly because the π electrons on curved graphene surface present a lesser energetic interaction with benzene than graphitic π-electrons, for which extended π-aromatic systems are stabilized by planarity [40]. Similarly, because of the lesser amount of aromatic π electrons on the CNP surface, it is expected that its E_a would also be lower than on graphite, and at 7.0 kJ/mol, this is validated.

Further, it can be seen by examining Table 9.1 that the C_6 (in-plane) rotation always requires less energy than a tumbling motion in the same environment. For instance, the $D_{\parallel}$ E_a for neat benzene is 4.5 kJ/mol; the $D_{\perp}$ is 8.1 kJ/mol; and the completely isotropic rotation is intermediate, 6.5 kJ/mol. Also, in the cyclophosphazene channels, the C_6 rotation is 2.1 kJ/mol and the rotation perpendicular to that is 4.5 kJ/mol, and, on the Ca-montmorillonite, the SAW motion on the lower loaded sample is 8.3 kJ/mol while the ISO motion, which involves some component of end-over-end rotation, is 8.8 kJ/mol. However, it has been suggested that adsorbed benzene, especially in micropores, has important solid-like properties [45, 61]. The E_a for the low-temperature C_6 rotation of a monolayer of two-dimensional solid benzene-d_6 on graphitized carbon black (Carbopack B) is 7.9 kJ/mol, and the authors postulated that the E_a was due to disruption of the π-π bonds during a 35° out-of-plane jump, which would be required to attain the steric clearance in order to execute the jump [51]. The E_a for the same motion in solid benzene is 16.8 kJ/mol, which is approximately twice that for the solid monolayer, and possibly represents disruption of π-π bonds on two sides of the benzene plane required to activate the jump. Because the isosteric heat

of adsorption for benzene on graphite (ca 40 kJ/mol) is larger than the heat of condensation (30.7 kJ/mol at the boiling point, 80°C), the benzene-graphene interaction must be stronger than the benzene-benzene interaction, and one would expect that, especially for motions which involve some out-of-plane component that would disrupt the π-π sorption interaction , the E_a for the motion of benzene on the surface of graphene would be greater than the E_a for the motion of benzene on benzene. Similarly, the E_a for the motion of benzene constrained in micropores should be greater than the motion of benzene constrained in solid benzene. This hypothesis is somewhat validated by our results: the E_a of 10.1 kJ/mol for the exchange motion of benzene on graphite with a liquid phase (and this must involve out-of-plane motion) is greater than the E_a of 8.1 kJ/mol for $D_{\perp}$ rotation of neat benzene. Further supporting this idea for benzene constrained on two sides within a micropore, the E_a for the surface diffusivity of benzene on two other activated carbons was close to that for solid benzene, 16 kJ/mol, as measured by Dubinin et al [45]. However, the measurement obtained in this study assuming a Lorentzian peak for benzene on activated carbon was 10.2 kJ/mol, but additional analysis with a closer simulated fit, using an improved motional model, might be provide a higher E_a. Such a model was attempted here (Appendix.A.3), but did not provide a sufficiently good fit.

The value of 10.1 kJ/mol obtained in this study for the surface diffusion of benzene on graphite is substantially higher than the value of 3.8 kJ/mol for benzene on Carbopack B (graphitized carbon black) measured by Grundke and Boddenberg in their study which suggested the pseudoisotropic motional model [42]. Several

facts indicate that the value obtained in this dissertation is more correct. First, the E_a value of surface diffusivity has been shown in general [28] to approximate the net heat of adsorption, and the net heat of adsorption has been measured at 9.7 kJ/mol, C_{BET} of 47 ([38] from Kaneko, verbal communication). The net heat of adsorption is obtained from the Brunauer-Emmett-Teller (BET) constant, C_{BET}, using adsorption isotherm data for benzene on graphite:

$$C_{BET} = \exp [(Q_1 - Q_L)/RT], \qquad \textbf{(Eqn. 9.2)}$$

where Q_1 is the heat of adsorption for the monolayer, Q_L is the molar heat of vaporization, and $Q_1 - Q_L$ is the net heat of adsorption [28, 38, 62]. Given the value of 30.7 kJ/mol for the molar heat of vaporization at the boiling point of benzene (80^oC) [63], this results in a Q_1 value of 40.4 kJ/mol, approximately the isosteric heat of benzene on graphite (Table 1.1). Second, Grundke and Boddenberg [42] used a larger temperature range than used in this work to calculate Arrhenius value and made estimations of the pseudoisotropic motion's contribution to actual peak width at lower temperatures. Third, the ratio of E_a/ Q_0^{st}, discussed below, favors 10.1 kJ/mol over 3.8 kJ/mol.

9.3.3 Compensation Effects, Enthalpy/Entropy Correlations and Fractal Dimensions

As mentioned above, beginning with Gilliland [36], several workers have noted the occurrence of a Hammett-type LFER between E_a and Q_0^{st} [43, 64]. Table 9.2 (on the following page) lists values of E_a and Q_0^{st} have been obtained from the literature for several sorption systems, especially graphitic carbons, although self-diffusivity values are somewhat rare in the literature [28], The concept that the energy required to move along a surface would be smaller than the energy required

to jump completely into the gas phase is a common assumption in physisorption isotherm equations, such as BET or FHH [48, 62] (See the Introduction Chapter). The E_a of 10.4 kJ/mol for the LSAG is 25% of the Q_0^{st} value of benzene on graphite (ca. 40 kJ/mol) and the E_a of 10.2 kJ/mol for the soot is 33% of the Q_0^{st} value for benzene on hexane soot (37.5 kJ/mol) [65]. These ratios are close to those

Table 9.2. Ratios of the energies of activation (E_a) for diffusivity to the isosteric heats (Q_0^{st}) of adsorption for benzene-d_6 on different solids

Substrate	ML Fraction	Adsorbate (if not benzene)	Technique for Diffusivity Measurement	E_a (kJ/mol)	Q_0^{st} (kJ/mol)	E_a / Q_0^{st}
Graphite						
LSAG[a]	7.30		^{2}H NMR (Lorentzian peak)	10.1 (±1.1)	ca. 43	0.24
graphitized carbon black (Carbopack B)[b]	1.00		^{2}H NMR (Lorentzian peak)	3.8	43	0.09
graphitized carbon black (Spheron)[c]		butane	flow	16	32	0.50
Carbon						
CNP[d]	0.25		^{2}H NMR (Lorentzian peak)	7.0 (±0.1)	-	-
bonded C18[e]			flow	13.5	35.3	0.38
carbon black[f]		CH_2Cl_2	flow	3.4	8.3	0.41
Activated carbon						
AC[g]	0.04		^{2}H NMR (Lorentzian peak)	10.2 (±0.1)	est. 45	est 0.23
activated carbon[h]	sat		^{1}H NMR T_1	5-7	42-49	ca. 0.14
charcoal[f]		n-heptane	flow	10	13	0.77
activated carbon[i]			simulation	43.9	52.7	0.83
activated carbon[k]			PFG ^{1}H NMR	16	-	
Carbon Nanotubes						
CNS[j]	0.28		^{2}H NMR (Lorentzian peak)	9.3 (±1.4)	est. 35	0.27
CNS[j]	0.14		^{2}H NMR (Lorentzian peak)	7.6 (±0.5)	est. 35	0.22
SWCNT[l]	0.01		^{2}H NMR (Lorentzian peak)	4.8 (±0.4)	est 13.2	0.36
Neat Benzene						
bulk benzene[m]	sat		^{1}H liquid NMR T_1	6.5	30.7	0.21
bulk benzene[k]	sat		PFG ^{1}H NMR	19	30.7	0.62
Variable Loading						
Soot[n]	0.25		^{2}H NMR (Lorentzian peak)	12.3 (±0.2)	-	-
Soot[n]	0.34		^{2}H NMR (Lorentzian peak)	10.1 (±0.8)	-	-
Soot[n]	0.68		^{2}H NMR (Lorentzian peak)	9.0 (±0.1)	ca 38	0.24
graphite[o]	0.50		simulation	7.8	ca. 43	0.18
graphite[o]	0.80		simulation	7.5	ca. 43	0.17
silica gel[f]	sat	toluene	flow	13	15	0.87
silica sol-gel[p]	1.00		flow	7.53	36.2	0.21
silica sol-gel[p]	0.63		flow	10.01	38	0.26
silica sol-gel[p]	0.38		flow	14.85	40	0.37

[a]Chapter 6; [b]E_a from [42]; [c][47]; [d]Chapter 5; [e][64]; [f][60]; [g]Chapter 8; [h][66]; [i][67]; [j]E_a from Chapter 7 and Q_0^{st} from [40]; [k][45]; [l]Chapter 7 and est. Q_0^{st} from [68]; [m]E_a calculated from data in [50] and Q_0^{st} is enthalpy of fusion at the boiling point per [63]; [n]E_a from Chapter 4 and Q_0^{st} for monolayer loaded hexane soot [65]; [o][69]; [p][30].

observed for ratio (~0.4) of the E_a values for surface diffusion of for the gas/solid adsorption of hydrocarbons on C18 bonded phases and the corresponding Q_0^{st} [33]. (See the discussion in the Introduction Chapter concerning the applicability of treating benzene/C18 interactions, which are often considering to be partitioning, with this approach.) A value near 0.5 is considered indicative of dispersive sorption interactions [43, 70]. Rigby's [30] analysis of Boddenberg, Haul, and Opperman's [71] data for the diffusivity of benzene on a silica sol-gel (Aerosil) at variable temperatures and loadings led him to suggest a surface diffusion model for benzene in which a fraction of the molecules are clustered onto adsorption sites with higher adsorption energies, primarily accounting for the Q_0^{st} value, and the remaining benzenes are loosely held and "flying" across the surface, primarily accounting the for diffusivity values [30]. He described the site distribution as "homogeneously heterogeneous" and provided evidence that the pattern of site distribution is related to the fractal dimension [30]. Different diffusivities at different loadings indicate different geometrical fractal dimensions [30]. This interpretation differs from the more traditional explanation, elaborated by Arena [72], that higher submonolayer coverages provides lower D_0 values because of molecular crowding. For benzene on a *homogeneous* surface, the crowding has been modeled to cause benzene to occupy a tilted configuration and to diffuse more slowly over the surface [37, 69, 73, 74]. However, Rigby is suggesting that the same pattern of diffusivity over a range of submonolayer loadings on a *heterogeneous* surface indicates different surface sites with different fractal dimensions. A chemically heterogeneous surface can be distinguished from a homogeneous surface by the pattern of increasing heats

of adsorption with lower loadings for the former [43].

Entropy/enthalpy relationships in equilibrium thermodynamic values have been observed for many surface processes [34, 75-77], including the adsorption of hydrocarbons on CNTs [40]. The occurrence of a compensation relationship

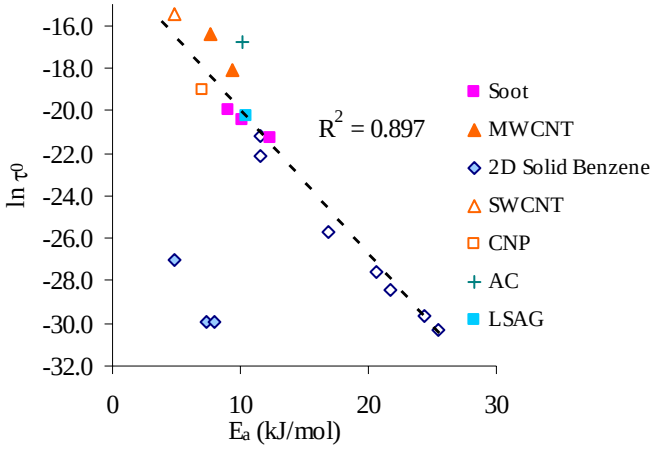

Figure 9.3. Compensation plot for surface diffusivity of benzene-d_6 on BCs and other solids. 2D solid benzene samples were collected with relaxation measurements at temperatures less than 140K (the 2D liquid-solid phase transition). Dashed line is best fit for remaining 2D liquid benzene samples.

between the pre-exponential factor for the jump rate (correlation time) and the energy of activation is the basis for the correlation between the pre-exponential factor and the fractal dimension [29]. The pre-exponential factor of the Arrhenius equation, τ_0 (or, its reciprocal, k_0) represents the entropic contribution (number of possible surface sites) to the reorientational jump rate of a surface diffusing molecule [78], as mentioned above; the E_a represents the enthalpic contribution; and a correlation of the two defines one type of compensation effect [29, 32, 47]. The net result of this compensation effect is to minimize changes in the absolute rate of

diffusivity with changes in temperature. These values are plotted for the BCs in the present study along with values reported by Rigby for benzene surface diffusing on other solid phases (Figure 9.3). All of the τ_0 values were obtained from the Lorentzian peak widths ($\delta\nu$) of spectra collected with ^2H static solid-state NMR. A

Table 9.3. Diffusivity, fractal dimensions, and pore sizes for BCs and others adsorbents

Solid Phase	% ML Coverage	Ea (kJ/mol)	τ_0 (s)[a]	Pore Dia. at 1% w/w Load	D_0 (/s)[b]	Fractal dimension
			BCs[c]			
CNP	25%	7.0	5.3×10^{-9}	1 nm	7.9×10^{-12}	2.5498[d]
LSAG	733%	10.1	2.1×10^{-9}	25 nm	1.3×10^{-8}	2.007[d]
CNW	14%	7.6	7.7×10^{-8}	2 nm	2.2×10^{-12}	2.5442[d]
CNS	28%	9.3	1.3×10^{-8}	1 nm	3.1×10^{-12}	2.5266[d]
SWCNT	1%	4.8	2.0×10^{-7}	1.3 nm	3.6×10^{-13}	[e]
AC	4%	10.2	5.3×10^{-8}	0.6 nm	2.9×10^{-13}	2.803[d]
Soot	68%	9.0	2.2×10^{-9}	20 nm	7.7×10^{-9}	2.3895[d]
Soot	34%	10.2	1.3×10^{-9}	11 nm	3.9×10^{-9}	2.3895[d]
Soot	4%	12.4	5.9×10^{-10}	2 nm	2.8×10^{-10}	2.3895[d]
			Others			
Carbopack B	1%	3.8	3.3×10^{-9}	40 nm	2.0×10^{-8}	2.226[f]
alumina	1%	11.6	2.5×10^{-10}	2.5 nm	1.0×10^{-9}	2.35[f]
Pt/alumina cat	1%	11.6	6.0×10^{-10}	2.5 nm	4.3×10^{-10}	2.31[f]
fumed silica C1	1%	20.7	1.0×10^{-12}	10 nm	4.0×10^{-6}	2.611[d]
sol-gel silica G1	1%	16.8	6.6×10^{-12}	11 nm	7.6×10^{-7}	2.525[d]
sol-gel silica G2	1%	21.7	4.4×10^{-13}	20 nm	3.8×10^{-5}	2.639[d]
Pt/G1 cat	1%	24.4	1.4×10^{-13}	[g]	-	2.71[f]
Pd/G2 cat	1%	25.5	6.6×10^{-14}	[g]	-	2.73[f]

[a]Values of τ calculated from peak width using Eqn. 4.5; [b]calculated with Eqn. 4.9; [c]all values can also be found in Chapters 3-8; [d]values determined from the FHH equation using N_2 isotherm data; [e]N_2 isotherm not performed; [f]per Rigby, based on τ_0 and comparison to C1 as a reference; [g]not specified in reference.

general trend can be observed, confirming the existence of a compensation effect in the surface diffusion of benzene. The greater scatter in the data for the BC samples in this study, as compared to the data points from Rigby, is due in part to differences in loading. Rigby's samples were al l loaded at very close to one monolayer,

whereas, with the exception of the LSAG, all of the BC samples were loaded with submonolayer quantities of benzene-d_6. Nevertheless, excluding the 2D solid values [2, 79], a linear plot of the compensation effect gives a correlation coefficient of 0.90. The values plotted in Figure 9.3 are listed in Table 9.3. This compensation effect displayed in Rigby's data is his justification for considering that the mechanism of surface diffusion of benzene-d_6 physisorbed on the various solid phases that he compares, which range from silica catalysts to graphitized carbon black, is essentially the same.

Figure 9.4 a) shows a plot of correlation time, τ_0, vs. fractal dimension, d, which is at the heart of Rigby's projection of fractal dimensions based on ^{2}H NMR data. The data used by him appears very linear because all but three of the points were predicted from the line. Only the solid blue diamonds have fractal dimensions determined from FHH plots [28-30]. The BC fractal values in this dissertation were all determined from FHH plots, but, nevertheless, most of the BC values do not fall close to this line. Rather they form a roughly linear trend oblique to Rigby's line. There are two possible explanations for this offset: (1) It is a function of the lower loading of the BC samples. This idea is supported by the fact that the LSAG, which is loaded at greater than 1 monolayer, is offset from Rigby's line in the opposite direction than the other BCs, which are all at submonolayer loadings, and is in accord with Rigby's study of variable loaded Aerosil in which different fractal dimensions were measured at different loadings [30]. It is also supported by the spread of values for the soot samples, which had different submonolayer loadings. The soot sample with the lowest loading falls near the trend with other BC samples

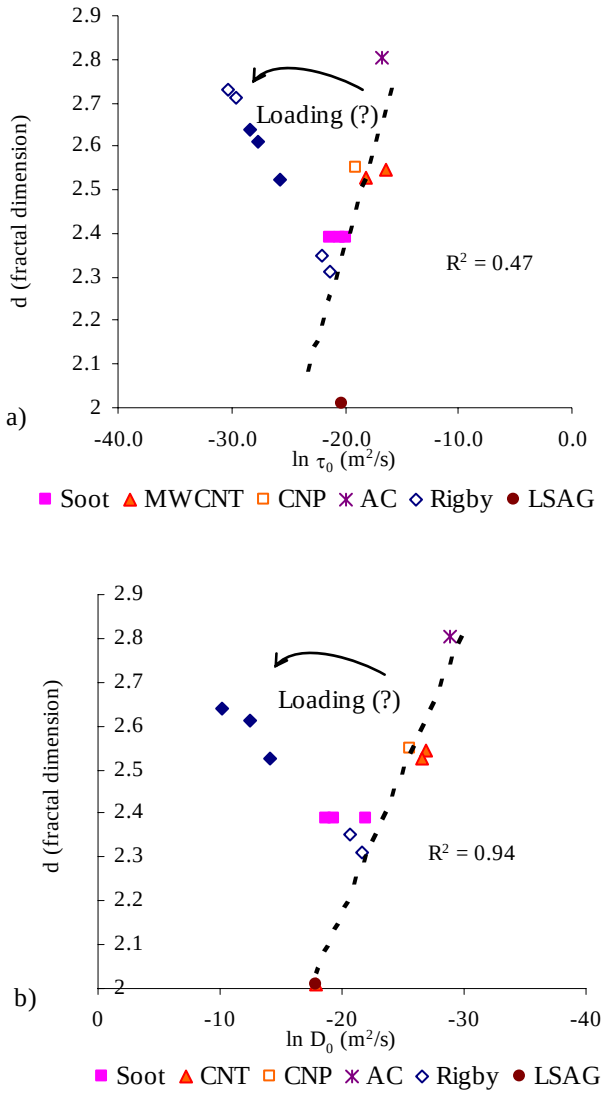

Figure 9.4 a) correlation time of benzene-d_6 vs. fractal dimension of solid phase; b) diffusivity of benzene-d_6 vs. fractal dimension of solid phase, assuming that the benzene occupies the smallest pores available and using the cumulative volume pore size distributions from Chapter 3; dashed lines are best fit of BC data with correlation coefficient displayed, and the linearity of the plot is greatly improved if pore sizes of the diffusion path are consider, i.e., the plot of d vs. D_0 is much more linear than the plot of d vs. τ_0, with R^2 values of 0.47 and 0.94, respectively..

and the soot sample with the highest loading is closer to Rigby's monolayer-loaded data. Also, (2) the solid phases in the Rigby sample set are catalysts consisting of Si

or Al, and benzene may fundamentally interact differently (e.g., cation-π interactions) with these solid phases than with graphene surface; i.e., Rigby's assumption of the similar mechanism for the surface diffusion of benzene on these samples may not be true. However, as discussed earlier, the existence of the compensation effect suggests that adsorption occurs by the same mechanism. However, in support of Rigby's hypothesis is the fact that the low-temperature studies of benzene as a 2D *solid* plot as a separate group, but with the same apparent slope as the 2D *liquid* points, and these points include a zeolite, a silicate, and a graphitized carbon black, Carbopack B.

Because the specific pore paths taken by the benzene molecules as it diffuses along the BC surfaces are of interest, values of the surface diffusivity were calculated by assuming that the benzene first fills the smallest pores. Even though this assumption is common in pore-size-distribution equations from N_2 adsorption isotherm data [80], the particle size of the sorbent has been used by previous researchers (Boddenberg's group) when calculating diffusivity rates from reorientational jump rates [30, 42], and the present study is the first application of pore size data to surface diffusivity rates measured by static solid-state ^{2}H NMR. Therefore, the pore sizes used to calculate diffusivities were those indicated at the 1% volume filling on the cumulative pore volume distribution curves shown in Chapter 3 because our sample were filled with 1% w/w of benzene-d_6. Because benzene-d_6 has a density of 0.95 g/ml, the 1% volume is approximately the same as the 1% by weight. These calculations were performed in Chapters 4-8 for specific solid phases, and those values are collected here for comparison with each other

(Table 9.3). The pore sizes of Rigby's solid phases were collected from the literature, where available, and diffusivity values shown are based on these pore sizes. Figure 9.4 b) is exactly the same as Figure 9.4 a), except that diffusivity, D_0,

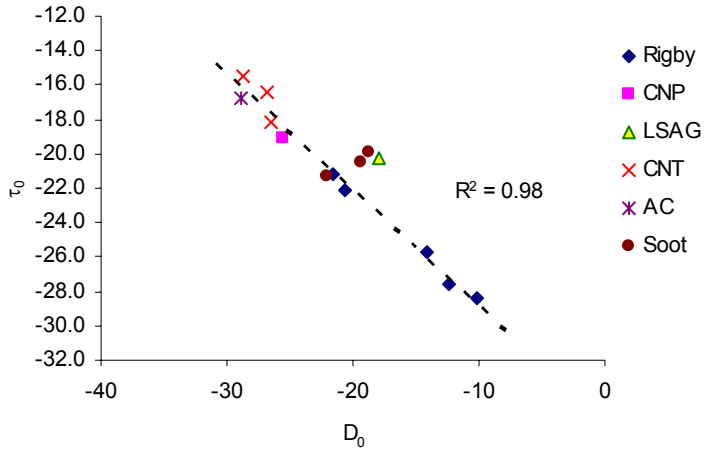

Figure 9.5. Plot of correlation time vs. diffusivity (calculated as described in the text) for benzene-d_6 on various solid phases. Line is best fit for points other than LSAG and two of the soot loadings.

is plotted instead of τ_0. This appears to improve the linearity of the graphene data, given a best fit line with an R^2 value of 0.94. Finally, a plot of diffusivity vs. correlation time (Figure 9.5) places the values of Rigby and the BC values on the same line. Only the higher loadings of soot and the LSAG do not fall on this line, and their displacement may indicate an inaccurate (too large) measure from the cumulative pore volume distribution curve of the pore size occupied by the volume of benzene loaded onto these samples. For these two samples, in particular, this could be a problem because (1) the soot pore size distribution was not obtained from

an isotherm performed by the author, but was estimated from a broad group specified in a list, and (2) the LSAG cumulative distribution is very broad at 1%, and the LSAG has a greater than monolayer loading. Excluding these three points, a best fit line of the remaining data has a R^2 of 0.98.

9.3.4 General Remarks

The above discussion of pore sizes and self-diffusivity (τ_0) values demonstrates that the pore shapes and sizes direct the motion of the benzene adsorbed within them. Thus, ^{2}H NMR can be used to define the diffusion paths of benzene molecules for samples containing small mesopores and micropores. For slit-shaped pores, application of the Lorentzian peak width to calculate jump rates might be improved by peak fitting to an isotropic motional model with weighted population distributions at configurations parallel to the slit surfaces. It is also possible that an important population of benzene molecules within a micropore occupy a favored slant configuration (such as that modeled in the Appendix to Chapter 8), especially at higher loadings [61, 69] and future refinements of a motional model could reveal this. Further, it would seem that ^{2}H NMR potentially could detect preferred orientations on the planar graphite surface to confirm the slant models predicted by the simulated surface diffusion of Fodi and Hentschke [37]. However, monolayer and submonolayer concentrations of the benzene molecules on the homogeneous planar LSAG surface approach the limits of detection for the NMR (0.25μl per Chapter 2), while for higher surface area samples, such as the porous graphites Carbopack B, or CNTs, the pore structure imposes surface roughness, which reduces the surface homogeneity and negates the

hypothetical condition of the experiment.

It would seem that the fractal geometry of a CNT would be related to its diameter, given the relationship between CNT chirality and tube diameter [81] mentioned in the Introduction (Chapter 1). However, most of the benzene appears to be moving within interstitial pores between agglomerates of CNTs adsorbed to each other because the pore size filled at 1% loading is smaller than the inner diameters of the CNTs. Nevertheless, it is possible that the external curvature of the CNT (also dependent on its chirality and diameter) would be expressed in the pore shape (Figure 9.6) and, thus, affects the fractal dimension.

Lastly, motional analysis of benzene sorbed onto MWC indicates that the char may not be as rigid as the other BCs examined , and this structural flexibility,

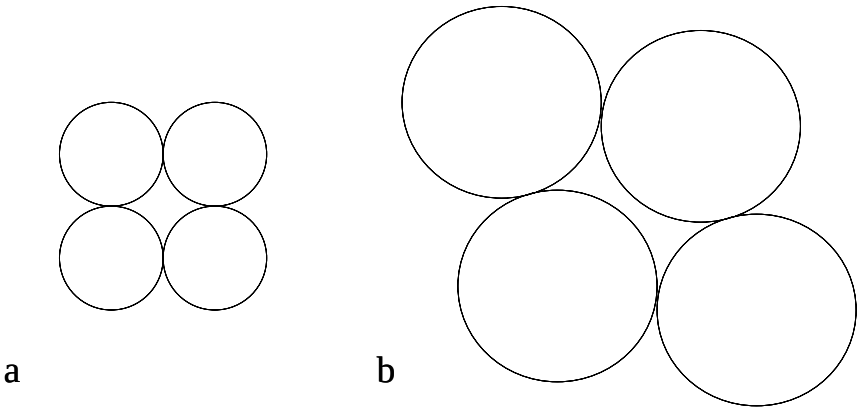

Figure 9.6. Diagram of two possible packing arrangements for CNTs, which adsorb strongly at different geometric sites and have different sizes, after Greg and Sing [62] referring to general pore geometries.

along with the abundance of $Ca^{2+,}$ strongly affects the Arrhenius behavior of the benzene-d_6 [82, 83]. Even though it has been demonstrated by that sorption of planar molecules is favored over similar nonplanar compounds [12], the implied interaction enhancement may not necessarily require structural rigidity of BCs. For nongraphitized natural charcoals, such as the MWC, a polymer model may serve better than graphite. Fractal analysis for environmental sorbents has been used to predict slow sorption behavior [84]. Similarly, the possible changes with aging observed in the present study for the CNP and CNT can be attributed to slow diffusion into isolated pores. This has been observed for CNTs by other researchers [85] and is similar to the slow inter-cage motion observed for benzene on zeolites [86].

9.4 CONCLUSIONS

The use of planar graphite as a model BC surface is supported by the equivalence of the E_a values for the motion of benzene-d_6 on soot and activated carbon to that for the low-surface-area graphite, as measured with the Lorentzian peak of the ^2H solid-state NMR spectrum. Similarly, the magnitude of this E_a, 10.1 ($\pm$1.1) kJ/mol, supports physisorption processes, rather than chemisorption. The BCs which showed energies of activation less than this consisted of either curved graphene surfaces, CNTs with Ea's of 9.3 ($\pm$1.4) kJ/mol and 7.6 ($\pm$0.5) kJ/mol, or amorphous carbon, CNP with Ea of 7.0 (+0.1) kJ/mol. However, the expected increase of energy of activation with graphitic crystallinity was not observed. The occurrence of an entropy/enthalpy compensation effect was observed as well as an LFER between the energies of activation for surface diffusion and the isosteric heats

of adsorption (0.25-0.33). The size of this ratio (much less than 1) also supports nonspecific adsorption interactions. Further, the shape of the ^{2}H NMR peak for benzene-d_6 on the activated carbon sample indicates that at least some of the benzene-d_6 molecules may be more strongly held to the surface and experience more restricted motion than those molecules which provide the overall Lorentzian shape of the ^{2}H NMR peak. Additionally, the motion of benzene-d_6 on the MWC appears to be very different from that on the other solid phases, and it is suspected that this can be attributed to the flexible, expandable nature of the adsorbent. In general, the surface diffusion of benzene-d_6 on BCs revealed a strong influence of pore shape on the diffusion path, as indicated from the correlation of τ_0 with both D_0 and fractal dimension. Surface roughness, as measured by the fractal dimension determined from the FHH equation, is a function of the individual graphene structure and the nature of the porosity.

References

1. Mauter, M. S.; Elimelech, M., Environmental applications of carbon-based nanomaterials. *Environmental Science & Technology* **2008,** *42*, (16), 5843-5859.
2. Do, D. D.; Do, H. D., Effects of quadrupole moments of graphite surface on adsorption of simple gases on graphitized thermal carbon black. *Colloids and Surfaces A: Physicochem. Eng. Aspects* **2007,** *300*, 50-59.
3. Isirikyan, A. A.; Kiselev, A. V., The absolute adsorption isotherms of vapors of nitrogen, benzene and *n*-hexane, and the heats of adsorption of benzene and *n*-hexane on graphitized carbon blacks. I. graphitized thermal blacks. *Journal of Physical Chemistry* **1961,** *65*, (4), 601-607.
4. Dubinin, M. M.; Polyakov, N. S.; Kadlez, O.; Kataeva, L. I.; Petukhova, G. A., Heterogeneous microporous structures and adsorption properties of carbon adsorbents. 12.* Porous structure and adsorption properties of active carbons. *Russian Chemical Bulletin* **1993,** *42*, (8), 1304-1308.
5. Poole, C. F.; Schuette, S. A., *Contemporary Practice of Chromatography*. Elsevier: New York, 1984.
6. Giddings, C. J., *Unified Separation Science*. John Wiley & Sons, Inc.: New York, NY, 1991; p 320 p.

7. Chun, Y.; Sheng, G.; Chiou, C. T., Evaluation of current techniques for isolation of chars as natural adsorbents. *Environmental Science & Technology* **2004,** *38*, 4227-4232.
8. Chun, Y.; Sheng, G.; Chiou, C. T.; Xing, B., Compositions and sorptive properties of crop residue-derived chars. *Environmental Science & Technology* **2004,** *38*, 4649-4655.
9. Sander, M.; Pignatello, J. J., Characterization of charcoal adsorption sites for aromatic compounds: Insights drawn from single-solute and bi-solute competitive experiments. *Environmental Science & Technology* **2005,** *39*, 1606-1615.
10. Braida, W. J.; Pignatello, J. J.; Lu, Y.; Ravikovitch, P. I.; Neimark, A. V.; Xing, B., Sorption hysteresis of benzene in charcoal particles. *Environmental Science & Technology* **2003,** *37*, 409-417.
11. Kwon, S.; Pignatello, J., Effect of natural organic substances on the surface and adsorptive properties of environmental black carbon (char): pseudo pore blockage by model lipid components and its implications for N-probed surface properties of natural sorbents. *Environmental Science & Technology* **2005,** *39*, (20), 7932-7939.
12. Zhu, D.; Pignatello, J. J., Characterization of aromatic compounds sorptive interactions with black carbon (charcoal) assisted by graphite as a model. *Environmental Science & Technology* **2005**, (37).
13. Zhu, D.; Kwon, S.; Pignatello, J., Adsorption of single-ring organic compounds to wood charcoals prepared under different thermochemical conditions. *Environmental Science & Technology* **2005,** *39*, 3990-3998.
14. Certificate of Analysis - Standard Reference Material 2975 - Diesel Particulate Matter (Industrial Forklift). **2001**.
15. Braun, A.; Mun, B. S.; Huggins, F. E.; Huffman, G. P., Carbon speciation of diesel exhaust and urban particulate matter NIST standard reference materials with C(1s) NEXAFS spectroscopy. *Environmental Science & Technology* **2007,** *41*, 173-178.
16. Nguyen, T. H.; Ball, W. P., Absorption and adsorption of hydrophobic organic contaminants to diesel and hexane soot. *Environmental Science & Technology* **2006,** *40*, 2958-2864.
17. Nguyen, T. H.; Brown, R. A.; Ball, W. P., An evaluation of thermal resistance as a measure of black carbon content in diesel soot, wood char, and sediment. *Organic Geochemistry* **2004,** *35*, 217-234.
18. Nguyen, T. H.; Sabbah, I.; Ball, W. P., Sorption nonlinearity for organic contaminants with diesel soot: method development and isotherm interpretation. *Environmental Science & Technology* **2004,** *38*, 3595-3603.
19. Roth, C. M.; Goss, K.-U. a. S., Rene P., Sorption of a diverse set of organic vapors to diesel soot and road tunnel aerosols. *Environmental Science & Technology* **2005,** *39*, 6632-6637.
20. Pfeifer, P.; Avnir, D., Chemistry in noninteger dimensions between two and three. I. Fractal theory of heterogeneous surfaces. *Journal of Chemical Physics* **1983,** *79*, (7), 3558-3565.
21. Neimark, A. V.; Unger, K. K., Method of discrimination of surface fractality. *Journal of Colloid and Interface Science* **1993,** *158*, 412-419.

22. Tang, P.; Chew, N. Y. K.; Chan, H.-K.; Raper, J. A., Limitation of determination of surface fractal dimension using N_2 adsorption isotherms and modified Frenkel-Halsey-Hill theory. *Langmuir* **2003,** *19*, 2632-2638.
23. Ehrburger-Dolle, F., Some new correlations between Dubinin-Radushkevich and Freundlich equations and fractal dimension of microporous solids. *Langmuir* **1994,** *10*, 2052-2055.
24. Sun, C.-H.; Li, F.; Cheng, H.-M.; Lu, G.-Q., Fractal effects on the measurement of the specific surface areas of single-walled carbon nanotubes. *Carbon* **2005,** *43*, 1785-1787.
25. Jaroniec, M., Evaluation of the fractal dimension from a single adsorption isotherm. *Langmuir* **1995,** *11*, 2316-2317.
26. Schieferstein, E.; Heinrich, P., Diffusion coefficients calculated for microporous solids from structural parameters evaluated by fractal geometry. *Langmuir* **1997,** *13*, 1723-1728.
27. Pfeifer, P.; Ehrburger-Dolle, F.; Rieker, T. P.; Gonzalez, M. T.; Hoffman, W. P.; Molina-Sabio, M., Nearly space-filling fractal networks of carbon nanopores. *Physical Review Letters* **2002,** *88*, (11), 115502-1-115502-4.
28. Rigby, S. P., NMR and modelling studies of structural heterogeneity over several lengthscales in amorphous catalyst supports. *Catalysis Today* **1999,** *53*, 207-223.
29. Rigby, S. P., Fractal theory for the compensation effect observed in a surface diffusion process studied using deuteron NMR. *Langmuir* **2002,** *18*, 1613-1618.
30. Rigby, S. P., A model for the surface diffusion of molecules on a heterogeneous surface. *Langmuir* **2003,** *19*, 364-376.
31. Rigby, S. P., Predicting surface diffusivities of molecules from equilibrium adsorption isotherms. *Colloids and Surfaces A: Physicochem. Eng. Aspects* **2005,** *262*, 139-149.
32. Bond, G. C.; Keane, M. A.; Kral, H.; Lercher, J., Compensation phenomena in heterogeneous catalysis: general principles and a possible explanation. *Catalysis Reviews* **2000,** *42*, (3), 323-383.
33. Miyabe, K.; Guiochon, G., Thermodynamic characteristics of surface diffusion in reversed-phase liquid chromatography. *Journal of Physical Chemistry B* **1999,** *103*, 11086-11097.
34. Miyabe, K.; Guiochon, G., Correlation between surface diffusion and molecular diffusion in reversed-phase liquid chromatography. *Journal of Physical Chemistry B* **2001,** *105*, 9202-0209.
35. Miyabe, K.; Suzuki, M., Adsorption characteristics of octadecysilyl-silica gel in gaseous systems. *AIChE Journal* **1994,** *39*, (11), 1791-1798.
36. Gilliland, E. R.; Baddour, R. F.; Perkinson, G. P.; Sladek, K. J., Diffusion on surfaces. I. Effect of concentration on the diffusivity of physically adsorbed gases. *Ind. Eng. Chem.; Fundam.* **1974,** *13*, 95-99.
37. Fodi, B.; Hentschke, R., Molecular dynamics simulation of a binary hydrocarbon mixture near an adsorbing wall: benzene/I-heptane on graphite. *Langmuir* **1998,** *14*, 429-437.
38. Do, D. D.; Do, H. D., Characterization of micro-mesoporous carbonacenous materials. Calculations of adsorption isotherm of hydrocarbons. *Langmuir* **2002,** *18*, 93-99.

39. Kruk, M.; Li, Z.; Jaroniec, M., Nitrogen adsorption study of surface properties of graphitized carbon blacks. *Langmuir* **1999,** *15*, 1435-1441.
40. Diaz, E.; Ordonex, S.; Vega, A., Adsorption of volatile organic compounds onto carbon nanotubes, carbon nanofibers, and high-surface-area graphites. *J. Colloid and Interface Science* **2007,** *305*, 7-16.
41. Eastman, M. A.; Nanny, M. A., Fitting of deuterium quadrupole echo spectra with multiple motional models. *Journal of Magnetic Resonance* **2007,** *184*, 302-314.
42. Grundke, V.; Boddenberg, B., One and two component adsorption layers of *n*-hexane and benzene on graphite studied by ^{2}H NMR spectroscopy. *Molecular Physics* **1993,** *79*, (6), 1215-1226.
43. Choi, J.-G.; Do, D. D.; Do, H. D., Surface diffusion of adsorbed molecules in porous media: monolayer, multilayer, and capillary condensation regimes. *Ind. Eng. Chem. Res.* **2001,** *40*, 4005-4031.
44. Gauden, P. A.; Terzyk, A. P.; Cwiertnia, M. S.; Rychlicki, G.; Newcombe, G.; Kowalczyk, P., Benzene adsorption on carbonaceous materials: The influence of pore structure on the state of the adsorbate. *Applied Surface Science* **2006,** *253*, 2525-2539.
45. Dubinin, M. M.; Vartapetian, R. S.; Voloshchuk, A. M., NMR study of translational mobility of molecules adsorbed on active carbons. *Carbon* **1988,** *29*, (4), 515-520.
46. Xiong, J.; Maciel, G. E., Deuterium NMR studies of local motions of benzene adsorbed on Ca-montmorillonite. *Journal of Physical Chemistry B* **1999,** *103*, 5543-5549.
47. Ross, J. W.; Good, R. J., Adsorption and surface diffusion of *n*-butane on spheron 6 (2700°) carbon black. *Journal of Physical Chemistry* **1956,** *60*, 1167-1171.
48. Adamson, A.; Gast, A. P., *Physical Chemistry of Surfaces*. John Wiley & Sons: New York, 1997; p 784.
49. Villanueva-Garibay, J. A.; Muller, K., Solid-state ^{2}H NMR studies of cyclophosphazene inclusion compounds: order and dynamics of the benzene guests. *Journal of Physical Chemistry B* **2004,** *108*, 15057-15068.
50. Schwartz, M.; Duan, D.; Berry, R. J., Molecular dynamics study of anisotropic translational and rotational diffusion in liquid benzene. *J. Phys. Chem. A* **2005,** *109*, (38), 8637-8641.
51. Voss, V.; Boddenberg, B., Anisotropic reorientation dynamics of benzene molecules adsorbed on graphite, alumina, and zeolite Y. *Surface Science* **1993,** *298*, (241-250).
52. Gedat, E.; Schreiber, A.; Albrecht, J.; Emmler, T.; Shenderovich, I.; Findenegg, G. H.; Limbach, H.-H.; Buntknowsky, G., ^{2}H solid-state NMR study of benzene-d_6 confined in mesoporous silica SBA-15. *Journal of Physical Chemistry B* **2002,** *106*, 1977-1984.
53. Wakai, C.; Nakahara, M., Attractive potential effect on the rotational correlation times for benzene-d_6 in organic solvents. *Bulletin of the Chemical Society of Japan* **1996,** *69*, 853-860.
54. Auerbach, S. M.; Bull, L. M.; Henson, N. J.; Metin, H. L.; Cheetham, A. K., Behavior of benzene in Na-X and Na-Y zeolites: comparative study by ^{2}H NMR and molecular mechanics. *Journal of Physical Chemistry* **1996,** *100*, 5923-5930.

55. Ok, J. H.; Vold, R. R.; Vold, R. L.; Etter, M. C., Deuterium nuclear magnetic resonance measurements of rotation and libration of bezene in a solid-state cyclamer. *Journal of Physical Chemistry B* **1989,** *93*, 7618-7624.
56. Nishikiori, S.-I.; Soma, T.; Iwamoto, T., In-plane and out-of-plane motion of benzene trapped in $Cd(py)_2\{Ag(CN)_2\}_2$ host as studied by deuterium NMR. *Journal of Inclusion Phenomena and Molecular Recognition in Chemistry* **1997,** *27*, 233-243.
57. Silbernagel, B. G.; Garcia, A. R.; Newsam, J. M.; Hulme, R., Molecular motion of benzene, *n*-hexane, and cyclohexane in potassium zeolite studied by deuterium NMR. *Journal of Physical Chemistry* **1989,** *93*, 6506-6511.
58. Chopra, N.; Chapman, R. G.; Chuang, Y.-F.; Sherman, J. C.; Burnell, E. E., Guest dynamics in carceplexes: a ^{2}H NMR study. *J Chem Soc Faraday Trans* **1995,** *91*, (21), 4127-4131.
59. Sato, T.; Kunimori, K.; Hayashi, S., Dynamics of benzene, cyclohexane and *n*-hexane in KL zeolite studied by ^{2}H NMR. *Physical Chemistry Chemical Physics* **1999,** *1*, (3839-3843).
60. Carman, P. C.; Raal, F. A., Diffusion and flow of gases and vapours through micropores. III. Surface diffusion coefficients and activation energies. *Proceedings of the Royal Society of London. Series A. Mathematical and Physical Sciences* **1951,** *209*, (1096), 38-58.
61. Gauden, P.; Terzyk, A. P.; Rychlicki, G.; Kowalczyk, P.; Lota, K.; Raymundo-Pinero, E.; Frackowiak, E.; Beguin, F., Thermodynamic properties of benzene adsorbed in activated carbons and multi-walled carbon nanotubes. *Chemical Physics Letters* **2006,** *421*, 409-414.
62. Gregg, S. J.; Sing, K. S. W., *Adsorption, Surface Area, and Porosity*. Academic Press: New York, NY, 1982.
63. Schwarzenbach, R. P.; Gschwend, P. M.; Imboden, D. M., *Environmental Organic Chemistry, 2nd ed.* John Wiley and Sons Inc.: New York, NY, 2003.
64. Miyabe, K.; Guiochon, G., Thermodynamic characteristics of surface diffusion in reversed-phase liquid chromatography
Journal of Physical Chemistry B **1999**, (103), 11086-11097.
65. Aubin , D. G.; Abbatt, J. P., Laboratory measurements of thermodynamics of adsorption of small aromatic gases to *n*-hexane soot surface. *Environmental Science & Technology* **2006,** *40*, 179-187.
66. Thompson, J. K.; Krebs, J. J.; Resing, H. A., NMR relaxation times of benzene adsorbed on charcoal: molecular rotation and diffusion. *Journal of Chemical Physics* **1965,** *43*, (11), 3853-3865.
67. Prasetyo, I.; Do, D. D.; Do, H. D., Surface diffusion of strong adsorbing vapours on porous carbon. *Chemical Engineering Science* **2002,** *57*, 133-141.
68. Crespo, D.; Yang, R. T., Adsorption of organic vapors on single-walled carbon nanotubes. *Ind. Eng. Chem Res* **2006,** *45*, (16), 5524-5530.
69. Hentschke, R.; Schurmann, B. L., A molecular dynamics simulation of liquid benzene adsorbed on graphite. *Surface Science* **1992,** *262*, 180-188.
70. Kapoor, A.; Yang, R. T., Surface diffusion on energetically heterogeneous surfaces. *AIChE Journal* **1989,** *35*, (10), 1735-1738.
71. Boddenberg, G.; R., H.; Opperman, G., NMR spin echo studies on mobility

and diffusion of benzene adsorbed on silica. *Journal of Colloid and Interface Science* **1972,** *38*, 210-216.
72. Arena, M. V.; Deckert, A. A.; J.L., B.; George, S. M., Surface diffusion and desorption of pentane isomers on Ru(001)
Journal of Physical Chemistry **1990,** *94*, 6792-6797.
73. Vernov, A.; Steele, W. A., Computer simulations of benzene adsorbed on graphite. 2. 298K. *Langmuir* **1991,** *7*, 2817-2820.
74. Do, D. D.; Nicholson, D.; Do, H. D., On the anatomy of the adsorption heat versus loading as a function of temperature and adsorbate for a graphitic surface. *Journal of Colloid and Interface Science* **2008,** *325*, 7-22.
75. Kobayashi, T.; Babu, P. K.; Chung, J. H.; Oldfield, E.; Wieckowski, A., Coverage dependence of CO surface diffusion on Pt nanoparticles: an EC-NMR study. *Journal of Physical Chemistry C* **2007,** *111*, 7078-7083.
76. Fletcher, A. J.; Thomas, K. M., Compensation effect for the kinetics of adsorption/desorption of gases/vapors on microporous carbon materials. *Langmuir* **2000,** *16*, 6253-6266.
77. Liu, L.; Guo, Q. X., Isokinetic relationship,isoequilibrium relationship, and enthalpy-entropy compensation. *Chemical Reviews* **2001,** *101*, 673-695.
78. Rigby, S. P.; Gladden, L. F., The prediction of transport properties of porous media using fractal models and NMR experimental techniques. *Chemical Engineering Science* **1999,** *54*, 3503-35512.
79. Boddenberg, B.; Grosse, R., A deuteron NMR study on a benzene multilayer on graphite. *Z. Naturforsch* **1987,** *421*, 272-274.
80. Nguyen, T. X.; Bhatia, S. K., Probing the pore wall structure of nanoporous carbons using adsorption. *Langmuir* **2004,** *20*, 3532-3535.
81. Bachilo, S. M.; Balzano, L.; Herrera, J. E.; Pompeo, F.; Resasco, D. E.; Weisman, R. B., Narrow (*n,m*)-Distribution of single-walled carbon nanotubes grown using a solid supported catalyst. *Journal of the American Chemical Society Communications* **2003,** *125*, 11186-11187.
82. Vartapetyan, R. S.; Khosina, E. V., Porous structure of rigid and swelling adsorbents according to pulsed NMR data on the mobility of adsorbed water and benzene molecules. *Colloid Journal* **2006,** *68*, 1-19.
83. Khozina, E. V.; Vartapetyan, R. S., Adsorption and mobility of water and benzene molecules in carbon and polymer adsorbents. *Adsorption* **2005,** *11*, 341-356.
84. Dachs, J., Conformation entropy drives slow sorption of organic chemicals into fractal sorbents. *Langmuir* **2002,** *18*, 7089-7091.
85. Kondratyuk, P.; Wang, Y.; Liu, J.; Johnson, J. K.; Yates, J. T., Jr., Inter- and intratube self-diffusion in *n*-heptane adsorbed on carbon nanotubes. *Journal of Physical chemistry* **2007,** *111*, 4578-4584.
86. Bull, L. M.; Henson, N. J.; Cheetham, A. K.; Newsam, J. M.; Heyes, S. J., Behavior of benzene in siliceous faujasite: a comparative study of deuteron NMR and molecular dynamics. *J. Phys. Chem.* **1993,** *97*, 11776-11780.

CHAPTER 10. SUGGESTIONS FOR FUTURE RESEARCH

10.1 MOLECULAR MOTION OF BENZENE-d_6 ON A NATURAL WOOD CHAR COMBUSTED AT DIFFERENT TEMPERATURES

It is known that wood chars found in natural systems are similar to many activated carbons because both are formed by combustion of plant material [1-4]. However, activated carbons undergo "steam activation" and are commonly heated to temperatures higher than occur in forest fires [5, 6] Therefore, although activated carbons are often used as model chars for their role as environmental sorbents for the prediction of the fate and transport of hydrophobic organic contaminants, natural chars are known to be more heterogeneous chemically and more polymeric in character than rigid activated carbons [3, 7-12] While higher charring temperatures are known to enhance the carbon content, graphitic character, and structural rigidity of natural chars, the difference in the molecular motion of the sorbate molecules within a given char heated to different temperatures has not been studied [13-15] Static solid-state ^{2}H NMR of deuterated benzene has been used to evaluate sorption interactions for polymers, BCs, clathrates, and other sorbents [16-21] and has also been used to measure fractal dimensions for different solid phases [22] Fractal dimensions for wood chars have not been measured with this technique, but natural polymers have been measured by other methods and tied to slow sorption processes and contaminant sequestration [23]. Collecting static solid-state ^{2}H NMR spectra of benzene sorbed at variable loading and variable temperatures onto different samples of the same wood char heated to 673K, 873K and 1073K would be provide information about sorbate-sorbent interactions and fractal dimensions, which can lead to better prediction of the fate and transport of hydrophobic organic

contaminants in natural settings. Associated characterization of the char at different temperatures by (1) N_2 adsorption analysis for surface area, pore-size distributions, fractal dimension from the Frenkel-Hill-Halsey, (2) elemental composition, i.e., % carbon, hydrogen, Ca, Fe, (3) surface chemical functionalities by infrared spectroscopy, X-ray diffraction, and Boehm titration, (4) temperature-programmed desorption [24], and (5) imaging by high-resolution transmission electron microscopy [25], would provide a good chemical and physical framework for the interpretation of the molecular motion.

10.2 VISUALIZATION OF FRACTAL PORE NETWORKS USING STATIC SOLID-STATE ^{2}H NMR OF BENZENE-d_6 AND N_2 ADSORPTION ANALYSIS

The surface diffusivity of a sorbate on a porous sorbent is an important parameter in chromatography [26], catalysis [27, 28], and transport of contaminants through soils and sediments [9]. The flow of a sorbate across the grain surfaces in a porous medium is related to the sorbate-sorbent interactions, solubility in the aqueous phase (or vapor pressure, if no liquid phase is present), the nature of the solid framework and the associated pore network [29-31]. Both pore networks and surface roughness are related to the fractal nature of the solid phase [23, 32-34]. All of these variable are known, but not well understood, so that one researcher complained that whatever is not understood in a system of flow through a porous medium is simply attributed to surface diffusion [31]. Static solid-state ^{2}H NMR of benzene sorbate molecules at low loadings on packed sorbents often produce Lorentzian, pseudoisotropic spectra (Chapter 4-8), which can be used to measure surface diffusivity rates and, with variable-temperature experiments, can measure the energy of activation and pre-exponential factor [35]. The reorientational jump

rates, which are measured in the NMR, can be determined by fitting to simulated spectra or by the spectral peak width at half-height [35-37]. If a spectrum cannot be fitted to a simulated spectra for isotropic motion (implied in the Lorentzian peak shape [35]), then it seems likely that the motion may not be strictly isotropic. For instance, the benzene may spend more time at certain sites or contain a wobble or other motional component [38, 39]. Various motional models have been simulated by previous workers for benzene on solid phases, for example, large- and small-angle wobbles on Ca-montmorillonite [21], and cartwheels in zeolite cages [19]. However, for benzene diffusing within a pore network and presenting a generally Lorentzian ^{2}H NMR peak shape, specific models could be developed for fitting the peaks at variable loadings. Thus, given the tie between pore networks and molecular motion across the sorbent surface, the motional model would act to visualize the pores and their networks, and, hopefully, cast light upon the nature of the fractal dimension and the tortuosity of the pore network.

Above are only a couple of areas of research addressing questions which are associated with this study, which has, hopefully, made a modest contribution to research in the area of the molecular motion and interactions of sorbates on porous solid phases and the associated environmental chemistry implications. Future studies of this and similar data using absolute rate theory or a statistical mechanical approach (mentioned on p. 34) would be likely to provide even greater mechanistic detail. Such analyses of temperature programmed desorption data in tandem with static solid-state ^{2}H NMR would provide equilibrium and kinetics values of the vapor/solid equilibrium as well as surface diffusion kinetics (e.g., Arena et al. [27]),

which, coupled with spectroscopic data with possible information about the transition state orientation(s) of desorbing physisorbed molecules, could greatly enhance understanding of the particular sorption mechanism and molecular interactions which occur during sorption.

References

1. Braida, W. J.; Pignatello, J. J.; Lu, Y.; Ravikovitch, P. I.; Neimark, A. V.; Xing, B., Sorption hysteresis of benzene in charcoal particles. *Environmental Science & Technology* **2003,** *37*, 409-417.
2. Chun, Y.; Sheng, G.; Chiou, C. T., Evaluation of current techniques for isolation of chars as natural adsorbents. *Environmental Science & Technology* **2004,** *38*, 4227-4232.
3. Chun, Y.; Sheng, G.; Chiou, C. T.; Xing, B., Compositions and sorptive properties of crop residue-derived chars. *Environmental Science & Technology* **2004,** *38*, 4649-4655.
4. Karapanagioti, H.; Childs, J.; Sabatini, D. A., Impacts of heterogeneous organic matter on phenanthrene sorption: different soil and sediment samples. *Environmental Science & Technology* **2001,** *35*, 4684-4690.
5. Bonsal, R. C.; Goyal, M., *Activated Carbon Adsorption*. Taylor and Francis: Boca Raton, FL, 2005; p 497.
6. Chen, B.; Zhou, D.; Zhu, L., Transitional adsorption and partition of nonpolar and polar aromatic contaminants by biochars of pine needles with different pyrolytic temperatures. *Environmental Science & Technology* **2008,** *42*, (14), 5137-5143.
7. Luthy, R. G.; Aiken, G. R.; Brusseau, M. L.; Cunningham, S. D.; Gschwend, P. M.; Pignatello, J. J.; Reinhard, M.; Traina, S. J.; Weber, W. J.; Westall, J. C., Sequestration of hydrophobic organic contaminants by geosorbents. *Environmental Science & Technology* **1997,** *31*, (12), 3341-3347.
8. Cornelissen, G.; Gustafsson, O.; Bucheli, T. D.; Jonker, M. T. O.; Koelmans, A. A.; van Noort, P. C. M., Extensive sorption of organic compounds to black carbon, coal, and kerogen in sediments and soils: mechanisms and consequences for distribution, bioaccumulation, and biodegradation. *Environmental Science & Technology* **2005,** *39*, (18), 6881-6895.
9. Allen-King, R. M.; Grathwohl, P.; Ball, W. P., New modeling paradigms for the sorption of hydrophobic organic chemicals to heterogeneous carbonaceous matter in soils, sediments and rocks. *Advances in Water Resources* **2002,** *25*, 985-1016.

10. Dall'Ora, M.; Jensen, P. A.; Jensen, A. D., Suspension combustion of wood: influence of pyrolysis conditions on char yield, morphology, and reactivity. *Energy and Fuels* **2008,** *22*, (5), 2955-2962.
11. Endo, S.; Grathwohl, P.; Schmidt, T. C., Absorption or adsorption? Insights from molecular probles *n*-alkanes and cycloalkanes into modes of sorption by environmental solids. *Environmental Science & Technology* **2008,** *42*, 3989-3995.
12. Keiluweit, M.; Kleber, M., Molecular-level interactions in soils and sediments: the role of aromatic #-systems. *Environmental Science & Technology* **2009**.
13. Bornemann, L. C.; Kookana, R. S.; Welp, G., Differential sorption behaviour of aromatic hydrocarbons on charcoals prepared at different temperatures from grass and wood. *Chemosphere* **2007,** *67*, 1033-1042.
14. Thompson, J. K.; Krebs, J. J.; Resing, H. A., NMR relaxation times of benzene adsorbed on charcoal: molecular rotation and diffusion. *Journal of Chemical Physics* **1965,** *43*, (11), 3853-3865.
15. Zhu, D.; Kwon, S.; Pignatello, J., Adsorption of single-ring organic compounds to wood charcoals prepared under different thermochemical conditions. *Environmental Science & Technology* **2005,** *39*, 3990-3998.
16. Ok, J. H.; Vold, R. R.; Vold, R. L.; Etter, M. C., Deuterium nuclear magnetic resonance measurements of rotation and libration of bezene in a solid-state cyclamer. *Journal of Physical Chemistry B* **1989,** *93*, 7618-7624.
17. Boddenberg, B.; Burmeister, R., ^{2}H n.m.r. study on the rotation and diffusion kinetics of propene and benzene in NaX and AgNaX zeolites. *Zeolites* **1988,** *8*, 488-494.
18. Bull, L. M.; Henson, N. J.; Cheetham, A. K.; Newsam, J. M.; Heyes, S. J., Behavior of benzene in siliceous faujasite: a comparative study of deuteron NMR and molecular dynamics. *J. Phys. Chem.* **1993,** *97*, 11776-11780.
19. Auerbach, S. M.; Bull, L. M.; Henson, N. J.; Metin, H. L.; Cheetham, A. K., Behavior of benzene in Na-X and Na-Y zeolites: comparative study by ^{2}H NMR and molecular mechanics. *Journal of Physical Chemistry* **1996,** *100*, 5923-5930.
20. Nishikiori, S.-I.; Soma, T.; Iwamoto, T., In-plane and out-of-plane motion of benzene trapped in $Cd(py)_2\{Ag(CN)_2\}_2$ host as studied by deuterium NMR. *Journal of Inclusion Phenomena and Molecular Recognition in Chemistry* **1997,** *27*, 233-243.
21. Xiong, J.; Maciel, G. E., Deuterium NMR studies of local motions of benzene adsorbed on Ca-montmorillonite. *Journal of Physical Chemistry B* **1999,** *103*, 5543-5549.
22. Rigby, S. P., Fractal theory for the compensation effect observed in a surface diffusion process studied using deuteron NMR. *Langmuir* **2002,** *18*, 1613-1618.
23. Ehrburger-Dolle, F., Some new correlations between Dubinin-Radushkevich and Freundlich equations and fractal dimension of microporous solids. *Langmuir* **1994,** *10*, 2052-2055.
24. Abu, A.; Smith, S., Assessing sequestration of selected polycyclic aromatic hydrocarbons by use of adsorption modeling and temperature-programmed desorption. *Environmental Science & Technology* **2005,** *39*, 7585-7591.

25. Harris, P. J. F.; Liu, Z.; Suenaga, K., Imaging the atomic structure of activated carbon. *Journal of Physics: Condensed Matter* **2008,** *20*.
26. Carman, P. C.; Raal, F. A., Diffusion and flow of gases and vapours through micropores. III. Surface diffusion coefficients and activation energies. *Proceedings of the Royal Society of London. Series A. Mathematical and Physical Sciences* **1951,** *209*, (1096), 38-58.
27. Arena, M. V.; Deckert, A. A.; J.L., B.; George, S. M., Surface diffusion and desorption of pentane isomers on Ru(001)
Journal of Physical Chemistry **1990,** *94*, 6792-6797.
28. Rigby, S. P., NMR and modelling studies of structural heterogeneity over several lengthscales in amorphous catalyst supports. *Catalysis Today* **1999,** *53*, 207-223.
29. Bruch, L. W.; Diehl, R. D.; Venables, J. A., Progress in the measurement and modeling of physisorbed layers. *Reviews of Modern Physics* **2007,** *79*, 1381-1454.
30. Choi, J.-G.; Do, D. D.; Do, H. D., Surface diffusion of adsorbed molecules in porous media: monolayer, multilayer, and capillary condensation regimes. *Ind. Eng. Chem. Res.* **2001,** *40*, 4005-4031.
31. Gritti, F.; Guiochon, G., Effect of surface coverage of C18-bonded silica particles on the obstructive factor and intraparticle diffusion mechanism. *Chemical Engineering Science* **2006,** *61*, 7636-7650.
32. Jaroniec, M., Evaluation of the fractal dimension from a single adsorption isotherm. *Langmuir* **1995,** *11*, 2316-2317.
33. Pfeifer, P.; Avnir, D., Chemistry in noninteger dimensions between two and three. I. Fractal theory of heterogeneous surfaces. *Journal of Chemical Physics* **1983,** *79*, (7), 3558-3565.
34. Pfeifer, P.; Ehrburger-Dolle, F.; Rieker, T. P.; Gonzalez, M. T.; Hoffman, W. P.; Molina-Sabio, M., Nearly space-filling fractal networks of carbon nanopores. *Physical Review Letters* **2002,** *88*, (11), 115502-1-115502-4.
35. Grundke, V.; Boddenberg, B., One and two component adsorption layers of *n*-hexane and benzene on graphite studied by ^{2}H NMR spectroscopy. *Molecular Physics* **1993,** *79*, (6), 1215-1226.
36. Greenfield, M. S.; Ronemus, A. D.; Vold, R. L.; Vold, R. R.; Ellis, P. D.; Raidy, T. E., Lineshapes of deuterium quadrupole echoes. *Journal of Magnetic Resonance* **1989,** *72*, 89-107.
37. Eastman, M. A.; Nanny, M. A., Fitting of deuterium quadrupole echo spectra with multiple motional models. *Journal of Magnetic Resonance* **2007,** *184*, 302-314.
38. Nishikiori, S.-I., Out-of-plane motion of the guest benzene molecule trapped in a $[Cd(dmen)_2(CN)]_2[Cd(CN)_4]$ host as studied by ^{2}H-NMR. *Journal of Inclusion Phenomena and Macrocyclic Chemistry* **1999,** *34*, 331-343.
39. Villanueva-Garibay, J. A.; Muller, K., Solid-state ^{2}H NMR studies of cyclophosphazene inclusion compounds: order and dynamics of the benzene guests. *Journal of Physical Chemistry B* **2004,** *108*, 15057-15068.

APPENDICES

A1. SAMPLE PREPARATION AND BENZENE-d_6 CALIBRATION DETAILS

A1.1. VAPOR MANIFOLD DEPOSITION SYSTEM

A1.1.1. Manifold design and construction

A stainless-steel, copper-gasketed manifold (Figure A1.1) was constructed and its volume measured to be 876 (±10) ml of liquid isopropanol. The manifold was attached

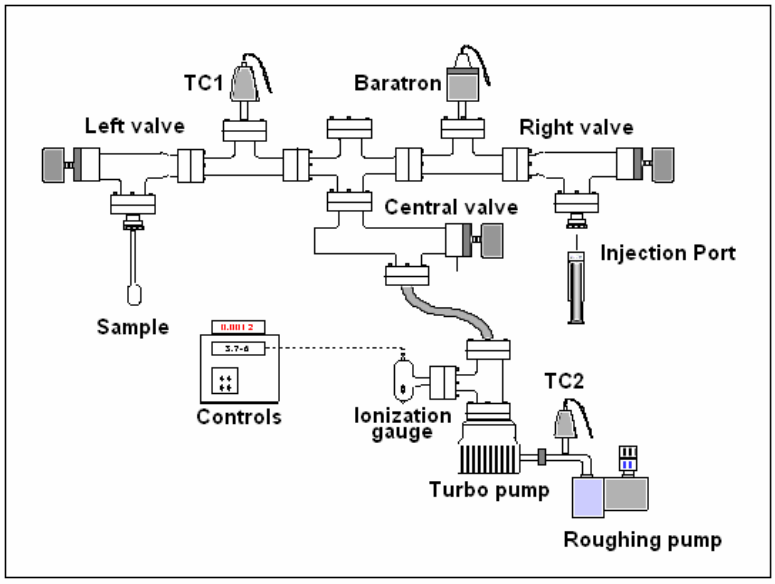

Figure A1.1. Vapor deposition manifold schematic [1].

to a Varian V70LP turbo-pumping system with a Model 571 equipped with two pressure transducers: a Varian TC1 thermal convector detector with a range of from 10^{-3} torr to 760 torr and a Baratron Model 626A 1 torr capacitance manometer, with a range of from 5×10^{-4} torr to 1 torr, accurate to ±0.25% within that range. The

Bayard-Alpert ionization gauge sensitive to 10^{-10} torr. The manifold system contained three isolatable (valved) ports: (1) the vacuum port, labeled "Central valve" on Figure A1.1, (2) an injection port (on the "Right Valve"), sealed with a 6 mm silicone/PFTE-lined septum, and (3), on the "Left Valve, " an Ultratorr connector for attachment of the sample tube.

A1.1.2 Calibration of the mass of benzene vapor within the manifold

The uncertainty in the amount of benzene-d_6 within the vapor deposition manifold system was calculated using propagation of error for the ideal gas law:

$$n = (P_1 - P_2)V / RT, \qquad \textbf{(Eqn}.\text{A1.1)}$$

where n is the number of moles, P_1 is the initial pressure, P_2 the final pressure, V the volume of the manifold, R is the universal gas constant, and T the temperature in Kelvin. Therefore, the relative uncertainty, σ_n/n, where σ is the standard deviation, is [2]:

$$\sigma_n/n = [(\sigma_P/P)^2 + (\sigma_V/V)^2 + (\sigma_T/T)^2]^{1/2} \qquad \textbf{(Eqn.}\ \text{A1.2)}$$

$$= [0.005^2 + 0.0011^2 + 0.001^2]^{1/2} = 1.2\%$$

The above values of relative uncertainty were obtained as follows: First, the uncertainty of the pressure for each reading according to the manufacturer is $\pm$0.25% and the process requires two measurements for a total of 0.5%. The volume of the manifold was calculated by summing the manifold components. The volume of the manifold with all valves closed and with the transducers removed was measured by pouring liquid methanol from a one-liter graduated cylinder into the manifold until the manifold was full, obtaining a value of 0.860 ($\pm$0.01) liter. The uncertainty in this measurement (performed three times) was the value of the smallest increment on the graduated cylinder (10 ml). The volume occupied by the

vapor in the Baratron gauge was specified by the manufacturer to be 6.3 ml, and the volume of a separate (inoperable) Varian TC1 gauge was measured with methanol to be 10 ml. After summing the volume of the main part of the manifold with the volumes from the two transducers, the result is the total volume of 0.876 (±0.01) liters, giving a relative uncertainty for the volume term in Eqn. A1.2 of ±1.1%. Third, the temperature uncertainty was 0.25°C (0.1% for 293K), based on a reasonable amount of interpolation between 1°C increments on the thermometer when viewed with a magnifying glass. The temperature inside the manifold was assumed to be equilibrated with the external room temperature.

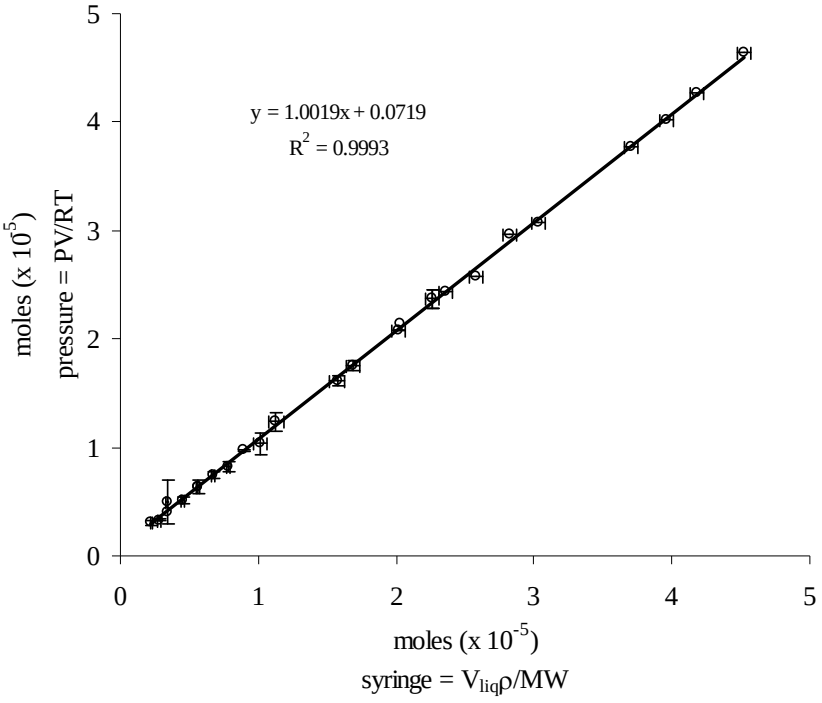

Figure A1.2. Calibration line for the amount of benzene injected with a microliter syringe into the manifold versus the amount of benzene in the manifold calculated with the ideal gas law from the pressure reading. Error bars in the *x* value indicate uncertainty due to the syringe (±0.01 below 1.00 and ±0.05 between 1.00 and 4.50), and errors bars in the *y* indicate uncertainty due to the manifold (±1.2%).

The accuracy and precision of the injection procedure were evaluated by comparing the predicted pressure readings for specific masses of benzene gas to the observed pressure readings for repeated injections of benzene and benzene-d_6 with gas- tight syringes. The data was plotted as moles calculated from the observed pressure using the ideal gas law (*y*-axis) vs. the moles calculated from the volume of liquid benzene within the syringe. Two syringes were used: (1) a 5 μl syringe with 0.05 μl markings and (2) a 1 μl syringe with 0.01 μl markings. The least squares linear fit provides the standard estimate of error (uncertainty in the number of moles of benzene on, pressure axis) for the syringe/pressure calibration line, which is calculated to be 6.04×10^{-7} torr or 0.05 μl benzene, which is the measurement error for the less precise syringe. Pressure corrections using the van der Waals' equation $[P - a(n/V)^2][V - nb] = nRT$, and constants for benzene ($a = 18.9\ L^2/mol^2$ and $b = 0.12$ L/mol [3]), were negligible because the pressures involved are well below the region in which van der Waals' forces would be active. The plot is presented in Figure A1.2.

A1.1.3. Sealing of accurate quantities of benzene within NMR sample tubes

The sample tubes consisted of 10 mm o.d. NMR tubes which were specially modified by a glassblower. Specifically, 8" long, 10 mm o.d. NMR tubes were divided into 3cm long segments, of which one end was rounded and closed (sealed) and the other end tapered and fused into an 8" long, 6 mm i.d. glass tube. The BC powder was introduced into a preweighed tube through the 6mm open end of the sample tube using a fat (10 mm dia.) Pasteur pipet as a funnel, and the BC and tube were then weighed to determine the mass of BC in the sample tube. The scale was accurate to 0.1 mg. Then, the tube with sample was centrifuged at 7000 rpm for 10

minutes, and a glass wool plug was inserted into the upper portion of the tube to prevent elutriation of BC grains upon exposure to vacuum. The 6mm diameter end of the sample tube was inserted into the sample port (just below the "Left Valve" in Figure A1.1) of the manifold and gently evacuated to 10^{-3} torr, at which point the sample was isolated from the manifold by closing the sample ("Left") valve. The manifold itself was evacuated to less than 10^{-6} torr before closing off the vacuum at the Central Valve and injecting the benzene-d_6. The sample tube was then submerged into liquid N_2 and was opened to the manifold, allowing the benzene-d_6 vapor to condense upon the BC (1% w/w). Once the 1 torr Baratron manometer reached the desired pressure reading, which had been precalculated to result in the correct amount of benzene for a 1% w/w loading on the BC, the sample was isolated from the manifold, and excess benzene-d_6 in the rest of the manifold was vacuum-pumped away. The benzene-d_6 in the sample tube was then forced to the BC at the bottom of the sample tube by repeated application of hot air from a hair dryer to the upper portion of the sample tube while the lower portion which contained the BC remained immersed in liquid N_2. The complete condensation of benzene-d_6 at the bottom of the sample tube with the BC was verified by opening the sample tube to the manifold and observing minimal pressure change (<0.005 torr) upon the application of hot air to the outside of the upper sample tube while its lower portion remained submerged in liquid N_2. The manifold and sample were then backfilled to 200-400 torr with N_2 gas, which was injected through the septum at the sample port, and the sample was then flame-sealed with the BC/benzene-d_6 portion fully submerged in liquid N_2. The presence of N_2 gas in the sample tube was observed to enhance the reproducibility of area measurements in spectra of neat benzene-d_6 in

preliminary experiments (data not shown). Further, if there was any effect of the motion due to the gas pressure in the tube, then, in order to compare the results with environmental conditions, a pressure near 1 atm would be desirable. However, an internal pressure of 1 atm would prevent efficient sealing of the sample tube, and, therefore, pressures close to 0.5 atm (200-400 torr) were used. The final sample tube length was no greater than 2.7 cm in order to fit into the probe of the solid-state NMR.

A1.2. CALIBRATION OF THE QUANTITY OF BENZENE-d_6 WITH SAMPLE TUBES USING NMR PEAK AREA

A1.2.1 Preparation of the NMR calibration curve

The amount of benzene-d_6 in each sample was monitored by comparison to an external calibration curve. The NMR quantitation calibration curve was constructed from the amount of benzene-d_6 measured by the NMR instrument (peak area) to the amount of benzene-d_6 originally condensed into the sample tubes as measured by the pressure differences within the manifold. Replicate NMR spectra of the calibration samples were collected using identical acquisition parameters at two different temperatures, 25°C and -75°C, for five sample tubes containing different amounts of neat benzene-d_6, 1.09 ($\pm$0.05) μl, 1.38 ($\pm$0.05) μl, 1.94 ($\pm$0.05) μl, 4.08 ($\pm$0.05) μl, and 7.1 ($\pm$0.1) μl, which had been prepared as described above. Each of the quantitation calibration standards of neat benzene were sealed in 5mm tubes, but were analyzed in the 10mm coil. The acquisition parameters for the -75°C quantitation spectra are 3600 scans, 0.5 s pulse delay, 40μs pulse spacing, 0.5 kHz spectral width, 2.25 μs pulse width, and 1024 data points, and the parameters for the 25°C spectra were 120 scans, 10 s pulse delay, 20 μs echo pulse spacing,

2.25 μs pulse width, and 1024 data points. Different acquisition parameters were needed at 25°C than at -75°C because the benzene-d_6 exists as a liquid at 25°C and has a relaxation time (T_1) of 1.5 s, much longer than in the solid phase. Peak areas, obtained from the Spinsight software, were then plotted against the volume of benzene-d_6 in each sample tube as calculated using the ideal gas law and the final and initial pressure measurements, detailed above, and the area values for the standard samples, normalized to the largest amount of benzene-d_6, 7.07 μl. The -75°C spectra were normalized to the area obtained for 7.07 μl sample at -75°C, and the 25°C spectra were normalized to the area obtained for 7.07 μl sample at 25°C. An average value and standard deviation for the normalized areas from both temperatures for each neat benzene-d_6 calibration sample was calculated, as displayed in the Table A1.2 (on the next page). The average normalized area values for all five neat benzene calibration samples and their standard deviations at both temperatures are also listed in Table A1.2.

Table A1.1. Calibration NMR area values for neat benzene-d_6

Benzene Volume (μl)	Average Normalized NMR Intensity (25°C)[a]	n (25°C)	σ (25°C)	Average Normalized NMR Intensity (-75°C)[a]	n (-75°C)	σ (-75°C)	Average Normalized NMR Intensity (25°C and -75°C)[a]	n (25°C and -75°C)	σ (25°C and -75°C)
1.09	0.11	2	0.00[b]	0.15	2	0.01	0.12	4	0.02
1.38	0.20	2	0.06[b]	0.21	2	0.00	0.20	4	0.05
1.94	0.34	3	0.04	0.32	4	0.02	0.33	7	0.03
4.08	0.64	3	0.09	0.60	6	0.10	0.62	9	0.09
7.07	1.00	3	0.19	1.00	11	0.07	1.00	14	0.09
0	0[c]			0[c]			0[c]		

[a]25°C spectra were normalized to the average area for the 7.07 μl sample at 25°C, and -75°C to the average area for that sample at -75°C; [b]value is the difference between the average and the highest or lowest; [c]0 point not actually measured.

The values are similar and the values of the slopes and Pearson correlation coefficients are also similar (slope of 0.1442 and 0.1461 and R^2 of 0.996 and 0.984 for 25°C and -75°C, respectively). Consequently, normalized areas for spectra from both temperatures were combined into one calibration plot. Because the standard deviation increases with sample size, a weighted least squares fit might be preferable at higher loadings. However, the BC samples were only from the lower-loaded part of the curve (< 3 μl), where the variation in the standard deviation is small and appears random. To calculate the uncertainty in the volume of benzene-d_6 which would be predicted from the NMR calibration curve (Figure A1.3), it is necessary to convert uncertainty in y into predicted uncertainty in x, x_p:

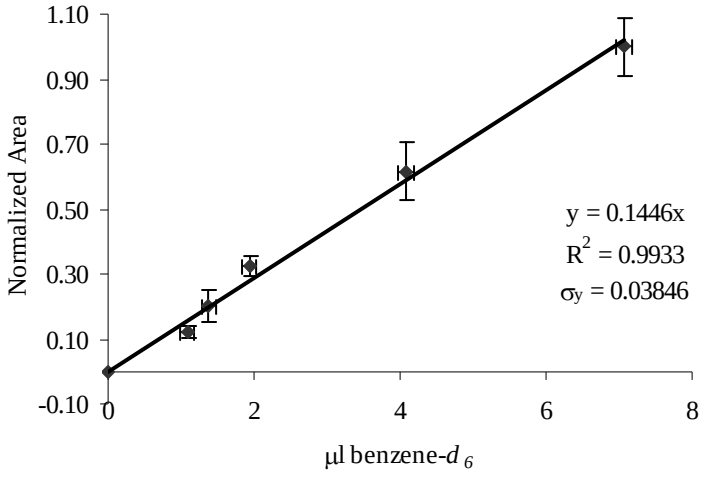

Figure A1.3. Calibration curve of neat benzene-d_6 versus the normalized NMR area for spectra acquired at 25°C and -75°C; y-error bars represent the standard deviation of the areas from replicate spectra of the flamed-sealed calibration standards; x-error bars were calculated with the 1.2% relative standard deviation of the measurement of the number of moles of benzene-d_6 contained within the manifold (Section A1.1.2).

$$y = (0.1446)x_p. \qquad \textbf{Eqn}.\ \text{A1.3}$$

$$\sigma_y = (0.1446)\sigma_{xp} \qquad \textbf{Eqn}.\ \text{A1.4}$$

$$\sigma_{xp} = \sigma_y/0.1446 = 0.03846/0.1446 = 0.26\ \mu\text{l}. \qquad \textbf{Eqn}.\ \text{A1.5}$$

Therefore, for benzene-d_6 volumes between 0.1-3 μl, the precision of benzene-d_6 loaded via the vapor deposition manifold into a given sample tube can be measured at less than $\pm$0.05 μl, although the accuracy of the volume of benzene-d_6 within a given sample tube can be confirmed with the NMR only to a precision of $\pm$0.25 μl. The error range for the loadings of benzene-d_6 specified for particular samples in the remainder of this dissertation will be reported as $\pm$0.1 μl.

A1.2.2 Plotting the sample areas on the NMR calibration curve

In order to confirm that the amount of benzene-d_6 within each sample tube was the amount which was loaded according to the vapor deposition manifold and in order to monitor changes over time in the amount of benzene-d_6 within the sample tube, NMR spectra for each sample containing benzene-d_6 on BC were obtained at 25°C using identical acquisition parameters to those used to construct the NMR calibration curve. The value of each area was normalized to the NMR area obtained at 25°C for the 7.07 μl sample, just as had been done for the calibration curve, and the normalized areas for the amount of benzene-d_6 on each BC sample was plotted (Figure A1.4) against the calibration curve. All the samples are below the calibration line, and most of them by more than the 0.26 μl uncertainty. Some possible causes for this deviation of benzene-d_6 mass within the sample tubes as predicted by the NMR quantitation curve are discussed below, and,

because the loss of NMR area appears to be sample dependent, additional discussion is included with the results sections for each BC.

Leakage of benzene vapor after sealing but before NMR data collection due to a poor seal is a possible cause. However, for most of the samples, quantitation spectra which were obtained at various ages do not show a trend of sample loss with time, which

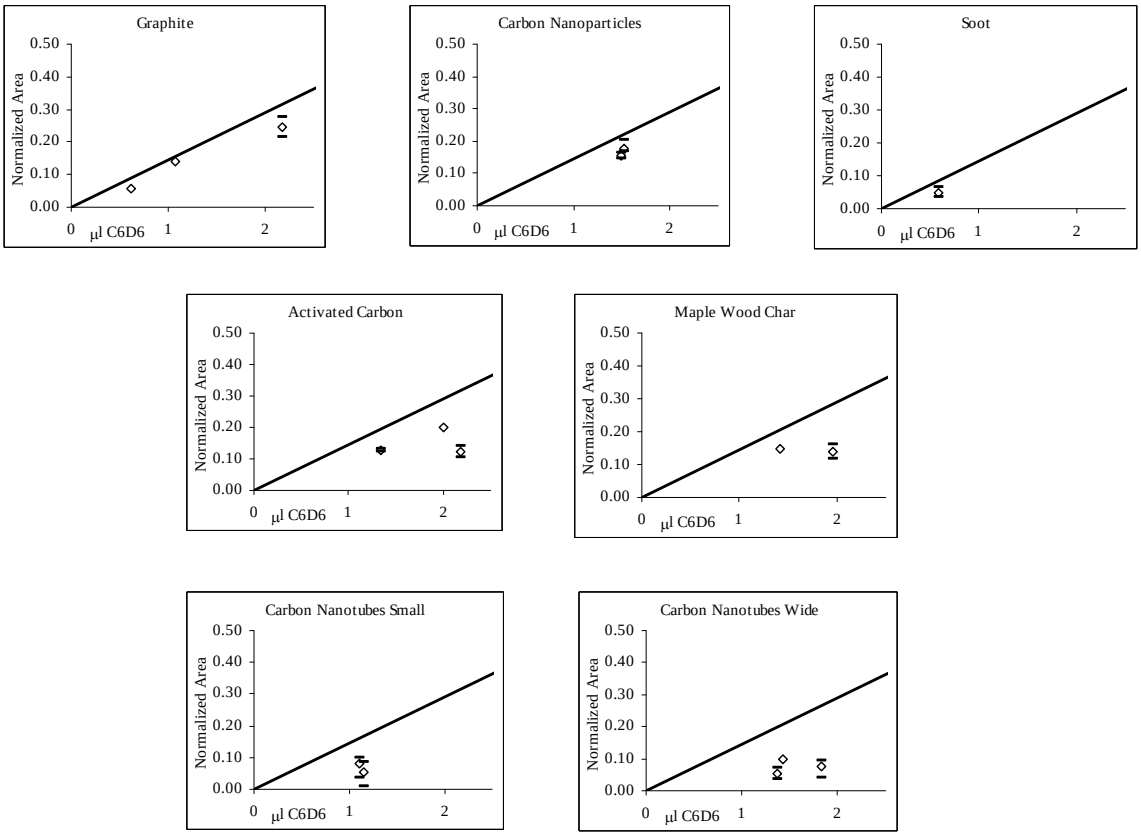

Figure A1.4. Normalized areas quantitation spectra for each solid phase plotted versus the calibration line for neat benzene-d_6. Open signal are average data points and solid lines above and below indicate the range from replicate spectra. See text for explanation.

one would expect if a leak were present. However, two of the samples, ActC2, an activated carbon sample, and MWC3, a maple wood char sample, showed a signal loss of 30% and 20% of the NMR area, which may indicate some leakage of

benzene-d_6 from the tubes. Another consideration is the fact that, because the sample tubes were longer than the NMR coil, almost all of the sample tubes included some benzene which was outside of the coil, and this may account for the below-calibration values. However, almost all of the sample tubes extended outside the 1 cm long coil at least somewhat, and yet many of the samples plotted very close to the line. In fact, in related studies performed in our laboratory on humic and fulvic acid samples using the same procedures, the large majority of samples fell directly *on* the line. Even among the BC samples, the quantitation behavior appears to sample dependent: specifically, replicate samples containing benzene-d_6 loaded onto the same solid phase tend to show a similar offset from the standard calibration line, whether near or far from the standard curve, whether the quantitation run was performed within a few hours or a few months of sample sealing. The top row of Fig 2.4 shows quantitation plots for replicate samples on the graphite, the carbon nanoparticles, and the soot samples, and all of these data points are close to the calibration line. For each individual sample, between one and three quantitation NMR spectra were collected, the open symbols indicating the average values and the lines indicating the upper and lower value. The middle row in Fig. 2.4 contains similar plots for activated carbon and maple wood char, and the calibration data for these solid phases are all a little further from the standard curve than were those in the top row. However, each of those plots include a sample which had lost benzene over time, as documented by a loss of NMR area observed for spectra collected under identical conditions at different ages, but using acquisition parameters other than those developed for the quantitation curve. Lastly, the quantities of benzene-d_6 on the carbon nanotubes according to the calibration curve (bottom row of Fig 2.4)

are well below the expected benzene quantities as compared to other solid phases. The fact that quantitative measurements for replicate samples of these same solid phases plot together indicates that the low signal obtained on the NMR quantitation run does NOT necessarily reflect a low amount of benzene, but is a function of the sample itself. It is interesting that the only quantitation runs that plot near the calibration line are samples of graphite, carbon nanoparticles, and soot, all of which provide an NMR peak which can be modeled as isotropic motion.

Possible reasons for the loss of signal in our samples may be considered: 1) surface relaxation due to the presence of paramagnetic impurities (although this should be less significant for quadrupolar nuclei than for dipolar nuclei [4], 2) accumulation of phase errors which occur during motional reorientational jumps, 3) echo attenuation due to exchange between phases, or 4) for the carbon nanotubes, an effect on the magnetic field experienced by the benzene-d_6 molecules due to the magnetic anisotropy of graphite and the circular orientation of the graphenic layers in the nanotubes. The occurrence of signal loss in static solid-state $_2$H NMR has been mentioned by previous workers [5, 6]. First, exchange from one physical environment to another with a different frequency can result in a shift change. Thus, when a spin returns to its original frequency, it is out-of-phase with the spins which did not undergo exchange, and this decreases the total signal at this frequency [5]. In our samples, even though all the deuterons are at the same frequency, the existence of separate exchanging populations with different motional modes could have the same effect. Second, echo attenuation at different temperatures is routinely used as an analytical tool to identify phase transition temperature [7]. This implies that one cannot expect the same deuteron count from samples that have different

motions, even if they actually contain the same number of deuterons. Finally, in their explanation for modeling the isotropic motion using a solids instrument, Xiong and Maciel [8] refer to the difficulty of direct deuteron counting.

> . . . counting the number of deuterons that experience different types of motions in a system requires simulations of all of the types of motions present in the system, because the integrated intensity associated with each line shape depends strongly on the correlation time(s) of the corresponding dynamic processes. **One cannot simply use integrated areas for spin counting of deuterons, if the motion is in an 'intermediate' range** (emphasis added).

By "intermediate", the authors are describing samples in which at least two motional modes exist in appreciable fractions, and with substantial exchange between those populations occurring.

In summary, the standard curve was obtained from spectra of benzene-d_6 molecules which all existed in the same phase (all solid or all liquid). However, the spectra of the samples involves adsorbed benzene-d_6 which can accelerate dephasing [6]. Thus, the liquid benzene from which the calibration curve was constructed may not be quantitatively comparable on the NMR to a sample of an equal amount of adsorbed benzene on a given solid phase. Notwithstanding these difficulties in sample quantitation, use of the curve is helpful to identify samples that may have lost some benzene after sealing, such as ActC2, to estimate the amount of that loss, and to identify samples with unusual characteristics that interfere with the amplitude of the NMR signal (such as the CNW samples).

A1.3 NOTE ABOUT LEAST-SQUARES FITTING PROCEDURES

All of the above linear least-squares fits, as well as other linear least-square fits shown in subsequent chapters of the dissertation (particularly the Arrhenius plots) were performed using the ordinary least-squares fitting method as detailed in

Skoog and West [2]. Calculated values for the slope of the line, the Pearson correlation coefficient (R^2), and the standard deviation in *y* were verified using Excel. The values of the standard deviation of the slope, which were calculated only as per Skoog and West [2], were used to calculate the error range for the Arrhenius activation energies.

References

1. Brothers, L. C.; Lei, H.; Eastman, M. A.; Nanny, M. A., Molecular motion of adsorbed benzene on humic acid. *Abstracts of Papers, 227th ACS National Meting, Anaheim, CA, United States, March 28-April 1, 2004* **2004**.
2. Skoog, D. A.; West, D. M., *Fundamentals in Analytical Chemistry, 4th Edition*. CBS College Publishing: New York, New York, 1982; p 859 p.
3. Barrow, G. M., *Physical Chemistry, 5th Ed.* McGraw-Hill Book Co.: New York, NY, 1988; p 859 p.
4. Levitt, M. H., *Spin Dynamics: Basics of Magnetic Resonance*. John Wiley & Sons: West Sussex, England, 2001; p 686 p.
5. Sanders, J. K. M.; Hunter, B. K., *Modern NMR Spectroscopy: a Guide for Chemists*. Oxford University Press: New York, 1987; p 308 p.
6. Duer, M. J., *Introduction to Solid-State NMR Spectroscopy*. Oxford Press: Oxford, U.K., 2004.
7. Ok, J. H.; Vold, R. R.; Vold, R. L.; Etter, M. C., Deuterium nuclear magnetic resonance measurements of rotation and libration of bezene in a solid-state cyclamer. *Journal of Physical Chemistry B* **1989,** *93*, 7618-7624.
8. Xiong, J.; Maciel, G. E., Deuterium NMR studies of local motions of benzene adsorbed on Ca-montmorillonite. *Journal of Physical Chemistry B* **1999,** *103*, 5543-5549.

A2. DEUTERIUM FITTING PROGRAM (DFP)

The following provides a brief explanation of the application of the Deuterium Fitting Program per Eastman and Nanny [1], including copies of input and output files (1) for the generation of libraries of simulated spectra in the Library Creation Program (LCP) and Deuterium Motional Simulation (DMS) modules and (2) for the fitting of experimental spectra to simulated spectra from the created libraries in the Deuterium Fitting Program (DFP) module. Complete details are available at the website http://chem.okstate.edu/~dfp.

A2.1. LIBRARY CREATION PROGRAM

The basic procedure for creating a library using the LCP and DMS modules of DFP will be explained briefly below, using as an example a large-angle wobble (LAW) motion illustrated in Figure A2.1 below.

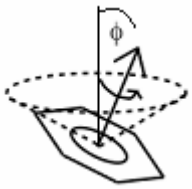

Figure A2.1 Diagrammatic illustration of LAW. ϕ is the angle between vertical and the C_6 axis, and, in the 10-site model, ϕ occupies 6 sites around the outer cone (dashed line), 3 sites around a half-cone (not displayed), and 1 site for ϕ = 0.

The input file for the generation of one library using LCP and DMS is shown below. For the input motion, in addition to a 48° LAW motion (Frame 1), an independent C_6 rotation is included in the modeled motion (Frame 2), and this C_6

motion is specified as a C_3 rotation because the simulated spectra are identical [1, 2]. As explained in Section 1.2.1, the Principle Axis System (PAS) refers to a coordinate system specific to the deuteron(s) in the molecule, and, for benzene-d_6, this system is oriented with the *z*-axis along the C-D bond, the *y*-axis parallel to the molecule's C_6 axis, and the *x*-axis within the molecular plane. The initial PAS orientation relative to LAB aligns the *z*-axis of the PAS with the static magnetic field of the instrument, B_0. The molecular motion is described as jumping between sites, which are specified by a final set of Euler angles (after the molecule has been rotated through the Euler angles specified in the input, e.g., 48° wobble with C_6 rotation) for the PAS relative to the laboratory framework (LAB). For each site, LCP calculates a transformation of the PAS through the Euler angles listed in the input file to a final set of Euler angles, and these final Euler angles (from PAS to LAB) define one jump site for the molecule's motion. In order to accurately describe the molecular motion, the reader must accurately describe the Euler angles, and Section A2.2 (below) describes one method for this. The example library shown below will consist of 4 simulated spectra with the ranges of jump rate for each frame as listed.

```
Library_Name: BDLAWc101b
System_name: benzene
Model_name: LAWc101b
Quadrupole_omega_Q(kHz): 183.00
Quadrupole_eta: 0.04
Number_of_sites: 30
Number_of_frames: 2
Number_of_sites_in_1_frame: 10
Number_of_sites_in_2_frame: 3
First_angle_set1: 0.0 0.0 0.0
First_angle_set2: 0.0 24.0 0.0
First_angle_set3: 120.0 24.0 240.0
First_angle_set4: 240.0 24.0 120.0
First_angle_set5: 0.0 48.0 0.0
```

First_angle_set6: 60.0 48.0 300.0
First_angle_set7: 120.0 48.0 240.0
First_angle_set8: 180.0 48.0 180.0
First_angle_set9: 240.0 48.0 120.0
First_angle_set10: 300.0 48.0 60.0
Second_angle_set1: 0.0 90.0 90.0
Second_angle_set2: 120.0 90.0 90.0
Second_angle_set3: 240.0 90.0 90.0
Perform_corrections(1)_or_ideal(0): 1
Number_of_pw90_values: 1
pw90_1: 2.25
Number_of_tau_values: 1
tau_1_microsec: 40.0
Vary_angle?_1_for_yes(0_for_no): 0
Kinetic_Mode: 2
Number_of_kinetic_matrices_frame_1: 2
Number_of_kinetic_matrices_frame_2: 2
minrate_first_angle_set: 8000.0
maxrate_first_angle_set: 40000.0
minrate_second_angle_set: 5000000.0
maxrate_second_angle_set: 500000000.0
Powder_Average_Method(1_is_Conroy): 1
Number_of_angles_in_the_powder_average: 1154
p1: 121
p2: 459
Number_of_points_in_the_FID: 4096
Dwell_time_for_FID_microsec: 2.0
Weighting_function_typeG0E1: 1
Weighting_function_parameter(kHz): 1.0

A2.2. VISUALIZATION OF MODELED MOTION: EULER ANGLES AND STEREONET PROJECTION

A stereonet can be employed to a manipulate a plane in three-dimensional space, including features imbedded in the plane [3]. Thus, the final PAS Euler angles can be determined using the stereonet and verified with the final output angles provided by LCP, and the user can be assured that the Euler angles input describe the desired motion. Because of the challenge of illustrating an out-of-plane rotation, such as a wobble motion, a lower hemisphere stereonet representation is employed below for only 1 of the 30 sites occupied by the benzene molecule during a LAW motion as defined by

the Euler angles $(\alpha,\beta,\gamma) = (120^o,48^o,240^o)$ for Frame 1 and $(\alpha,\beta,\gamma) = (0^o,90^o,90^o)$ for Frame 2. Figure A2.2 (see next page) demonstrates the use of a stereonet to perform these Euler angle rotations on a benzene molecule. Whenever the molecule is executing two independent motions, the first motion involves the reorientation of the molecule itself away from an original "crystallite" orientation, and the second motion cannot involve any other actual physical change in the molecular orientation, but only reorientation of the molecular axes. The first six frames of Figure A2.2 rotate the molecule itself through the first set of Euler angles for this site $(\alpha,\beta,\gamma) = (120^o,48^o,240^o)$. The last two frames of Figure A2.2 rotate the molecule through the Euler angles $(\alpha,\beta,\gamma) = (0^o,90^o,90^o)$, which places the molecule in the first of three C_6 rotation positions. Note that the second set of Euler angles can be accomplished by rotation of the axes *only* and do not involve any additional out-of-plane reorientations. Additionally, the second set of Euler angles results in the proper PAS position of the quadrupole tensor within the molecule, that is z_{EFG} (along the C-D bond) > y_{EFG} (through the aromatic π electrons) > x_{EFG} (bisecting the C-C bonds in the molecular plane). The final PAS position is the same as that calculated by DFP $(\alpha,\beta,\gamma) = (8.8, 68.2, 46.1)$, including motions through both Frames 1 and 2, as shown by Figure A2.3.

Now that the rotations for one site have demonstrated that orientations of the axes for the PAS can be obtained by direct rotation of the coordinate system through the Final Euler Angles produced by DMS using the stereonet display, it can be seen that the motion of the molecular plane through all of the sites in the motion can be mapped by plotting the coordinates of that axis which is the normal to the plane (the *y*-axis of the PAS). Such a stereonet map is shown in the last frame of Figure A2.3 for 11 of the 30

sites of the LAW motion (only some of the 48° wobble-angle sites were mapped). These sites form a ring around the center. Sites 13, 14, and 15 all have the Frame 1 coordinates of (0,48,0) and, therefore, plot nearly on top of one other on the horizontal axis of the stereonet. Because these locations were plotted by doing stereonet rotations within PowerPoint and then cutting and pasting the very large location dots directly onto this "map" stereonet, the location of the points could be more precise. The associated inner-angle sites would plot closer to the center and would also have a circular distribution. Because the *z*-axis of the molecule corresponds to the *y*-axes of the PAS, the points plotted correspond to the normals of the benzene's molecular plane.

A2.3 FITTING OF EXPERIMENTAL SPECTRA

After collecting the NMR data, transforming the spectrum, and performing the phase corrections, the experimental spectrum is saved as an ascii file, which is then converted within the CONV module of DFP to the proper form in a file with the ending "_c". The fitting input file is then prepared in order to direct the program to the appropriate experimental spectral file and use the desired libraries in the fitting. The amplitude of the experimental spectrum is compared at each frequency data point of every simulated spectrum in the library, and the match which gives the lowest R value (the sum of the squares of the differences between the simulation and the experimental values, averaged over the number of data points in the spectrum) is selected. In addition, fitting to combinations of motional models (more than one library) can be accomplished and the results give the percentages of that motion as well as the simulation values from each library. A sample input is shown below.

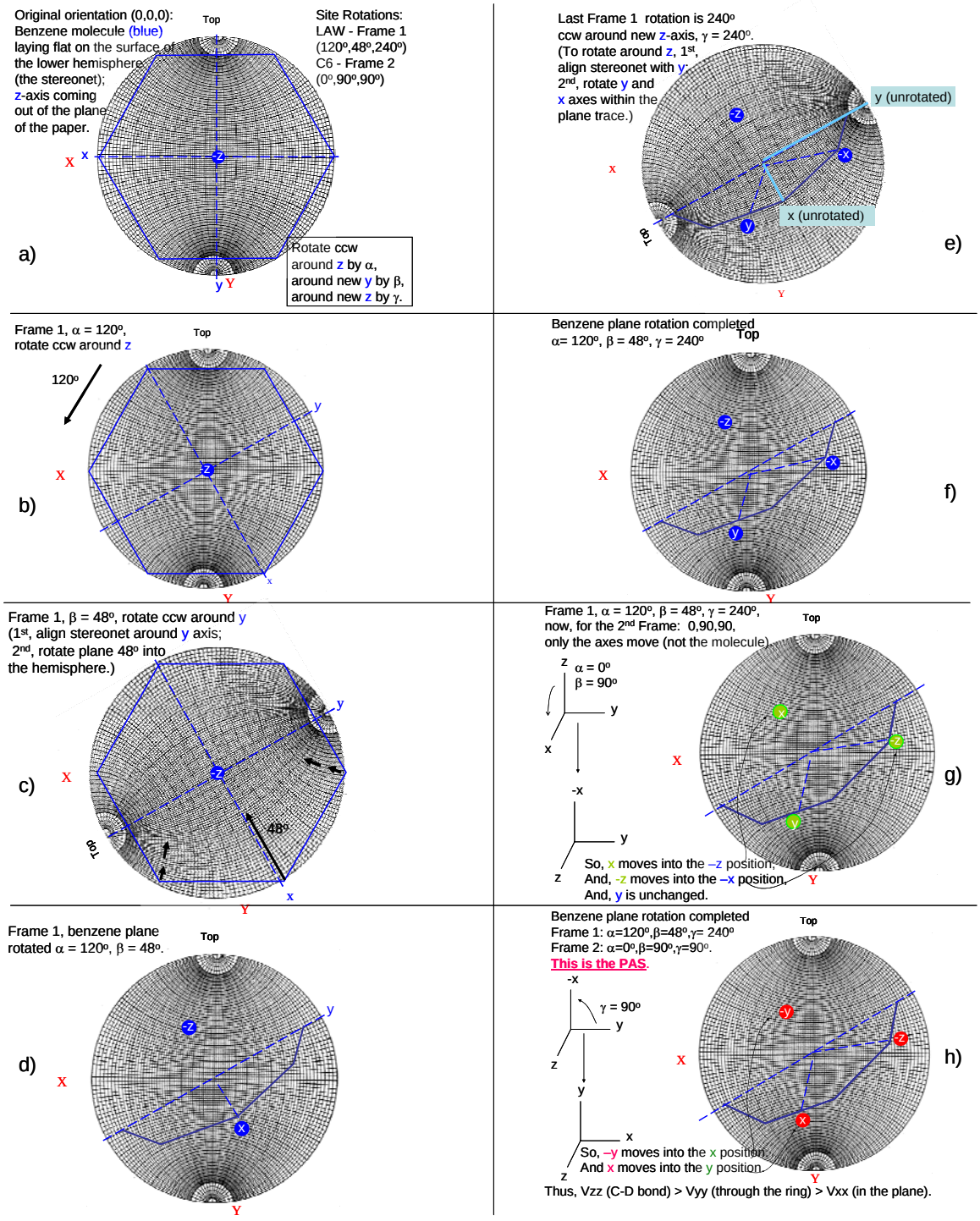

Figure A2.2 Step-by-step rotation of a benzene molecule rotated in a) to f) through the Euler angles of Frame 1, in which the molecule moves relative to the original crystallite orientation within the instrument's static magnetic field, B_0; and then in g) and h), through the Euler angles of Frame 2, in which only the *x*-,*y*-, and *z*-axes change orientations relative to one another.

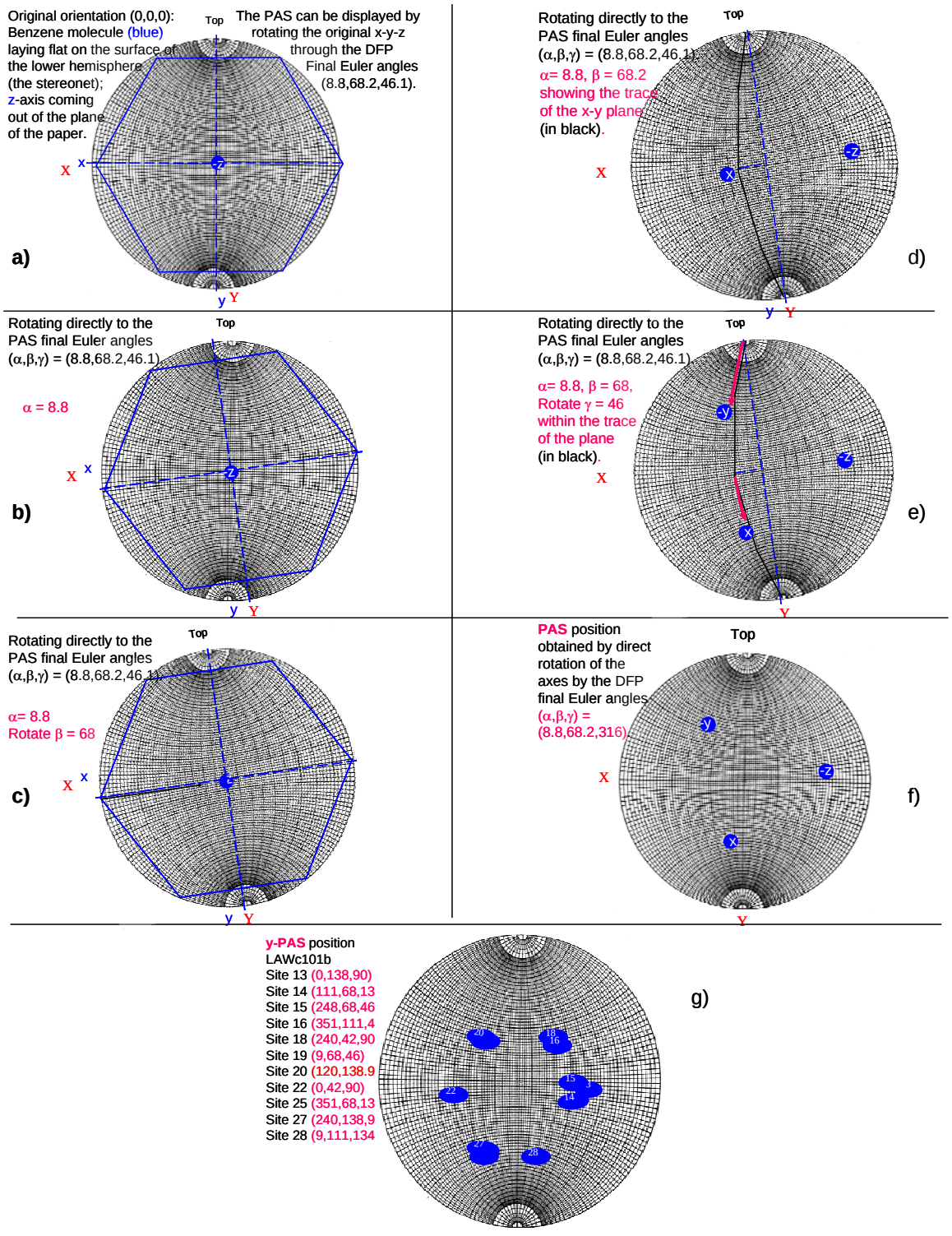

Figure A2.3 Sections a-f) display step-by-step rotations of the *x*-,*y*-, and *z*-axes of the original crystallite orientation through the Final Euler Angles to the PAS; g) maps the normals of the benzene plane (*y*-axes of the PAS) for 11 sites of the LAW motion. Note that the f) section of Figure A2.3 is identical to the f) section of Figure A2.2, as should be.

Number_of_libraries: 3
Name_of_library1: BDSAWc10_40m
Name_of_library2: BDLAWc13_40m
Name_of_library3: BDISOicoc102m
Number_of_spectra_to_fit: 1
Name_of_this_Calculation: ActC2_4k1k_ILS
Output_filename: fitDFP_ActC2_4k1k_ILS
Verbose(1_for_long_output): 0
number_of_points_in_data: 4096
number_of_points_to_output: 3200
Fitting_method(2=syst,4=SA): 2
Make_ave(0=no): 0
Calc_sigmR(0=no): 0
INPUT_FOR_SPECTRUM_1:
File_name_of_spectrum: ActC2_RT2040_081505_4k1k.asc40u_c
90_degree_pw: 2.25
Tau: 40.0
Number_of_libraries_to_use: 3
Library_Number: 1
Library_Number: 2
Library_Number: 3
Calc_sigma(0)_OR_set_sigma_1(1): 0
variable_name: SAW_spec
variable_type(0_position_in_spectral_lib): 0
library_number: 1
variable_name: SAW_prct
variable_type(1_percent_of_spectrum): 1
library_number: 1
variable_name: LAW_spec
variable_type(0_position_in_spectral_lib): 0
library_number: 2
variable_name: LAW_prct
variable_type(1_percent_of_spectrum): 1
library_number: 2
variable_name: ISO_spec
variable_type(0_position_in_spectral_lib): 0
library_number: 3
variable_name: ISO_prct
variable_type(1_percent_of_spectrum): 1
library_number: 3

After completion of the fit run, an output file is generated, shown below. Using Excel or a similar program, the experimental and simulated amplitude values for each

frequency can be used to construct figures that display the spectrum and its fitted simulation, as shown in Figure A2.4 below.

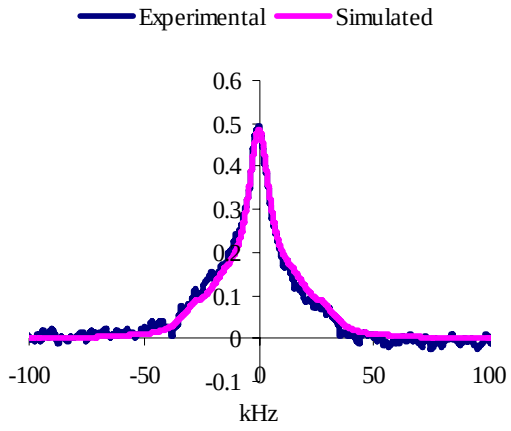

Figure A2.4 Experimental and simulated ^{2}H static solid-state NMR spectrum

The file below details all of the information about the above fits. The fit consists of 0.33% of the SAW spectrum shown below (jump rate 5 x 10^{3} rad/s, a wobble angle of 22°, and a C6 jump rate of 1.58 x 10^{7} rad/s), 97.17% of the LAW spectrum (jump rate 2.92 x 10^{4} rad/s, a wobble angle of 44°, and a C6 jump rate of 3.98 x 10^{6} rad/s), and 2.5% of the ISO spectrum (jump rate 1.89 x 10^{5} rad/s).

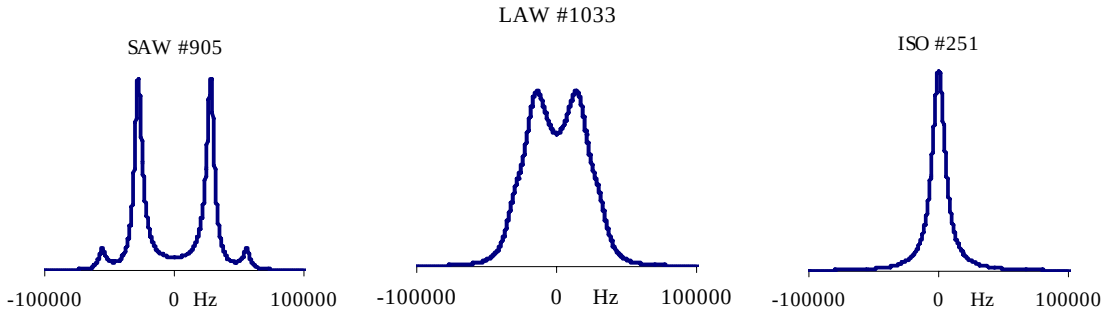

Figure A2.5. Particular simulated spectra selected by DFP as the components of the experimental spectrum fitted above in Figure A2.4.

Below is a copy of the output fit file.

Fri Aug 17 00:41:06 2007
DFP Version 28e
Name of this Calculation: ActC2_4k1k

Short Output (verbose=0)
"Number of Points in the X,Y Data: 4096 "
Maximum Number of Libraries Used: 3
Number of Spectra Fit in this run: 9
OUTPUT FOR LIBRARY 1: BDSAWc10_40m
"Library Type(1=MXQET,0=DMS): 0"
Number of spectra in this library: 1100
SYSTEM parameters for benzene system:
e^2qQ/h (kHz) 183.000000 Eta 0.040000
Kinetic Mode: -2
First Frame Range of Rates: 5000 to 1e+06
Second Frame Range of Rates: 1e+06 to 5e+08
MODEL parameters for SAWc10_40m model:
Total number of sites: 30
Angle Set 1 (10 sites):
0 0 0
0 12 0
120 12 240
240 12 120
0 24 0
60 24 300
120 24 240
180 24 180
240 24 120
300 24 60
Angle Set 2 (3 sites):
0 90 0
120 90 0
240 90 0
Angle varied is number 2 in set 1
Angle takes on 11 values:
4
6
8
10
12
14
16
18
20
22
24
ACQUISITION and PROCESSING parameters:
Dwell time (us): 2
Spectral width (kHz): 500
Number of Points Calculated: 0 Points in Spectrum: 4096

Tau1 1 (us): 40
Exponential weighting used with parameters (kHz):
Exponential: 1.000000
CALCULATION parameters:
Number of angles in the powder average: 1154
Corrected Calculation
Pulse Width 1 (us): 2.25
OUTPUT FOR LIBRARY 2: BDLAWc13_40m
"Library Type(1=MXQET,0=DMS): 0"
Number of spectra in this library: 1100
SYSTEM parameters for benzene system:
e^2qQ/h (kHz) 183.000000 Eta 0.040000
Kinetic Mode: -2
First Frame Range of Rates: 5000 to 1e+06
Second Frame Range of Rates: 1e+06 to 5e+08
MODEL parameters for LAWc13_40m model:
Total number of sites: 30
Angle Set 1 (10 sites):
0 0 0
0 22 0
120 22 240
240 22 120
0 44 0
60 44 300
120 44 240
180 44 180
240 44 120
300 44 60
Angle Set 2 (3 sites):
0 90 0
120 90 0
240 90 0
Angle varied is number 2 in set 1
Angle takes on 11 values:
26
27.8
29.6
31.4
33.2
35
36.8
38.6
40.4
42.2
44
ACQUISITION and PROCESSING parameters:

Dwell time (us): 2
Spectral width (kHz): 500
Number of Points Calculated: 0 Points in Spectrum: 4096
Tau1 1 (us): 40
Exponential weighting used with parameters (kHz):
Exponential: 1.000000
CALCULATION parameters:
Number of angles in the powder average: 1154
Corrected Calculation
Pulse Width 1 (us): 2.25
OUTPUT FOR LIBRARY 3: BDISOicoc17m
"Library Type(1=MXQET,0=DMS): 0"
Number of spectra in this library: 400
SYSTEM parameters for benzene system:
e^2qQ/h (kHz) 183.000000 Eta 0.000000
Kinetic Mode: -1
First Frame Range of Rates: 50000 to 1e+07
Second Frame Range of Rates: 0 to 0
MODEL parameters for ISOicom2 model:
Total number of sites: 32
Angle Set 1 (32 sites):
0 0 0
0 37.377368 0
120 37.377368 240
240 37.377368 120
60 41.810315 300
180 41.810315 180
300 41.810315 60
22.238756 70.528779 337.761244
97.761244 70.528779 262.238756
142.23875 70.528779 217.761244
217.76124 70.528779 142.238756
262.23875 70.528779 97.761244
337.76124 70.528779 22.238756
60 79.187683 300
180 79.187683 180
300 79.187683 60
0 100.812317 0
120 100.812317 240
240 100.812317 120
37.761244 109.471221 322.238756
82.238756 109.471221 277.761244
157.76124 109.471221 202.238756
202.23875 109.471221 157.761244
277.76124 109.471221 82.238756
322.23875 109.471221 37.761244

0 138.189685 0
120 138.189685 240
240 138.189685 120
60 142.622632 300
180 142.622632 180
300 142.622632 60
0 180 0
Angle Set 2 (0 sites):
No Angle is varied
ACQUISITION and PROCESSING parameters:
Dwell time (us): 2
Spectral width (kHz): 500
Number of Points Calculated: 0 Points in Spectrum: 4096
Tau1 1 (us): 20
Tau1 2 (us): 40
Exponential weighting used with parameters (kHz):
Exponential: 1.000000
CALCULATION parameters:
Number of angles in the powder average: 1154
Corrected Calculation
Pulse Width 1 (us): 2.25
"Method of fitting is Classic Simulated Annealing, varying only spectral numbers"
Number of Variables in the Fit: 6
Number of Libraries used in the Fit of Spectrum 1: 3
Names of the Libraries:
Lib No: 1 Name: BDSAWc10_40m
Lib No: 2 Name: BDLAWc13_40m
Lib No: 3 Name: BDISOicoc17m
Calculation of the asymmetry standard deviation:
Fitting of the 1 -th spectrum:
Pw90 (us) for library 1: 2.250000
Tau (us) for library 1: 40.000000
Min Spectral Number for library 1: 1
Max Spectral Number for library 1: 1100
Angle varied is number 2 in angle set 1
Pw90 (us) for library 2: 2.250000
Tau (us) for library 2: 40.000000
Min Spectral Number for library 2: 1
Max Spectral Number for library 2: 1100
Angle varied is number 2 in angle set 1
Pw90 (us) for library 3: 2.250000
Tau (us) for library 3: 40.000000
Min Spectral Number for library 3: 201
Max Spectral Number for library 3: 400
Only spectral number variables will vary in SA

T Reduced According to a Simple Curve
T Curve Parameter: 0.950000
Inital Acceptance Ratio: 0.950000
Stop Criterion for R: 1.000000e-07
Number of repeats of SA input: 20
Starting Control Parameter: 0.0324648
Initial ranges of the variables:
SAW_spec Min: 1 Max: 1100
LAW_spec Min: 1 Max: 1100
ISO_spec Min: 201 Max: 400
Total Number of Fitting Steps Taken: 2000000
Total Number of SA Repeats: 20
Final Value of R: 0.000378276
OVERALL BEST FIT of the 2000 BEST:
R = 0.000378276
Coefficient: 6.019308 and Spectrum number from library 1: 905
Pw90 (us) for library 1: 2.250000
Tau (us) for library 1: 40.000000
Angle varied is number 2 in angle set 1
Varied Angle Value: 22.000000
Kinetic rates for library 1 (rad/s): 5000 1.58E+07
Coefficient: 1778.786282 and Spectrum number from library 2: 1033
Pw90 (us) for library 2: 2.250000
Tau (us) for library 2: 40.000000
Angle varied is number 2 in angle set 1
Varied Angle Value: 44.000000
Kinetic rates for library 2 (rad/s): 29240.2 3.98E+06
Coefficient: 45.711804 and Spectrum number from library 3: 251
Pw90 (us) for library 3: 2.250000
Tau (us) for library 3: 40.000000
Kinetic rates for library 3 (rad/s): 189286 0
Chi^2(N+A): 153.127 Q(N+A): 1 nu: 584
Single Best Fit to Experimental Spectrum 1:
ActC2_RT2040_081505_4k1k.asc40u
"Values of X, Yexp, and Ycal: "
250 -0.006528 -0.000005
249.8779 -0.005778 -0.000005
249.7558 -0.004842 -0.000005
249.6337 -0.004062 -0.000005
249.5116 -0.003666 -0.000005
249.389499 -0.003822 -0.000005
249.267399 -0.004583 -0.000005
-249.145299 -0.01409 -0.000005
-249.267399 -0.01372 -0.000005
-249.389499 -0.012705 -0.000005
-249.5116 -0.011013 -0.000005

-249.6337 -0.01409 -0.000005
-249.7558 -0.01372 -0.000005
-249.8779 -0.012705 -0.000005
-250 -0.011013 -0.000005
Total time taken for calculation: 1400.000000
FITTING SUMMARY TABLES
OVERALL BEST FITS
Spectrum Tau pw90 R
ActC2_RT2040_081505_4k1k.asc40u 40 2.25 3.78E-04
Spectrum nu Sigma_N chi^2(N) Q(N) Sigma_(N+A)Ave chi^2(N+A) Q(N+A)
ActC2_RT2040_081505_4k1k.asc40u 584 1.15E-02 1.70E+03 0.00E+00 3.45E-02 1.53E+02 1.00E+00
Library Number 1: BDSAWc10_40m
Rate units are: rad/s
Spectrum Coef Error Percent Error Angle Error Rate 1 Error Rate 2 Error
ActC2_RT2040_081505_4k1k.asc40u 6.02 6.04 0.33 0.33 22 2 5.00E+03 4.01E+03 1.58E+07 1.57E+07
Library Number 2: BDLAWc13_40m
Rate units are: rad/s
Spectrum Coef Error Percent Error Angle Error Rate 1 Error Rate 2 Error
ActC2_RT2040_081505_4k1k.asc40u 1778.79 6.04 97.17 0.65 44 1.8 2.92E+04 2.34E+04 3.98E+06 3.96E+06
Library Number 3: BDISOicoc17m
Rate units are: rad/s
Spectrum Coef Error Percent Error Angle Error Rate 1 Error Rate 2 Error
ActC2_RT2040_081505_4k1k.asc40u 45.71 6.04 2.5 0.33 0 0 1.89E+05 5.11E+03 0.00E+00 0.00E+00

References

1. Eastman, M. A.; Nanny, M. A., Fitting of deuterium quadrupole echo spectra with multiple motional models. *Journal of Magnetic Resonance* **2007,** *184*, 302-314.
2. Ok, J. H.; Vold, R. R.; Vold, R. L.; Etter, M. C., Deuterium nuclear magnetic resonance measurements of rotation and libration of bezene in a solid-state cyclamer. *Journal of Physical Chemistry B* **1989,** *93*, 7618-7624.
3. Spencer, E. W., *Introduction to the Structure of the Earth*. McGraw-Hill, Inc.: New York, NY, 1977; p 640.

A3. STATIC SOLID-STATE ^{2}H NUCLEAR MAGNETIC RESONANCE (NMR) QUANTITATION FOR BENZENE-d_6 ON CARBON NANOTUBE (CNT) AT DIFFERENT AGES: SPECTRA WITH NMR AREAS

Each of the figures below displays spectra collected at nearly the same ages with the same instrumental parameters and are, unless otherwise noted, displayed with the same vertical scale within each figure for quantitative comparison. The experimental spectra are also overlain by a simulated fit from the ISO library.

A3.1 CNS SAMPLES

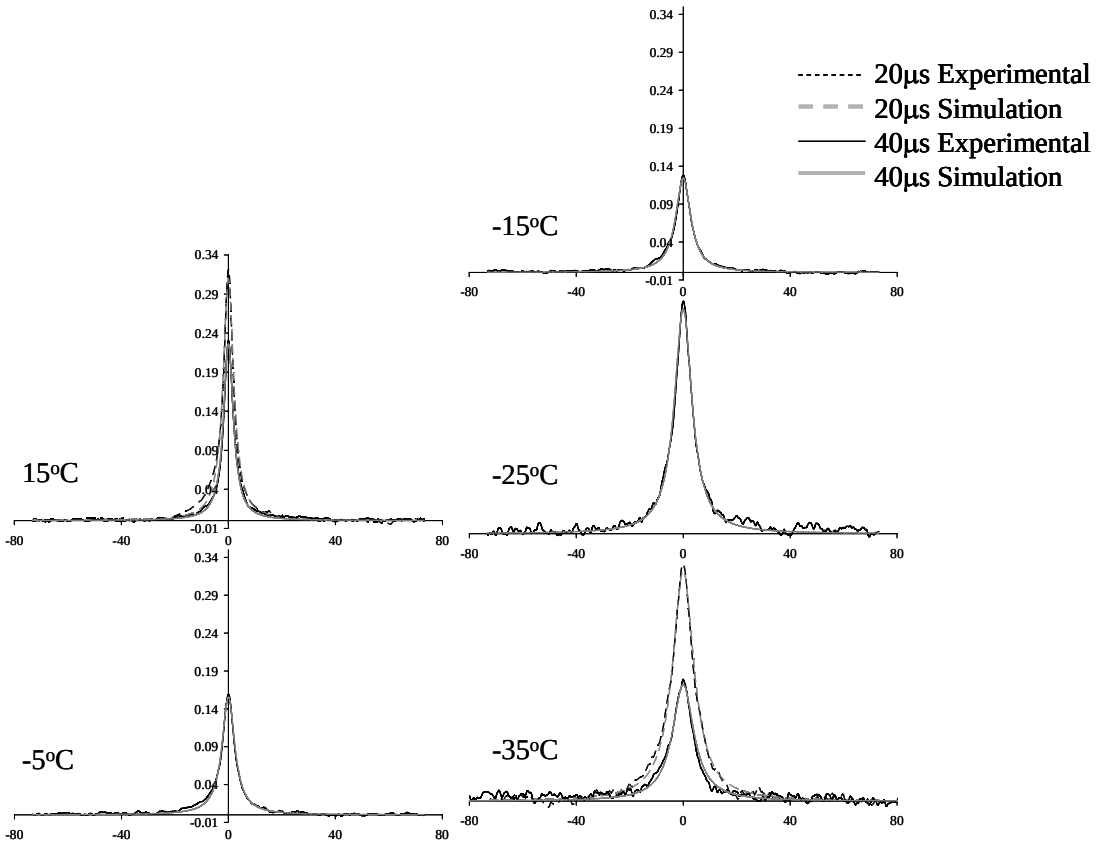

Figure A3.1 Sample CNS1, aged 1-2 days, experimental and ISO simulated spectra; spectra with *y*-axis were collected with 21600 scans; -25°C 14400 scans; -35°C 7200 scans.

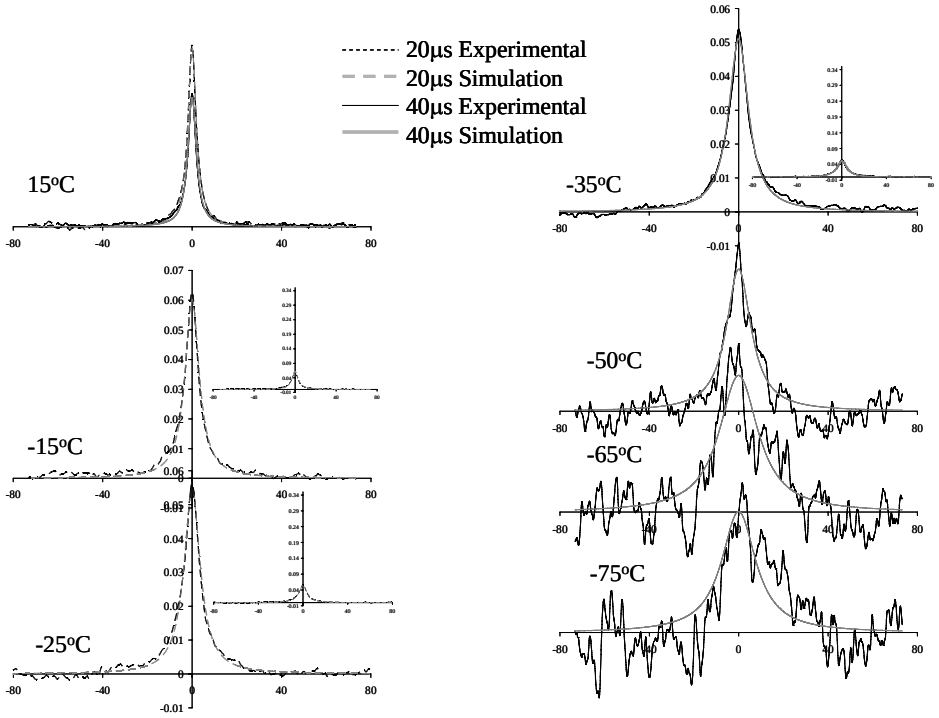

Figure A3.2. Sample CNS1, aged 77-119 days, experimental and ISO simulated spectra; spectra with *y*-axis were collected with 21600 scans; 15°C 7200 scans; -50°C, -65°C, -75°C, 3600 scans.

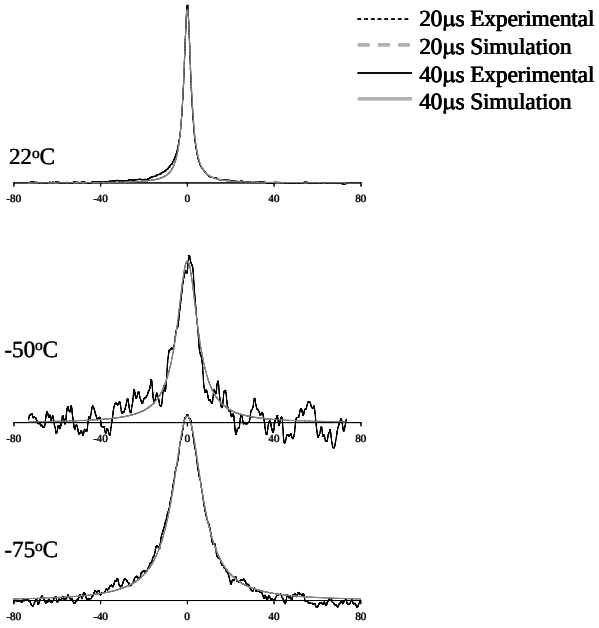

Figure A3.3. Sample CNS1, aged 164-254 days, experimental and ISO simulated spectra; 22°C 86400 scans; -50°C 30528 scans, -75°C 57600 scans.

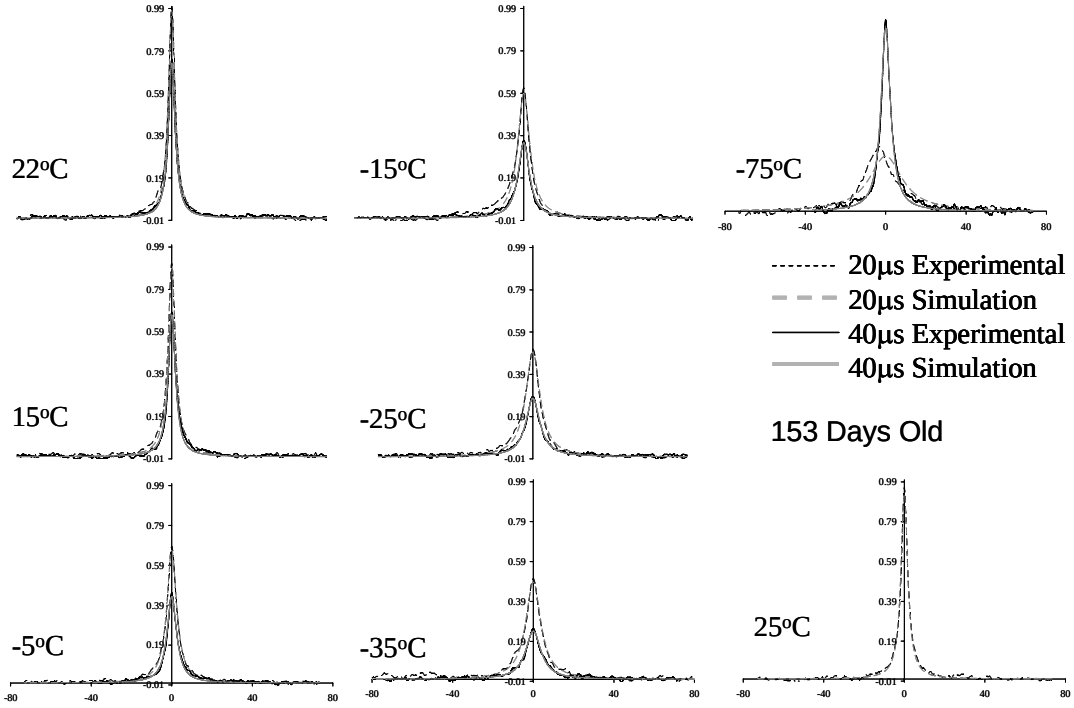

Figure A3.4. Sample CNS3 samples aged 1-2 days, except as noted; all spectra 7200 scans except -75ºC 3600 scans.

Table A3.1. CNS pseudo-ISO peak widths at half-height, δν (±1kHz), for spectra at different ages with 40µs τ_{echo} processed with 1 kHz line broadening

Sample	Temp (C)	Ages		
CNS1		Days 2-3	Days 77-119	Days 164-259
	22			4478[e]
	15	4763[a]	5819[c]	
	-5	6513[a]		
	-15	7705[a]		
	-25	9246[b]		
	-35	10957[c]		
	-50		13100[d]	12743[d]
	-75			19063[d]
CNS3		Days 1-11		
	22	4112[c]		
	15	4443[c]		
	-5	6180[c]		
	-15	7173[c]		
	-25	8715[c]		
	-35	10429[c]		
	-75	38546[d]		

[a]21600 scans; [b]14400 scans; [c]7200 scans; [d]3600 scans
[e]86400 scans; [f]30528 scans; [g]57600 scans.

Table A3. 2. CNS peak areas at different ages from static solid-state ^{2}H NMR spectra, collected with 21,600 scans using 40μs τ_{echo} processed at 1 kHz line broadening

Sample	Temp (C)	Ages[a]
CNS1		Days 2-3
	15	36.2
	-5	31.4
	-15	27
CNS3		Days 1-11
	22.5	12.8
	15	12
	-5	11.2
	-15	10
	-25	9.4
	-35	9.2

[a]Spectra were not collected using 21,600 scans and 40μs τ_{echo} values for times later than 3 days, although data was collected under other conditions for up to 259 days. Those data show comparable values (1.4 and 1.3) at different ages (days and 77 days, respectively) for the 20/40μs peak area ratio for spectra collected at the same temperature, 15°C, indicating no loss of benzene over time. However, the decrease in signal area with temperature points to the occurrence of a phase change over these temperatures.

A3.2 CNW SAMPLES

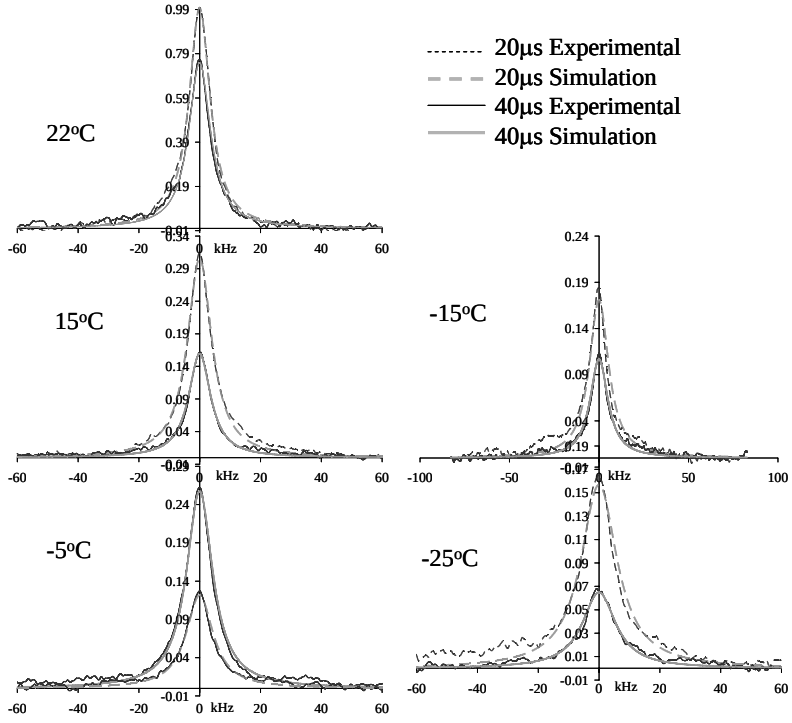

Figure A3.5. CNW2 samples aged 1-4 days; all spectra 21600 scans except 40 μs -25°C, which used 13096 scans.

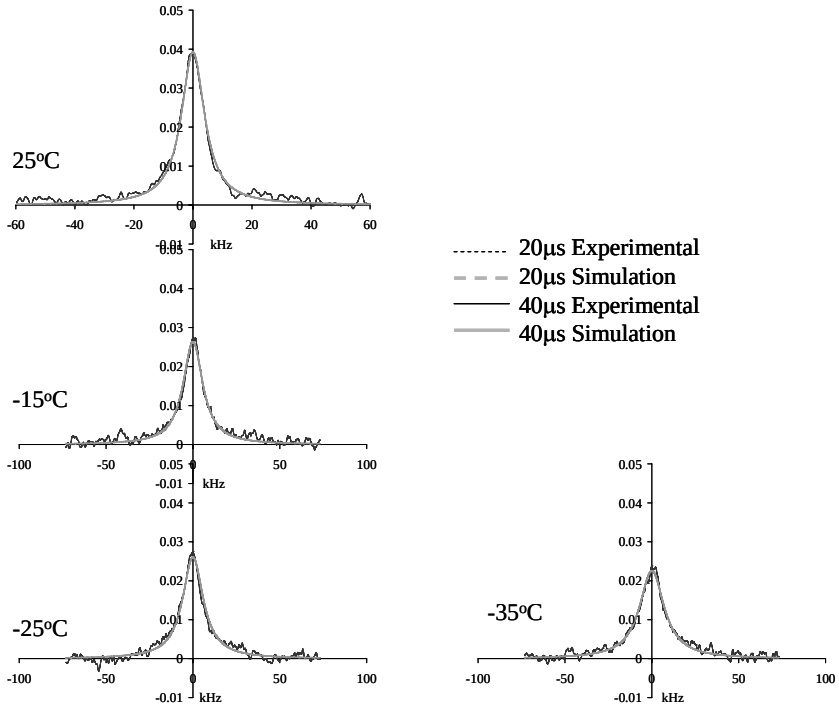

Figure A3.6. CNW2 samples aged 80-81 days; all spectra 21600 scans.

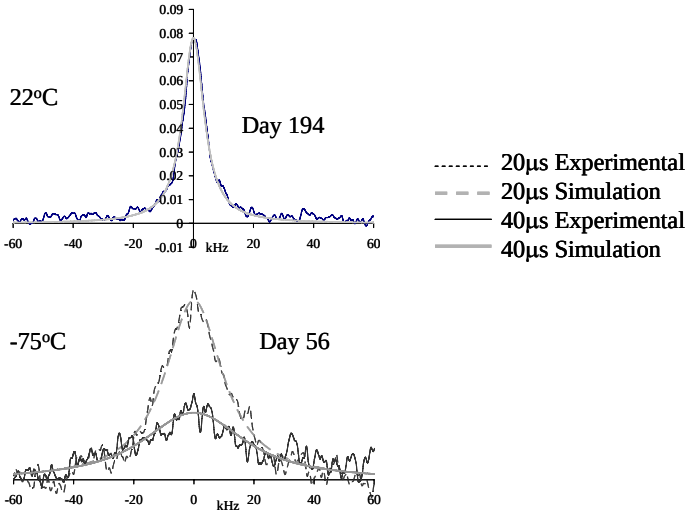

Figure A3.7. CNW2 samples ages listed; 22°C 21600 scans; -75°C 3600 scans.

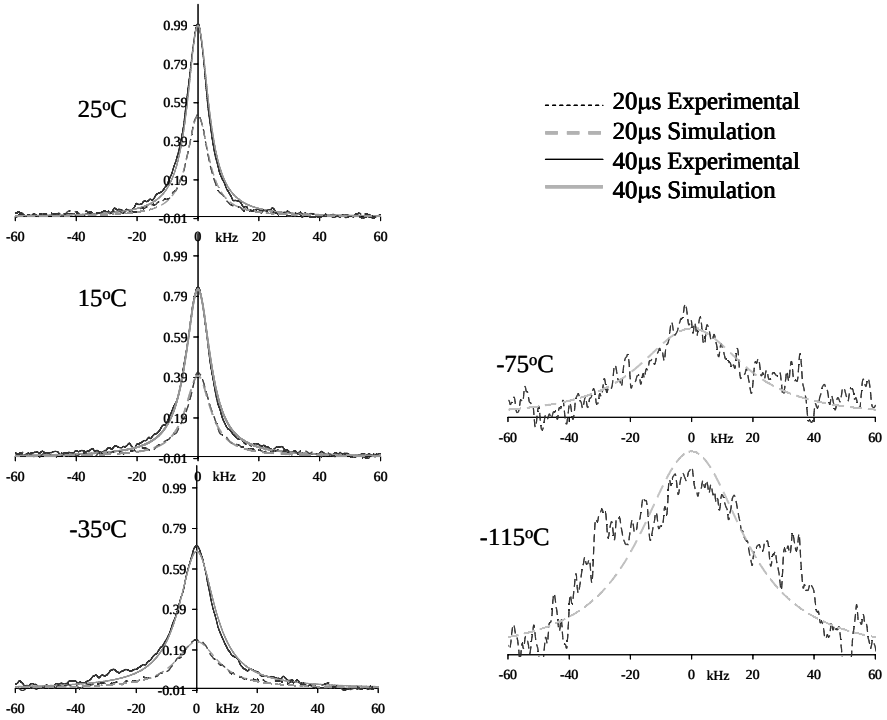

Figure A3.8. CNW4 samples ages 1-2 days; all spectra 21600 scans, except -75°C and -115°C 3600 scans.

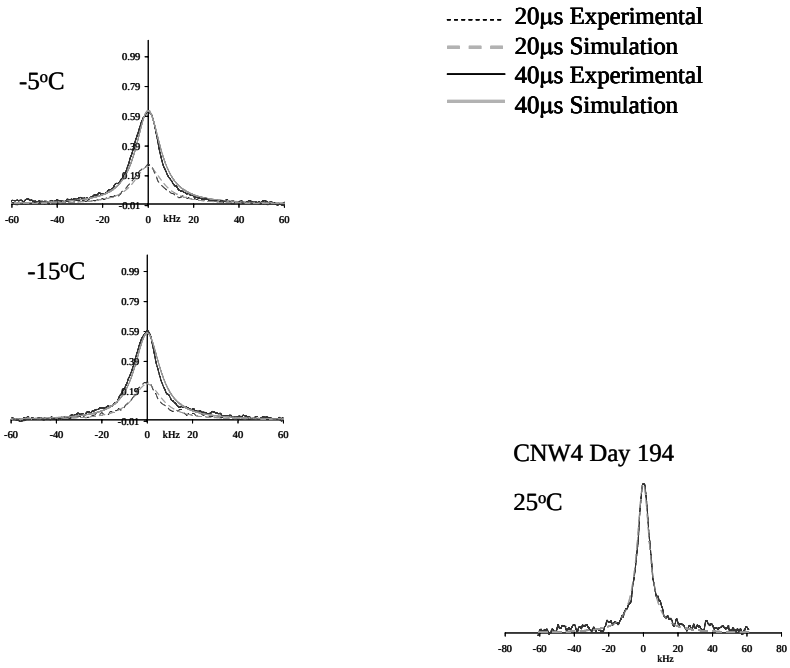

Figure A3.9. CNW4 samples aged 21 days, except as indicated; all spectra 21600 scans, except 25°C 7200 scans.

Table A3.3. CNW pseudo-ISO peak widths at half-height, δν (+2 kHz), for spectra collected at different ages with 40μs techo and processed with 1 kHz line broadening

Sample	Temp (C)	Ages		
CNW2		Days 1-4	Day 80	Day 156
	25	9.7[a,b]	10.7[b]	10.6[a,c]
	15	10.2[b]	10.6[b]	
	-5	12.7[b]		
	-15	14.9[b]	13.4[b]	
	-25	16.4[d]	18.1[b,e]	
	-35		22.9[b]	
	-75			49.3[f,g]
CNW4		Days 1-2	Day 14-21	Day 52
	25	9.7[a,b]		11.6[a,c]
	15	11.2[b]		
	-5		17.2[b]	
	-15		17.7[b]	
	-25			
	-35	20.8[b]		
	-75	58.1[f,g]		
	-115	61[g,h]		

[a]22.5°C; [b]21,600 scans; [c]86,400 scans; [d]13,096 scans; [e]average value for duplicate samples (18.4 and 17.7 kHz, respectively, on Days 80 and 81); [f]3600 scans; [g]peak appearance is a mix of Lorentzian and Pake; [h]7200 scans.

Table A3.4. CNW peaks areas for spectra collected at different ages with 21,600 scans using 40μs τ_{echo} processed with 1 kHz line broadening

Sample	Temp (C)	Ages		
CNW2		Days 1-4	Day 80	Day 156
	25	9.7[a,b]	10.7[b]	10.6[a,c]
	15	10.2[b]	10.6[b]	
	-5	12.7[b]		
	-15	14.9[b]	13.4[b]	
	-25	16.4[d]	18.1[b,e]	
	-35		22.9[b]	
	-75			49.3[f,g]
CNW4		Days 1-2	Day 14-21	Day 52
	25	9.7[a,b]		11.6[a,c]
	15	11.2[b]		
	-5		17.2[b]	
	-15		17.7[b]	
	-25			
	-35	20.8[b]		
	-75	58.1[f,g]		
	-115	61[g,h]		

[a]22.5°C; [b]21,600 scans; [c]86,400 scans; [d]13,096 scans; [e]average value for duplicate samples (18.4 and 17.7 kHz, respectively, on Days 80 and 81); [f]3600 scans; [g]peak appearance is a mix of Lorentzian and Pake; [h]7200 scans.

A3.3. SAMPLE SWCNT2

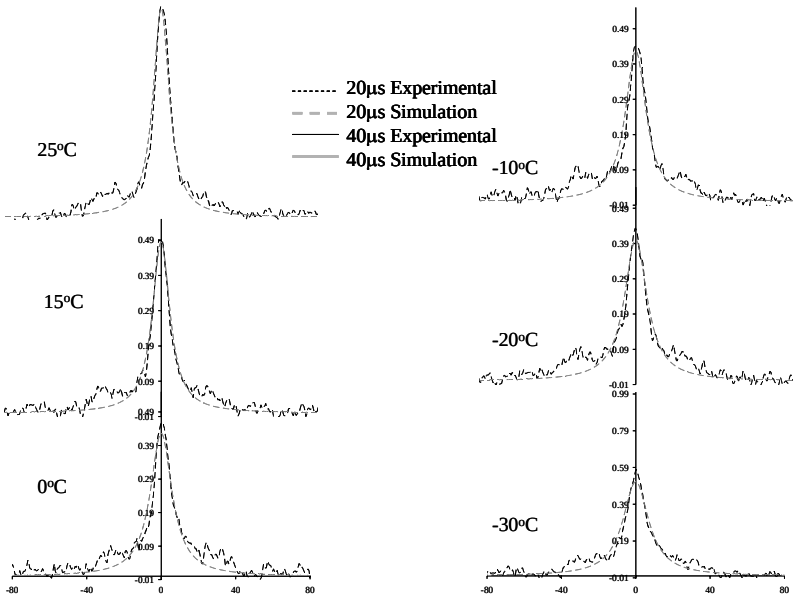

Figure A3.10. Sample SWCNT2, aged 1 day; all spectra 3600 scans, except 25°C 7200 scans.

A4. FITS OF SAMPLE ActC2 WITH AN ATTEMPTED MOTIONAL MODEL SHOWING PREFERENTIAL ORIENTATION OF BENZENE MOLECULES IN MICROPORES

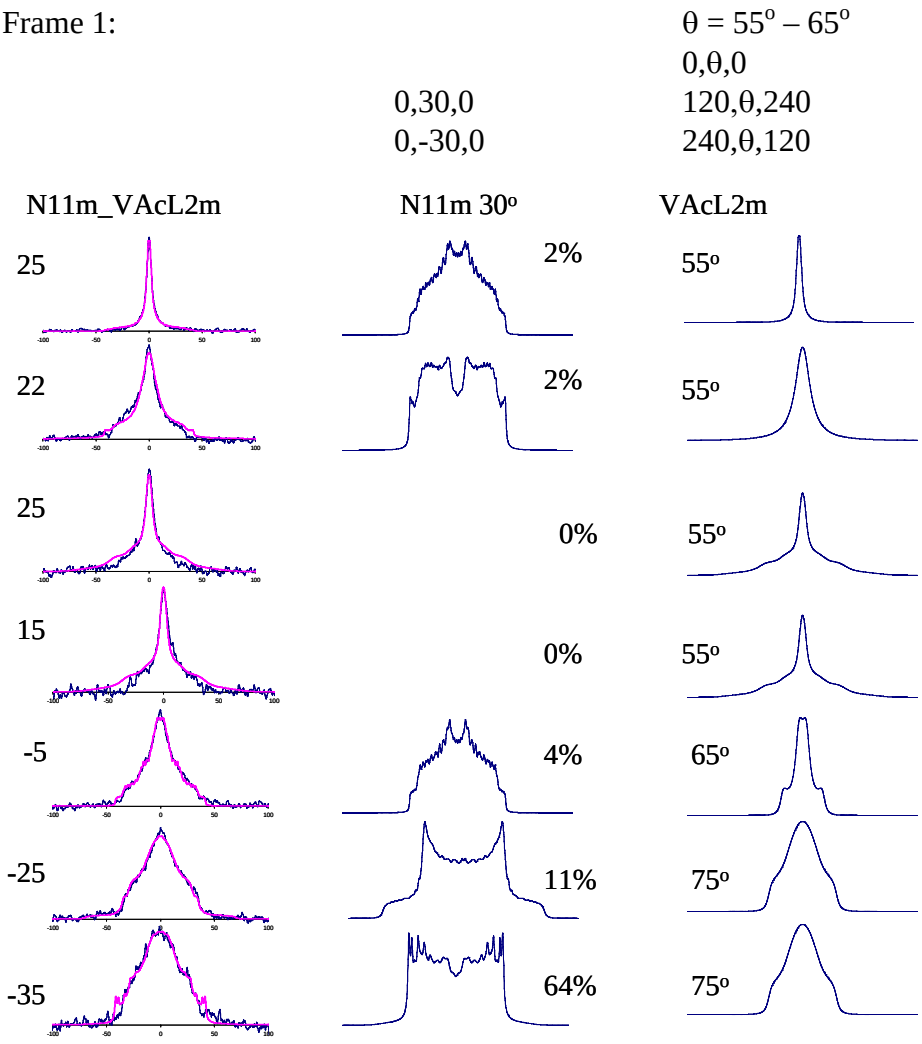

Figure A4.1. Fits on the left (experimental in blue, simulated in pink) to two-component motional models; on the right are simulated component spectra selected in the fit with the Euler angles for their respective first motional frame (both motions also include a second frame with a C_6 rotation), along with the % of the 30° wag component (N11m) and the selected θ angle for the VAcL2m.

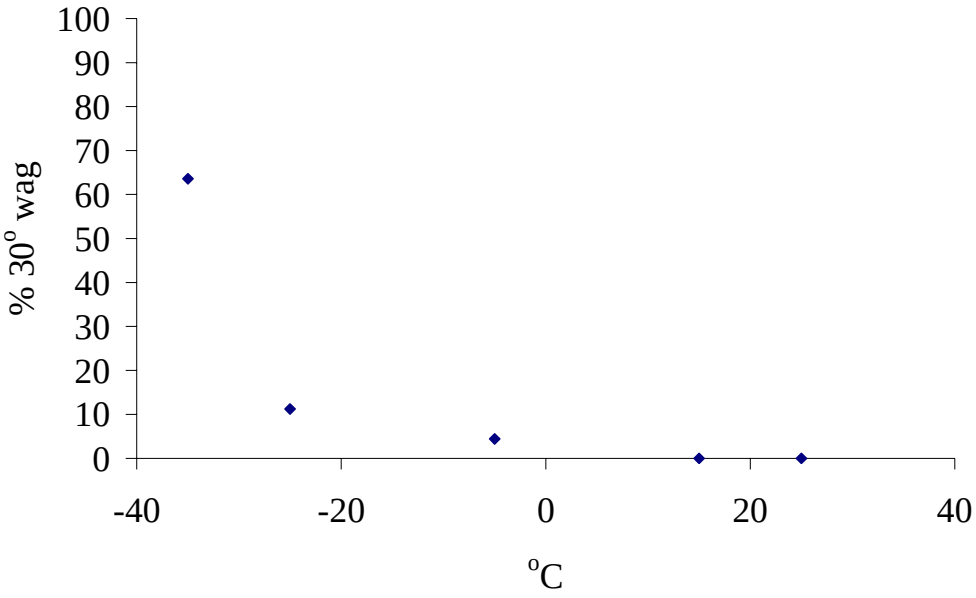

Figure A4.2. Plot of 30° wag component (N11m) at different temperatures.

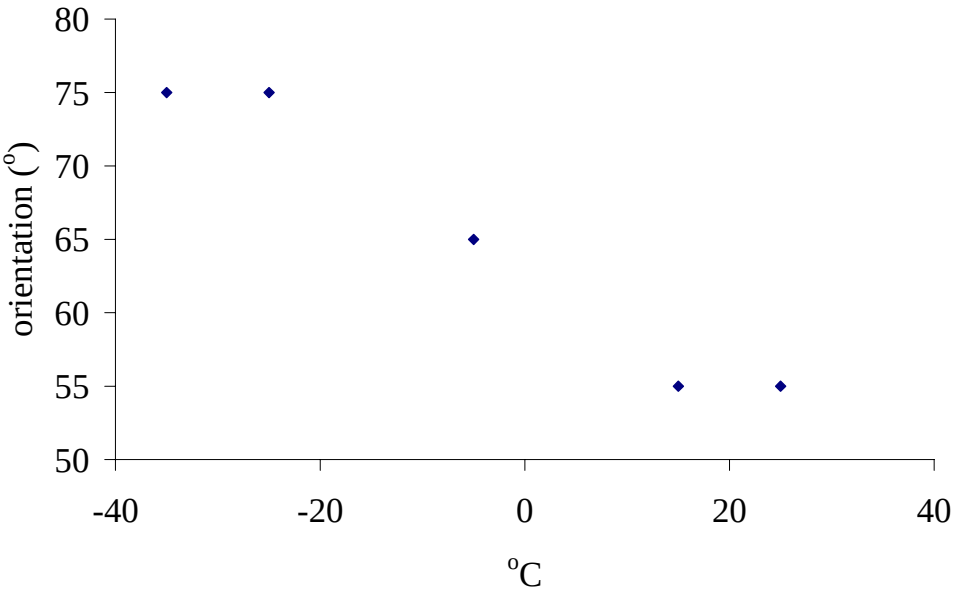

Figure A4.3. Plot of the θ orientation of the VAc2Lm (wobble-like) component.

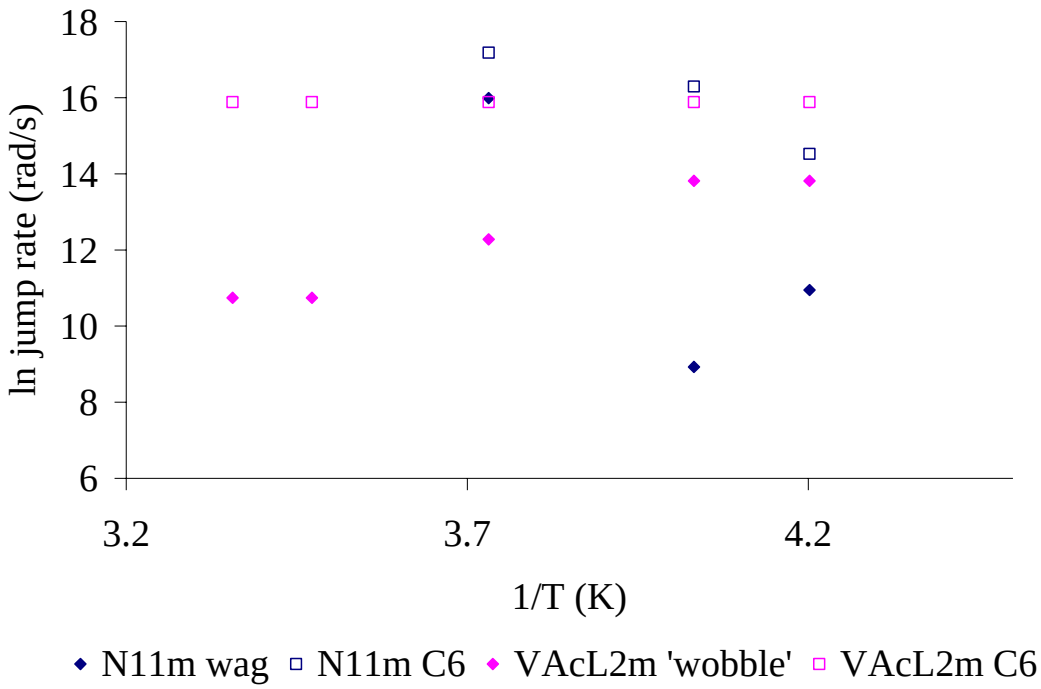

Figure A4.4. Arrhenius plots for the fitted motions.

The N11m wag library contained 196 spectra with 30° wag rates ranging from 1 x 10_3 rad/s to 5 x 10^8 rad/s and C_6 rates ranging from 1 x 10^4 rad/s to 1 x 10^9 rad/s. The VAcL2m "wobble-like" library contained 80 spectra with "wobble" rates ranging from 1 x 10^4 rad/s to 1 x 10^6 rad/s and associated C_6 rates from 1 x 10^6 rad/s to 1 x 10^6 to 5 x 10^8 rad/s. The "wobble-like" motion only contained sites on the outer cone, whereas a wobble also contains sites in the middle of the cone. The "wobble-like" angle, θ, could take on values of 55°, 60°, 65°, 70°, or 75°.